Hybrid approach, combining computational and machine-learning models, for the analysis of myocardial strain and cardiac function evaluation.

Marion Taconné

COLLEGE SCIENCES
DOCTORAL DE LA VIE
BRETAGNE ET DE LA SANTE

Université de Rennes

THÈSE DE DOCTORAT DE

L'UNIVERSITÉ DE RENNES

ÉCOLE DOCTORALE N° 637
Sciences de la Vie et de la Santé
Spécialité : *Analyse et Traitement de l'Information et des Images Médicales*

Par

Marion TACONNÉ

Hybrid approach, combining computational and machine-learning models, for the analysis of myocardial strain and cardiac function evaluation

Thèse présentée et soutenue à Rennes, le 30 août 2023
Unité de recherche : Laboratoire Traitement du Signal et de l'Image (LTSI), UMR Inserm 1099

Rapporteurs avant soutenance :

Valentina D.A. CORINO	Professeure associée des Universités, Politecnico Milano
Julien OSTER	Chargé de Recherche Inserm (HdR), Université de Lorraine

Composition du Jury :

Président :	Jens-Uwe VOIGT	Professeur des Universités et Praticien Hospitalier, University Hospitals Leuven
Examinateurs :	Valentina D.A. CORINO	Professeure associée des Universités, Politecnico Milano
	Julien OSTER	Chargé de Recherche Inserm (HdR), Université de Lorraine
	Alfredo HERNÁNDEZ	Directeur de Recherche Inserm, Université de Rennes
Dir. de thèse :	Erwan DONAL	Professeur des Universités et Praticien Hospitalier, CHU de Rennes
Co-dir. de thèse :	Virginie LE ROLLE	Maitre de conférences (HdR), LTSI-Inserm, Université de Rennes

Remerciements

First of all, I would like to thank every member of the jury for having accepted the invitation. It was such an honour for me. I want to thank the professor Jens-Uwe Voigt, the associate professor Valentina D.A. Corino, and the doctor Julien Oster, for the quality of their comments, their questions and theirs suggestions.

Je voudrais ensuite remercier profondément mes directeurs de thèse Erwan Donal et Virginie le Rolle, dont la présence a rendu ces trois années de recherche passionnantes. Leur engagement indéfectible dans mon projet de thèse et leurs compétences respectives ont été les principaux moteurs de ma réussite. Je suis particulièrement reconnaissante envers Virginie pour ses précieux conseils, sa présence et sa bienveillance constante. Elle a été à la fois ma mentore et mon soutien infaillible tout au long de ces années. Quant à Erwan, son expertise et ses encouragements m'ont permis d'aborder ma recherche avec finesse et de faire le pont vers la pratique clinique. Toujours de bon conseil, il a su créer une dynamique collaborative en m'entourant d'une superbe équipe clinique prête à s'associer à des ingénieurs. Je tiens donc à remercier Arnaud Hubert, Vasileios Panis et particulièrement Adrien Al Wazzan pour le temps consacré et leurs expertises. Je les remercie pour leurs précieuses contributions dans mes travaux de thèse.

Je souhaite également remercier Alfredo Hernandez et Elena Galli pour leur implication et leur expertise précieuse dans mon travail de recherche. Leur contribution a été inestimable et a grandement enrichi mes travaux. Je suis honorée d'avoir pu travailler avec une équipe aussi passionnée et inspirante et je n'oublie pas le travail de me prédécesseurs sur les différents projets: Kimi Owashi et Alban Gallard.

Je remercie aussi Lotfi Senhadji et Mireille Garreau, directeur et directrice successifs du LTSI pour leur accueil ainsi que la super atmosphère qui règne au laboratoire. Je remercie aussi Fabrice Tudoret pour son support technique et sa bonne humeur.

Je tiens aussi à remercier Fanny Noury, Marie-Bernadette Piel, Laurent Parize et Mariko Dunseath-Terao pour m'avoir accueillie dans leurs classes respectives à l'Université et m'avoir transmis leur goût de l'enseignement.

Un grand merci à tous les membres du laboratoire grâce auxquels il aura toujours été un plaisir de venir travailler. Je suis particulièrement reconnaissante d'avoir été entourée d'une si belle équipe de doctorants, postdoctorants et stagiaires avec qui j'ai pu travailler étroitement ou partager mes pauses déjeuner, remplies de rires, de bonne humeur et de pâtisseries.

Les mots ne suffisent pas à exprimer toute ma gratitude envers toutes les personnes qui m'ont soutenue et accompagnée tout au long de ce parcours académique. Je remercie également mes proches, ma famille et mes amis, pour leur soutien constant tout au long de cette aventure.

À tous ceux qui ont contribué de près ou de loin à mon parcours, je vous suis infiniment reconnaissant et je vous adresse mes plus sincères remerciements.

Résumé en français

L'insuffisance cardiaque est un état pathologique caractérisé par une capacité diminuée à pomper le sang et à fournir suffisamment d'oxygène et de nutriments à tous les organes [1, 2]. Initialement, le diagnostic est clinique et marqué par une congestion hydrique. Elle peut être liée soit à une insuffisance ventriculaire droite, soit à une insuffisance ventriculaire gauche, ou le plus souvent lié aux deux cavités ventriculaires. Elle est de plus en plus répandue et touche plus de 26 millions de personnes dans le monde [3], entraînant plus d'un million d'hospitalisations en Europe et en Amérique du Nord chaque année [4]. Le coût pour la société est significatif, estimé à 2% des dépenses totales de santé. Malgré de nombreuses avancées thérapeutiques, à la fois pharmacologiques et technologiques, son pronostic demeure préoccupant avec un taux d'événements majeurs à six mois (mortalité et hospitalisation pour insuffisance cardiaque) qui approche 50% après la première hospitalisation pour insuffisance cardiaque aiguë en France [5].

L'évaluation de la fonction ventriculaire gauche reste un enjeu majeur en cardiologie, car une multitude de traitements dépendent de cette évaluation. Malgré la pathophysiologie complexe et la variété de méthodes d'analyse de la fonction ventriculaire gauche, l'évaluation de la fraction d'éjection du ventricule gauche (FEVG) reste le paramètre de référence en routine clinique. Les limites de ce paramètre sont bien connues et comprennent le manque de reproductibilité intra- et inter-observateur, la sensibilité à la postcharge, au remodelage ventriculaire, et d'autres [6–8].

Pour pallier ces limites, l'analyse des courbes de strain, issues des images échocardiographiques semble être un outil prometteur pour l'évaluation de la fonction cardiaque [9–15]. Cette méthode acquiert de manière semi-automatique des courbes de déformation régionales qui représentent la déformation des parois de différentes régions du myocarde. Bien que de précédentes recherches aient suggéré que l'analyse du strain pourrait servir d'alternative pour quantifier la fonction cardiaque, les recommandations internationales actuelles négligent encore la valeur de cette approche [7]. La plupart des méthodes d'analyse du strain présentées dans la littérature sont basées sur les temps et les valeurs des pics des courbes de strain, ignorant leurs morphologies et dynamiques. Cette dernière partie est la plus difficile dû à la multidimensionnalité du problème. En effet, de nombreux facteurs entrent en jeu dans le processus de contraction du ventricule gauche : les interactions mécano-hydrauliques, l'activation électrique et sa propagation, etc.

Ces dernières années, la modélisation et l'apprentissage automatique ("machine learning") sont devenus de plus en plus populaires en recherche biomédicale, en particulier pour la prédiction, le diagnostic et la stratification des risques, ainsi que dans le développement de thérapies personnalisées [16–19]. Les deux approches, bien que différentes par essence, se sont avérées

précieuses pour aider à comprendre les interactions complexes et multifactorielles de cette pathologie. La modélisation se distingue par l'intégration de connaissances physiologiques dans la chaîne de traitement des données. Ces types de méthodes sont au cœur des approches de type "jumeau numérique" qui ont un potentiel considérable pour améliorer les diagnostics, les traitements et la gestion des maladies, en permettant une approche plus précise et personnalisée au patient. L'apprentissage automatique, quant à lui, étant axée sur les données, permet des analyses de larges bases de données multimodales sans présupposés introduits par l'homme.

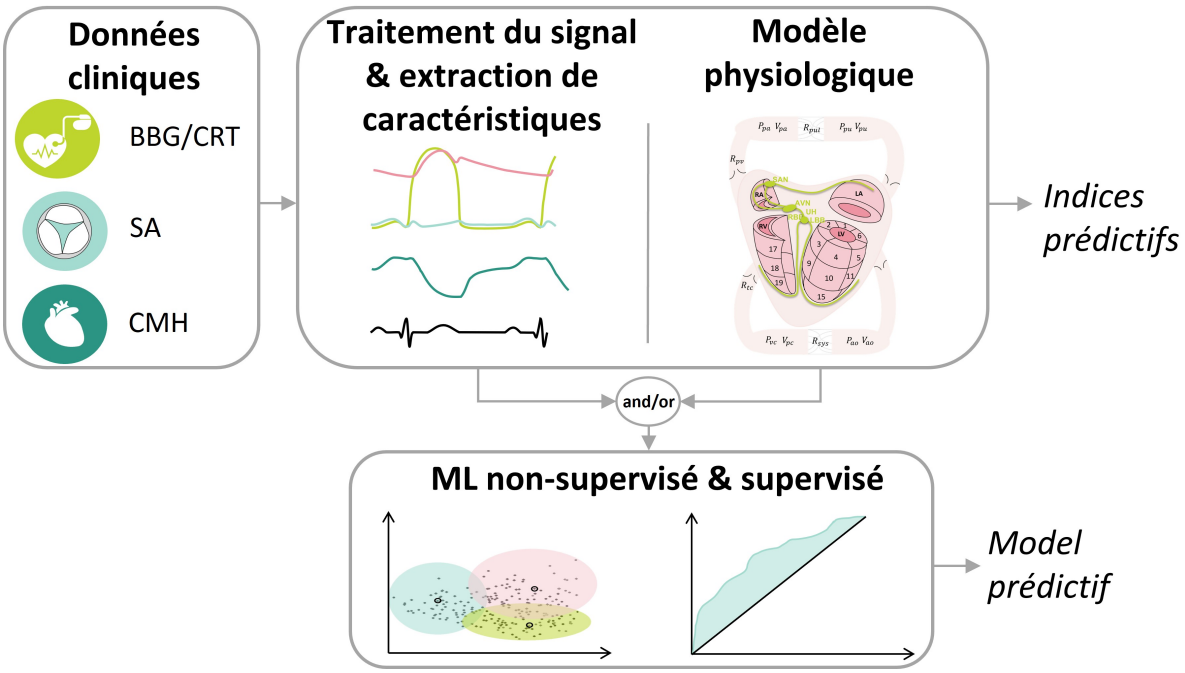

Figure 1: Illustration de la méthodologie avec : i) les bases de données cliniques : Bloc de Branche Gauche (BBG) / Cardiac Resynchronization Therapy (CRT), Sténose Aortique (SA) et CardioMyopathie Hyperthrophique (CMH), ii) le traitement du signal, l'extraction de caractéristiques et modèle physiologique et iii) le Machine Learning (ML) non-supervisé et supervisé.

Dans ce contexte, les travaux de thèse concernent l'évaluation de la fonction cardiaque en utilisant des méthodologies comprenant des modèles computationnels et des algorithmes d'apprentissage automatique/Machine Learning (ML). La combinaison de ces deux approches a été déclinée à différents phénotypes d'insuffisance cardiaque (Figure 1) :

1. La première application de cette thèse consiste en la description d'un modèle computationnel et du processus d'identification pour la création de jumeau numérique de patient avec un bloc de branche gauche (BBG). Une forte correspondance a été observée entre les signaux de strain estimés et observés de 20 patients BBG et 10 patients sains de la base. Les résultats ont montré que les morphologies de strain sont liées à la fois au retard de conduction électrique et à l'hétérogénéité de contractilité du myocarde. L'approche à base de modèles permet d'apporter des informations complémentaires par région sur la

fonction électrique et mécanique du ventricule gauche à partir de l'analyse des données échocardiographiques.

2. La seconde application propose des approches combinant modélisation et ML pour analyser les courbes de strain des patients éligibles à la thérapie de resynchronisation cardiaque (CRT) et propose de nouvelles méthodes pour améliorer la prédiction de la réponse de chaque patient à la CRT.

   i) Dans un premier temps, des approches de regroupement (clustering) ont été proposées pour caractériser les profils de patient éligible à la CRT. Un premier clustering sur des données cliniques, électrocardiographiques, échocardiographiques et de nouveaux indices extraits des courbes de strain de 250 patients éligibles a été enrichi de cinq jumeaux numériques représentatifs des clusters. La réponse à la thérapie est définie par une diminution d'au moins 15% du volume systolique du ventricule gauche à six mois de suivi, et a été évaluée pour chaque patient. Le clustering a permis de proposer cinq phénotypes de patients insuffisants cardiaques avec des taux de réponse différents à la thérapie. Ces phénotypes de patients atteints d'insuffisance cardiaque et éligibles à la CRT se basent sur des indices classiques ainsi que de nouveaux indices tirés du strain, particulièrement interprétables physiologiquement.

   ii) Ensuite, une approche similaire a été appliquée sur les paramètres extraits des jumeaux numériques créés pour 162 patients de la base. Nos résultats soulignent l'importance à la fois de la contractilité myocardique et des temps d'activation électrique dans la réponse à la CRT. Cette approche combinée apparaît comme un outil prometteur pour améliorer la compréhension des mécanismes du ventricule gauche et l'évaluation de la fonction cardiaque chez les patients éligible à la CRT.

   iii) Enfin, une autre combinaison des techniques de ML et des jumeaux numériques a été appliquée à cette même base de données prospective. Les paramètres extraits des jumeaux numériques sont devenus les entrées d'un algorithme de ML supervisé et ont permis la création d'un classifieur de réponse ou non à la CRT. En plus de proposer des caractéristiques explicables aux courbes de strain personnalisées à chaque patient, les paramètres proposés améliorent la prédiction de la réponse à la thérapie de resynchronisation cardiaque.

   Les perspectives futures consisteront en la validation de ces méthodes sur des bases de données prospectives multicentriques plus importantes.

3. La troisième application consiste à proposer une méthode non invasive d'estimation de la pression du ventricule gauche afin d'obtenir des indices de travail myocardique dans le cas de la sténose aortique (SA). Un modèle computationnel similaire est utilisé, suivi d'un processus d'identification de parametres pour 67 patients atteints de SA. L'objectif est d'améliorer l'approche à base de modèle pour évaluer non invasivement la pression du ventricule gauche proposée dans notre équipe [20, 21]. Ensuite, de comparer et d'évaluer l'estimation de la pression du ventricule gauche avec la méthode de Fortuni et al. [22]

adaptée de Russel et al. [23, 24]. L'estimation de la pression ventriculaire gauche étant essentielle dans le calcul du travail myocardique, le travail calculé avec chaque méthode d'estimation de pression est comparé avec celui calculé avec la pression invasive chez des patients atteints de SA sévère et modérée de la base de données. Les deux méthodes présentent une bonne concordance avec les indices de travail myocardique calculés à partir de pressions invasives. L'évaluation du travail myocardique pourrait avoir une importance significative dans la prédiction du pronostic des patients atteints de sténose aortique asymptomatique sévère sans dysfonctionnement du ventricule gauche. De plus, il pourrait aider dans la décision du remplacement de valve ainsi que des critères d'intervention chirurgicale qui continuent d'être débattus pour ces patients.

4. La dernière application consiste à proposer des caractéristiques extraites des courbes de strain pour la classification des patients atteints de cardiomyopathie hypertrophique (CMH) présentant un risque de mort subite. L'algorithme d'apprentissage automatique combine des données hétérogènes : cliniques, d'imagerie et des paramètres extraits des courbes de strain du ventricule gauche. La prédiction de mort subite et d'arythmie ventriculaire se révèle être de meilleure qualité pour ces patients atteints de CMH avec ces nouveaux paramètres extraits du strain. Cette nouvelle méthode d'extraction de paramètres issus des courbes de strain est complètement automatisée.

L'approche adoptée dans ce travail de thèse, combinant à la fois de la modélisation et des méthodes classiques de traitement du signal et d'apprentissage automatique, constitue une proposition originale visant à rapprocher la modélisation cardiaque de la pratique clinique quotidienne. La méthodologie proposée représente une avancée vers l'utilisation de techniques intégrant des connaissances explicites pour évaluer la fonction cardiaque, dans le but d'améliorer l'interprétabilité des indices extraits de l'échocardiographie. Ces applications sont de bons exemples de la manière dont les approches classiques de machine learning basées sur le traitement du signal et de données peuvent être combinées à des jumeaux numériques.

BIBLIOGRAPHIE

[1] Kemp C.D. and Conte J.V. The pathophysiology of heart failure. *Cardiovasc. Pathol.*, vol. 21, 365–371 (2012).

[2] Maddox T.M., Januzzi J.L., Allen L.A., Breathett K., Butler J., Davis L.L., Fonarow G.C., Ibrahim N.E., Lindenfeld J.A., Masoudi F.A., Motiwala S.R., Oliveros E., Patterson J.H., Walsh M.N., Wasserman A., Yancy C.W., and Youmans Q.R. 2021 Update to the 2017 ACC Expert Consensus Decision Pathway for Optimization of Heart Failure Treatment: Answers to 10 Pivotal Issues About Heart Failure With Reduced Ejection Fraction: A Report of the American College of Cardiology Solution Set Oversight Committee. *J. Am. Coll. Cardiol.*, vol. 77 (2021).

[3] Virani S.S., Alonso A., Benjamin E.J., Bittencourt M.S., Callaway C.W., Carson A.P., Chamberlain A.M., Chang A.R., Cheng S., Delling F.N., Djousse L., Elkind M.S., Ferguson J.F., Fornage M., Khan S.S., Kissela B.M., Knutson K.L., Kwan T.W., Lackland D.T., Lewis T.T., Lichtman J.H., Longenecker C.T., Loop M.S., Lutsey P.L., Martin S.S., Matsushita K., Moran A.E., Mussolino M.E., Perak A.M., Rosamond W.D., Roth G.A., Sampson U.K., Satou G.M., Schroeder E.B., Shah S.H., Shay C.M., Spartano N.L., Stokes A., Tirschwell D.L., VanWagner L.B., and Tsao C.W. *Heart disease and stroke statistics—2020 update a report from the American Heart Association*, vol. 141. Am Heart Assoc (2020).

[4] Ambrosy A.P., Fonarow G.C., Butler J., Chioncel O., Greene S.J., Vaduganathan M., Nodari S., Lam C.S., Sato N., Shah A.N., and Gheorghiade M. The global health and economic burden of hospitalizations for heart failure: Lessons learned from hospitalized heart failure registries. *J. Am. Coll. Cardiol.*, vol. 63, 1123–1133 (2014).

[5] Tuppin P., Cuerq A., Peretti C.D., Fagot-campagna A., Danchin N., Juillière Y., Allemand H., Bauters C., Drici M.d., Hagège A., Jondeau G., Jourdain P., Leizorovicz A., and Paccaud F. Two-year outcome of patients after a first hospitalization for heart failure : A national Devenir à deux ans après une première hospitalisation pour. *Archives of Cardiovascular Diseases*, 158–168 (2014).

[6] Lang R.M., Badano L.P., Mor-Avi V., Afilalo J., Armstrong A., Ernande L., Flachskampf F.A., Foster E., Goldstein S.A., Kuznetsova T., Lancellotti P., Muraru D., Picard M.H., Rietzschel E.R., Rudski L., Spencer K.T., Tsang W., and Voigt J.U. Recommendations for cardiac chamber quantification by echocardiography in adults: An update from the American society of echocardiography and the European association of cardiovascular imaging. *Eur. Heart J. Cardiovasc. Imaging*, vol. 16, 233–271 (2015).

[7] Glikson M., Nielsen J.C., Kronborg M.B., Michowitz Y., Auricchio A., Barbash I.M., Barrabés J.A., Boriani G., Braunschweig F., Brignole M., Burri H., Coats A.J., Deharo J.C., Delgado V., Diller G.P., Israel C.W., Keren A., Knops R.E., Kotecha D., Leclercq C., Merkely B., Starck C., Thylén I., Tolosana J.M., Leyva F., Linde C., Abdelhamid M., Aboyans V., Arbelo E., Asteggiano R., Barón-Esquivias G., Bauersachs J., Biffi M., Birgersdotter-Green U., Bongiorni M.G., Borger M.A., Celutkienė J., Cikes M., Daubert J.C., Drossart I., Ellenbogen K., Elliott P.M., Fabritz L., Falk V., Fauchier L., Fernández-Avilés F., Foldager D., Gadler F., De Vinuesa P.G.G., Gorenek B., Guerra J.M., Hermann Haugaa K., Hendriks J., Kahan T., Katus H.A., Konradi A., Koskinas K.C., Law H., Lewis B.S., Linker N.J., Løchen M.L., Lumens J., Mascherbauer J., Mullens W., Nagy K.V., Prescott E., Raatikainen P., Rakisheva A., Reichlin T., Ricci R.P., Shlyakhto E., Sitges M., Sousa-Uva M., Sutton R., Suwalski P., Svendsen J.H., Touyz R.M., Van Gelder I.C., Vernooy K., Waltenberger J., Whinnett Z., Witte K.K., Kronborg M.B., Michowitz Y., Auricchio A., Barbash I.M., Barrabés J.A., Boriani G., Braunschweig F., Brignole M., Burri H., Coats A.J., Deharo J.C., Delgado V., Diller G.P., Israel C.W., Keren A., Knops R.E., Kotecha D., Leclercq C., Merkely B., Starck C., Thylén I., and Tolosana J.M. 2021 ESC Guidelines on cardiac pacing and cardiac resynchronization therapy. *Eur. Heart J.*, vol. 42, 3427–3520 (2021).

[8] Stokke T.M., Hasselberg N.E., Smedsrud M.K., Sarvari S.I., Haugaa K.H., Smiseth O.A., Edvardsen T., and Remme E.W. Geometry as a Confounder When Assessing Ventricular Systolic Function: Comparison Between Ejection Fraction and Strain. *J. Am. Coll. Cardiol.*, vol. 70, 942–954 (2017).

[9] Donal E., Galli E., Hubert A., and Bouzille G. New indices of left ventricular function: let's move from ejection fraction to more physiological parameters. *J. Physiol.*, vol. 595, 3959–3960 (2017).

[10] Smiseth O.A., Torp H., Opdahl A., Haugaa K.H., and Urheim S. Myocardial strain imaging: How useful is it in clinical decision making? *Eur. Heart J.*, vol. 37, 1196–1207b (2016).

[11] Potter E. and Marwick T.H. Assessment of Left Ventricular Function by Echocardiography: The Case for Routinely Adding Global Longitudinal Strain to Ejection Fraction (2018).

[12] Springer Japan, Klaeboe L.G. and Edvardsen T. Echocardiographic assessment of left ventricular systolic function (2019).
Accessed on 25/10/2021 from: https://doi.org/10.1007/s12574-018-0405-5

[13] Magne J., Cosyns B., Popescu B.A., Carstensen H.G., Dahl J., Desai M.Y., Kearney L., Lancellotti P., Marwick T.H., Sato K., Takeuchi M., Zito C., Casalta A.C., Mohty D., Piérard L., Habib G., and Donal E. Distribution and Prognostic Significance of Left Ventricular Global Longitudinal Strain in Asymptomatic Significant Aortic Stenosis: An Individual Participant Data Meta-Analysis. *JACC Cardiovasc. Imaging*, vol. 12, 84–92 (2019).

[14] Risum N., Tayal B., Hansen T.F., Bruun N.E., Jensen M.T., Lauridsen T.K., Saba S., Kisslo J., Gorcsan J., and Sogaard P. Identification of Typical Left Bundle Branch Block Contraction by Strain Echocardiography Is Additive to Electrocardiography in Prediction of Long-Term Outcome after Cardiac Resynchronization Therapy. *J. Am. Coll. Cardiol.*, vol. 66, 631–641 (2015).

[15] van Everdingen W.M., Walmsley J., Cramer M.J., van Hagen I., De Boeck B.W., Meine M., Delhaas T., Doevendans P.A., Prinzen F.W., Lumens J., and Leenders G.E. Echocardiographic Prediction of Cardiac Resynchronization Therapy Response Requires Analysis of Both Mechanical Dyssynchrony and Right Ventricular Function: A Combined Analysis of Patient Data and Computer Simulations. *J. Am. Soc. Echocardiogr.*, vol. 30, 1012–1020.e2 (2017).

[16] Niederer S.A., Lumens J., and Trayanova N.A. Computational models in cardiology. *Nat. Rev. Cardiol.*, vol. 16, 100–111 (2019).

[17] Trayanova N.A. and Rice J.J. Cardiac electromechanical models: From cell to organ. *Front. Physiol.*, vol. 2 AUG, 1–19 (2011).

[18] Lopez-Jimenez F., Attia Z., Arruda-Olson A.M., Carter R., Chareonthaitawee P., Jouni H., Kapa S., Lerman A., Luong C., Medina-Inojosa J.R., et al. Artificial intelligence in cardiology: present and future. In *Mayo Clinic Proceedings*, vol. 95, 1015–1039. Elsevier (2020).

[19] Johnson K.W., Torres Soto J., Glicksberg B.S., Shameer K., Miotto R., Ali M., Ashley E., and Dudley J.T. Artificial Intelligence in Cardiology (2018).

[20] Owashi K.P., Hubert A., Galli E., Donal E., Hernández A.I., and Rolle V.L. Model-based estimation of left ventricular pressure and myocardial work in aortic stenosis. *PLoS One*, vol. 15, 1–18 (2020).

[21] Owashi K.P. *Model-based analysis of myocardial strains for the evaluation of cardio- vascular function*. Ph.D. thesis, Université Rennes 1 (2021).

[22] Fortuni F., Butcher S.C., van der Kley F., Lustosa R.P., Karalis I., de Weger A., Priori S.G., van der Bijl P., Bax J.J., Delgado V., and Ajmone Marsan N. Left ventricular myocardial work in patients with severe aortic stenosis Federico. *J. Am. Soc. Echocardiogr.*, page 124658 (2020).

[23] Russell K., Eriksen M., Aaberge L., Wilhelmsen N., Skulstad H., Remme E.W., Haugaa K.H., Opdahl A., Fjeld J.G., Gjesdal O., Edvardsen T., and Smiseth O.A. A novel clinical method for quantification of regional left ventricular pressurestrain loop area: A non-invasive index of myocardial work. *Eur. Heart J.*, vol. 33, 724–733 (2012).

[24] Russell K., Eriksen M., Aaberge L., Wilhelmsen N., Skulstad H., Gjesdal O., Edvardsen T., and Smiseth O.A. Assessment of wasted myocardial work: A novel method to quantify energy loss due to uncoordinated left ventricular contractions. *Am. J. Physiol. - Hear. Circ. Physiol.*, vol. 305, 996–1003 (2013).

Contents

Acronyms

LTSI *Laboratoire Traitement du Signal et de l'Image (Image and Signal Processing Laboratory)*.

SEPIA *Stimulation thÉrapeutique et monitoring Personnalisés pour l'Insuffisance cardiaque et les Apnées-bradycardies (LTSI team)*.

ACA Aborted Cardiac Arrest.

ACS Acute Coronary Syndrome.

ADASYN Adaptive synthetic sampling.

AHA American Heart Association.

AI Artificial Intelligence.

AR Apical Rocking.

ARP Absolute Refractory Period.

AS Aortic Stenosis.

AUC Area Under Curve.

AV AtrioVentricular.

AVA Aortic Valve Area.

AVC Aortic Valve Closure.

AVN AtrioVentricular Node.

AVO Aortic Valve Opening.

AVR Aortic Valve Replacement.

CAD Coronary Artery Disease.

CRT Cardiac Resynchronization Therapy.

CRT-D Cardiac Resynchronization Therapy Defibrillator.

CRT-P Cardiac Resynchronization Therapy Pacemaker.

CVS CardioVascular System.

DE Differential Evolution algorithm.

DL Deep Learning.

DSS Decision Support System.

DT Deceleration Time.

DTW Dynamic Time Warping.

EA Evolutionary Algorithm.

ECG Electrocardiogram.

EMDF Electro-Mechanical Driving Function.

ESC European Society of Cardiology.

FE Finite Element.

FPR False Positive Rate.

GA Genetic Algorithms.

GCW Global Constructive Work.

GLS Global Longitudinal Strain.

GNW Global Negative Work.

GPW Global Positive Work.

GWE Global Work Efficiency.

GWI Global Work Index.

GWW Global Wasted Work.

HCM Hypertrophic CardioMyopathy.

HF Heart Failure.

ICD Implantable Cardiac Defibrillator.

IVC IsoVolumetric Contraction.

IVR IsoVolumetric Relaxation.

LA Left Atrium.

LBB Left Bundle of Branch.

LBBB Left Bundle of Branch Block.

LGE Late Gadolinium Enhancement.

LHC Left Heart Catheterization.

LL Left Leg.

LV Left Ventricle.

LVEDD Left ventricle End-Diastolic Diameter.

LVEDV Left ventricle End-Diastolic Volume.

LVEF Left Ventricle Ejection Fraction.

LVESD Left ventricle End-Systolic Diameter.

LVESV Left ventricle End-Systolic Volume.

M2SL Multi-formalism Modeling and Simulation Library.

ML Machine Learning.

MRI Magnetic Resonance Imaging.

MVC Mitral Valve Closure.

MVO Mitral Valve Opening.

MW Myocardial Work.

NSVT Non-Sustained Ventricular Tachycardia.

NYHA New-York Heart Association.

OAT One-At-Time.

ODE Ordinary Differential Equations.

OOB 'Out-Of-Bag'.

PaGMO Parallel Global Multiobjective Optimizer.

PCA Principal Component Analysis.

PSL Pressure-Strain Loop.

PyGMO Equivalent of PaGMO in Python language.

RA Right Atrium.

RBB Right Bundle of Branch.

RF Random Forest.

RL Right Leg.

RMSE Root-Mean-Square Error.

ROC Receiver Operating Characteristic.

RRP Relative Refractory Period.

RV Right Ventricle.

SA Sensitivity Analysis.

SADE Self-Adaptive Differential Evolution.

SAN SinoAtrial Node.

SCD Sudden Cardiac Death.

SDD Slow Diastolic Depolarization.

SF Septal Flash.

SPAP Systolic Pulmonary Artery Pressure.

STE Speckle-Tracking Echocardiography.

SV Stroke Volume.

SVD Singular Value Decomposition.

SVM Support-Vector Machines.

SVT Sustained Ventricular Tachycardia.

TAPSE Tricuspid Annular Plane Systolic Excursion.

TAVI Transcatheter Aortic Valve Implantation.

TAVR Transcatheter Aortic Valve Replacement..

TDI Tissue Doppler Imaging.

TEE TransEsophageal Echocardiography.

TPR True Positive Rate.

TTE Trans-Thoracic Echocardiography.

UDP Upstroke Depolarization Period.

UH Upper bundle of His.

VTI Velocity Time Integral.

Introduction

Heart Failure (HF) is a pathological state characterized by a decreased ability to pump blood and provide enough oxygen and nutrients to the body's organs [1, 2]. Initially, the diagnosis is clinical and characterized by fluid congestion, and it can be either related to right ventricular failure or left ventricular failure, or most commonly related to both ventricular cavities. It is becoming increasingly prevalent worldwide and affects over 26 million people globally [3], resulting in over a million hospitalizations in Europe and North America each year [4]. The resulting cost to society is significant, estimated at 2% of overall healthcare expenditures. Despite the numerous therapeutic advances, both pharmacological and technological, its prognosis remains poor with a major event rate at 6 months (mortality and hospitalization for heart failure) that approaches 50% after the first hospitalization for acute heart failure in France [5].

The evaluation of left ventricular function remains a major challenge in cardiology, as a multitude of treatments depend on this evaluation [6]. Despite the complex pathophysiology and the variety of methods to analyze left ventricular function, the assessment of Left Ventricle Ejection Fraction (LVEF) is still the reference method used in clinical routine. The limitations of this feature are well known and include a lack of intra- and inter-observer reproducibility, sensitivity of measurement to afterload, ventricular remodeling, and others [6–8].

Myocardial strain measurements emerge as an ultrasound clinical tool in the 2000s [9] and since then remained mainly in the research domain [10]. This method semi-automatically acquires regional strain traces that represent tissue deformation of different regions of the myocardium. Recently, routine echocardiography starts to include strain measurements as complementary function parameters [7] and they appear as a promising tool for the assessment of myocardial function [11–19]. However, although these prior researches have suggested that analyzing strain traces could serve as an alternative to quantify cardiac function, current guidelines still neglect the value of this approach [6]. In fact, the analysis of strain curves is a difficult issue because of the multidimensionality of the problem and physiological mechanisms involved in the LV contraction process: mechano-hydraulic interactions, electrical activation and propagation... [19, 20] and lack of standardization [21].

This analysis of the patient strain curves could benefit from Artificial Intelligence (AI) tools. In fact, Machine Learning (ML) approaches appear as particularly relevant because of the high-volume multiparametric features extracted from cardiac ultrasound images and the high heterogeneity of patient profiles. For instance, supervised [22, 23] and unsupervised [24] ML methods have been used to predict the response to cardiac resynchronization therapy and identify phenogroups of

patients. Our team has been particularly active in this field [25–33]. In [25], integral-derived longitudinal strain (automatic quantification of strain curves) was proposed to quantify dyssynchrony. In [33], a complete Machine Learning pipeline was proposed to improve the estimation of CRT response and was further validated in [26]. A quantitative analysis of myocardial deformation was presented in [28], for the selection of the most informative echocardiographic views and features for the estimation of CRT response, based on the Random Forest. In [27], features, extracted from regional longitudinal strains, were analyzed using a clustering approach (K-Means) and five clusters were defined, associated with groups of below-average to excellent responders. In [29], myocardial work and integral-derived longitudinal strain were compared in the prediction of CRT-response. In [34], supervised and unsupervised ML methods were used to underscore the value of RV-derived parameters for the prediction of CRT response/survival. Despite these encouraging results, we strongly believe that classification performances should be improved by including knowledge in the data processing.

In this context, model-based analysis or digital twins seems particularly appropriate since it allows the integration of physiological knowledge and could permit to access underlying mechanisms hard to experimentally measure. Most of the cardiac models proposed rely on the Finite Element (FE) method, which uses a 3D mesh geometry to simulate cardiac mechanical activity [35–46]. However, these models are computationally expensive and not easily personalized. They also often fail to consider dynamic loading conditions and interventricular interactions, which require increased model complexity to integrate. To address these challenges, alternative approaches have been proposed that use lower dimension models to represent patient anatomy [17, 47–50], allowing for better clinical translation and inclusion of heart hemodynamics within the entire circulation. In that way, our team had a work history in the modeling methodologies from the formalization of the model integration problem to sensitivity analysis, parameter identification and specification [51–66]. Although these different models have shown promising results, there is a need to adapt these studies to non-invasive, patient-specific data and bring these digital twins to the clinical field and provide patient-specific strain curves interpretation.

The main objective of this thesis is to **propose new methods to analyze LV strain curves of HF patients based on computational model/digital twins and machine learning**. These methods aim at ensuring a more precise and personalized understanding of the left ventricular function of heart failure patients. Explainable AI methods, integrating ML and physiological in-silico models (patient digital twin), need to be proposed to combine physiological knowledge with observed data, using model-based reasoning, to improve the interpretability of the approach while minimizing overfitting and limited robustness. The previous contributions of *LTSI* team (*SEPIA*) are the basis of the work presented here. This methodological framework plays a crucial role in developing new methods for analyzing experimental strain curves. Cardiovascular models, sensitivity analysis and identification methods, proposed by *SEPIA* team, will be used to create accurate physiological markers to the interpretation of cardiac strain based on digital twins and ML.

This approach was applied in four contexts associated with different HF phenotypes (Figure 2):

- Model-based analysis of myocardial strains in left bundle branch block,
- Prediction of response to CRT and characterization of responder profiles,
- Assessment of myocardial work in aortic stenosis patients,
- Prediction of sudden death risk in patients with hypertrophic cardiomyopathy.

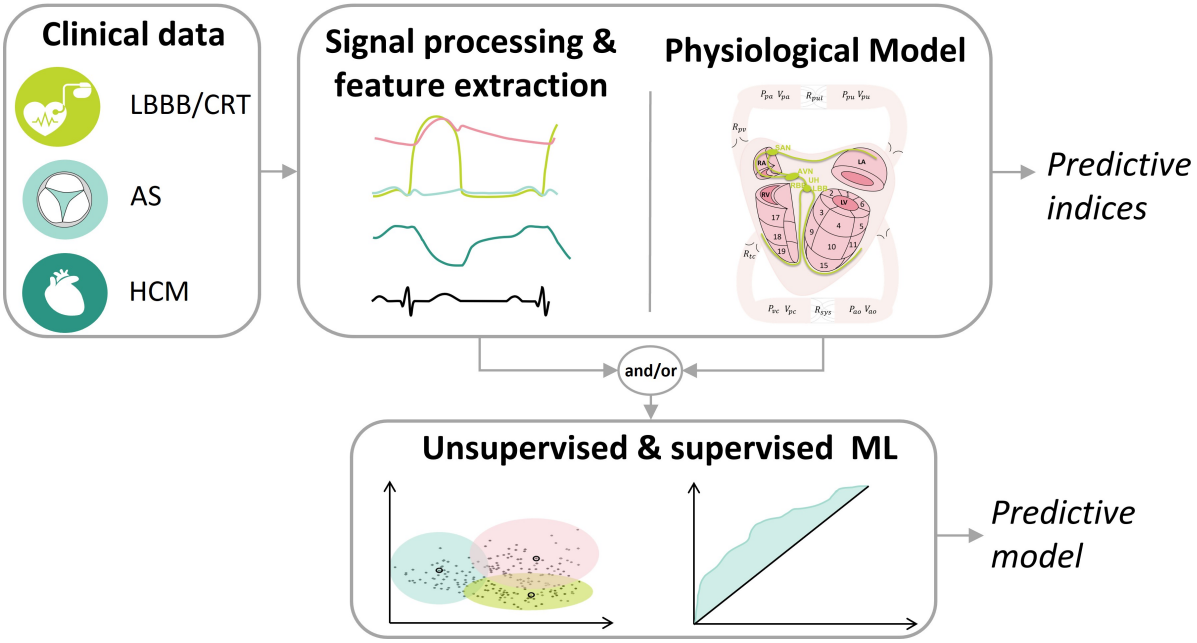

Figure 2: Methodological illustration with: i) the clinical database: Left Bundle of Branch Block (LBBB) / Cardiac Resynchronization Therapy (CRT), Aortic Stenosis (AS) and Hypertrophic CardioMyopathy (HCM), ii) the signal processing and feature extraction and the physiological model, and iii) the unsupervised and supervised Machine Learning (ML).

This thesis is organized as follows:

Chapter 1 presents a description of the main physiological functions that are studied in this work.

Chapter 2 describes the methods and tools for modeling, simulation and analysis that are proposed and applied in this thesis, including supervised and unsupervised ML approaches, a description of the modeling and simulation framework (M2SL), the sensitivity analysis methods (Morris screening method) and the parameter identification approach (Evolutionary algorithms).

Chapter 3 addresses a **model-based analysis of myocardial strains in left bundle branch block**. Model-based approaches may provide a better understanding of myocardial deformations observed in LBBB, since these approaches explicitly represent the fundamental physiological mechanisms involved. Indeed, computational modeling appears as an efficient tool to integrate knowledge, concerning cardiac electrical activation, mechanical properties, and hemodynamic conditions, in the data processing. Chapter 3 aims at proposing a model-based approach for

creating a digital twin able to replicate the patient's myocardial strain curves and analyze the patient-specific parameters of the digital twin model created.

Chapter 4 concerns **the characterization of the responder profiles for Cardiac Resynchronization Therapy (CRT) patient selection**. Cardiac Resynchronization Therapy typically results in reverse remodeling of the left ventricle and has been shown to have a significant positive effect on the management of HF patients with specific conditions. However, despite the significant success observed in randomized clinical trials, around 30% of patients who receive CRT do not respond to treatment [67–70]. Recent studies have shown a relation between strain curves morphologies and CRT response. Nonetheless, evaluating desynchrony patterns in these patients presents a significant challenge. In fact, strains morphologies reflect the dynamics associated with both electrical conduction delays and mechanical cardiac activities. The challenge was to propose a multiparametric approach to address the multifactorial and complexity of the problem as well as the among of data and integrate physiological knowledge to allow a translation to the clinical practice.

Chapter 5 issue focus on **the non-invasive Myocardial Work (MW) estimation of aortic stenosis patients based on a computational model**. Aortic Stenosis (AS) is characterized by a narrowing of the aortic valve opening and a resulting pressure overload on the left ventricle. AS severity is primarily assessed through echocardiography, but treatment decisions also consider ventricular function and symptomatology. The need for reliable methods to evaluate myocardial function impairment in AS patients independently of loading conditions is essential. Myocardial work indices are an interesting afterload-independent alternative to evaluate accurate cardiac function using strain signals and LV pressure curve. Due to the transaortic pressure gradient, the LV pressure estimation of Russel et al. [71, 72] could not be applied. The challenge here was to improve the model-based approach to assess non-invasively LV pressure proposed in our team [57, 58] and to compare the LV pressure estimation with the adapted method of Russel et al. by Fortuni et al. [73]. Chapter 5 will propose an evaluation of the MW calculated with the two LV pressure estimation methods and invasive values in severe and moderate AS patients.

Chapter 6 concerns **the Sudden Cardiac Death (SCD) prediction in Hypertrophic CardioMyopathy (HCM) patients**. Hypertrophic CardioMyopathy (HCM) represents a major cause of Sudden Cardiac Death (SCD), particularly in the young people, with a risk of about 1% per year [74, 75]. Identification of patients at risk of SCD is then a major clinical challenge. However, current international guidelines rely on retrospective evaluations of old HCM cohorts and are based on limited and pre-selected clinical and imaging predictor variables to select patients at risk of SCD [76, 77]. The objective is to propose a machine learning classifier for at-risk patients based on their LV strain curves. Chapter 6 will propose a complete data-processing and machine learning chains for the evaluation of these patients.

BIBLIOGRAPHY

[1] Kemp C.D. and Conte J.V. The pathophysiology of heart failure. *Cardiovasc. Pathol.*, vol. 21, 365–371 (2012).

[2] Maddox T.M., Januzzi J.L., Allen L.A., Breathett K., Butler J., Davis L.L., Fonarow G.C., Ibrahim N.E., Lindenfeld J.A., Masoudi F.A., Motiwala S.R., Oliveros E., Patterson J.H., Walsh M.N., Wasserman A., Yancy C.W., and Youmans Q.R. 2021 Update to the 2017 ACC Expert Consensus Decision Pathway for Optimization of Heart Failure Treatment: Answers to 10 Pivotal Issues About Heart Failure With Reduced Ejection Fraction: A Report of the American College of Cardiology Solution Set Oversight Committee. *J. Am. Coll. Cardiol.*, vol. 77 (2021).

[3] Virani S.S., Alonso A., Benjamin E.J., Bittencourt M.S., Callaway C.W., Carson A.P., Chamberlain A.M., Chang A.R., Cheng S., Delling F.N., Djousse L., Elkind M.S., Ferguson J.F., Fornage M., Khan S.S., Kissela B.M., Knutson K.L., Kwan T.W., Lackland D.T., Lewis T.T., Lichtman J.H., Longenecker C.T., Loop M.S., Lutsey P.L., Martin S.S., Matsushita K., Moran A.E., Mussolino M.E., Perak A.M., Rosamond W.D., Roth G.A., Sampson U.K., Satou G.M., Schroeder E.B., Shah S.H., Shay C.M., Spartano N.L., Stokes A., Tirschwell D.L., VanWagner L.B., and Tsao C.W. *Heart disease and stroke statistics—2020 update a report from the American Heart Association*, vol. 141. Am Heart Assoc (2020).

[4] Ambrosy A.P., Fonarow G.C., Butler J., Chioncel O., Greene S.J., Vaduganathan M., Nodari S., Lam C.S., Sato N., Shah A.N., and Gheorghiade M. The global health and economic burden of hospitalizations for heart failure: Lessons learned from hospitalized heart failure registries. *J. Am. Coll. Cardiol.*, vol. 63, 1123–1133 (2014).

[5] Tuppin P., Cuerq A., Peretti C.D., Fagot-campagna A., Danchin N., Juillière Y., Allemand H., Bauters C., Drici M.d., Hagège A., Jondeau G., Jourdain P., Leizorovicz A., and Paccaud F. Two-year outcome of patients after a first hospitalization for heart failure : A national Devenir à deux ans après une première hospitalisation pour. *Archives of Cardiovascular Diseases*, 158–168 (2014).

[6] Glikson M., Nielsen J.C., Kronborg M.B., Michowitz Y., Auricchio A., Barbash I.M., Barrabés J.A., Boriani G., Braunschweig F., Brignole M., Burri H., Coats A.J., Deharo J.C., Delgado V., Diller G.P., Israel C.W., Keren A., Knops R.E., Kotecha D., Leclercq C., Merkely B., Starck C., Thylén I., Tolosana J.M., Leyva F., Linde C., Abdelhamid M., Aboyans V., Arbelo E., Asteggiano R., Barón-Esquivias G., Bauersachs J., Biffi M., Birgersdotter-Green U., Bongiorni M.G., Borger M.A., Celutkienė J., Cikes M., Daubert J.C., Drossart I., Ellenbogen K., Elliott P.M., Fabritz L., Falk V., Fauchier L., Fernández-Avilés F., Foldager D., Gadler F., De Vinuesa P.G.G., Gorenek B., Guerra J.M., Hermann Haugaa K., Hendriks J., Kahan T., Katus H.A., Konradi A., Koskinas K.C., Law H., Lewis B.S., Linker N.J., Løchen M.L., Lumens J., Mascherbauer J., Mullens W., Nagy K.V., Prescott E., Raatikainen P., Rakisheva A., Reichlin T., Ricci R.P., Shlyakhto E., Sitges M., Sousa-Uva M., Sutton R., Suwalski P., Svendsen J.H., Touyz R.M., Van Gelder I.C., Vernooy K., Waltenberger J., Whinnett Z., Witte K.K., Kronborg M.B., Michowitz Y., Auricchio A., Barbash I.M., Barrabés J.A., Boriani G., Braunschweig F., Brignole M., Burri H., Coats A.J., Deharo J.C., Delgado V., Diller G.P., Israel C.W., Keren A., Knops R.E., Kotecha D., Leclercq C., Merkely B., Starck C., Thylén I., and Tolosana J.M. 2021 ESC Guidelines on cardiac pacing and cardiac resynchronization therapy. *Eur. Heart J.*, vol. 42, 3427–3520 (2021).

[7] Lang R.M., Badano L.P., Mor-Avi V., Afilalo J., Armstrong A., Ernande L., Flachskampf F.A., Foster E., Goldstein S.A., Kuznetsova T., Lancellotti P., Muraru D., Picard M.H., Rietzschel E.R., Rudski L., Spencer K.T., Tsang W., and Voigt J.U. Recommendations for cardiac chamber quantification by echocardiography in adults: An update from the American society of echocardiography and the European association of cardiovascular imaging. *Eur. Heart J. Cardiovasc. Imaging*, vol. 16, 233–271 (2015).

[8] Stokke T.M., Hasselberg N.E., Smedsrud M.K., Sarvari S.I., Haugaa K.H., Smiseth O.A., Edvardsen T., and Remme E.W. Geometry as a Confounder When Assessing Ventricular Systolic Function: Comparison Between Ejection Fraction and Strain. *J. Am. Coll. Cardiol.*, vol. 70, 942–954 (2017).

[9] D'Hooge J., Heimdal A., Jamal F., Kukulski T., Bijnens B., Rademakers F., Hatle L., Suetens P., and Sutherland G.R. Regional Strain and Strain Rate Measurements by Cardiac Ultrasound: Principles, Implementation and Limitations. *Eur. J. Echocardiogr.*, vol. 1, 154–170 (2000).

[10] Gorcsan J. and Tanaka H. Echocardiographic assessment of myocardial strain. *J. Am. Coll. Cardiol.*, vol. 58, 1401–1413 (2011).

[11] Smiseth O.A., Torp H., Opdahl A., Haugaa K.H., and Urheim S. Myocardial strain imaging: How useful is it in clinical decision making? *Eur. Heart J.*, vol. 37, 1196–1207b (2016).

[12] Potter E. and Marwick T.H. Assessment of Left Ventricular Function by Echocardiography: The Case for Routinely Adding Global Longitudinal Strain to Ejection Fraction (2018).

[13] Springer Japan, Klaeboe L.G. and Edvardsen T. Echocardiographic assessment of left ventricular systolic function (2019).
Accessed on 25/10/2021 from: https://doi.org/10.1007/s12574-018-0405-5

[14] Donal E., Galli E., Hubert A., and Bouzille G. New indices of left ventricular function: let's move from ejection fraction to more physiological parameters. *J. Physiol.*, vol. 595, 3959–3960 (2017).

[15] Magne J., Cosyns B., Popescu B.A., Carstensen H.G., Dahl J., Desai M.Y., Kearney L., Lancellotti P., Marwick T.H., Sato K., Takeuchi M., Zito C., Casalta A.C., Mohty D., Piérard L., Habib G., and Donal E. Distribution and Prognostic Significance of Left Ventricular Global Longitudinal Strain in Asymptomatic Significant Aortic Stenosis: An Individual Participant Data Meta-Analysis. *JACC Cardiovasc. Imaging*, vol. 12, 84–92 (2019).

[16] Risum N., Tayal B., Hansen T.F., Bruun N.E., Jensen M.T., Lauridsen T.K., Saba S., Kisslo J., Gorcsan J., and Sogaard P. Identification of Typical Left Bundle Branch Block Contraction by Strain Echocardiography Is Additive to Electrocardiography in Prediction of Long-Term Outcome after Cardiac Resynchronization Therapy. *J. Am. Coll. Cardiol.*, vol. 66, 631–641 (2015).

[17] van Everdingen W.M., Walmsley J., Cramer M.J., van Hagen I., De Boeck B.W., Meine M., Delhaas T., Doevendans P.A., Prinzen F.W., Lumens J., and Leenders G.E. Echocardiographic Prediction of Cardiac Resynchronization Therapy Response Requires Analysis of Both Mechanical Dyssynchrony and Right Ventricular Function: A Combined Analysis of Patient Data and Computer Simulations. *J. Am. Soc. Echocardiogr.*, vol. 30, 1012–1020.e2 (2017).

[18] Voigt J.U., Exner B., Schmiedehausen K., Huchzermeyer C., Reulbach U., Nixdorff U., Platsch G., Kuwert T., Daniel W.G., and Flachskampf F.A. Strain-rate imaging during dobutamine stress echocardiography provides objective evidence of inducible ischemia. *Circulation*, vol. 107, 2120–2126 (2003).

[19] Mada R.O., Duchenne J., and Voigt J.U. Tissue Doppler, strain and strain rate in ischemic heart disease "How I do it". *Cardiovasc. Ultrasound*, vol. 12, 1–9 (2014).

[20] Voigt J.U. and Cvijic M. 2- and 3-Dimensional Myocardial Strain in Cardiac Health and Disease. *JACC Cardiovasc. Imaging*, vol. 12, 1849–1863 (2019).

[21] Voigt J.U., Pedrizzetti G., Lysyansky P., Marwick T.H., Houle H., Baumann R., Pedri S., Ito Y., Abe Y., Metz S., Song J.H., Hamilton J., Sengupta P.P., Kolias T.J., D'Hooge J., Aurigemma G.P., Thomas J.D., and Badano L.P. Definitions for a common standard for 2D speckle tracking echocardiography: consensus document of the EACVI/ASE/Industry Task Force to standardize deformation imaging. *Eur. Heart J. Cardiovasc. Imaging*, vol. 16, 1–11 (2015).

[22] Hu S.Y., Santus E., Forsyth A.W., Malhotra D., Haimson J., Chatterjee N.A., Kramer D.B., Barzilay R., Tulsky J.A., and Lindvall C. Can machine learning improve patient selection for cardiac resynchronization therapy? *PLoS One*, vol. 14, 1–13 (2019).

[23] Kalscheur M.M., Kipp R.T., Tattersall M.C., Mei C., Buhr K.A., Demets D.L., Field M.E., Eckhardt L.L., and Page C.D. Machine Learning Algorithm Predicts Cardiac Resynchronization Therapy Outcomes: Lessons from the COMPANION Trial. *Circ. Arrhythmia Electrophysiol.*, vol. 11, 1–11 (2018).

[24] Cikes M., Sanchez-Martinez S., Claggett B., Duchateau N., Piella G., Butakoff C., Pouleur A.C., Knappe D., Biering-Sørensen T., Kutyifa V., Moss A., Stein K., Solomon S.D., and Bijnens B. Machine learning-based phenogrouping in heart failure to identify responders to cardiac resynchronization therapy. *Eur. J. Heart Fail.*, vol. 21, 74–85 (2019).

[25] Bernard A., Donal E., Leclercq C., Schnell F., Fournet M., Reynaud A., Thebault C., Mabo P., Daubert J.C., and Hernandez A. Impact of cardiac resynchronization therapy on left ventricular mechanics: Understanding the response through a new quantitative approach based on longitudinal strain integrals. *J. Am. Soc. Echocardiogr.*, vol. 28, 700–708 (2015).

[26] Gallard A., Hubert A., Smiseth O., Voigt J.U., Le Rolle V., Leclercq C., Bidaut A., Galli E., Donal E., and Hernandez A.I. Prediction of response to cardiac resynchronization therapy using a multi-feature learning method. *Int. J. Cardiovasc. Imaging*, vol. 37, 989–998 (2020).

[27] Gallard A., Galli E., Hubert A., Bidaut A., Le Rolle V., Smiseth O., Voigt J.U., Donal E., and Hernández A.I. Echocardiographic view and feature selection for the estimation of the response to CRT. *PLoS One*, vol. 16, page e0252857 (2021).

[28] Gallard A., Bidaut A., Hubert A., Sade E., Marechaux S., Sitges M., Separovic-Hanzevacki J., Le Rolle V., Galli E., Hernandez A., and Donal E. Characterization of Responder Profiles for Cardiac Resynchronization Therapy through Unsupervised Clustering of Clinical and Strain Data. *J. Am. Soc. Echocardiogr.*, vol. 34, 483–493 (2021).

[29] Hubert A., Gallard A., Rolle V.L., Smiseth O.A., Leclercq C., Voigt J.u., Galli E., Galand V., Hernandez A., and Donal E. Left ventricular strain for predicting the response to cardiac resynchronization therapy: twomethods for one question. *Eur. Hear. J. - Cardiovasc. Imaging*, 1–8 (2021).

[30] Galli E., Leclercq C., Hubert A., Bernard A., Smiseth O.A., Mabo P., Samset E., Hernandez A., and Donal E. Role ofmyocardial constructive work in the identification of responders to CRT. *Eur. Heart J. Cardiovasc. Imaging*, vol. 19, 1010–1018 (2018).

[31] Galli E., Leclercq C., Fournet M., Hubert A., Bernard A., Smiseth O.A., Mabo P., Samset E., Hernandez A., and Donal E. Value of Myocardial Work Estimation in the Prediction of Response to Cardiac Resynchronization Therapy. *J. Am. Soc. Echocardiogr.*, vol. 31, 220–230 (2018).

[32] Hubert A., Le Rolle V., Leclercq C., Galli E., Samset E., Casset C., Mabo P., Hernandez A., and Donal E. Estimation of myocardial work from pressure–strain loops analysis: an experimental evaluation. *Eur. Heart J. Cardiovasc. Imaging*, vol. 19, 1372–1379 (2018).

[33] Donal E., Hubert A., Le Rolle V., Leclercq C., Martins R., Mabo P., Galli E., and Hernandez A. New Multiparametric Analysis of Cardiac Dyssynchrony: Machine Learning and Prediction of Response to CRT. *JACC Cardiovasc. Imaging*, vol. 12, 1887–1888 (2019).

[34] Galli E., Le Rolle V., Smiseth O.A., Duchenne J., Aalen J.M., Larsen C.K., Sade E.A., Hubert A., Anilkumar S., Penicka M., Linde C., Leclercq C., Hernandez A., Voigt J.U., and Donal E. Importance of Systematic Right Ventricular Assessment in Cardiac Resynchronization Therapy Candidates: A Machine Learning Approach. *J. Am. Soc. Echocardiogr.*, vol. 34, 494–502 (may 2021).

[35] Le Rolle V., Galli E., Danan D., El Houari K., Hubert A., Donal E., and Hernández A.I. Sensitivity Analysis of a Left Ventricle Model in the Context of Intraventricular Dyssynchrony. *Acta Biotheor.*, vol. 68, 45–59 (2019).

[36] Sack K.L., Dabiri Y., Franz T., Solomon S.D., Burkhoff D., and Guccione J.M. Investigating the role of interventricular interdependence in development of right heart dysfunction during LVAD support: A patient-specific methods-based approach. *Front. Physiol.*, vol. 9, 1–13 (2018).

[37] Park J.I., Heikhmakhtiar A.K., Kim C.H., Kim Y.S., Choi S.W., Song K.S., and Lim K.M. The effect of heart failure and left ventricular assist device treatment on right ventricular mechanics: A computational study. *Biomed. Eng. Online*, vol. 17, 1–13 (2018).

[38] Ichi Okada J., Washio T., Nakagawa M., Watanabe M., Kadooka Y., Kariya T., Yamashita H., Yamada Y., Ichi Momomura S., Nagai R., Hisada T., and Sugiura S. Multi-scale, tailor-made heart simulation can predict the effect of cardiac resynchronization therapy. *J. Mol. Cell. Cardiol.*, vol. 108, 17–23 (2017).

[39] Crozier A., Blazevic B., Lamata P., Plank G., Ginks M., Duckett S., Sohal M., Shetty A., Rinaldi C.A., Razavi R., Smith N.P., and Niederer S.A. The relative role of patient physiology and device optimisation in cardiac resynchronisation therapy: A computational modelling study. *J. Mol. Cell. Cardiol.*, vol. 96, 93–100 (2016).

[40] Niederer S.A., Lamata P., Plank G., Chinchapatnam P., Ginks M., Rhode K., Rinaldi C.A., Razavi R., and Smith N.P. Analyses of the Redistribution of Work following Cardiac Resynchronisation Therapy in a Patient Specific Model. *PLoS One*, vol. 7, 1–9 (2012).

[41] Constantino J., Hu Y., and Trayanova N.A. A computational approach to understanding the cardiac electromechanical activation sequence in the normal and failing heart, with translation to the clinical practice of CRT. *Prog. Biophys. Mol. Biol.*, vol. 110, 372–379 (2012).

[42] Garcia-Blanco E., Ortigosa R., Gil A.J., Lee C.H., and Bonet J. A new computational framework for electro-activation in cardiac mechanics. *Comput. Methods Appl. Mech. Eng.*, vol. 348, 796–845 (2019).

[43] Aguado-Sierra J., Krishnamurthy A., Villongco C., Chuang J., Howard E., Gonzales M.J., Omens J., Krummen D.E., Narayan S., Kerckhoffs R.C., and McCulloch A.D. Patient-specific modeling of dyssynchronous heart failure: A case study. *Prog. Biophys. Mol. Biol.*, vol. 107, 147–155 (2011).

[44] Augustin C.M., Gsell M.A., Karabelas E., Willemen E., Prinzen F.W., Lumens J., Vigmond E.J., and Plank G. A computationally efficient physiologically comprehensive 3D–0D closed-loop model of the heart and circulation. *Comput. Methods Appl. Mech. Eng.*, vol. 386, page 114092 (2021).

[45] Zhang Y., Wang V.Y., Morgan A.E., Kim J., Ge L., Guccione J.M., Weinsaft J.W., and Ratcliffe M.B. A Novel MRI-Based Finite Element Modeling Method for Calculation of Myocardial Ischemia Effect in Patients With Functional Mitral Regurgitation. *Front. Physiol.*, vol. 11, 1–13 (2020).

[46] Oomen P.J., Phung T.K.N., Weinberg S.H., Bilchick K.C., and Holmes J.W. A rapid electromechanical model to predict reverse remodeling following cardiac resynchronization therapy. *Biomech. Model. Mechanobiol.*, vol. 21, 231–247 (2022).

[47] Lumens J., Leenders G.E., Cramer M.J., De Boeck B.W., Doevendans P.A., Prinzen F.W., and Delhaas T. Mechanistic evaluation of echocardiographic dyssynchrony indices patient data combined with multiscale computer simulations. *Circ. Cardiovasc. Imaging*, vol. 5, 491–499 (2012).

[48] Willemen E., Schreurs R., Huntjens P.R., Strik M., Plank G., Vigmond E., Walmsley J., Vernooy K., Delhaas T., Prinzen F.W., and Lumens J. The left and right ventricles respond differently to variation of pacing delays in cardiac resynchronization therapy: A combined experimental-computational approach. *Front. Physiol.*, vol. 10, 1–13 (2019).

[49] Leenders G.E., De Boeck B.W., Teske A.J., Meine M., Bogaard M.D., Prinzen F.W., Doevendans P.A., and Cramer M.J. Septal rebound stretch is a strong predictor of outcome after cardiac resynchronization therapy. *J. Card. Fail.*, vol. 18, 404–412 (2012).

[50] Regazzoni F., Salvador M., Africa P.C., Fedele M., Dedè L., and Quarteroni A. A cardiac electromechanical model coupled with a lumped-parameter model for closed-loop blood circulation. *J. Comput. Phys.*, vol. 457, page 111083 (2022).

[51] Hernández A.I., Le Rolle V., Defontaine A., and Carrault G. A multiformalism and multiresolution modelling environment: Application to the cardiovascular system and its regulation. *Philos. Trans. R. Soc. A Math. Phys. Eng. Sci.*, vol. 367, 4923–4940 (2009).

[52] Hernández A.I., Le Rolle V., Ojeda D., Baconnier P., Fontecave-Jallon J., Guillaud F., Grosse T., Moss R.G., Hannaert P., and Thomas S.R. Integration of detailed modules in a core model of body fluid homeostasis and blood pressure regulation. *Prog. Biophys. Mol. Biol.*, vol. 107, 169–182 (2011).

[53] Le Rolle V., Hernández A.I., Richard P.Y., Donal E., and Carrault G. Model-based analysis of myocardial strain data acquired by tissue Doppler imaging. *Artif. Intell. Med.*, vol. 44, 201–219 (2008).

[54] Le Rolle V., Carrault G., Richard P.Y., Pibarot P., Durand L.G., and Hernández A.I. A tissue-level electromechanical model of the left ventricle: Application to the analysis of intraventricular pressure. *Acta Biotheor.*, vol. 57, 457–478 (2009).

[55] Rolle V.L., Ojeda D., and Hernández A.I. Embedding a cardiac pulsatile model into an integrated model of the cardiovascular regulation for heart failure followup. *IEEE Trans. Biomed. Eng.*, vol. 58, 2982–2986 (2011).

[56] Le Rolle V., Beuchee A., Praud J.P., Samson N., Pladys P., and Hernández A.I. Recursive identification of an arterial baroreflex model for the evaluation of cardiovascular autonomic modulation. *Comput. Biol. Med.*, vol. 66, 287–294 (2015).

[57] Owashi K.P. *Model-based analysis of myocardial strains for the evaluation of cardio- vascular function*. Ph.D. thesis, Université Rennes 1 (2021).

[58] Owashi K.P., Hubert A., Galli E., Donal E., Hernández A.I., and Rolle V.L. Model-based estimation of left ventricular pressure and myocardial work in aortic stenosis. *PLoS One*, vol. 15, 1–18 (2020).

[59] Calvo M., Le Rolle V., Romero D., Béhar N., Gomis P., Mabo P., and Hernández A.I. Model-based analysis of the autonomic response to head-up tilt testing in Brugada syndrome. *Comput. Biol. Med.*, vol. 103, 82–92 (2018).

[60] Calvo M., Le Rolle V., Romero D., Béhar N., Gomis P., Mabo P., and Hernández A.I. Recursive model identification for the analysis of the autonomic response to exercise testing in Brugada syndrome. *Artif. Intell. Med.*, vol. 97, 98–104 (2019).

[61] Ugalde H.M.R., Ojeda D., Rolle V.L., Andreu D., Guiraud D., Bonnet J.L., Henry C., Karam N., Hag A., Mabo P., Carrault G., and Hern A.I. Model-Based Design and Experimental Validation of Control Modules for Neuromodulation Devices. *IEEE Trans. Biomed. Eng.*, vol. 63, 1551–1558 (2016).

[62] Guerrero G., Rolle V.L., and Hernandez A. Sensitivity Analysis of a Cardiorespiratory Model for the Study of Sleep Apnea. *Comput. Cardiol. (2010).*, vol. 2018-Septe, 18–21 (2018).

[63] Ojeda D., Le Rolle V., Harmouche M., Drochon A., Corbineau H., Verhoye J.P., and Hernandez A.I. Sensitivity analysis and parameter estimation of a coronary circulation model for triple-vessel disease. *IEEE Trans. Biomed. Eng.*, vol. 61, 1208–1219 (2014).

[64] Ojeda D., Rolle V.L., Romero-Ugalde H.M., Gallet C., Bonnet J.L., Henry C., Bel A., Mabo P., Carrault G., and Hernández A.I. Sensitivity analysis of vagus nerve stimulation parameters on acute cardiac autonomic responses: Chronotropic, inotropic and dromotropic effects. *PLoS One*, vol. 11, 1–19 (2016).

[65] Al-Omar S., Le Rolle V., Pladys P., Samson N., Hernandez A., Carrault G., and Praud J.P. Influence of nasal CPAP on cardiorespiratory control in healthy neonate. *J. Appl. Physiol.*, vol. 127, 1370–1385 (2019).

[66] Duport O., Rolle V.L., Galli E., Danan D., Darrigrand E., Donal E., and Hernández A.I. Model-based analysis of myocardial contraction patterns in ischemic heart disease. *IRBM* (2022).

[67] Zareba W., Klein H., Cygankiewicz I., Hall W.J., McNitt S., Brown M., Cannom D., Daubert J.P., Eldar M., Gold M.R., Goldberger J.J., Goldenberg I., Lichstein E., Pitschner H., Rashtian M., Solomon S., Viskin S., Wang P., and Moss A.J. Effectiveness of cardiac resynchronization therapy by QRS morphology in the multicenter automatic defibrillator implantation trial-cardiac resynchronization therapy (MADIT-CRT). *Circulation*, vol. 123, 1061–1072 (2011).

[68] Cleland J.G., Abraham W.T., Linde C., Gold M.R., Young J.B., Claude Daubert J., Sherfesee L., Wells G.A., and Tang A.S. An individual patient meta-analysis of five randomized trials assessing the effects of cardiac resynchronization therapy on morbidity and mortality in patients with symptomatic heart failure. *Eur. Heart J.*, vol. 34 (2013).

[69] W ILLIAM T. A BRAHAM , M.D., W ESTBY G. F ISHER , M.D., A NDREW L. S MITH , M.D., D AVID B. D ELURGIO M., A NGEL R. L EON , M.D., E VAN L OH , M.D., D USAN Z. K OCOVIC , M.D., M ILTON P ACKER , M.D., A LFREDO L. C LAVELL , M.D., D AVID L. H AYES , M.D., M YRVIN E LLESTAD , M.D., AND J OHN M ESSENGER , M.D. F.T.M.S.T.G.R.., AND A. CARDIAC RESYNCHRONIZATION IN CHRONIC HEART FAILURE W. *N. Engl. J. Med.*, vol. 346, 305–310 (2002).

[70] Daubert C., Behar N., Martins R.P., Mabo P., and Leclercq C. Avoiding non-responders to cardiac resynchronization therapy: A practical guide. *Eur. Heart J.*, vol. 38, 1463–1472 (2017).

[71] Russell K., Eriksen M., Aaberge L., Wilhelmsen N., Skulstad H., Remme E.W., Haugaa K.H., Opdahl A., Fjeld J.G., Gjesdal O., Edvardsen T., and Smiseth O.A. A novel clinical method for quantification of regional left ventricular pressurestrain loop area: A non-invasive index of myocardial work. *Eur. Heart J.*, vol. 33, 724–733 (2012).

[72] Russell K., Eriksen M., Aaberge L., Wilhelmsen N., Skulstad H., Gjesdal O., Edvardsen T., and Smiseth O.A. Assessment of wasted myocardial work: A novel method to quantify energy loss due to uncoordinated left ventricular contractions. *Am. J. Physiol. - Hear. Circ. Physiol.*, vol. 305, 996–1003 (2013).

[73] Fortuni F., Butcher S.C., van der Kley F., Lustosa R.P., Karalis I., de Weger A., Priori S.G., van der Bijl P., Bax J.J., Delgado V., and Ajmone Marsan N. Left ventricular myocardial work in patients with severe aortic stenosis Federico. *J. Am. Soc. Echocardiogr.*, page 124658 (2020).

[74] Maron B.J., Olivotto I., Spirito P., Casey S.A., Bellone P., Gohman T.E., Graham K.J., Burton D.A., and Cecchi F. Epidemiology of Hypertrophic Cardiomyopathy–Related Death. *Circulation*, vol. 102, 858–864 (2000).

[75] Maron B.J., Shirani J., Poliac L.C., Mathenge R., Roberts W.C., and Mueller F.O. Sudden death in young competitive athletes: Clinical, demographic, and pathological profiles. *JAMA*, vol. 276 (1996).

[76] O'Mahony C., Jichi F., Pavlou M., Monserrat L., Anastasakis A., Rapezzi C., Biagini E., Gimeno J.R., Limongelli G., McKenna W.J., Omar R.Z., Elliott P.M., Ortiz-Genga M., Fernandez X., Vlagouli V., Stefanadis C., Coccolo F., Sandoval M.J.O., Pacileo G., Masarone D., Pantazis A., Tome-Esteban M., Dickie S., Lambiase P.D., and Rahman S. A novel clinical risk prediction model for sudden cardiac death in hypertrophic cardiomyopathy (HCM Risk-SCD). *Eur. Heart J.*, vol. 35, 2010–2020 (2014).

[77] Ommen S.R., Mital S., Burke M.A., Day S.M., Deswal A., Elliott P., Evanovich L.L., Hung J., Joglar J.A., Kantor P., Kimmelstiel C., Kittleson M., Link M.S., Maron M.S., Martinez M.W., Miyake C.Y., Schaff H.V., Semsarian C., and Sorajja P. 2020 AHA/ACC Guideline for the Diagnosis and Treatment of Patients With Hypertrophic Cardiomyopathy: A Report of the American College of Cardiology/American Heart Association Joint Committee on Clinical Practice Guidelines. *J. Am. Coll. Cardiol.*, vol. 76, e159–e240 (2020).

Chapter

1

Context: The Cardiac Function

The evaluation of the cardiac function is essential to evaluate the heart's ability to maintain the blood flow circulation and supply the metabolic requirements. In the case of heart failure, a pathology that affects more than 26 million people around the word, the cardiac function is deficient.

This chapter will present three phenotypes of this chronic and degenerative pathology:

- Heart failure with left bundle of branch block,
- Aortic stenosis,
- Hypertrophic cardiomyopathy.

A general description of the cardiovascular system with it physiology and the electrical and mechanical function will be first presented. Then, the two main modalities: electrocardiogram and the echocardiography used in this work to evaluate the cardiac function will be described.

These three heart failure phenotypes, by different way, significantly affect the cardiac function, and particularly the left ventricle ability to eject blood. Due to its multifactorial nature, the cardiac function evaluation is still a main concern in heart failure patient care.

1.1 Cardiovascular system

The CardioVascular System (CVS), or vascular system, includes the blood circulatory system that contains the heart, blood vessels, and blood. This system, by transporting blood through the entire body, protects it from disease. It maintains a stable temperature and pH, ensure the supply of oxygen, nutriments, and hormones thought the different body part.

The CVS is divided in two circulatory loops (Figure 1.1), linked together in a closed-loop circulatory system:

- The pulmonary circulation aims at transporting deoxygenated blood from the right part of the heart to the lungs trough pulmonary arteries and providing oxygenated blood back into the heart through pulmonary vein.
- The systemic circulation transports the oxygenated blood from the left part of the heart to the entire body via the aorta. It returns it back to the heart thanks systemic veins for another cycle.

Arteries, which are vessels with muscular and elastic thick wall, subdivide into smaller structures named arterioles. The arterioles are then connected to the capillaries, which are the smallest blood vessels.

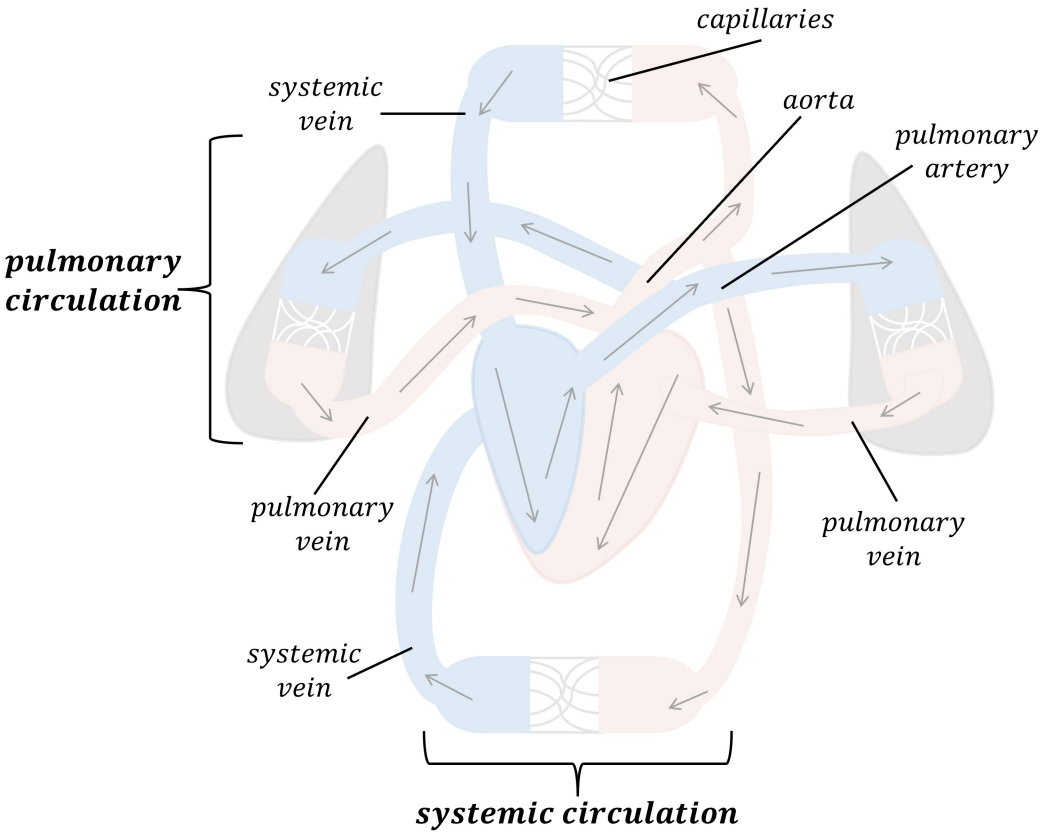

Figure 1.1: Circulatory system, with the systemic and pulmonary circulation around the heart. The blue part represents the deoxygenated blood and the red one the oxygenated blood.

1.1.1 The heart physiology

The heart is a muscular organ. Its function is to pump blood through the blood vessels of the circulatory system to maintain the good supply of oxygen and nutriment, as well as the elimination of CO_2 and wastes. It is made up of three-layered structures. From the inside of the heart to the outside, one can find the endocardium, the myocardium, and the pericardium. The endocardium is localized inside the heart chambers and forms the valves surfaces. The myocardium is the bulk of the muscle and delimits the walls of the heart. Finally, the pericardium covers the whole heart in a double-walled sac structure.

The heart is divided into two parts: the left and the right sides, and composed of four chambers. The two upper chambers are the atria, and the two lower are the ventricles (Figure 1.2).

The left and right part are separated by the inter-atrial and inter-ventricular septa, respectively, for

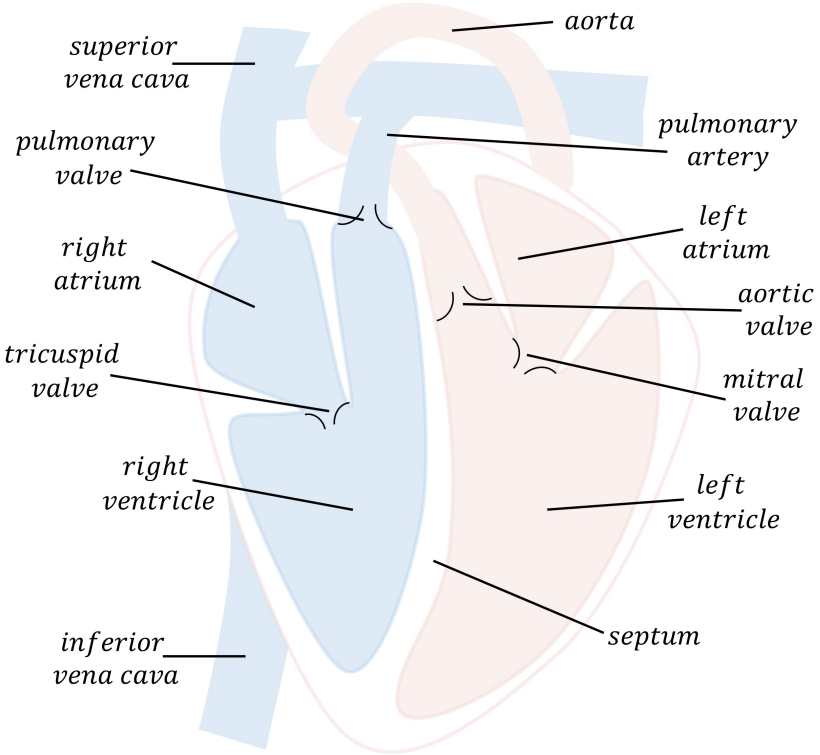

Figure 1.2: Heart anatomy with the four chambers: left and right atria, left and right ventricles and the four valves: pulmonary, tricuspid, mitral and aortic valves.

the atria and ventricles.

The right atrium and the right ventricle are involved in the systemic circulation by receiving the deoxygenated blood from the superior and inferior vena cava and in the pulmonary circulation by pushing the blood to the lungs, via the pulmonary valve. The tricuspid valve separates the right ventricle from the atrium.

On the other hand, the mitral valve separates the left atrium from the left ventricle. The left ventricle receives the oxygenated blood from the pulmonary vein and return it to the entire body through the aorta after passing the aortic valve.

The valves are separated into two types: the atrioventricular valves, located between atria and ventricles (mitral and tricuspid valves) and the semilunar valves, located between the ventricle and the arteries (aortic and pulmonary valves). The valves maintain the unidirectional flow in the heart chambers thanks to the opening and the closing of their flaps (cusps and leaflets). These opening and closing, are driven by the blood pressure of the two chambers around the valves. The opening allows the blood to flow in the right direction, and the closing stops potential backward blood flow.

1.1.2 Electrical system

To contract, the heart has its independent electrical conduction system. This conduction system is a network of different cells that keep the heart beating.

Two types of cells control heartbeat: conducting cells (cardiac pacemaker cells) that carry the electric signals and muscle cells (cardiomyocytes) that control heart contractions. The electrical conduction network sends electrical signals to start a heartbeat, contract the myocardium and cause the heart muscle fiber depolarization.

The heartbeat is established by the sinoatrial node that creates an excitation signal. Then, it travels into the AtrioVentricular (AV) node, the bundle of His, then down to the right and left bundle of branch that led into the Purkinje fibers [1]. Figure 1.3 illustrates the electrical conduction pathway. In this path, the atria and the ventricles are contracted by their muscle tissue impulses.

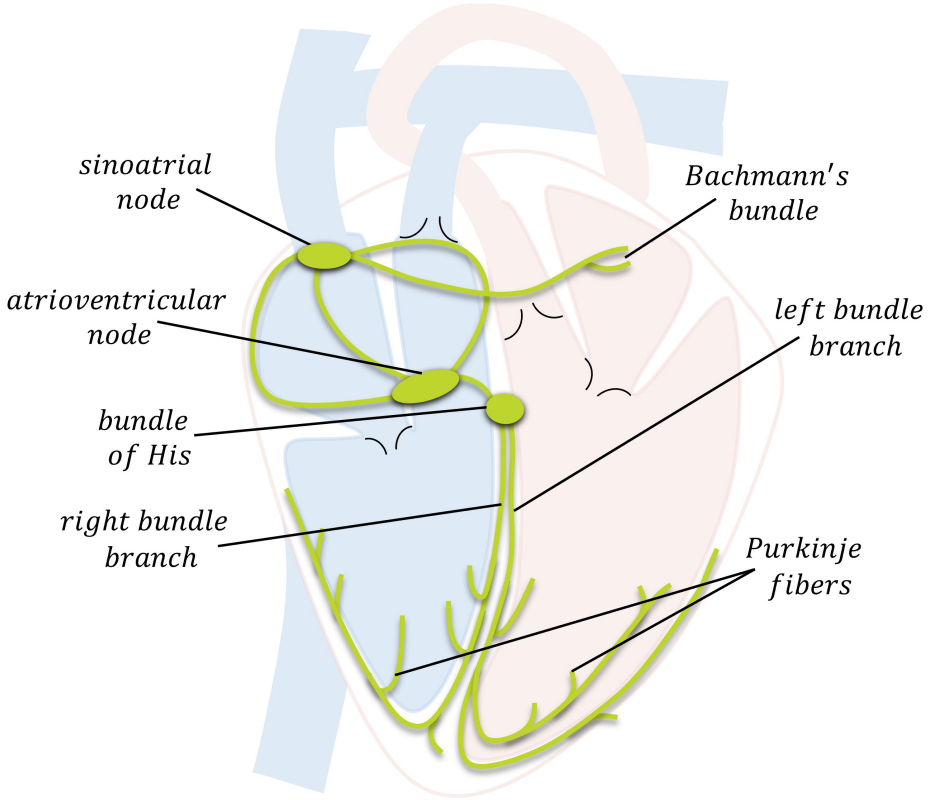

Figure 1.3: Cardiac electrical conduction pathway with the sinoatrial node, the atrioventricular node, the bundle of His, the right and left bundle of branch and the Purkinje fibers.

In a lower level, the electric changes (voltage) in the cell are named cardiac action potential and could be divided in five phases. (Figure 1.4):

- **Phase 4:** The baseline phase is the resting state.

- **Phase 0:** After the resting state, a fast depolarization period opens an influx of sodium (Na+) ions. In pacemaker cell, this depolarization occurs spontaneously but in the muscle cells. It is caused by the electrical excitation of nearby cells.
- **Phase 1:** A rapid inactivation of Na+ channels, followed by an opening of potassium (K+) channels that cause a brief repolarization. This phase does not occur to pacemaker cells.
- **Phase 2:** Called plateau, this phase is due to the nearly balanced charge caused by the influx of calcium (Ca2+) ions and the outgoing flow of K+. This phase caused an almost constant potential for non-pacemaker cells.
- **Phase 3:** The repolarization phase occurs when the Ca2+ channels close and K+ ions predominate. During this phase, Na+ channels will begin to recover and restore the resting state.

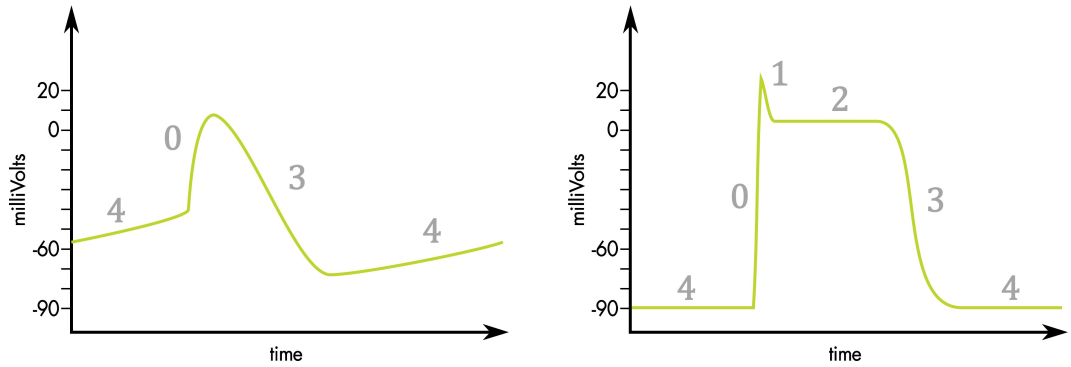

Figure 1.4: Electrical phases of a cardiac pacemaker cell (left) and a muscle cell (right).

The resting potential is measured by the difference in voltage between the inside and outside the cell. In muscle or cardiac cell at the resting potential is about -90mV.

An Absolute Refractory Period (ARP) is defined as the interval of time during which a second action potential cannot be initiated, regardless of the power of the stimulus. It is longer in cardiac muscle. The Relative Refractory Period (RRP) is the time during which a second action potential can be initiated.

1.1.3 Mechanical behavior

Cardiac muscle

The myocardium (cardiac muscle) is composed of several layers of cardiac muscle cells named cardiomyocytes. These cardiomyocytes are composed of one nucleus, a cytoplasm (sarcoplasm) and a plasma membrane (sarcolemma). They are shaped cylindrically with numerous inter-connected sarcomeres. Sarcomere is the fundamental contractile unit of cardiomyocytes. It is composed of thick and thin protein filaments of myosin (thick) and actin (thin). Cardiomyocytes are joined by intercalated discs thanks to two types of junctions: GAP junction and desmosomes.

The cardiac contraction is control by action potential. The muscle structure, in intercalated discs, is responsible for the transmission of force. It allows action potentials to spread easily between cells and the transfer of ions. This ion concentration variation produces depolarization of the heart muscle and a muscle contraction.

Cycle

The cardiac cycle has two main periods, diastole, and systole, which can be broken down into four phases (Figure 1.5):

- **Phase 1:** IsoVolumetric Relaxation (IVR),
- **Phase 2:** Inflow,
- **Phase 3:** IsoVolumetric Contraction (IVC),
- **Phase 4:** Ejection.

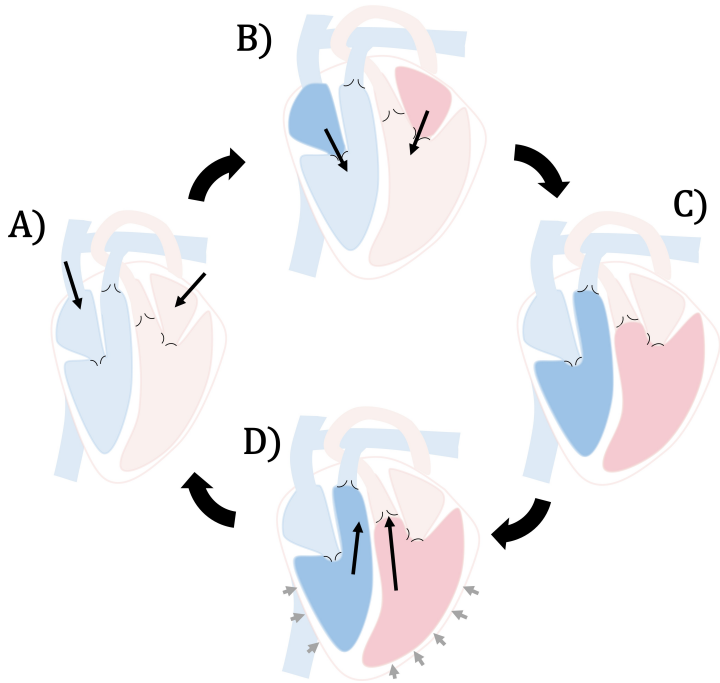

Figure 1.5: Cardiac cycle: a) isovolumic relaxation, b) inflow, c) isovolumic contraction, c)ejection.

The cardiac cycle starts with both the atria and ventricles being relaxed. Blood flows from areas of high pressure to low pressure, causing the atria to fill until the pressure rises and blood flows into the ventricles. This also increases the pressure in the ventricles, leading to their contraction and the pumping of blood from the right ventricle into the pulmonary artery and from the left ventricle into the aorta. The electrical activity at the cellular level controls and initiates this mechanical cardiac activity.

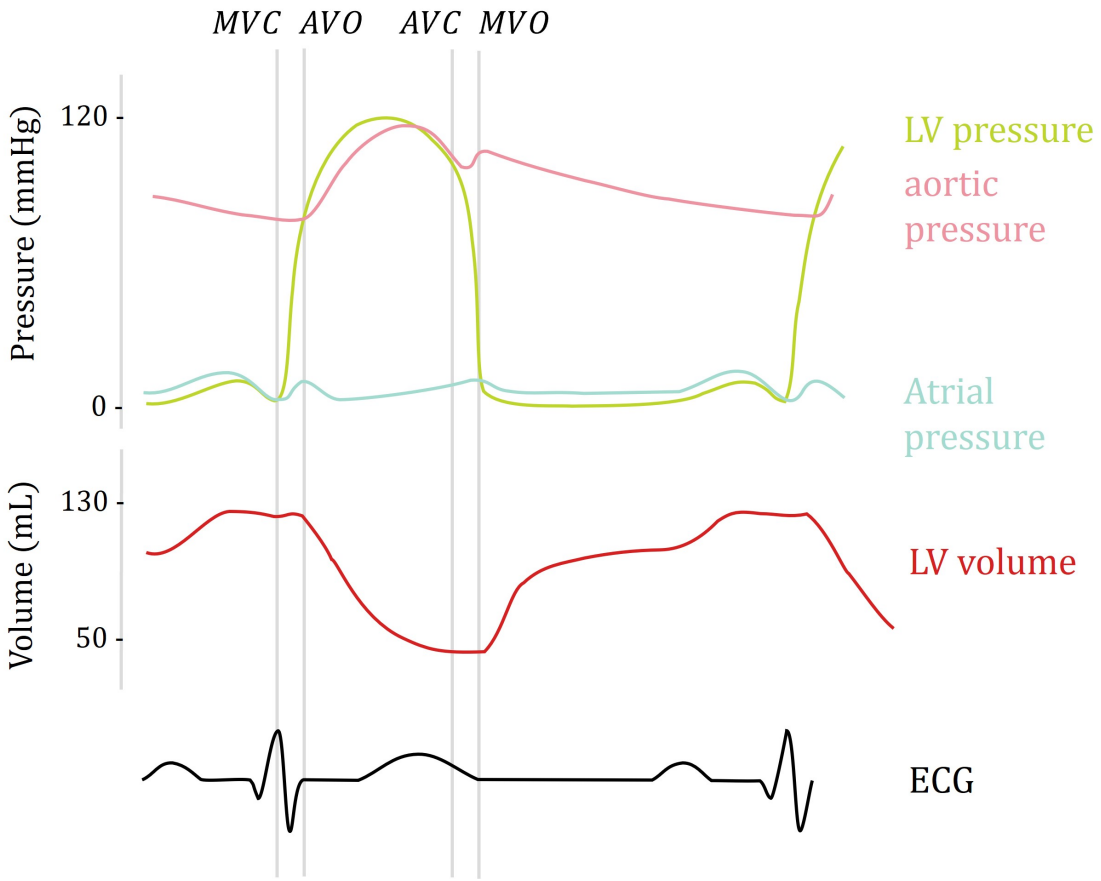

Figure 1.6: Wigger diagram with the left ventricle (LV), aortic and atrial pressures, the LV volume, and the ECG. The opening and closure of the mitral and aortic valve are added (MVC: mitral valve closure, AVO: aortic valve opening, AVC: aortic valve closure, and MVO: mitral valve opening.

These variations of pressures and volumes in the different chambers could be represented in a Wigger diagram (Figure 1.6).

1.2 Modalities

1.2.1 Electrocardiogram

Cardiac electrical function could be measured by electrocardiography. It is measured using electrodes on the thorax skin and represented by a voltage versus time graph, known as electrocardiogram (ECG or EKG). These electrodes detect the small electrical changes caused by depolarization and repolarization of the cardiac muscle parts.

A standard 12-lead ECG is composed of 10 electrodes, divided into two groups: the peripheral electrodes and the precordial electrodes. There are four peripheral electrodes placed on the patient's extremities (RA, LA, RL and LL). The other six electrodes are located in the precordial

region (V1, V2, V3, V4, V5 and V6) [2]. They are named and placed as follows:

- **RA:** On the right arm.
- **LA:** On the left arm.
- **RL:** On the right leg.
- **LL:** On the left leg.
- **V1:** In the fourth intercostal space (between ribs 4 and 5) just to the right of the sternum.
- **V2:** In the fourth intercostal space (between ribs 4 and 5) just to the left of the sternum.
- **V3:** Between V2 and V4.
- **V4:** In the fifth intercostal space (between ribs 5 and 6) in the mid-clavicular line.
- **V5:** Horizontally even with V4, in the left anterior axillary line.
- **V6:** Horizontally even with V4 and V5 in the mid-axillary line.

The patient heart beat could be followed on its ECG with the progression of depolarization in this order: sinoatrial node, AV node, bundle of His, LBB and RBB and Purkinje fibers to finish in the ventricles. This normal pathway is characterized on ECG. In fact, the ECG tracing produce four phase with typical pattern (Figure 1.7) [3] :

- **P wave:** It represents atrial depolarization.
- **QRS complex:** It represents ventricular depolarization. The amplitude of the QRS complex is significantly larger than the P-wave due to the higher number of depolarizing cells in the ventricles compared with the atria.
- **T wave:** The T wave represents ventricular repolarization
- **U wave:** This last phase is often missing because of its very low amplitude and thus ignore by clinicians.

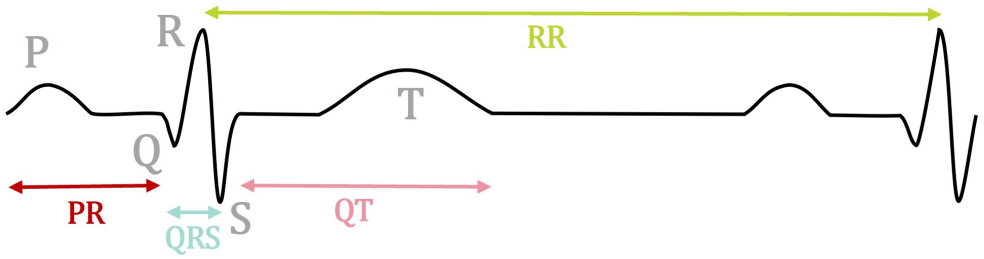

Figure 1.7: ECG trace of a normal patient with the P, T and U wave, the QRS complex (*in blue*), the PR (*in red*), QT (*in pink*) and RR (*in green*) intervals.

Based on these phases, three intervals could be defined:

- **RR interval:** It defined the instantaneous heart rate (HR) and it separates two consecutive R waves.

— **PR interval:** This interval is measured between the start of the P wave and the beginning of the QRS complex. It reflects the time the electrical impulse takes to travel from the sinoatrial node through the AV node.

— **QT interval:** It represents the time between the start of the QRS complex and the end of the T wave. It also represents the length of the ventricular depolarization and repolarization phases.

ECG gather a large among of information about the cardiac structure and its electrical conduction through the different parts of the heart. It could also warn about potential the conduction system damage or the muscle cells and help to follow the drug's effect or the proper functioning of implanted devices.

1.2.2 Echocardiography

As electrocardiography, echocardiography is another modality routinely used in diagnosis, management, and follow-up of heart diseases [4, 5]. This modality is widely used because it is non-invasive, harmless for the patient, fast, time real, relatively cheap, and widely available for the clinicians.

This type of imaging is based on standard ultrasound or Doppler ultrasound and produce a real time moving image of the heart. Ultrasound transmits sound waves with specific frequencies. The ultrasound pulses echo off tissues and are returned to the probe, which records. These differences of record due to the properties of the different crossed tissues provide a display as an image and video.

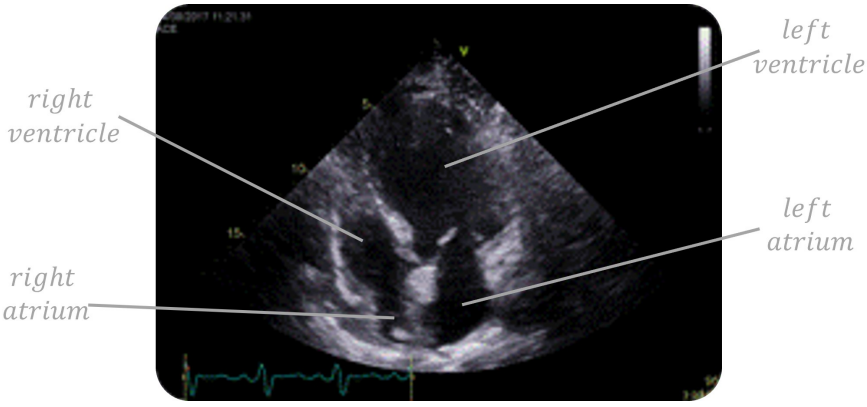

Figure 1.8: Transthoracic echocardiography (apical 4-chamber view).

Echocardiographic modes

Several modes could be used in echocardiography:

— **Color Doppler:** allows seeing and measure the flow of blood in the heart and arteries.

- **M-mode or 1D mode:** Less frequently used, it has specific uses and has the benefit of very high temporal fidelity.
- **B-mode or 2D mode:** It is the most commonly used in echocardiography and offers an image of the anatomy of the heart, allowing to see the different chambers (Figure 1.8) and valves structures during the heart cycle.
- **3D mode:** This new mode aims at providing 3 dimensions images, created from multiple images in 2D.

Echocardiograms provide information about the shape, size, function, and strength of the different heart chambers. The movement of the walls and the cardiac valve function could also be evaluated [6, 7]. It also estimates the cardiac function, thanks indices such as a calculation of the cardiac output, ejection fraction, systolic and diastolic function, valve area ...

Echocardiographic views

Cardiac ultrasound could refer to Trans-Thoracic Echocardiography (TTE) or TransEsophageal Echocardiography (TEE). TTE is the most common, and it is performed on the chest of the patient. TEE is more invasive and uses a special probe that is inserted into the esophagus.

During a transthoracic echocardiographic examination, several views could be observed [7]. Parasternal long and short axis; apical 2-, 3- and 4-chamber; subxiphoid, and inferior-vena-cava views.

The apical views are mostly used for the hemodynamic assessment of the heart. They well illustrated the global cardiac function with the systolic and diastolic functions as well as the valve behaviors.

Strain

Strain imaging is an advanced echocardiographic technique that assesses myocardial function by evaluating deformation of the myocardium (Figure 1.9). Two methods exist to track the movement of specific points on the heart wall and computing strain curves:

- Tissue Doppler Imaging (TDI) is a Doppler-based technique that measures the velocity of blood flow or tissue movement to calculate the strain of the heart muscle. It can be used to measure both longitudinal and radial strain of the myocardium.
- Speckle-Tracking Echocardiography (STE) is a feature-tracking technique that uses the natural speckle patterns present in ultrasound images to track the movement of specific points on the heart wall. STE does not rely on blood flow to track the motion, and it can provide a full-volume analysis of the heart. STE can also provide strain measurements in multiple planes, including longitudinal, radial, and circumferential.

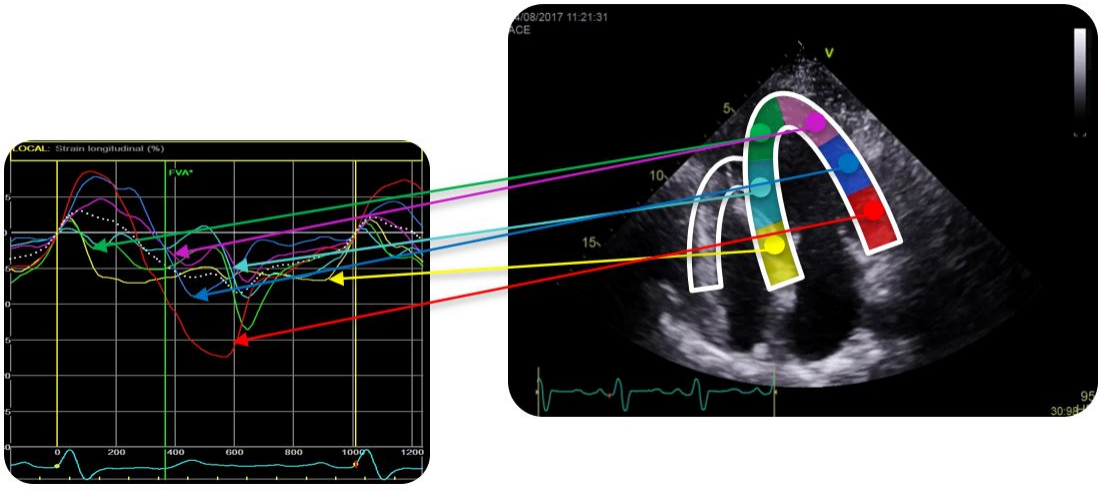

Figure 1.9: Echocardiography of the 4-chamber view with the 6 segments and the strain curves.

TDI is considered more sensitive to detect abnormalities in systolic function, while STE can provide a more detailed and accurate assessment of the heart's mechanical function. TDI is also more limited by the quality of the image and the presence of tissue interfaces or artifacts that may affect the accuracy of the results. STE is less dependent on image quality and can provide more robust results. Currently, STE technique is more used, and we will focus on this technique in the rest of this thesis.

With STE, strain curves could be acquired for different regions (called segments: s) and represent tissue deformation in 3 spatial directions: longitudinal, radial, and circumferential. The strain (ε) is expressed as a percentage. It is defined as the variation in the myocardial segment length (l_s) relative to its original length ($l_{s,ref}$), usually taken at end-diastole [8].

$$\varepsilon_s = \frac{(l_s - l_{s,ref})}{l_{s,ref}} \cdot 100 \tag{1.1}$$

Thus, positive longitudinal strain represents fiber elongation or relaxation and negative longitudinal strain indicates fiber shortening or contraction.

To gather the entire LV deformation, the 2-, 3-, and 4-chamber views could be used. In fact, the orientation of the probe during the echocardiography allows accessing all the ventricular wall. The six segments of the 2- and 4 chamber views and the six or four segments of the 3-chamber views create a 16 or 18 segmental ventricle, as illustrated in Figure 1.10 in order to access to the longitudinal deformation of the entire ventricle. Global Longitudinal Strain (GLS) value could be computed as the average of the maximum deformation of the longitudinal strain curve.

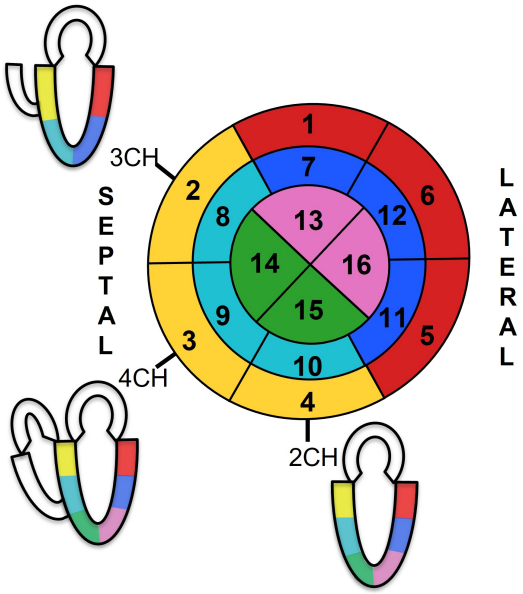

Figure 1.10: Six segmental segments for the three-echo view (2-, 3- and 4-chamber) with the representation of the LV in a bull eye with the echocardiography device vendor colors: 1: basal anterior, 2: basal anteroseptal, 3: basal inferoseptal, 4: basal inferior, 5: basal inferolateral, 6: basal anterolateral, 7: mid anterior, 8: mid anteroseptal, 9: mid inferoseptal, 10: mid inferior, 11: mid inferolateral, 12: mid anterolateral, 13: apical anterior, 14: apical septal, 15: apical inferior, 16: apical lateral

Echocardiographic indices/features

On a TTE one can measure structural element such as LV diameter at the end of systole (LVESD) or diastole (LVESD). The LV volumes are also computed: (LVESV and LVEDV). They are computed by a method called "Simpson Bi-plane" [7] which simplified the ventricle in disk layers of same size and sum all these disk volumes. To clinically simplify the computation of each disks' length, only two lengths could be used to estimate the entire LVESV and LVEDV by assuming that the LV is bullet shaped [7]. From these measurements and as it was previously mentioned, one of the major indicators of HF is Left Ventricle Ejection Fraction and it can be computed (in percentage):

$$LVEF = \frac{LVEDV - LVESV}{LVEDV} \cdot 100 \tag{1.2}$$

In a normal case, the LVEF is between 55 and 70%.

The LV atria can also be measured by TTE. The same could be done for the right ventricle, especially thanks to the 4-chamber view with the surface measurement at the end of systole and diastole.

Other indices can be extracted from TTE to diagnose HF. These indices measured the blood flow in the LV, and especially the blood flow velocity through the mitral valve. Figure 1.11 is a schematic

representation of the velocity of the blood composed by two waves.

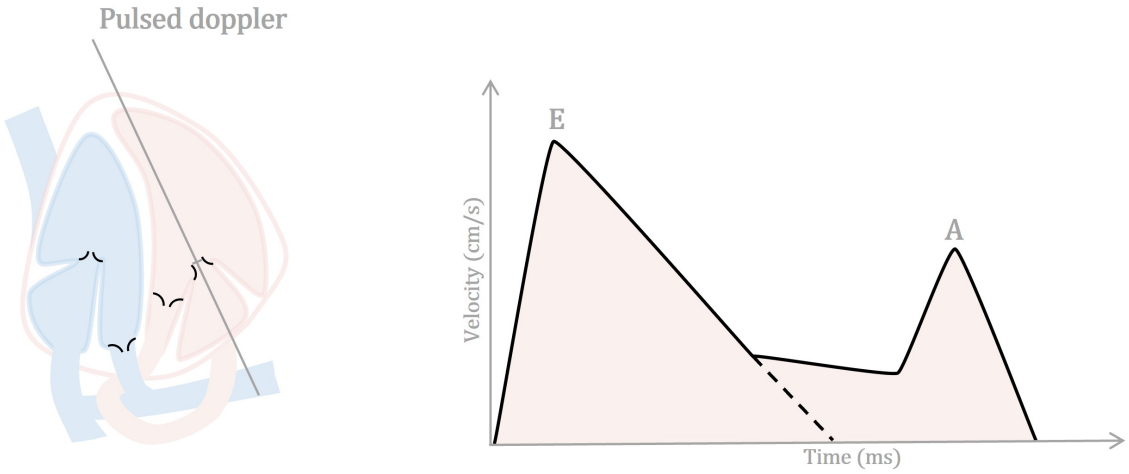

Figure 1.11: Scheme of the blood flow through the mitral valve. The E and A pic are represented, and the dotted line represent the decrease of speed after the E pic (used to compute DT).

The E-wave reflect the passive blood flow from the left atrium to the left ventricle and marks the start of diastole. This flow is pushed by the pressure gradient between the LA and the LV. The A-wave represents blood flow generated by active atrial contraction. From these two wave velocities, we could compute the E/A ratio [9]. In a healthy case, the E/A ratio must be higher than 1. If it is not the case, the patient presents a diastolic dysfunction. Moreover, if this ratio is above 2, it is a sign of a LV pressure too high.

Another feature could be extracted from this examination: The Deceleration Time. It is the time interval between the peak of E-wave to the projected baseline (see Figure 1.11). DT indicates the duration for equalizing the pressure difference between the left atrium and the left ventricle (through the mitral valve) and it leads to the diagnosis of HF.

Moreover, from this velocity curve, an integral could be computed: the mitral Velocity Time Integral, also called stroke distance. This integral allows prediction of HF evolution [10]. A similar integral could be computed at the LV exit, at the level of aorta, it is the aortic VTI.

The motion of the mitral annulus (that circle the valve) can be studied during systole and diastole. During systole, it travels toward the apex of the heart and go back during diastole. The mitral annular plane diastolic motion is then particularly interesting and as the blood is velocity could be recorded. Two main negative waves can be observed, e'-wave and a'-wave, and reflect the same event as the E-wave and A-wave, respectively. Experimentally, the e'-wave and a'-wave are measured separately for the septal and lateral walls and the average of these two velocity measurements are gathered under the name e', respectively for a'. Classically, a ratio between the blood flow velocity and the mitral annulus velocity in computed as E/e' [9, 11]. The motion of the mitral annulus also presents a main wave during systole. Similar to the e'-wave and a'-wave,

this systolic wave is the average of the two pics measured on the septal and lateral walls. This wave is named s' and is well correlate to the LVEF [12].

TTE allows to visually detect Septal Flash (SF). SF is a typical pattern of contraction and elongation of the septal wall of the LV [13]. It is a fast movement of the septal wall during systole and is an indicator of response to CRT [13–18]. Similarly, one could detect Apical Rocking on TTE. It is a typical movement of the apical part of the myocardium [13]. As Septal Flash, Apical Rocking is an indicator of CRT response [13, 14].

Other indices could also be extracted of the LV and predict a CRT response. For example, the Tricuspid Annular Plane Systolic Excursion (TAPSE) which is the measurement of the tricuspid annulus motion to the apex during systole or the Systolic Pulmonary Artery Pressure (SPAP) which allows to estimation of pulmonary arterial pressure during systole thanks the pressure gradient are one of them.

To sum up, various indices could be extracted from echo-measurements and can characterize myocardial function:

- **The structure:** LVESD LVESD, LVESV, LVEDV and LVEF, left atrium volume, the RV surface at end-systole and end-diastole.
- **The flow:** E-wave, A-wave, E/A, DT, mitral and aortic VTI, e'-wave, a'-wave, E/e'.
- **The atypical movements:** Septal Flash (SF) and Apical Rocking (AR).
- **The deformations:** with the strain curves and indices that can be extracted from them, developed in the next chapter (Section 2.2).

1.3 Heart failure

Heart Failure (HF) is a pathological state characterized by a decreased ability to pump blood and provide enough oxygen and nutrients to the body's organs. It is often caused by conditions that affect the heart's strength or elasticity. It is a chronic condition that tends to worsen over time [19–22].

HF can involve the left and/or the right ventricle. Several conditions could cause heart failure by changing the structure and/or the structure of the heart such as:

- Coronary artery disease,
- Heart attack,
- Hypertension,
- Valve disease,
- Cardiomyopathy,

— Myocarditis (inflammation of the heart muscle),

— Arrhythmias (abnormal heart rhythms).

This section will, now, focuses on three phenotypes of HF patients: aortic stenosis patients, patients with hypertrophic cardiomyopathy and HF patients with left bundle of branch.

1.3.1 Left bundle of branch block

Left Bundle of Branch Block (LBBB) is an anomaly of the cardiac conduction circuit. The electrical signal is partially or completely blocked in the left branch of the His bundle before reaching the left ventricle and lead it to contraction (Figure 1.12). Because of this blocking in the LBB, the signal only spread to the Right Bundle of Branch (RBB) and lead the LV contraction slower and with a delay compared to the RV. This results to a dyssynchrony in the heart contraction and a less effective blood ejection.

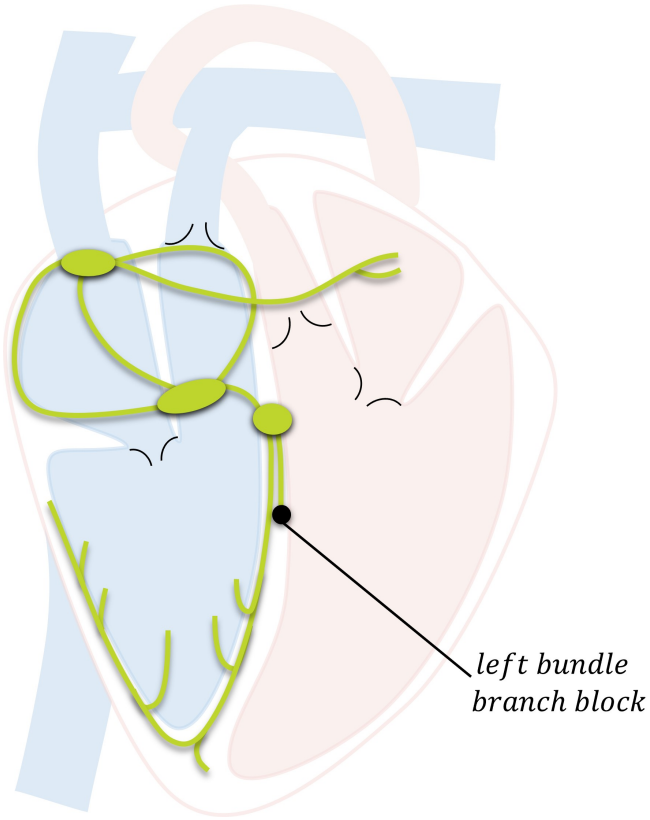

Figure 1.12: Left bundle branch block (LBBB). The electrical impulses are blocked in the left branch of the His bundle (illustrated by the black point)

There are several causes of LBBB [23–25]:

— **Myocardial infarction (or heart attack):** occurs when blood flow decreases or stops to the coronary artery of the heart.

- **Valve disease:** is the inability of one or more of the valves to work properly (open and close).
- **Hypertension:** is defined by high blood pressure.
- **Cardiomyopathy:** is the thickened, stiffened or weakened heart muscle.
- **Myocarditis:** is the inflammation of the heart muscle.

25% of heart failure patients present LBBB and in this case or for patients who present acute chest pain and/or syncope, LBBB could have great consequences. For other patients without other pathology, LBBB has no major consequence and needs no treatment.

LBBB diagnosis is mainly done by a 12-leads ECG and these following criteria are usually used:

- The QRS duration is superior to 120 ms for at least one derivation.
- V1 has a QS complex (QRS complex is often entirely negative) or a small R wave followed by a large S wave.
- V6 has a high and wide R wave, no Q wave and present T wave inversions.

For this critical patients, pharmacological treatments or the implantation of a Cardiac Resynchronization Therapy (CRT) device could be used.

Cardiac Resynchronization Therapy is a treatment of choice in patients with systolic heart failure and LBBB with wide QRS (>120 ms), who remain symptomatic despite optimized medical therapy.

Cardiac resynchronization therapy

Cardiac Resynchronization Therapy (CRT) is a device-based implantation (Figure 1.13). The device provides small electrical signals through its leads. It aims at synchronizing the ventricle contraction that implies a more effective heart pumping and stabilize the electromechanical system [26].

There are two types of CRT devices:

- **The Cardiac Resynchronization Therapy Pacemaker (CRT-P) or biventricular pacemaker:** it is a kind of pacemaker.
- **The Cardiac Resynchronization Therapy Defibrillator (CRT-D):** It is similar to the previous one but includes also a built-in implantable cardioverter defibrillator.

This therapy is proposed to symptomatic patients who have systolic heart failure, with severely reduced LV ejection fraction (<35%) and significant intraventricular conduction delay (QRS duration >120 ms), most of them are LBBB patients [25]. However, around 30% of implanted patients, according to the European and the United States guideline, does not respond to the CRT (defined as a decrease $\geq$15% in LV end-systolic volume). In addition to the LV end-systolic volume (and LVEF), the New-York Heart Association (NYHA) functional class is also commonly used to evaluate the response to CRT based on a reduction in symptoms and an improvement in functional status.

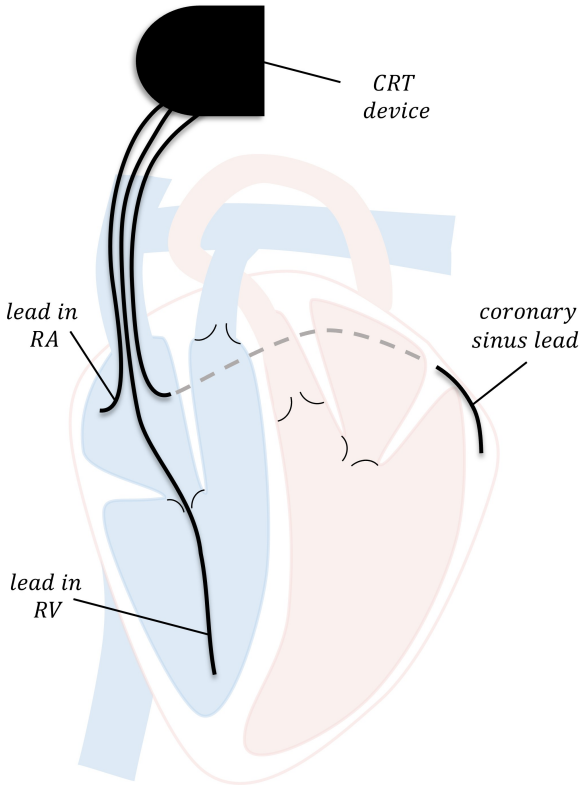

Figure 1.13: Cardiac resynchronization therapy (CRT), localization of the 3 leads in the right atria (RA), right ventricle (RV) and in the coronary sinus.

Improving the patient selection for cardiac resynchronization therapy (CRT) is essential to lead to better outcomes and cost-effectiveness [26–35]. By identifying patients who will benefit from CRT, we can ensure that the therapy is being used for the most appropriate patients, reducing the risk of complications and increasing the chances of success.

Alternative pacing location (conduction system pacing) are currently explore to improve the CRT response. This pacing technique provides a more physiological simultaneous electrical activation of the ventricles via the His Purkinje system [29]. Studies are ongoing to evaluate the benefits of this technique, and it was not explored during this thesis [36–39].

1.3.2 Aortic stenosis

Aortic Stenosis (AS) is the most common primary valvular heart disease, leading to an intervention with growing prevalence due to the aging population. Valvular heart disease is the inability of one or more of the valves to work properly, causing disruption in blood flow (see Figure 1.5). There are two different type of valve disease: valvular regurgitation.

- **Valvular regurgitation:** It happens when the valve does not close completely and allow the blood to flow back.

– **Valvular stenosis:** It happens when the valve opening is smaller than normal and restricts the blood flood to pass.

In both case, this causes serious implications because it restrains the good supply (oxygen and nutriment) and elimination (CO_2 and wastes) through the blood circulation in the entire body.

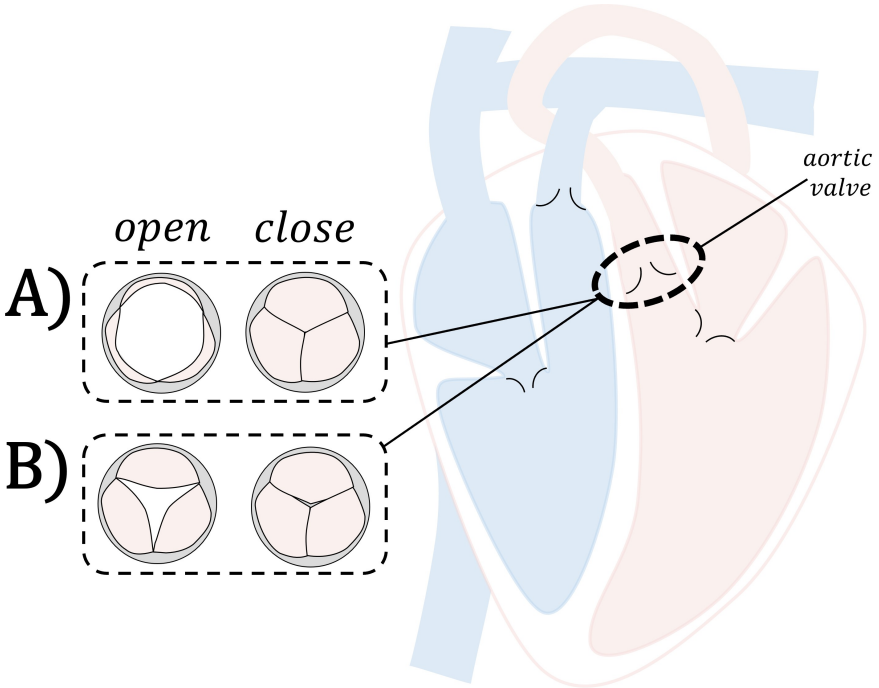

Figure 1.14: Aortic valve localization, a) Healthy vs b) Stenosis aortic valve.

AS is characterized by a reduction of the aortic valve orifice size (Figure 1.14). This surface reduction restricts the blood to flows out the LV and provide oxygenated blood to the entire body via aorta. It also develops a pressure gradient across the aortic valve and a chronic pressure overload in the LV. An AS patient needs to provide extra work to pump enough blood and thus leads to heart failure.

Current recommendations [40, 41] state that Aortic Valve Replacement (AVR) is a class I indication in cases of symptoms or reduced left ventricular ejection fraction (LVEF <50%) [42]. Whatever, LVEF is preserved in many patients with AS even when symptoms develop and/or the narrowing of the valve is severe. Echocardiographic exam [43] is usually the way to diagnose AS. It allows the quantification of aortic valve and transaortic gradient, as well as the assessment of LV morphology and function. Unfortunately, valvular parameters such as Aortic Valve Area (AVA) and transvalvular gradient did not permit an ideal risk stratification [41, 44–48]. Depending on the severity of the aortic reduction, the signs and symptoms, and the condition of the organs (heart and lungs), different treatments could be proposed. Early treatment can help to reverse or slow down the progress of this disease. Other possible treatments may include Aortic Valve Replacement (AVR), using mechanical or biological prostheses. This is done by a heart-open

surgery or a Transcatheter Aortic Valve Implantation (TAVI).

1.3.3 Hypertrophic cardiomyopathy

Hypertrophic CardioMyopathy (HCM) is a genetic disorder characterized by thickening of the heart (Figure 1.15). The hypertrophied heart walls make the pumping function harder.

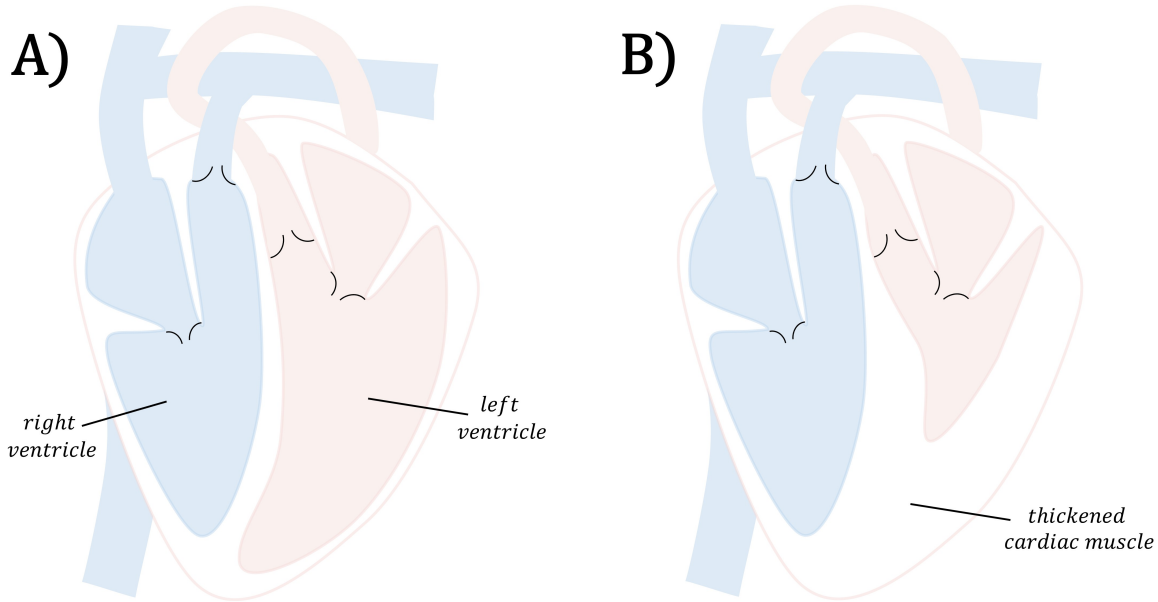

Figure 1.15: a) Normal heart, b) Hypertrophic heart

Hypertrophied myocardial areas are characterized by myocardial disarray, interstitial and focal fibrosis. These areas constitute the substrate of ventricular arrhythmias which classically occurs in addition to an excess of sympathetic tone, like exercise or stress, and/or ischemia [49, 50]. In these hypertrophied areas, the myocardial disarrays involve a local electrical conduction delay secondary to fibrotic replacement and emergence of anisotropic areas.

A minority of the HCM patients present symptoms such as shortness of breath or chest pain. Because of this absence of symptoms, or few symptoms, HCM is often undiagnosed. Unless a small number of HCM patients present symptoms, HCM represents a major cause of Sudden Cardiac Death (SCD), particularly in the young population, with a risk of about 1% per year [51, 52].

Primary prevention of SCD is based on Implantable Cardiac Defibrillator (ICD) [53, 54] with good effectiveness but at the cost of an invasive procedure and device complications including infection and inappropriate shocks [55]. Identification of patients at risk of SCD is still a major clinical challenge unless risk of SCD score was proposed by the European Society of Cardiology (ESC) [56].

1.4 Conclusion

The evaluation of LV function currently remains a major challenge in cardiology. Even if LVEF remains a reference diagnostic tool, its dependence on the afterload and the geometry of the left ventricle makes it an insufficient indicator on its own. Despite an abundant literature, the use of strain, evaluated in echocardiography, struggles to be integrated into daily care. The evaluation of myocardial deformations, specifically through the estimation of strain curves in echocardiography, appears as particularly promising. However, the complexity and multidimensionality of the problem, as well as the various processes involved in ventricular contraction, make analyzing myocardial strains a difficult task. Therefore, new methods are necessary to jointly analyze echocardiography data and, especially, strain morphology acquired from different regions of the myocardium. Moreover, recent research demonstrates the growing importance of phenotyping, partly thanks to imaging techniques. Medical doctors provide therapies and strategies that have been proven relevant in randomized trials, allowing for the provision of care to patients with potentially serious heart diseases. However, it is important to note that randomized studies demonstrate the value of a strategy or treatment at the level of a target population, not at the individual level. By using echocardiographic data, we can attempt to better characterize patients and clearly evaluate them, thereby enabling the provision of more appropriate and personalized treatment strategies.

BIBLIOGRAPHY

[1] Lilly L.S. *Pathophysiology of heart disease: A collaborative project of medical students and faculty*. Lippincott Williams & Wilkins (2015).

[2] Corrado D., Pelliccia A., Heidbuchel H., Sharma S., Link M., Basso C., Biffi A., Buja G., Delise P., Gussac I., Anastasakis A., Borjesson M., Bjørnstad H.H., Carr F., Deligiannis A., Dugmore D., Fagard R., Hoogsteen J., Mellwig K.P., Panhuyzen-Goedkoop N., Solberg E., Vanhees L., Drezner J., Estes N.A., Iliceto S., Maron B.J., Peidro R., Schwartz P.J., Stein R., Thiene G., Zeppilli P., and McKenna W.J. Recommendations for interpretation of 12-lead electrocardiogram in the athlete. *Eur. Heart J.*, vol. 31, 243–259 (2010).

[3] Meek S. ABC of clinical electrocardiography: Introduction. I—Leads, rate, rhythm, and cardiac axis. *BMJ*, vol. 324 (2002).

[4] Spencer K.T., Kimura B.J., Korcarz C.E., Pellikka P.A., Rahko P.S., and Siegel R.J. Focused cardiac ultrasound: Recommendations from the american society of echocardiography. *J. Am. Soc. Echocardiogr.*, vol. 26, 567–581 (2013).

[5] Hanton G., Eder V., Rochefort G., Bonnet P., and Hyvelin J.M. Echocardiography, a non-invasive method for the assessment of cardiac function and morphology in preclinical drug toxicology and safety pharmacology (2008).

[6] Parisi A.F., Moynihan P.F., Feldman C.L., and Folland E.D. Approaches to determination of left ventricular volume and ejection fraction by real-time two-dimensional echocardiography. *Clin. Cardiol.*, vol. 2, 257–263 (1979).

[7] Lang R.M., Badano L.P., Mor-Avi V., Afilalo J., Armstrong A., Ernande L., Flachskampf F.A., Foster E., Goldstein S.A., Kuznetsova T., Lancellotti P., Muraru D., Picard M.H., Rietzschel E.R., Rudski L., Spencer K.T., Tsang W., and Voigt J.U. Recommendations for cardiac chamber quantification by echocardiography in adults: An update from the American society of echocardiography and the European association of cardiovascular imaging. *Eur. Heart J. Cardiovasc. Imaging*, vol. 16, 233–271 (2015).

[8] Voigt J.U., Pedrizzetti G., Lysyansky P., Marwick T.H., Houle H., Baumann R., Pedri S., Ito Y., Abe Y., Metz S., Song J.H., Hamilton J., Sengupta P.P., Kolias T.J., D'Hooge J., Aurigemma G.P., Thomas J.D., and Badano L.P. Definitions for a common standard for 2D speckle tracking echocardiography: consensus document of the EACVI/ASE/Industry Task Force to standardize deformation imaging. *Eur. Heart J. Cardiovasc. Imaging*, vol. 16, 1–11 (2015).

[9] Mitter S.S., Shah S.J., and Thomas J.D. A Test in Context: E/A and E/e to Assess Diastolic Dysfunction and LV Filling Pressure (2017).

[10] Mishra R.K., Devereux R.B., Cohen B.E., Whooley M.A., and Schiller N.B. Prediction of heart failure and adverse cardiovascular events in outpatients with coronary artery disease using mitral E/A ratio in conjunction with e-wave deceleration time: The heart and soul study. *J. Am. Soc. Echocardiogr.*, vol. 24 (2011).

[11] Park J.H. and Marwick T.H. Use and Limitations of E/e' to Assess Left Ventricular Filling Pressure by Echocardiography. *J. Cardiovasc. Ultrasound*, vol. 19 (2011).

[12] Kadappu K.K. and Thomas L. Tissue doppler imaging in echocardiography: Value and limitations (2015).

[13] Stankovic I., Prinz C., Ciarka A., Daraban A.M., Kotrc M., Aarones M., Szulik M., Winter S., Belmans A., Neskovic A.N., Kukulski T., Aakhus S., Willems R., Fehske W., Penicka M., Faber L., and Voigt J.U. Relationship of visually assessed apical rocking and septal flash to response and long-term survival following cardiac resynchronization therapy (PREDICT-CRT). *Eur. Heart J. Cardiovasc. Imaging*, vol. 17, 262–269 (2016).

[14] Gorcsan J. and Lumens J. Rocking and Flashing With RV Pacing: Implications for Resynchronization Therapy . *JACC Cardiovasc. Imaging*, vol. 10, 1100–1102 (2017).

[15] Walmsley J., Huntjens P.R., Prinzen F.W., Delhaas T., and Lumens J. Septal flash and septal rebound stretch have different underlying mechanisms. *Am. J. Physiol. Heart Circ. Physiol.*, vol. 310, H394–H403 (2016).

[16] Calle S., Delens C., Kamoen V., De Pooter J., and Timmermans F. Septal flash: At the heart of cardiac dyssynchrony. *Trends Cardiovasc. Med.*, vol. 30, 115–122 (2020).

[17] Aalen J.M., Remme E.W., Larsen C.K., Andersen O.S., Krogh M., Duchenne J., Hopp E., Ross S., Beela A.S., Kongsgaard E., Bergsland J., Odland H.H., Skulstad H., Opdahl A., Voigt J.U., and Smiseth O.A. Mechanism of Abnormal Septal Motion in Left Bundle Branch Block: Role of Left Ventricular Wall Interactions and Myocardial Scar. *JACC Cardiovasc. Imaging*, vol. 12, 2402–2413 (2019).

[18] Aalen J.M., Donal E., Larsen C.K., Duchenne J., Lederlin M., Cvijic M., Hubert A., Voros G., Leclercq C., Bogaert J., Hopp E., Fjeld J.G., Penicka M., Linde C., Aalen O.O., Kongsgård E., Galli E., Voigt J.U., and Smiseth O.A. Imaging predictors of response to cardiac resynchronization therapy: Left ventricular work asymmetry by echocardiography and septal viability by cardiac magnetic resonance. *Eur. Heart J.*, vol. 41, 3813–3823 (2020).

[19] Mosterd A. and Hoes A.W. Clinical epidemiology of heart failure. *Heart*, vol. 93, 1137–1146 (2007).

[20] Kemp C.D. and Conte J.V. The pathophysiology of heart failure. *Cardiovasc. Pathol.*, vol. 21, 365–371 (2012).

[21] Yancy C.W., Januzzi J.L., Allen L.A., Butler J., Davis L.L., Fonarow G.C., Ibrahim N.E., Jessup M., Lindenfeld J.A., Maddox T.M., Masoudi F.A., Motiwala S.R., Patterson J.H., Walsh M.N., and Wasserman A. 2017 ACC Expert Consensus Decision Pathway for Optimization of Heart Failure Treatment: Answers to 10 Pivotal Issues About Heart Failure With Reduced Ejection Fraction: A Report of the American College of Cardiology Task Force on Expert Consensus Decision Pathways. *J. Am. Coll. Cardiol.*, vol. 71 (2018).

[22] Maddox T.M., Januzzi J.L., Allen L.A., Breathett K., Butler J., Davis L.L., Fonarow G.C., Ibrahim N.E., Lindenfeld J.A., Masoudi F.A., Motiwala S.R., Oliveros E., Patterson J.H., Walsh M.N., Wasserman A., Yancy C.W., and Youmans Q.R. 2021 Update to the 2017 ACC Expert Consensus Decision Pathway for Optimization of Heart Failure Treatment: Answers to 10 Pivotal Issues About Heart Failure With Reduced Ejection Fraction: A Report of the American College of Cardiology Solution Set Oversight Committee. *J. Am. Coll. Cardiol.*, vol. 77 (2021).

[23] Francia P., Balla C., Paneni F., and Volpe M. Left bundle-branch block - Pathophysiology, prognosis, and clinical management (2007).

[24] Surkova E., Badano L.P., Bellu R., Aruta P., Sambugaro F., Romeo G., Migliore F., and Muraru D. Left bundle branch block: From cardiac mechanics to clinical and diagnostic challenges (2017).

[25] Elsevier Inc., Strauss D.G., Selvester R.H., and Wagner G.S. Defining left bundle branch block in the era of cardiac resynchronization therapy (2011).
Accessed on 25/10/2021 from: http://dx.doi.org/10.1016/j.amjcard.2010.11.010

[26] Bax J.J., Abraham T., Barold S.S., Breithardt O.A., Fung J.W., Garrigue S., Gorcsan J., Hayes D.L., Kass D.A., Knuuti J., Leclercq C., Linde C., Mark D.B., Monaghan M.J., Nihoyannopoulos P., Schalij M.J., Stellbrink C., and Yu C.M. Cardiac resynchronization therapy: Part 1 - Issues before device implantation (2005).

[27] Dickstein K., Vardas P.E., Auricchio A., Daubert J.C., Linde C., McMurray J., Ponikowski P., Priori S.G., Sutton R., Van Veldhuisen D.J., Vahanian A., Bax J., Ceconi C., Dean V., Filippatos G., Funck-Brentano C., Hobbs R., Kearney P., McDonagh T., Popescu B.A., Reiner Z., Sechtem U., Sirnes P.A., Tendera M., Vardes P., Widimsky P., Anker S.D., Blanc J.J., Gasparini M., Hoes A.W., Israel C.W., Kalarus Z., Merkely B., Swedberg K., and Camm A.J. 2010 Focused Update of ESC Guidelines on device therapy in heart failure (2010).

[28] Ponikowski P., Voors A.A., Anker S.D., Bueno H., Cleland J.G., Coats A.J., Falk V., González-Juanatey J.R., Harjola V.P., Jankowska E.A., Jessup M., Linde C., Nihoyannopoulos P., Parissis J.T., Pieske B., Riley J.P., Rosano G.M., Ruilope L.M., Ruschitzka F., Rutten F.H., Van Der Meer P., Sisakian H.S., Isayev E., Kurlianskaya A., Mullens W., Tokmakova M., Agathangelou P., Melenovsky V., Wiggers H., Hassanein M., Uuetoa T., Lommi J., Kostovska E.S., Juilliere Y., Aladashvili A., Luchner A., Chrysohoou C., Nyolczas N., Thorgeirsson G., Weinstein J.M., Lenarda A.D., Aidargaliyeva N., Bajraktari G., Beishenkulov M., Kamzola G., Abdel-Massih T., Celutkiene J., Noppe S., Cassar A., Vataman E., AbirKhalil S., van Pol P., Mo R., Straburzynska-Migaj E., Fonseca C., Chioncel O., Shlyakhto E., Zavatta M., Otasevic P., Goncalvesova E., Lainscak M., Molina B.D., Schaufelberger M., Suter T., Yilmaz M.B., Voronkov L., and Davies C. 2016 ESC Guidelines for the diagnosis and treatment of acute and chronic heart failure. *Eur. Heart J.*, vol. 37, 2129–2200m (2016).

[29] Glikson M., Nielsen J.C., Kronborg M.B., Michowitz Y., Auricchio A., Barbash I.M., Barrabés J.A., Boriani G., Braunschweig F., Brignole M., Burri H., Coats A.J., Deharo J.C., Delgado V., DIller G.P., Israel C.W., Keren A., Knops R.E., Kotecha D., Leclercq C., Merkely B., Starck C., Thylén I., Tolosana J.M., Leyva F., Linde C., Abdelhamid M., Aboyans V., Arbelo E., Asteggiano R., Barón-Esquivias G., Bauersachs J., Biffi M., Birgersdotter-Green U., Bongiorni M.G., Borger M.A., Celutkienė J., Cikes M., Daubert J.C., Drossart I., Ellenbogen K., Elliott P.M., Fabritz L., Falk V., Fauchier L., Fernández-Avilés F., Foldager D., Gadler F., De Vinuesa P.G.G., Gorenek B., Guerra J.M., Hermann Haugaa K., Hendriks J., Kahan T., Katus H.A., Konradi A., Koskinas K.C., Law H., Lewis B.S., Linker N.J., Løchen M.L., Lumens J., Mascherbauer J., Mullens W., Nagy K.V., Prescott E., Raatikainen P., Rakisheva A., Reichlin T., Ricci R.P., Shlyakhto E., Sitges M., Sousa-Uva M., Sutton R., Suwalski P., Svendsen J.H., Touyz R.M., Van Gelder I.C., Vernooy K., Waltenberger J., Whinnett Z., Witte K.K., Kronborg M.B., Michowitz Y., Auricchio A., Barbash I.M., Barrabés J.A., Boriani G., Braunschweig F., Brignole M., Burri H., Coats A.J., Deharo J.C., Delgado V., DIller G.P., Israel C.W., Keren A., Knops R.E., Kotecha D., Leclercq C., Merkely B., Starck C., Thylén I., and Tolosana J.M. 2021 ESC Guidelines on cardiac pacing and cardiac resynchronization therapy. *Eur. Heart J.*, vol. 42, 3427–3520 (2021).

[30] Leyva F., Nisam S., and Auricchio A. 20 years of cardiac resynchronization therapy (2014).

[31] Bax J.J., Abraham T., Barold S.S., Breithardt O.A., Fung J.W., Garrigue S., Gorcsan J., Hayes D.L., Kass D.A., Knuuti J., Leclercq C., Linde C., Mark D.B., Monaghan M.J., Nihoyannopoulos P., Schalij M.J., Stellbrink C., and Yu C.M. Cardiac resynchronization therapy: Part 2 - Issues during and after device implantation and unresolved questions (2005).

[32] Zareba W., Klein H., Cygankiewicz I., Hall W.J., McNitt S., Brown M., Cannom D., Daubert J.P., Eldar M., Gold M.R., Goldberger J.J., Goldenberg I., Lichstein E., Pitschner H., Rashtian M., Solomon S., Viskin S., Wang P., and Moss A.J. Effectiveness of cardiac resynchronization therapy by QRS morphology in the multicenter automatic defibrillator implantation trial-cardiac resynchronization therapy (MADIT-CRT). *Circulation*, vol. 123, 1061–1072 (2011).

[33] Cleland J.G., Abraham W.T., Linde C., Gold M.R., Young J.B., Claude Daubert J., Sherfesee L., Wells G.A., and Tang A.S. An individual patient meta-analysis of five randomized trials assessing the effects of cardiac resynchronization therapy on morbidity and mortality in patients with symptomatic heart failure. *Eur. Heart J.*, vol. 34 (2013).

[34] Duchenne J. Finding New Insights in Cardiac Resynchronization Therapy and the Pathophysiology behind Left Ventricular Dyssynchrony. *J. Clin. Med.*, 10–12 (2022).

[35] Daubert C., Behar N., Martins R.P., Mabo P., and Leclercq C. Avoiding non-responders to cardiac resynchronization therapy: A practical guide. *Eur. Heart J.*, vol. 38, 1463–1472 (2017).

[36] Vijayaraman P., Zalavadia D., Haseeb A., Dye C., Madan N., Skeete J.R., Vipparthy S.C., Young W., Ravi V., Rajakumar C., Pokharel P., Larsen T., Huang H.D., Storm R.H., Oren J.W., Batul S.A., Trohman R.G., Subzposh F.A., and Sharma P.S. Clinical outcomes of conduction system pacing compared to biventricular pacing in patients requiring cardiac resynchronization therapy. *Hear. Rhythm*, vol. 19, 1263–1271 (2022).

[37] Kong N.W. and Upadhyay G.A. Cardiac resynchronization considerations in left bundle branch block. *Front. Physiol.*, vol. 13, 1–9 (2022).

[38] Ezzeddine F.M., Pistiolis S.M., Pujol-Lopez M., Lavelle M., Wan E.Y., Patton K.K., Robinson M., Lador A., Tamirisa K., Karim S., Linde C., Parkash R., Birgersdotter-Green U., Russo A.M., Chung M., and Cha Y.M. Outcomes of conduction system pacing for cardiac resynchronization therapy in patients with heart failure: A multicenter experience. *Hear. Rhythm* (2023).

[39] Zhang S., Zhou X., and Gold M.R. Left Bundle Branch Pacing: JACC Review Topic of the Week. *J. Am. Coll. Cardiol.*, vol. 74, 3039–3049 (2019).

[40] Otto C.M., Nishimura R.A., Bonow R.O., Carabello B.A., Erwin J.P., Gentile F., Jneid H., Krieger E.V., Mack M., McLeod C., O'Gara P.T., Rigolin V.H., Sundt T.M., Thompson A., Toly C., O'Gara P.T., Beckman J.A., Levine G.N., Al-Khatib S.M., Armbruster A., Birtcher K.K., Ciggaroa J., Deswal A., Dixon D.L., Fleisher L.A., de las Fuentes L., Gentile F., Goldberger Z.D., Gorenek B., Haynes N., Hernandez A.F., Hlatky M.A., Joglar J.A., Jones W.S., Marine J.E., Mark D., Palaniappan L., Piano M.R., Spatz E.S., Tamis-Holland J., Wijeysundera D.N., and Woo Y.J. 2020 ACC/AHA guideline for the management of patients with valvular heart disease. *J. Thorac. Cardiovasc. Surg.*, vol. 162 (2021).

[41] Bonow RO, Carabello B, de Leon AC Jr, Edmunds LH Jr, Fedderly BJ, Freed MD, Gaasch WH, McKay CR, Nishimura RA, O'Gara PT, O'Rourke RA R.S. *2014 AHA/ACC guideline for the management of patients with valvular heart disease: Executive summary :A report of the american college of cardiology/american heart association task force on practice guidelines*, vol. 129. Am Heart Assoc (2014).

[42] Taniguchi T., Morimoto T., Shiomi H., Ando K., Kanamori N., Murata K., Kitai T., Kadota K., Izumi C., Nakatsuma K., Sasa T., Watanabe H., Kuwabara Y., Makiyama T., Ono K., Shizuta S., Kato T., Saito N., Minatoya K., Kimura T., Kimura T., Taniguchi T., Shiomi H., Saito N., Imai M., Tazaki J., Toyota T., Higami H., Kawaji T., Ando K., Shirai S., Kourai K., Arita T., Miura S., Yamaji K., Aoyama T., Kanamori N., Onodera T., Murata K., Furukawa Y., Kitai T., Kim K., Kadota K., Kawase Y., Iwasaki K., Miyawaki H., Misao A., Kuwayama A., Ohya M., Shimada T., Amano H., Nakagawa Y., Izumi C., Miyake M., Amano M., Takahashi Y., Yoshikawa Y., Nishimura S., Kuroda M., Shirotani M., Mitsuoka H., Miki S., Mizoguchi T., Kato M., Yokomatsu T., Kushiyama A., Yaku H., Watanabe T., Miyazaki S., Hirano Y., Matsuda M., Matsuda S., Sugioka S., Inada T., Nagao K., Takahashi N., Fukuchi K., Murakami T., Mabuchi H., Takeda T., Sakaguchi T., Maeda K., Yamaji M., Maenaka M., Tadano Y., Sakamoto H., Takeuchi Y., Motooka M., Nishikawa R., Eizawa H., Yamane K., Kawato M., Kinoshita M., Aida K., Tamura T., Toyofuku M., Takahashi K., Ko E., Akao M., Ishii M., Masunaga N., Ogawa H., Iguchi M., Unoki T., Takabayashi K., Hamatani Y., Yamashita Y., Inoko M., Minamino-Muta E., Kato T., Himura Y., Ikeda T., Ishii K., Komasa A., Sato Y., Hotta K., Tsuji S., Hiraoka Y., Higashitani N., Kouchi I., Kato Y., Ikeguchi S., Inuzuka Y., Nishio S., Seki J., Shinoda E., Yamada M., Kawamoto A., Maeda C., Konishi T., Jinnai T., Sogabe K., Tachiiri M., Matsumura Y., Ota C., Kitaguchi S., Morikami Y., Sakata R., Minakata K., Minatoya K., Hanyu M., Yamazaki F., Koyama T., Komiya T., Yamanaka K., Nishiwaki N., Nakajima H., Ohnaka M., Osada H., Meshii K., Saga T., Onoe M., Nakayama S., Sakaguchi G., Iwakura A., Shiraga K., Ueyama K., Fujiwara K., Fukumoto A., Park M., Nishizawa J., and Kitano M. Prognostic Impact of Left Ventricular Ejection Fraction in Patients With Severe Aortic Stenosis. *JACC Cardiovasc. Interv.*, vol. 11, 145–157 (2018).

[43] Baumgartner H., Hung J., Bermejo J., Chambers J.B., Evangelista A., Griffin B.P., Iung B., Otto C.M., Pellikka P.A., and Quiñones M. Echocardiographic assessment of valve stenosis: EAE/ASE recommendations for clinical practice. *Eur. J. Echocardiogr.*, vol. 10, 1–25 (2009).

[44] Taniguchi T., Morimoto T., Shiomi H., Ando K., Kanamori N., Murata K., Kitai T., Kawase Y., Izumi C., Miyake M., Mitsuoka H., Kato M., Hirano Y., Matsuda S., Nagao K., Inada T., Murakami T., Takeuchi Y., Yamane K., Toyofuku M., Ishii M., Minamino-Muta E., Kato T., Inoko M., Ikeda T., Komasa A., Ishii K., Hotta K., Higashitani N., Kato Y., Inuzuka Y., Maeda C., Jinnai T., Morikami Y., Sakata R., and Kimura T. Initial Surgical Versus Conservative Strategies in Patients with Asymptomatic Severe Aortic Stenosis. *J. Am. Coll. Cardiol.*, vol. 66, 2827–2838 (2015).

[45] Tastet L., Tribouilloy C., Maréchaux S., Vollema E.M., Delgado V., Salaun E., Shen M., Capoulade R., Clavel M.A., Arsenault M., Bédard É., Bernier M., Beaudoin J., Narula J., Lancellotti P., Bax J.J., Généreux P., and Pibarot P. Staging Cardiac Damage in Patients With Asymptomatic Aortic Valve Stenosis. *J. Am. Coll. Cardiol.*, vol. 74, 550–563 (2019).

[46] Kang D.H., Park S.J., Lee S.A., Lee S., Kim D.H., Kim H.K., Yun S.C., Hong G.R., Song J.M., Chung C.H., Song J.K., Lee J.W., and Park S.W. Early Surgery or Conservative Care for Asymptomatic Aortic Stenosis. *N. Engl. J. Med.*, vol. 382, 111–119 (2020).

[47] Yokoyama Y., Takagi H., and Kuno T. Early surgery versus conservative management of asymptomatic severe aortic stenosis: A meta-analysis. *J. Thorac. Cardiovasc. Surg.* (2020).

[48] Patrizio Lancellotti, M.D., Ph.D., and Mani A. Vannan, M.B. B. Timing of Intervention in Aortic Stenosis Patrizio. *N. Engl. J. Med.*, 1–2 (2019).

[49] Varnava A.M., Elliott P.M., Sharma S., McKenna W.J., and Davies M.J. Hypertrophic cardiomyopathy: The interrelation of disarray, fibrosis and small vessel disease. *Heart*, vol. 84 (2000).

[50] Moore B., Semsarian C., Chan K.H., and Sy R.W. Sudden Cardiac Death and Ventricular Arrhythmias in Hypertrophic Cardiomyopathy (2019).

[51] Maron B.J., Olivotto I., Spirito P., Casey S.A., Bellone P., Gohman T.E., Graham K.J., Burton D.A., and Cecchi F. Epidemiology of Hypertrophic Cardiomyopathy–Related Death. *Circulation*, vol. 102, 858–864 (2000).

[52] Maron B.J., Shirani J., Poliac L.C., Mathenge R., Roberts W.C., and Mueller F.O. Sudden death in young competitive athletes: Clinical, demographic, and pathological profiles. *JAMA*, vol. 276 (1996).

[53] Gersh B.J., Maron B.J., Bonow R.O., Dearani J.A., Fifer M.A., Link M.S., Naidu S.S., Nishimura R.A., Ommen S.R., Rakowski H., Seidman C.E., Towbin J.A., Udelson J.E., and Yancy C.W. 2011 ACCF/AHA guideline for the diagnosis and treatment of hypertrophic cardiomyopathy: Executive summary: A report of the American College of cardiology foundation/American heart association task force on practice guidelines. *Circulation*, vol. 124, 2761–2796 (2011).

[54] Trayanova N.A. Learning for Prevention of Sudden Cardiac Death. *Circ. Res.*, vol. 128, 185–187 (2021).

[55] Lin G., Nishimura R.A., Gersh B.J., Phil D., Ommen S.R., Ackerman M.J., and Brady P.A. Device complications and inappropriate implantable cardioverter defibrillator shocks in patients with hypertrophic cardiomyopathy. *Heart*, vol. 95 (2009).

[56] O'Mahony C., Jichi F., Pavlou M., Monserrat L., Anastasakis A., Rapezzi C., Biagini E., Gimeno J.R., Limongelli G., McKenna W.J., Omar R.Z., Elliott P.M., Ortiz-Genga M., Fernandez X., Vlagouli V., Stefanadis C., Coccolo F., Sandoval M.J.O., Pacileo G., Masarone D., Pantazis A., Tome-Esteban M., Dickie S., Lambiase P.D., and Rahman S. A novel clinical risk prediction model for sudden cardiac death in hypertrophic cardiomyopathy (HCM Risk-SCD). *Eur. Heart J.*, vol. 35, 2010–2020 (2014).

Chapter

2 Methods and Tools

The methodological framework proposed in this thesis combines: i) physiological model-based approach, ii) signal/data processing and feature extraction, iii) supervised and unsupervised machine-learning.

Modeling and simulation methods and tools are presented in Section 2.1. A description of modeling and simulation tools is proposed, including M2SL, which is a multi-formalism modeling and simulation library developed by our team. This section also focuses on methods of sensitivity parameter analysis and includes a description of parameter identification strategy that was proposed in this thesis. Analyze the parameters of a model is a crucial step that enables a better understanding of the characteristics and behaviors of the model itself, and the system under study. Data processing and feature extraction, including longitudinal strain integrals and myocardial work indices, are described in Section 2.2. This second section is essential to process data both prior and after the model identification process, as well as for identifying possibles new markers of the LV function. Finally, Section 2.3 presents the machine-learning algorithm applied in this thesis.

2.1 Model-based approach

The implementation and investigation of integrated mathematical models require a set of appropriate simulations tools and parametric analysis methods. This chapter presents the modeling tools and methods used throughout this thesis: i) multi-formalism modeling and simulation environment (M2SL), which is a simulation toolkit developed by our group, ii) sensitivity parameter analysis used to evaluate and rank the parameters of a model and iii) parameter identification methods, that will be applied in this work in order to fit the model to experimental data.

2.1.1 Multi-formalism Modeling and Simulation Library (M2SL)

The different models used in this thesis were created and simulated in the M2SL. M2SL is a library designed and progressively improve in the *LTSI* laboratory during years by PhD students and researchers [1–4]. It is an object-oriented methodology. The models in M2SL are represented with different abstract classes, which define the structural elements of a model and/or sub-model and its behaviors. This library is entirely developed in *C++* language.

Model representation

To go further in the explanation of the modeling process, the formalism must be explained with some definitions.

- **An input:** It is a variable that enters in the model. This variable triggers and influences the behavior of the model. The user must define a range which the variable can take as value.
- **An output:** Similarly, it is a variable that exits the model.
- **A parameter:** It is a special kind of input variable. Parameters are usually used to constrain the simulation or as conditions. They are very important and influent in the simulation behaviors and outputs depending on the value given. They are also defined in a range of value.
- **A state variable:** It is a value that is intrinsic to the model. These variables are part of the different internal mechanism of behaviors of the model. They are usually used to compute the outputs variables with the input ones and the parameters. They also determine the status of the system that led the current and future behaviors. They could be access or not because it is not an output variable.

These definitions are gathered in Figure 2.1.

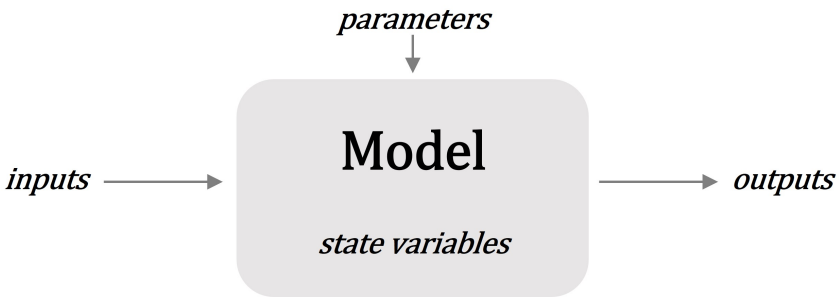

Figure 2.1: Input/ouput model formalisms.

A model M could be defined as a tuple denoted $M(F, I, O, E, P)$ where I, O and E denote the input, output and state variable sets, P denotes the parameter set of the model (I, O, E and P were defined just below), and F is the formalism in which the model is described [1]. M2SL library make able the combination of different model. Models are divided in two types of model objects: atomic models (M^a) and coupled models (M^c):

- M^a**:** An atomic model is a model with a specific component of a system using one particular formalism.
- M^c**:** A coupled model is a model composed of a set of components ($\{M_i\}$) and is noted $M^c(F, I, O, E, P, \{M_i\})$,

M_i are sub-models, they can be either atomic or coupled models.

To define each model in M2SL a simulator is created for each model and a global simulator is created and named *Root-Coordinator*. It is illustrated in Figure 2.2. The *Root-Coordinator* analyses the model hierarchy and creates a simulator for each sub model. The library is coded such as the appropriate simulator type is automatically chosen.

The simulator, created for coupled model, has special properties and are called *Coordinator*. They handle the connection of the internal components of a complex model and computes model outputs at the coupled level.

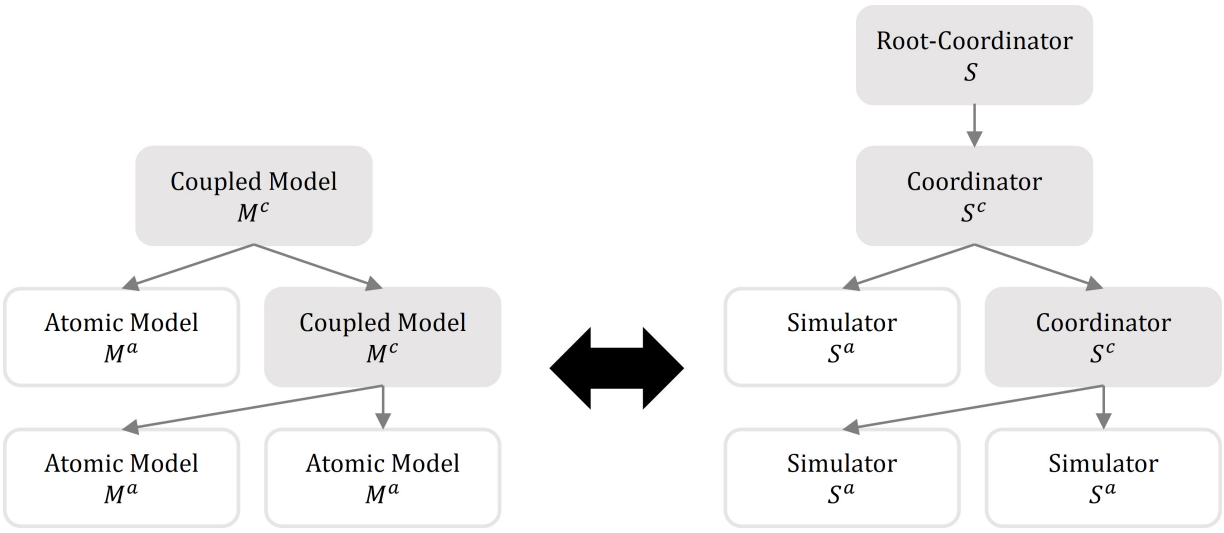

Figure 2.2: Model formalism with M2SL, translation between model hierarchy (*left part*) and simulator hierarchy (*right part*), adapted from [1].

The structures of tuple representation $M(F, I, O, E, P)$ could be described as:

- **Formalism (F):** It is chosen during the implementation. It could be algebraic equations, Ordinary Differential Equations, or algebraic equations with discrete time. Each formalism requires the implementation of specific behaviors.
- **Variables (I, O, E, P):** They are organized in four types as described before: inputs, outputs, states, and parameters.
- **Components:** They are the sub-models of the model.
- **Behaviors:** The behaviors are four followed procedures:
  1. Initialization: the calculation or simple assignment of initial values to all variables of the model.
  2. Variable synchronization: the update or modification of the internal state of the model due to a change in the input variables.
  3. Output calculation: the computation of the output variables from the current internal state and the input variables.
  4. Termination: the final procedure executed when the simulation ends

Simulation loop

After the implementation of the different components of the model and sub-models, the simulation of the model system could be performed. As before, the root-coordinator leads the simulation by defining and updating the global time of the simulation and coordinating the local time of the different sub-models. Then, three classical procedures are executed: initialization, simulation loop and finalization.

1. **Initialization:** First, the Initialization step prepares all the model and sub-models for the simulation. The simulators for each model are created according to its formalism, then the links between the simulator according to the hierarchical structure are created. Then the simulator is initialized by setting the initial values to all the variable and initiating the time.
2. **Simulation loop:** After the initialization, the simulation could start, and the simulation is done following steps that are repeated in a loop (Figure 2.3):

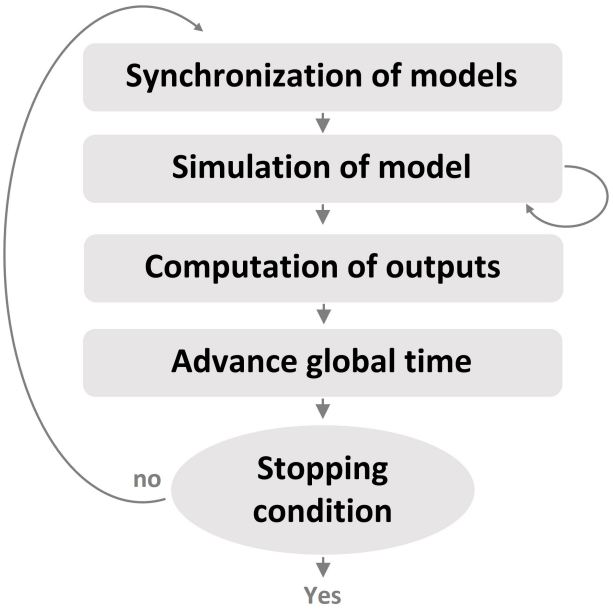

Figure 2.3: Model simulation loop steps with M2SL, adapted from [1].

- First, the synchronization of the models consists in updating all the variables calculated from the initialization step or the last simulation loop. In this last case, the output values become the new input values and some model internal values must be updated.
- The simulation of models calculates the internal transitions of the model to advance the local simulation time of one- or several-time steps. The number of time step done is set according to temporal synchronization between model (defining during the initialization phase) : fixed step simulation, adaptive step with the smallest synchronization step or adaptive step with fixed synchronization step.

- Because the simulation advanced, the state variables have been modified, and the output variables must be calculated according to this new state variable values and the new time step.
- The global time is then advanced.
- At the end of each iteration, a stopping condition is evaluated to evaluate if the simulation should stop. This stopping condition could be a target simulation time and/or could be defined by the user.

3. **Finalization:** At the very end, when the loop meets the stopping condition, all the resources acquired during the simulation are released.

2.1.2 Model analysis: sensitivity analysis

Sensitivity Analysis (SA) [5–8] is an important tool in understanding the behavior of complex models. When well conducted, it allows identifying the influence of the input parameters on the output(s) of the model. Thus, we can focus on a group of parameters that have major influence on specific output and thus help guide the parameter estimation or motivate further attention in the observation of certain inputs. On the contrary, groups with little influence can be then simplified or estimated, depending on the application [9].

There are a variety of SA methods and the choice of the appropriate method depends on various factors such as the computational cost and available computational resources as well as the linearity independence or interaction between parameters. A categorization can be done as follow [6]: the local sensitivity methods, global sensitivity methods and the in-between methods: the screening methods [10, 11].

Local versus global sensitivity analysis

Local methods represent the simplest way to perform a sensitivity analysis. The "local" term emphasizes the fact that the sensitivity of the parameters is studied in a small region of the parameter space.

One-At-Time analysis starts from a working point $X^{(0)} = \left[x_0^{(0)}, x_1^{(0)}, ...x_j^{(0)}, ...x_{n-1}^{(0)}\right]$ and a small variation/perturbation (Δ) of the parameter j is introduced in $X^{(0)}$, to become $\left[x_0^{(0)}, x_1^{(0)}, ...x_j^{(0)} + \Delta, ...x_{n-1}^{(0)}\right]$. This variation is predefined in a range of values and repeated with several values that could be Δ, $2 \cdot \Delta$, ... , $n \cdot \Delta$. When all these points are evaluated in the model, the results can be analyzed in several ways. First, the partial derivatives $\frac{\partial Y}{\partial x_j}$ can be estimated or averaged, which can be normalized and compared to the partial derivatives of other parameters.

The results can also be plotted with respect to the different values of the varying parameter. Figure 2.4 illustrates the effect of the parameter variation in three cases: no effect, linear effect and, non-linear effect.

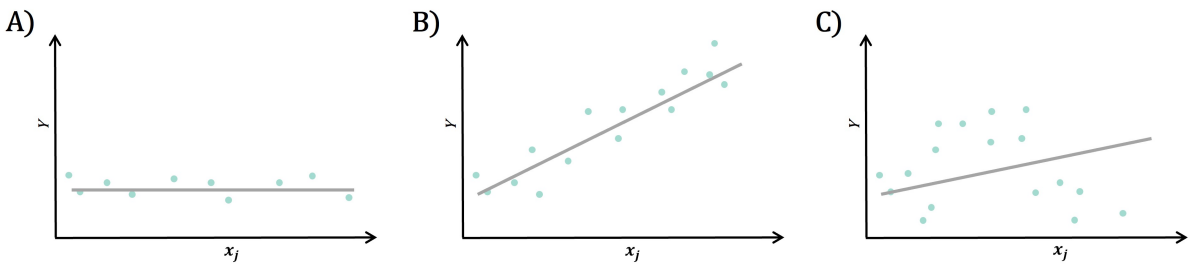

Figure 2.4: Three examples of parameter variation effect on an output Y: a) no effect, b) linear effect, c) non-linear effect, with the linear regression.

The effect of the parameter can be estimated visually or quantified using a linear regression.

Local SA are useful for their simplicity and reduced number of evaluations. However, as their name imply, the parameter space is not fully explored, since it does not consider simultaneous variations of parameters. Thus, local SA approaches cannot detect interactions between parameters. Moreover, the linear regression analysis presented before (Figure 2.4) supposes a linearity and failed in the case of non-linearity.

On the other hand, global sensitivity analysis does not constrain the parameters values to a specific region around a working point. The more commune approach of global SA is the variance-based approach. This approach tries to identify which part of the variability of an output (Y) can be attributed to the variability of each parameter x_j by varying and evaluating the parameters values and outputs across the whole input space [6, 12, 13]. These kinds of SA methods require lots of model evaluation to calculate the sensitivity indices and became exponential with many parameters. This is the major limitation of the application of global SA and reduces its application to very simplified model with a reduce number of parameters. To compensate this limitation, another type of approach was created in-between (see Figure 2.5): the screening methods.

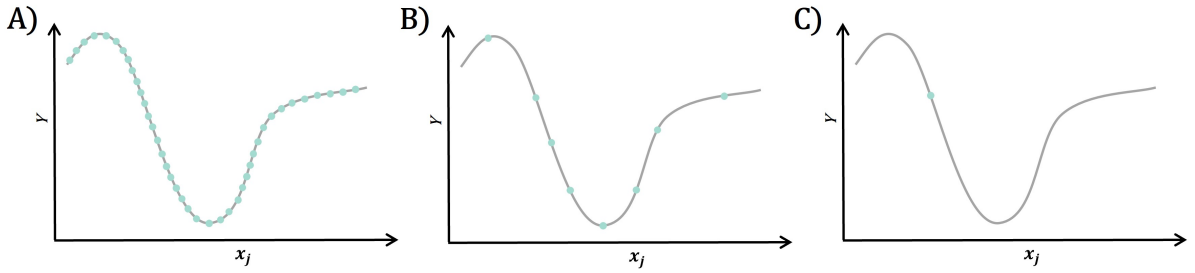

Figure 2.5: Illustration of the three different SA on an output Y: a) Global method, b) Screening method, c) Local method.

Screening sensitivity analysis

Screening Sensitivity Analysis method permits to identify and examines important parameters with relative low computational requirements [10, 11]. This method does not quantify the sensitivity of a parameter, but qualitatively identifies which parameters of a function are relatively influent on output. The most famous screening method is the Morris elementary effects method. This method provide insights into the relation between parameters and outputs and allows a characterization of the relative significance of each parameter. Using the Morris elementary effects method [7], the sensitivity of each parameter is estimated by repeated measurements of a simulation output Y with a set of parameters $X = [x_0, x_1, ...x_j, ...x_{n-1}]$, while changing one parameter value x_j at a time. For each parameter j, the range of possible values is selected in advance (usually based on literature and previous work values $\pm$30%). The resulting change in Y, compared to the simulation output using the initial values of **X**, is calculated by the elementary effect:

$$EE_j^* = \left| \frac{Y([x_0, \dots, x_j, \dots]) - Y([x_0, \dots, x_j + \Delta, \dots])}{\Delta} \right| \tag{2.1}$$

where Δ is the variation of the parameter. The Morris method consists, from a randomly chosen initial point, of forming a trajectory of $n + 1$ points (number of parameters + initial point) and in calculating for each of the points the corresponding elementary effect [7]. An illustration of a 2-dimension case is presented in Figure 2.6.

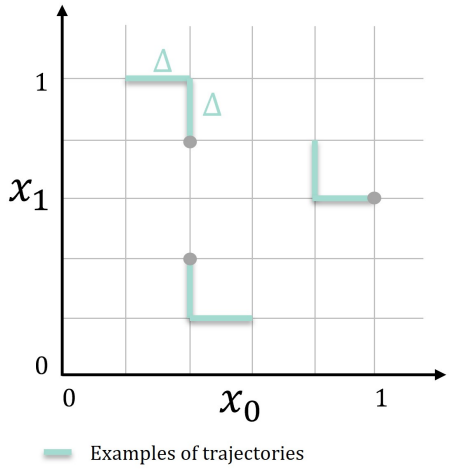

Figure 2.6: Example of the Morris screening method principle in a 2D space ($X = [x_0, x_1]$), with 3 initial points (in *grey*) and their trajectories (in *blue*).

Thus, a finite distribution F_j is obtained for each parameter j of r elementary effects, and it is possible to calculate the basic statistics indices such as μ_i which is the average of the EE_j or μ^* [14] to face the problem of negative and positive effect as well as the standard deviation (σ).

$$\mu_i = \frac{1}{r} \sum_{k=1}^{r} EE_k \tag{2.2}$$

$$\mu_i^* = \frac{1}{r}\sum_{k=1}^{r}|EE_k| \tag{2.3}$$

$$\sigma_i = \sqrt{\frac{\sum_{k=1}^{r}(EE_k - \mu_i)^2}{r}} \tag{2.4}$$

These indices are computed to derive sensitivity information of each parameter j:

- **The standard deviation (σ)**: It estimates the non-linear effects and the interactions with other parameters.
- **The mean of the absolute values (μ_i^*)**: It assesses the overall influence of the parameter on the output.

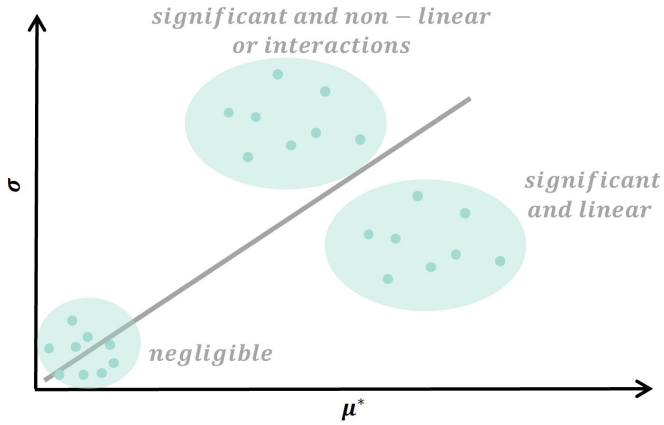

Figure 2.7: Morris elementary effects results example presented in a $\mu^* - \sigma$ plane. A parameter could be analyzed and defined as having a negligible effect, a significant linear effect, a significant but non-linear effect or interactions (adapted from [2]).

Moreover, as summarized in Figure 2.7, the $\mu^* - \sigma$ plane representation provides the following description of the parameters:

- Low μ_i^* and σ implies negligible effect on the output.
- Large μ_i^* but large σ reveals a significant and linear effects on the output.
- Large μ_i^* and σ implies significant and nonlinear effects on the output, or important interactions with other parameters.

2.1.3 Parameter Identification

Parameter Identification can be considered as an optimization problem where the objective is to find the best vector of parameter X_{opt} that minimizes an error function J_{error} also called fitness or objective function, defined as an error between simulated and observed data :

$$X_{opt} = \arg\min_{X \in \mathbf{X}} J_{error}(O_{sim}(X), O_{obs}) \tag{2.5}$$

These observed data (O_{obs}) could be one or several values measured or estimated but also signals or a combination of both, directly measured on a specific patient or averaged value(s) found in literature.

The field of mathematical optimization provides a wide variety of methods [15] to solve different kinds of problems, including analytic approaches, iterative methods, gradient-based methods, deterministic [16, 17] and stochastic approaches, among others. However, not all these methods are appropriate for the problem of parameter identification due to several reasons, including the high dimensionality of the problem, the non-linearity, and discontinuity of the underlying equations, and the complexity of the model equations that complicate the calculation of their derivatives or partial derivatives.

Classical optimization methods, such as Newton's method or Lagrange multipliers, linear programming approaches such as the simplex algorithm [18], and exhaustive exploration methods such as branch-and-bound [19] methods are not suitable for the problem of parameter identification due to the reasons mentioned above. The remaining methods include approaches that approximate numerically the derivatives of the objective function, methods that use heuristics to select interesting points in the parameter space, and methods based on a stochastic process.

Stochastic approaches are useful when the parameter space and objective function are not well understood or when the parameter exploration requires random perturbations to avoid local minima. Particle swarm optimization [20] is a popular stochastic approach that uses an iterative procedure where a list of solutions is maintained, and each candidate solution wanders the parameter space with a behavior that mixes exploration and attraction to good solutions. However, the convergence of approaches that constantly evolve a list of candidate solutions is not guaranteed, and it mostly depends on a good choice of algorithm parameters, such as the size of the candidate solution list and the number of iterations.

Evolutionary algorithms

Within the stochastic approach, Evolutionary Algorithm (EA) are optimization algorithms inspired by the biological theory of evolution [21, 22]. It follows the approach of maintaining a set of candidate solutions (*a population*), and repeatedly evolving this population with processes inspired by biological evolution: selection, reproduction, crossover, and mutation. The genetic information is the set of parameters needed for a simulation, and the representation of a good or bad adaptation to the environment is given by the error or fitness score computed by the error of fitness function.

Among the wide range of algorithms classified as EA, the most popular group used in optimization

is the Genetic Algorithms, initially conceived in [23] and formalized in [24]. These algorithms are defined by fitness and propriety shuch as crossover and mutation [25]. Figure 2.8 illustrates the classic steps of the algorithm.

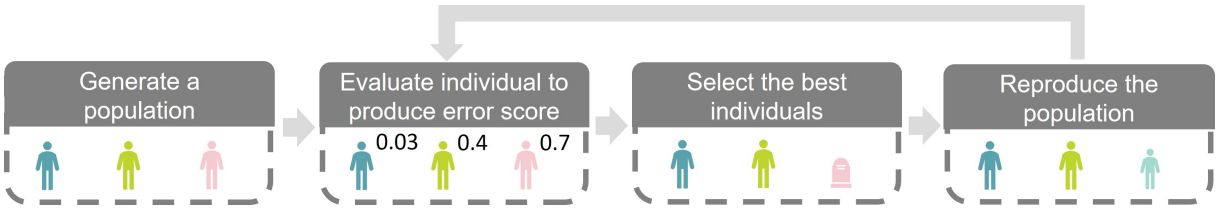

Figure 2.8: Evolutionary algorithm with the four main steps.

The population evolves as a result of the following procedure :

1. First a population of N individuals is initialized. Each individual is randomly initialized by a set of parameters respectively to the different defined value intervals.
2. Then each individual of the population is assigned with a score (error or fitness score), that quantifies the "good" adaptation of the individual in the environment. The score directly affects its chances to survive and reproduce. The computation of the score is done thanks to the function J_{error}.
3. According to their fitness and a stochastic process, a selection of individuals is performed. This step designates pairs of individuals that will reproduce.
4. A step of reproduction is done between a pair of individuals that cross over the parameter values of the "parents" and occurs with a predefined probability (p_c). Mutation could also be introduced in this new individual with a predefined probability (p_m) which slightly modifies one or more parameter value(s) of the set.
5. At this point, different strategies could be put in place, either the new generation completely replace the old one or a mix of the old and the new generations could create the new one. In any case, the new generation have the same N individuals.
6. Finally, if a stopping criterion is met, the algorithm stops or, in the contrary, the algorithm restarts from step 2. Possible stopping criteria could be a maximum number of generations (i.e. iterations) or when the individuals of the population have reached a certain error score.

As other stochastic approaches, EAs cannot assure convergence toward the unique optimal solution, and their performances depend on the parameters and choice of EA. However, EAs seem appropriate in our case because of its interesting compromise of space exploration, number of evaluations and quality of the solutions found.

In this thesis, the library used to create EA and customizes it was: PaGMO/PyGMO [26, 27] in *C++* or *Python* language. Many functions are already implemented in this library, but the EA definition and the link with the model simulation wrote in *C++* must be done.

Parallelized evolutionary algorithms

Based on EA principle, the approach could be complexified [26, 28]. Instead of having a population of N individuals evolving during T generation, one can initialize several populations evolving separately. Each population is evolving on its one island, separated from each other. After a predefined number T_e of generation, individuals could migrate from their island to another. Then the new mix of individuals from the original ones and the newcomers could again evolve separately until the new wave of migration (after another Te generations). Figure 2.9 illustrates this algorithm structure.

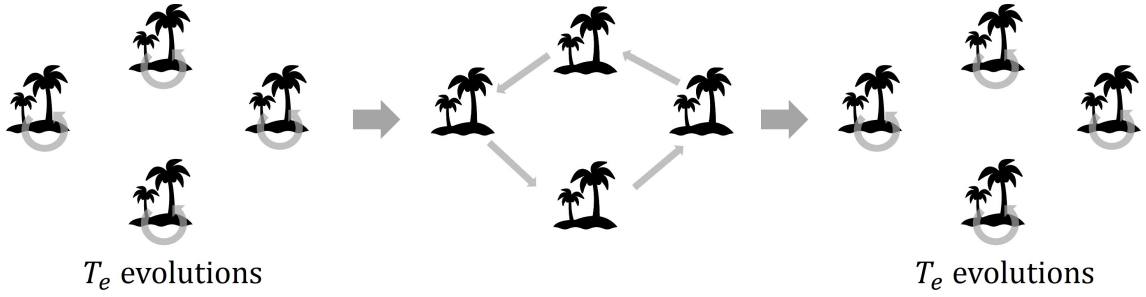

Figure 2.9: Evolutionary algorithm with islands: algorithm principle with a first step of T_e generations of separated evolutions, followed by a step of migration and then a step of separated evolution again.

The combination of islands is named archipelago and the link that connect the islands are gathered in a topology structure. The rules that lead the possible (or not) migrations and the number and choice of individual are named policies. Figure 2.10 represents examples of topology such as ring where an island is only connected to two neighbors to form a ring. The topology structure is completely customizable [26].

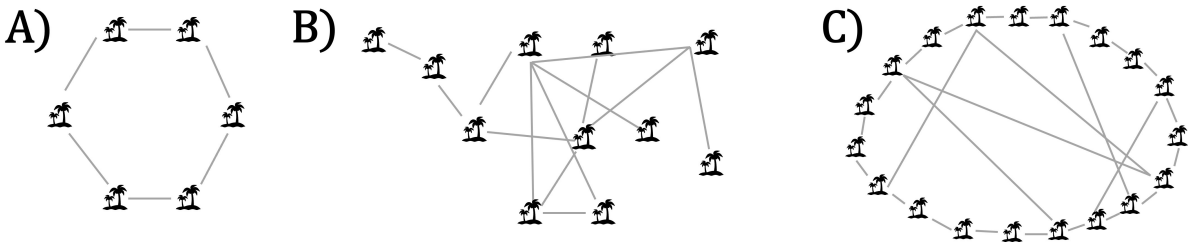

Figure 2.10: Example of topology with a) a ring b) Barabasis model [29] and c) Watts-Strogatz model [30] .

To give example of migration policies, the library used in this thesis: (PaGMO/PyGMO) already provided some. For example:

- A number N_b of the best individual could be selected to be migrants and move to another population.

- A number N_r of individuals randomly choose could be selected to be migrants.
- When the migrants arrive, they could be "accepted" directly and mix with the current individuals of the population.
- When the migrants arrive, they could be "accepted" only if their fitness/error score is better than all the current individuals of the population.

In this thesis, only few types of topology and policies combinations were explored and are mainly based on a ring topology of 3 or 4 islands only connected in one way with a selection of the best individuals as migrants and the acceptance of all the new comers.

This particular type of EA, by making evolve independently the population, permits to reduce the chance of being stuck in a local minimum. Moreover, this independent evolution could be parallelized on the computer and the increase of island number do not increase (a lot) the computation time but only the computer resources by making compute each island on a separate core for example.

2.1.4 Proposed approach

During this thesis, two previously proposed computational models were used [31, 32]. Sensitivity analyzes were crucial for comprehending the underlying mechanisms of the two different modeled systems. By conducting sensitivity analyses, we were able to identify the most important variables that needed to be taken into account for achieving successful multi-formalism and multiscale integration. Based on previous team work [32–38], we opted for Morris' screening method due to its advantageous balance between parameter space exploration and computational demands. Moreover, in order to establish a global rank of importance among parameters' effects provided by Morris' method, we calculated the Euclidean distance D_j in the $\mu^* - \sigma$ plane, from the origin to each (μ_j^*, σ_j) point:

$$D_j = \sqrt{(\mu_j^*)^2 + \sigma_j^2} \tag{2.6}$$

This could be then represented with a bar plot as illustrated in Figure 2.11. Due to its relatively low computational requirements, the Morris elementary method is a powerful approach to examine and identify important model parameters. It also underlines linear relations, but cannot discern nonlinear relations to parameter interactions. The implementation of sensitivity analyses was done in *Python* language with adapted algorithm of the SALib library [39]. The algorithm was modified in order to make the Morris screening method works when the model simulation does not provide output (simulation failed).

After conducting a sensitivity analysis, a reduced group of parameters is selected for patient-specific model identification. This helps to decrease the time and computational resources required for the calculations. reducing computational cost and calculation time. Various method could be chosen to solve this kind of problem: analytic approaches, iterative methods, gradient-

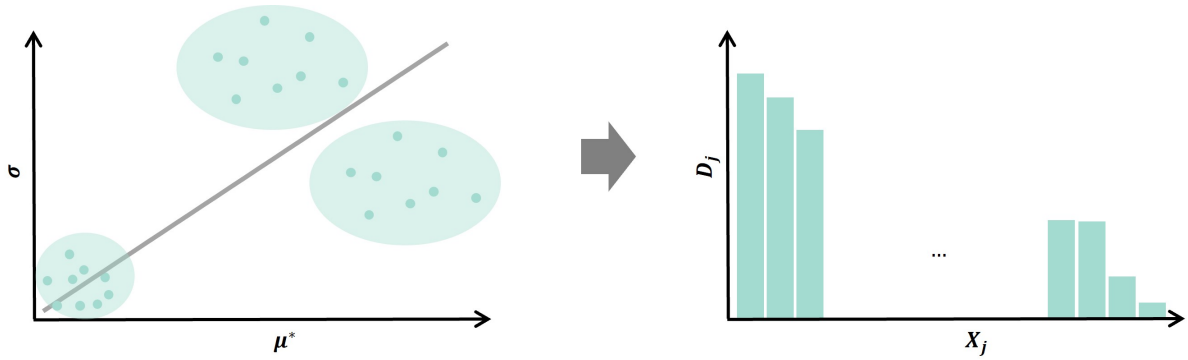

Figure 2.11: Other representation of the Morris elementary effects results based on the previous one computed by Euclidean distance.

based methods, deterministic and stochastic approaches. However, the method must be chosen appropriately to the problem and in the clinical application presented in this thesis, the complexity and dimensionality of the models make us reduce the choice of identification approaches. Moreover, the different nature of equations either non-linear, discontinuous, or not well understood, as well as the definition of the error function make us renounce to various methods that need computation of their derivatives or partial derivatives. Based on previous teamwork [32–35, 40], evolutionary algorithms were chosen to identify model parameters. Among the available evolutionary algorithms in the literature, the Differential Evolution algorithm (DE) [41] was preferred due to better performance in initial identifications [42]. The error function J_{error} will be adapted for each application, because its definition depends on the implemented model and the fitting data. In the last step of Chapter 4, the algorithm was parallelized in a ring topology of four islands thanks to parallel optimization library PaGMO/PyGMO. The EA algorithm tuning and error functions presented in this thesis are inspired from *SEPIA* team work [32–35, 40, 43, 44].

This model specification thanks to the parameter's identification aims at creating a personalized model for each patient based on its own data. This personalized model could also be named digital twin.

2.2 Features extraction from strain

In Addition to traditional clinical indices, ECG indices and LVEF, features from strain curves can be extracted to better understand myocardial function. To extract features from clinical examination is crucial to characterize LV cardiac function or dysfunction of a patient. Image or signal extracted features are a way to overcome the need of expertise in understanding the modality. Moreover, these features are vital indicators and are more reproducible when automation is provided for the extraction process.

As it was presented before in Section 1.2.2, myocardial deformation curves called strain curves

could be extracted from different echocardiographic views (especially the 2-, 3-, 4- chamber views). Several features could be extracted from strain curves for the mechanical characterization of the left ventricle, based on previous work of our team : i) integrals of the regional cardiac strain, ii) myocardial work and iii) distances between strain curves from dynamic time warping method.

2.2.1 Integrals

Briefly, the features propose by Bernard et al. [45] are based on estimation of the integral (area over the curve) of each available segmental strain signal, on different time supports.

To minimize the estimation error of these features, each strain curve is first processed by being upsampled to 500 Hz. As performed in previous works, strain values between -5% and 5% were then ignored from all calculations [45].

The first integral feature I^s_{avc} is calculated from the onset of the QRS to the instant of Aortic Valve Closure (AVC) of each segmental strain curves (s). It represents a quantification of the cumulative strain developed by a given segment s, which effectively contributes to LV ejection. A second integral I^s_{peak} is calculated from the onset of the QRS to the strain peak. It represents the global cumulative strain developed by the contraction of the segment. The third integral is calculated as:

$$E^s = I^s_{peak} - I^s_{avc} \tag{2.7}$$

and corresponds thus to the integral between the strain peak and aortic valve closure. This procedure (Figure 2.12) was applied to all segments of the echo view, for a total of 18 features by view. The onset of the QRS is used as reference for the calculation of all features.

2.2.2 Myocardial work

Recently, estimation of Myocardial Work (MW) was introduced in order to evaluate the heart chamber function and particularly the LV function [46–51]. Myocardial work is a very promised new tool to assess more precisely LV function, taking into account LV loading conditions. Thus, it overpasses the left ventricle ejection fraction (LVEF) index in the estimation of the LV function [52, 53]. Different preliminary studies claim that the evaluation of myocardial work could give additional information to assess LV function of patients with different cardiac pathologies [46–48, 54–63] and could be used as predictor [64, 65]. MW gives an estimation of the power over the cardiac cycle when the force cannot be measured clinically. However, an experimental or a good estimation of the LV pressure is required to compute MW. Although the LV pressure estimation method proposed by Russell et al. [54] could be used in some case, it is nether validated on all type of patients or usable in some pathological cases such as AS patients.

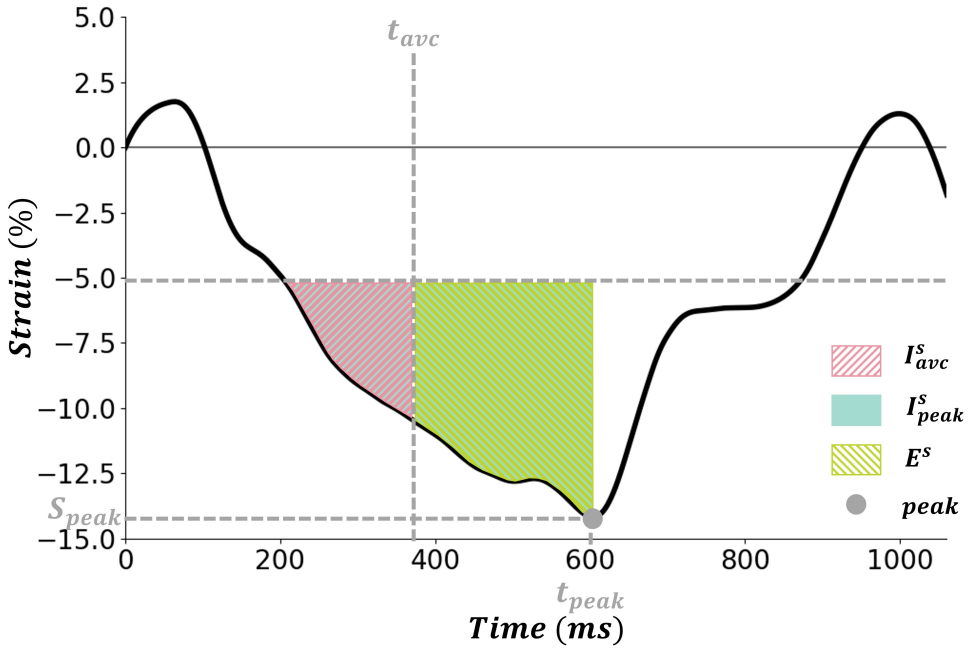

Figure 2.12: Strain integrals computation for the segmental strain curve s: I^s_{avc}, I^s_{peak} and its difference E^s delimited by the two timing: t_{avc} and t_{peak}.

Myocardial work indices

To overpass this limitation and provide a more functional approach where the MW could be computed at every time step, Russell et al. [66] proposed MW indices. MW indices were also calculated from strains and LV pressure: the instantaneous power was first computed by multiplying the strain-rate, obtained by differentiating the strain curve, and the instantaneous LV pressure. Then, segmental MW was calculated by integrating the power over time, during the cardiac cycle from Mitral Valve Closure (MVC) until Mitral Valve Opening (MVO) (Figure 2.13).

From each segmental MW curve, MW indices could be calculated: Global Positive Work (GPW), Global Negative Work (GNW), Global Constructive Work (GCW), Global Wasted Work (GWW), Global Work Index (GWI), and Global Work Efficiency (GWE) (Figure 2.14).

- **GPW:** It represents the LV contraction and gathers all the shortening phases.
- **GNW:** It is the opposite and gathers all the stretching phases.
- **GCW:** It represents the productive work, it gathers the shortening during the systole, (i.e. effective energy for blood ejection) and lengthening during IVR.
- **GWW:** It quantifies the energy loss; it corresponds to segmental stretching during the systole (i.e. energy loss for blood ejection) and shortening during the IVR phase.
- **GWI:** It is defined as the amount of work performed by the left ventricle during systole:

$$GWI = GPW + GNW \tag{2.8}$$

– **GWE:** It is defined as follows:

$$GWE = \frac{GCW}{GCW + GWW} \tag{2.9}$$

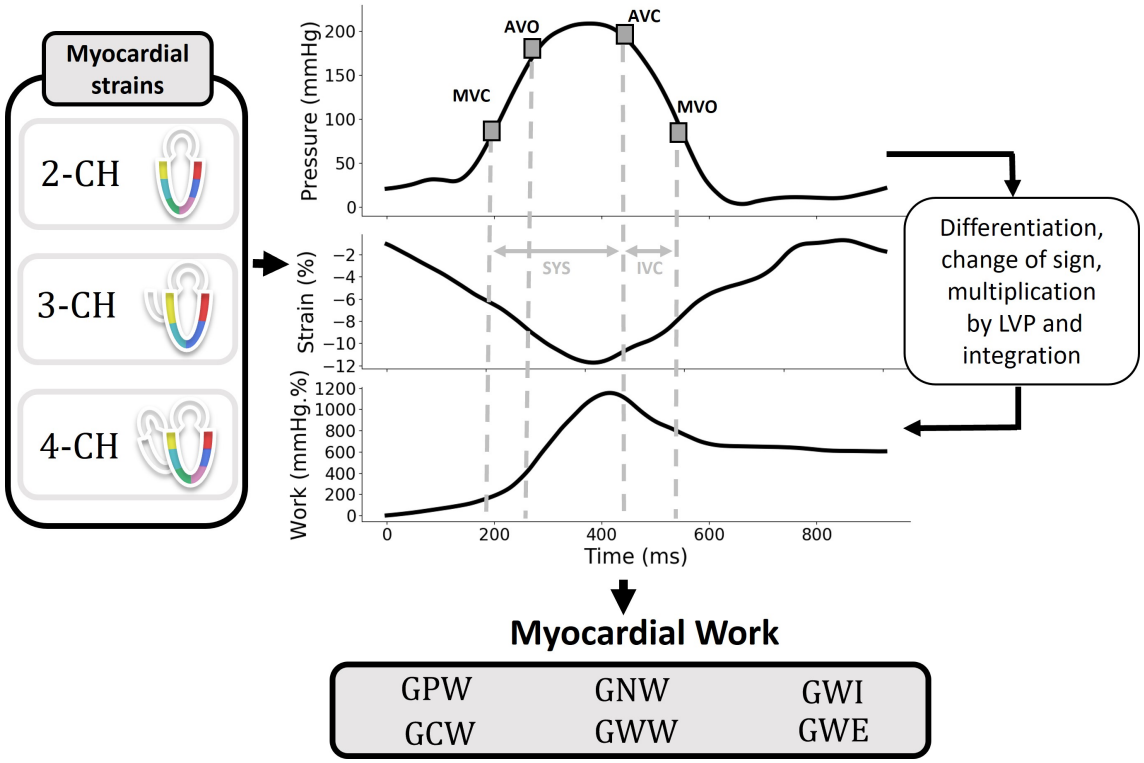

Figure 2.13: Work computation of Global Positive Work (GPW), Global Negative Work (GNW), Global Work Index (GWI), Global Constructive Work (GCW), Global Wasted Work (GWW) and Global Work Efficiency (GWE), with the LV pressure and the global strain curve.

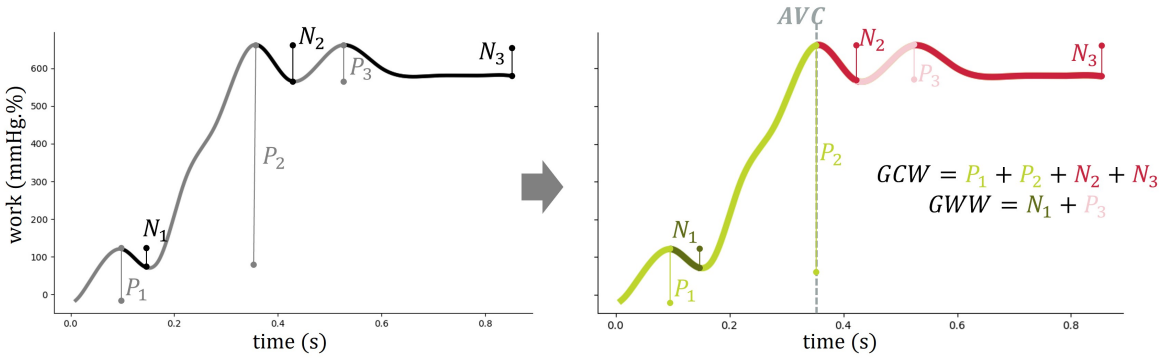

Figure 2.14: Work indices' computation with the GCW and the GWW defined thanks the shortening and lengthening before or after AVC

With the same idea of LV MW estimation, LV pressure–strain loop area reflects myocardial or stroke work [54, 55, 57, 67–69]. Especially [54], that have shown that regional differences in MW

have a strong correlation with regional myocardial glucose metabolism, evaluated using PET imaging. The regional work distribution pattern extracted in LV pressure-strain loop showed similarity with glucose uptake distribution.

These two methods: PSL area and MW indices have the same unit (mmHg.%) and both reflect a surrogate estimation of the power over the cardiac cycle.

2.2.3 Dynamic time warping

Dynamic Time Warping (DTW) is an algorithm for comparing two temporal sequences such as strain curves, which may vary in speed. It provides both a distance measure that is insensitive to local compression and stretches and the warping which optimally deforms one of the two series onto the other [70]. The main idea of the algorithm is to create a $N_1 \cdot N_2$ matrix (M) (N_1 and N_2 are the size of series s_1 and s_2) where $m_{i,j}$ is the distance between the points $s_1(i)$ and $s_2(j)$ (Figure 2.15).

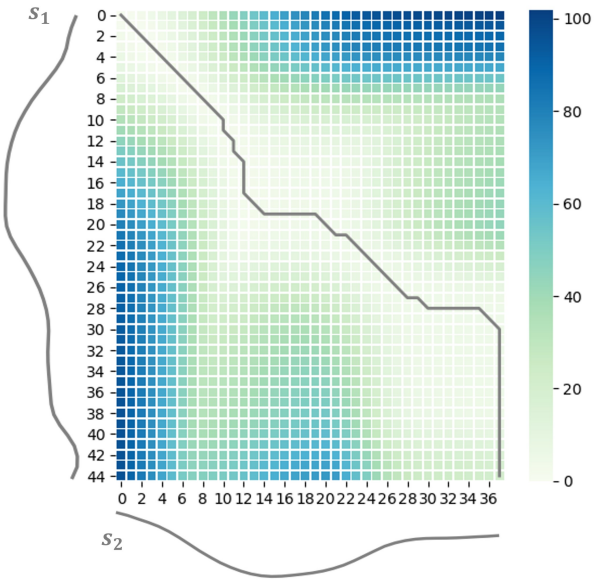

Figure 2.15: DTW matrix example where with the location of the best path (*grey*).

Then the path through the matrix that minimizes the distance must be found. The sum of the $m_{i,j}$ of this optimal path is a distance measure of the two series. It is also the best way to deform on series onto the other. Figure 2.16 represents the DTW mapping of a strain curve (s_i) with the average of the 6 strain curve of its view (V), its distance value is noted $DTW^{s_i,V}$. In this thesis, we will use DTW matrix to compute an Euclidean distance between pairs of strain curves and overcome potential physiological time lag between LV regions.

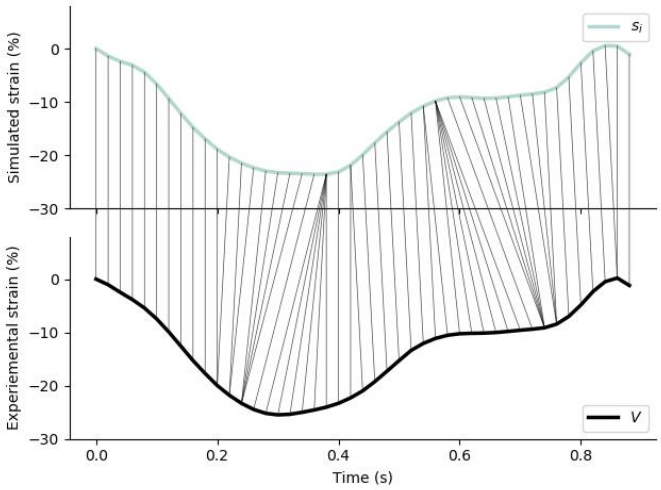

Figure 2.16: DTW mapping example with few points of the strain curve (s_i in *blue*) with the average of the 6 strain curves of its view (V in *black*).

2.2.4 Proposed approach

In each application, at least one these three types of feature was used. They are all computed thanks to strain curves and offered diverse information. Feature extraction is the first step of any ML approach presented in this thesis. It is an essential step to manage complex and multifactorial data as strain curves but also to propose new original features with interesting meanings.

2.3 Machine learning

ML techniques are increasingly used in clinical context to resolve more or less complex issues raised by clinicians. In this section, the basis of machine learning principles will be introduced by also pointing out that ML is not that far from "old fashion" statistic approaches. This section will be classically divided in supervised learning and unsupervised learning.

2.3.1 Supervised learning

Supervised learning is a part of machine learning. Supervised learning algorithm are used for problem where the whole feature of a database is associated with an available label [71]. The goal of these algorithms is to learn the function that maps each input data to its label (that will be the algorithm output). This process of learning the relation between the features and their label is known as training. Once this phase is complete, our algorithm is normally able to predict the label of new data, which the algorithm has no explicit knowledge of the true label.

Supervised learning can be separated into two types of problems:

- **Classification**. It assigns to the test data set specific categories (ex: label of "cat" and "dog").
- **Regression**. It is used to understand the relationship between dependent and independent variables and make projection. For example, the weight of an average boy of 10 years.

Figure 2.17 illustrates these 2 phases in an example dataset. We might train a supervised algorithm on a set of cats and dogs' pictures with their corresponding label (e.g. "cat" and "dog"). The algorithm will use various of interesting features in the pictures: colors, dimensions, patterns to link them to their corresponding label. After this training phase (Figure 2.17 *A*), we can use the trained algorithm to predict the label of new unseen pictures (Figure 2.17 *B*). This test phase is usually followed by a measure of the algorithm performance by the evaluation of the performance of the trained algorithm on this new dataset of unseen pictures. The database could be different from pictures, generally vectors (pictures could be represented as vectors)

The most widely used learning algorithms/estimators are:

- Support-Vector Machines (SVM) [72],
- Linear regression,
- Logistic regression,
- Naive Bayes [73],
- Linear discriminant analysis,
- Decision trees [74],
- K-nearest neighbor algorithm [75],

- Neural networks [76],
- Similarity learning.

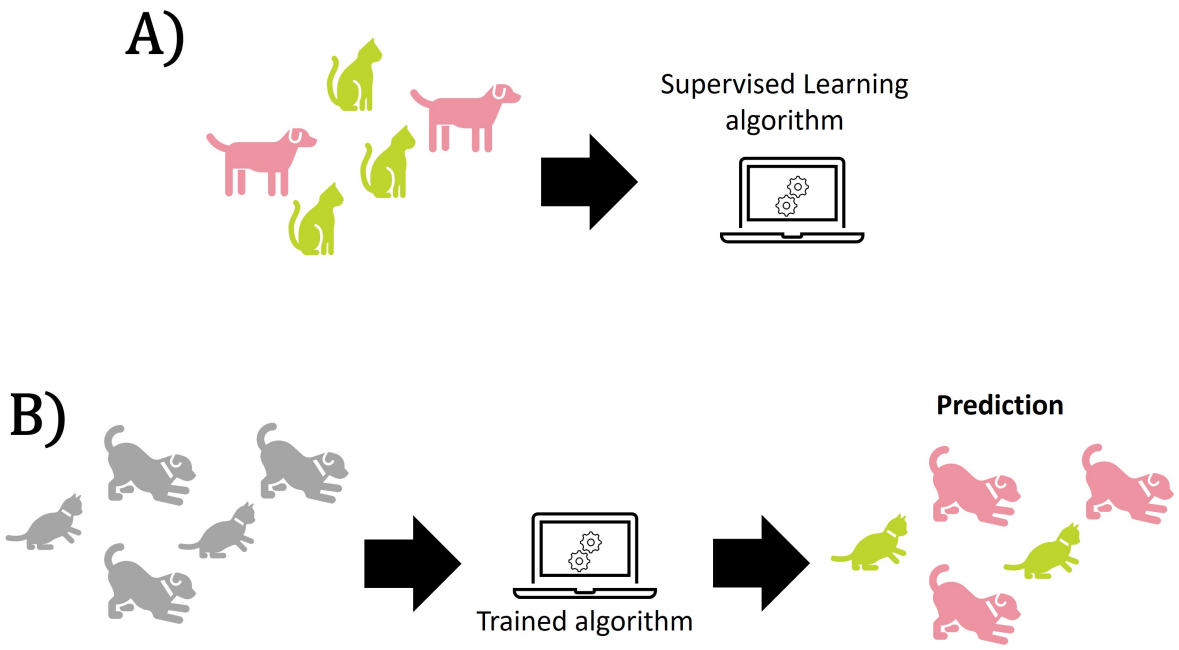

Figure 2.17: Supervised learning illustration with cat and dog labels, a) the training phase and b) the test phase on an unknown new dataset.

All these algorithms have pros and cons and must be chosen depending on the problem and the database.

Ensemble methods

Ensemble methods in ML aim to improve the generalization and robustness of a single estimator by combining several using the same learning algorithm. There are two main families of ensemble methods:

- Averaging methods involve building several estimators independently and then averaging their predictions (examples: Bagging methods and Random Forest (RF) [77]).
- Boosting methods involve building several estimators sequentially and attempting to reduce the bias of the combined estimator. The goal is to combine weak models to produce a powerful ensemble (examples: AdaBoost [78] and Gradient Tree Boosting [79, 80]).

Both averaging and boosting methods are effective at improving the performance of ML models, and their choice depends on the specific problem and the properties of the data.

Performance of an algorithm

They are several performance metrics for classification problem. The simplest one is the accuracy. It is a ratio between the number of correctly classified points to the total number of points. We can also summarize the classification results in a confusion matrix (see Figure 2.18).

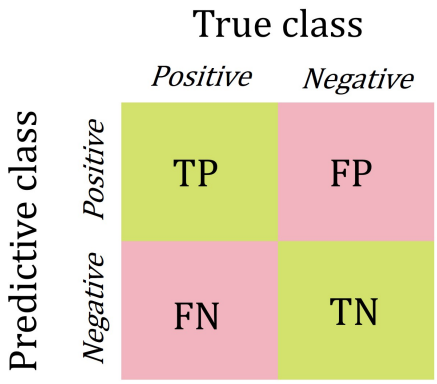

Figure 2.18: Confusion matrix of 2 classes (Positive/negative) with the TP: true positive, FN: false positive, FN: false negative, TN: true negative.

This matrix allows visualization of the performance measure of a binary classification or a multi-class classification. From this matrix we can easily access to the sensitivity also called True Positive Rate (TPR) or recall, the specificity, the False Positive Rate (FPR), the precision, and the F1 score:

$$Sensitivity = Recall = TPR = \frac{TP}{TP + FN} \tag{2.10a}$$

$$Specificity = \frac{TN}{TN + FP} \tag{2.10b}$$

$$FPR = 1 - Specificity \tag{2.10c}$$

$$Precision = \frac{TP}{TP + FP} \tag{2.10d}$$

$$F1score = \frac{2 \cdot Precision \cdot Recall}{Precision + Recall} \tag{2.10e}$$

A Receiver Operating Characteristic (ROC) curve could be then provided by plotted the FPR on the x-axis and the TPR on the y-axis. The Area Under Curve of this ROC curve is also a metric of a classification. By proposing FPR - TPR representation, one can want an optimal point on the ROC curve. We can obtain this optimal point by maximizing the G-mean metric:

$$G - mean = \sqrt{Sensitivity \cdot Specificity} \tag{2.11}$$

To perform a cross validation, it is necessary to separate the dataset in two group: the training set

and the testing set. One can add another completely independent dataset for the validation. Most of the time the training part represent 70% to 80% of the database and the testing 20% to 30%.

One method for testing the performance of a classification is the Cross-Validation. This method, as illustrated in Figure 2.19, consists of repeating several training-testing processes on a different training-testing subsets of the database.

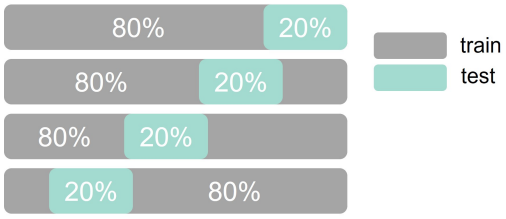

Figure 2.19: Cross validation illustration.

2.3.2 Unsupervised learning

Unsupervised learning algorithms work with data that is not explicitly labelled. These kinds of algorithm aim at finding some sort of underlying structure in the data [81, 82] (Figure 2.17). The main task of unsupervised algorithm could be separated in three:

- Clustering,
- Association,
- Dimensionality reduction.

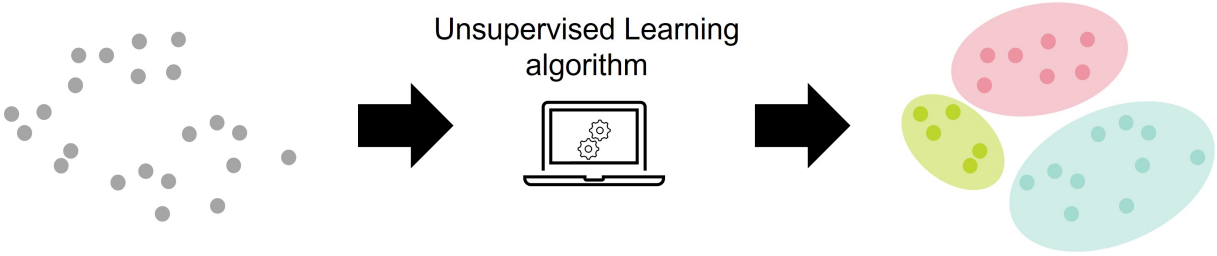

Figure 2.20: Unsupervised learning illustration (clustering).

Clustering

Clustering is a technique which groups unlabeled data based on their common characteristics and differences. They can be categorized into a few types: exclusive, overlapping, hierarchical, and probabilistic.

First, the most famous algorithm: K-means clustering [83]. This is an exclusive clustering method where data points are assigned into K groups, where K represents the number of clusters. The clusters are created based on the distance from each group's centroid (e.g. barycenter). The

"exclusive" term signifies that a data point can exist only in one cluster. On the other hand, "overlapping" clustering allows data points to belong to multiple. Soft K-mean is an example of overlapping clustering. The optimal number of clusters could be determined using the Silhouette score [84] or the Inertia score:

- The silhouette score (S) is a measure of how similar an object is to its own cluster (cohesion: a) compared to other clusters (separation/ dissimilarity: b):

$$S = \frac{1}{K}\sum_{k=1}^{K}\frac{1}{|C_k|}\sum_{i\in C_k}\frac{b_i - a_i}{\max(a_i, b_i)} \tag{2.12}$$

  where

$$a_i = \frac{1}{|C_k| - 1}\sum_{j\in C_k, j\neq i}\|x_i - x_j\| \tag{2.13}$$

$$b_i = \min_{k'\neq k}\left(\frac{1}{|C'_k|}\sum_{j\in C_{k'}}\|x_i - x_j\|\right. \tag{2.14}$$

  with K the number of cluster, C_k the data of the cluster k and x the data.

- The inertia (I) is a measure of how internally coherent clusters are:

$$I = \sum_{i=1}^{n}\min_{\mu}\|x_i - \mu\|^2 \tag{2.15}$$

  where n is the number of data, μ the group centers and x the data.

Then the hierarchical clustering algorithms, they could be agglomerative or divisive [85]. The agglomerative one starts from the bottom and merge the data points iteratively based on their similarity until a unique cluster is formed. The divided one is the opposite and starts from one cluster and divides the unique original cluster based on the differences between data points, and do it iteratively.

Finally, the probabilistic clustering: data points are clustered based on the likelihood that they belong to a particular distribution. The Gaussian Mixture Model is an example of probabilistic clustering algorithm [86].

Association

Association clustering aims at finding relationships between variables in a given dataset [87]. It is mostly used for market basket analysis and was not explored during this thesis.

Dimensionality reduction

Dimensionality reduction is a technique that could be used as a preprocessing of ML when the number of features, or the dimension is too high. It could also be used to better understand a

complex dataset and the most interesting features. The two main algorithms are:

- **Principal Component Analysis (PCA)**: This algorithm used to reduce redundancies and to compress datasets through feature extraction [88]. Thanks to linear transformation, it is created principal components ordered by the maximum variance, each principal component gathers. We can then represent the dataset in this new space with fewer dimensions.
- **Singular Value Decomposition (SVD)**: This algorithm factorizes the matrix of the dataset (A) into three low-rank matrices (U, S, V):

$$A = U \cdot S \cdot V^T \tag{2.16}$$

  where U and V are orthogonal matrices and S is a diagonal matrix where the diagonal values are the singular values of the matrix A.

2.3.3 Proposed approach

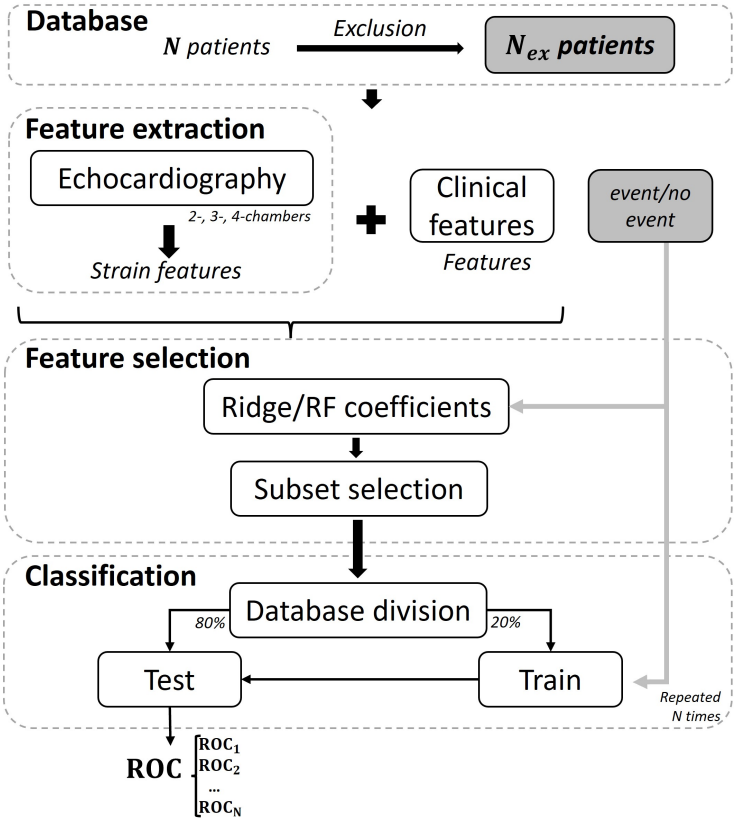

Figure 2.21: Diagram of the ML framework.

The ML methods used in this thesis will follow the framework depicted in Figure 2.21. Various types of data were collected and gathered, and strain curves features were extracted (see Section 2.2). A

crucial step of feature selection will then be proceeded, which plays a significant role in delivering the most effective inputs for classification, and also produces results on its own. In fact, the feature evaluation and selection establish a prioritization of features compared to others. In the case of unsupervised learning, it could provide information about similar feature or patients that allows dimensionality reductions of the database or clustering of patients. Following the feature selection step, which maximizes the classification results, various classification algorithms can be employed. In this thesis, several algorithms were tested, but Random Forest (RF) and ridge algorithms yielded the best result. For each classification, a cross validation was done. The two last steps were mainly written thanks *python* library scikit-learn [89].

2.4 Conclusion

This section presented the modeling and simulation methods and tools used in different studies of the thesis. It particularly introduced the application of the Multi-formalism Modeling and Simulation Library. Then, a brief state-of-the-art of sensitivity analysis and parameter identification was proposed, which is a major part of this work. In a second part, features extraction techniques on strain curves were proposed. Finally, it presented an overview of the classical machine learning concepts which will be used and developed in the next chapters.

This set of methods and tools constitute the basis of the methodology used during this thesis.

BIBLIOGRAPHY

[1] Defontaine A. *Modélisation multirésolution et multiformalisme de l'activité électrique cardiaque*. Ph.D. thesis, Université Rennes 1 (2006).

[2] Ojeda Avellaneda D. *Multi-resolution physiological modeling for the analysis of cardiovascular pathologies*. Ph.D. thesis, Université Rennes 1 (2018).

[3] Hernández A.I., Le Rolle V., Ojeda D., Baconnier P., Fontecave-Jallon J., Guillaud F., Grosse T., Moss R.G., Hannaert P., and Thomas S.R. Integration of detailed modules in a core model of body fluid homeostasis and blood pressure regulation. *Prog. Biophys. Mol. Biol.*, vol. 107, 169–182 (2011).

[4] Hernández A.I., Le Rolle V., Defontaine A., and Carrault G. A multiformalism and multiresolution modelling environment: Application to the cardiovascular system and its regulation. *Philos. Trans. R. Soc. A Math. Phys. Eng. Sci.*, vol. 367, 4923–4940 (2009).

[5] Saltelli A. Sensitivity analysis for importance assessment. *Risk Anal.*, vol. 22, 579–590 (2002).

[6] Saltelli A., Ratto M., Andres T., Campolongo F., Cariboni J., Gatelli D., Saisana M., and Tarantola S. *Global sensitivity analysis: The primer* (2008).

[7] Morris M.D. Factorial sampling plans for preliminary computational experiments. *Technometrics*, vol. 33, 161–174 (1991).

[8] Ghanem R., Owhadi H., and Higdon D. *Handbook of uncertainty quantification*. Springer (2017).

[9] Garcia Sanchez D., Lacarrière B., Musy M., and Bourges B. Application of sensitivity analysis in building energy simulations: Combining first- and second-order elementary effects methods. *Energy Build.*, vol. 68, 741–750 (2014).

[10] Campolongo F., Cariboni J., and Saltelli A. An effective screening design for sensitivity analysis of large models. *Environ. Model. Softw.*, vol. 22, 1509–1518 (2007).

[11] Campolongo F., Saltelli A., and Cariboni J. From screening to quantitative sensitivity analysis. A unified approach. *Comput. Phys. Commun.*, vol. 182, 978–988 (2011).

[12] Sobol I.M. Sensitivity estimates for nonlinear mathematical models and their Monte Carlo estimation. *Math. Model. Comput. Exp.*, vol. 1 (1993).

[13] Sobol I.M. Global sensitivity indices for nonlinear mathematical models and their Monte Carlo estimates. *Math. Comput. Simul.*, vol. 55 (2001).

[14] Campolongo F., Cariboni J., Saltelli A., and Schoutens W. Enhancing the Morris method. *Sensit. Anal. Model output, Los Alamos Natl. Lab. Los Alamos, NM*, 369–379 (2005).

[15] Nemhauser G. and Rinnooy Kan A. *Handbooks in operations research and management science*. Elsevier (2006).

[16] Minskyt M. Steps Toward Artificial Intelligence. *Proceeding IRE*, vol. 49 (1961).

[17] Nelder J.A. and Mead R. A Simplex Method for Function Minimization. *Comput. J.*, vol. 7 (1965).

[18] Dantzig G. *Linear Programming and Extensions*. Princeton university press (1998).

[19] Land A.H. and Doig A.G. An Automatic Method of Solving Discrete Programming Problems. *Econometrica*, vol. 28 (1960).

[20] Eberhart R. and Kennedy J. New optimizer using particle swarm theory. In *Proc. Int. Symp. Micro Mach. Hum. Sci.* (1995).

[21] Slowik A. and Kwasnicka H. Evolutionary algorithms and their applications to engineering problems. *Neural Comput. Appl.*, vol. 32, 12 363–12 379 (2020).

[22] Back T. An Overview of Evolutionary Algorithms for Parameter Optimization. *Evol. Comput.* (1993).

[23] Holland J.H. Adaptation in natural and artificial systems, University of Michigan press. *Ann Arbor, MI*, vol. 1 (1975).

[24] Goldberg D.E. Genetic Algorithms in Search, Optimization, and Machine Learning, Addison-Wesley, Reading, MA, 1989. *NN Schraudolph J..*, vol. 3 (1989).

[25] Eiben A.E. and Smith J.E. Introduction to evolutionary computing. In *Nat. Comput. Ser.*, vol. 28, 17–20. Springer (2015).

[26] Biscani F., Izzo D., and Yam C.H. A Global Optimisation Toolbox for Massively Parallel Engineering Optimisation. *arXiv preprint arXiv:1004.3824*, 1–11 (2010).

[27] Biscani F. and Izzo D. A parallel global multiobjective framework for optimization: pagmo. *J. Open Source Softw.*, vol. 5, page 2338 (2020).

[28] Alba E. and Tomassini M. Parallelism and Evolutionary Algorithms. *IEEE Trans. Evol. Comput.*, vol. 6, 443–462 (2002).

[29] Albert R. and Barabási A.L. Statistical mechanics of complex networks. *Rev. Mod. Phys.*, vol. 74, 47–97 (2002).

[30] Watts D.J. and Strogatz S.H. Strogatz - small world network Nature. *Nature*, vol. 393, 440–442 (1998).

[31] Owashi K., Galli E., Hubert A., Donal E., Hernandez A., and Le Rolle V. Patients-Specific Analysis of Myocardial Strains in Left Bundle Branch Block Based on Computational Models. *2020 Comput. Cardiol. Conf.*, vol. 47, 1–4 (2020).

[32] Owashi K.P., Hubert A., Galli E., Donal E., Hernández A.I., and Rolle V.L. Model-based estimation of left ventricular pressure and myocardial work in aortic stenosis. *PLoS One*, vol. 15, 1–18 (2020).

[33] Calvo M., Le Rolle V., Romero D., Béhar N., Gomis P., Mabo P., and Hernández A.I. Model-based analysis of the autonomic response to head-up tilt testing in Brugada syndrome. *Comput. Biol. Med.*, vol. 103, 82–92 (2018).

[34] Guerrero G., Rolle V.L., and Hernandez A. Sensitivity Analysis of a Cardiorespiratory Model for the Study of Sleep Apnea. *Comput. Cardiol. (2010).*, vol. 2018-Septe, 18–21 (2018).

[35] Ojeda D., Le Rolle V., Harmouche M., Drochon A., Corbineau H., Verhoye J.P., and Hernandez A.I. Sensitivity analysis and parameter estimation of a coronary circulation model for triple-vessel disease. *IEEE Trans. Biomed. Eng.*, vol. 61, 1208–1219 (2014).

[36] Ojeda D., Rolle V.L., Romero-Ugalde H.M., Gallet C., Bonnet J.L., Henry C., Bel A., Mabo P., Carrault G., and Hernández A.I. Sensitivity analysis of vagus nerve stimulation parameters on acute cardiac autonomic responses: Chronotropic, inotropic and dromotropic effects. *PLoS One*, vol. 11, 1–19 (2016).

[37] Le Rolle V., Galli E., Danan D., El Houari K., Hubert A., Donal E., and Hernández A.I. Sensitivity Analysis of a Left Ventricle Model in the Context of Intraventricular Dyssynchrony. *Acta Biotheor.*, vol. 68, 45–59 (2019).

[38] Duport O., Le Rolle V., Guerrero G., Beuchée A., and Hernández A. Sensitivity analysis of a cardio-respiratory model in preterm newborns for the study of patent ductus arteriosus. *2021 43rd Annual International Conference of the IEEE Engineering in Medicine & Biology Society (EMBC)*, 4420–4423 (2021).

[39] Herman J. and Usher W. SALib: An open-source Python library for Sensitivity Analysis. *J. Open Source Softw.*, vol. 2 (2017).

[40] Hernández A.I., Carrault G., and Mora F. Model-based interpretation of cardiac beats by evolutionary algorithms. *Comput. Cardiol.*, vol. 29, 93–96 (2002).

[41] Storn R. and Price K. Differential Evolution – A Simple and Efficient Heuristic for Global Optimization over Continuous Spaces. *J. Glob. Optim.*, vol. 11, 341–359 (1997).

[42] Owashi K.P. *Model-based analysis of myocardial strains for the evaluation of cardio- vascular function*. Ph.D. thesis, Université Rennes 1 (2021).

[43] Le Rolle V., Hernández A.I., Richard P.Y., Donal E., and Carrault G. Model-based analysis of myocardial strain data acquired by tissue Doppler imaging. *Artif. Intell. Med.*, vol. 44, 201–219 (2008).

[44] Le Rolle V., Carrault G., Richard P.Y., Pibarot P., Durand L.G., and Hernández A.I. A tissue-level electromechanical model of the left ventricle: Application to the analysis of intraventricular pressure. *Acta Biotheor.*, vol. 57, 457–478 (2009).

[45] Bernard A., Donal E., Leclercq C., Schnell F., Fournet M., Reynaud A., Thebault C., Mabo P., Daubert J.C., and Hernandez A. Impact of cardiac resynchronization therapy on left ventricular mechanics: Understanding the response through a new quantitative approach based on longitudinal strain integrals. *J. Am. Soc. Echocardiogr.*, vol. 28, 700–708 (2015).

[46] Vecera J., Penicka M., Eriksen M., Russell K., Bartunek J., Vanderheyden M., and Smiseth O.A. Wasted septal work in left ventricular dyssynchrony: A novel principle to predict response to cardiac resynchronization therapy. *Eur. Heart J. Cardiovasc. Imaging*, vol. 17, 624–632 (2016).

[47] Galli E., Vitel E., Schnell F., Le Rolle V., Hubert A., Lederlin M., and Donal E. Myocardial constructive work is impaired in hypertrophic cardiomyopathy and predicts left ventricular fibrosis. *Echocardiography*, vol. 36, 74–82 (jan 2019).

[48] Galli E., Hubert A., Le Rolle V., Hernandez A., Smiseth O.A., Mabo P., Leclercq C., and Donal E. Myocardial constructive work and cardiac mortality in resynchronization therapy candidates. *Am. Heart J.*, vol. 212, 53–63 (2019).

[49] Manganaro R., Marchetta S., Dulgheru R., Sugimoto T., Tsugu T., Ilardi F., Cicenia M., Ancion A., Postolache A., Martinez C., Kacharava G., Athanassopoulos G.D., Barone D., Baroni M., Cardim N., Hagendorff A., Hristova K., Lopez T., De La Morena G., Popescu B.A., Penicka M., Ozyigit T., Rodrigo Carbonero J.D., Van De Veire N., Von Bardeleben R.S., Vinereanu D., Zamorano J.L., Rosca M., Calin A., Moonen M., Magne J., Cosyns B., Galli E., Donal E., Carerj S., Zito C., Santoro C., Galderisi M., Badano L.P., Lang R.M., and Lancellotti P. Correlation between non-invasive myocardial work indices and main parameters of systolic and diastolic function: Results from the EACVI NORRE study. *Eur. Heart J. Cardiovasc. Imaging*, vol. 21, 533–541 (2020).

[50] Papadopoulos K., Tok Ö.Ö., Mitrousi K., and Ikonomidis I. Myocardial work: Methodology and clinical applications. *Diagnostics*, vol. 11, 1–15 (2021).

[51] Roemer S., Jaglan A., Santos D., Umland M., Jain R., Tajik A.J., and Khandheria B.K. The Utility of Myocardial Work in Clinical Practice. *J. Am. Soc. Echocardiogr.*, 1–12 (2021).

[52] Ilardi F., D'andrea A., D'ascenzi F., Bandera F., Benfari G., Esposito R., Malagoli A., Mandoli G.E., Santoro C., Russo V., Crisci M., Esposito G., and Cameli M. Myocardial work by echocardiography: Principles and applications in clinical practice (2021).

[53] Marzlin N., Hays A.G., Peters M., Kaminski A., Roemer S., O'Leary P., Kroboth S., Harland D.R., Khandheria B.K., Tajik A.J., and Jain R. Myocardial Work in Echocardiography. *Circ. Cardiovasc. Imaging*, vol. 16 (2023).

[54] Russell K., Eriksen M., Aaberge L., Wilhelmsen N., Skulstad H., Remme E.W., Haugaa K.H., Opdahl A., Fjeld J.G., Gjesdal O., Edvardsen T., and Smiseth O.A. A novel clinical method for quantification of regional left ventricular pressurestrain loop area: A non-invasive index of myocardial work. *Eur. Heart J.*, vol. 33, 724–733 (2012).

[55] Fortuni F., Butcher S.C., van der Kley F., Lustosa R.P., Karalis I., de Weger A., Priori S.G., van der Bijl P., Bax J.J., Delgado V., and Ajmone Marsan N. Left ventricular myocardial work in patients with severe aortic stenosis Federico. *J. Am. Soc. Echocardiogr.*, page 124658 (2020).

[56] Sahiti F., Morbach C., Cejka V., Albert J., Eichner F.A., Gelbrich G., Heuschmann P.U., and Störk S. Left Ventricular Remodeling and Myocardial Work: Results From the Population-Based STAAB Cohort Study. *Front. Cardiovasc. Med.*, vol. 8, 1–12 (2021).

[57] El Mahdiui M., van der Bijl P., Abou R., Ajmone Marsan N., Delgado V., and Bax J.J. Global Left Ventricular Myocardial Work Efficiency in Healthy Individuals and Patients with Cardiovascular Disease. *J. Am. Soc. Echocardiogr.*, vol. 32, 1120–1127 (sep 2019).

[58] Russell K., Eriksen M., Aaberge L., Wilhelmsen N., Skulstad H., Gjesdal O., Edvardsen T., and Smiseth O.A. Assessment of wasted myocardial work: A novel method to quantify energy loss due to uncoordinated left ventricular contractions. *Am. J. Physiol. - Hear. Circ. Physiol.*, vol. 305, 996–1003 (2013).

[59] Galli E., Leclercq C., Hubert A., Bernard A., Smiseth O.A., Mabo P., Samset E., Hernandez A., and Donal E. Role ofmyocardial constructive work in the identification of responders to CRT. *Eur. Heart J. Cardiovasc. Imaging*, vol. 19, 1010–1018 (2018).

[60] Chan J., Edwards N.F., Khandheria B.K., Shiino K., Sabapathy S., Anderson B., Chamberlain R., and Scalia G.M. A new approach to assess myocardial work by non-invasive left ventricular pressure-strain relations in hypertension and dilated cardiomyopathy. *Eur. Heart J. Cardiovasc. Imaging*, vol. 20, 31–39 (2019).

[61] Edwards N.F., Scalia G.M., Shiino K., Sabapathy S., Anderson B., Chamberlain R., Khandheria B.K., and Chan J. Global Myocardial Work Is Superior to Global Longitudinal Strain to Predict Significant Coronary Artery Disease in Patients With Normal Left Ventricular Function and Wall Motion. *J. Am. Soc. Echocardiogr.*, vol. 32, 947–957 (2019).

[62] Hiemstra Y.L., van der Bijl P., el Mahdiui M., Bax J.J., Delgado V., and Marsan N.A. Myocardial Work in Nonobstructive Hypertrophic Cardiomyopathy: Implications for Outcome. *J. Am. Soc. Echocardiogr.*, vol. 33, 1201–1208 (2020).

[63] Paolisso P., Gallinoro E., Mileva N., Moya A., Fabbricatore D., Esposito G., De Colle C., Beles M., Spapen J., Heggermont W., Collet C., Van Camp G., Vanderheyden M., Barbato E., Bartunek J., and Penicka M. Performance of non-invasive myocardial work to predict the first hospitalization for de novo heart failure with preserved ejection fraction. *ESC Hear. Fail.*, vol. 9, 373–384 (2022).

[64] Abawi D., Rinaldi T., Faragli A., Pieske B., Morris D.A., Kelle S., Tschöpe C., Zito C., and Alogna A. The non-invasive assessment of myocardial work by pressure-strain analysis: clinical applications. *Heart Fail. Rev.*, vol. 27, 1261–1279 (2022).

[65] Hedwig F., Nemchyna O., Stein J., Knosalla C., Merke N., Knebel F., Hagendorff A., Schoenrath F., Falk V., and Knierim J. Myocardial Work Assessment for the Prediction of Prognosis in Advanced Heart Failure. *Front. Cardiovasc. Med.*, vol. 8, 1–10 (2021).

[66] Russell K., Eriksen M., Aaberge L., Wilhelmsen N., Skulstad H., Gjesdal O., Edvardsen T., and Smiseth O.A. Assessment of wasted myocardial work: A novel method to quantify energy loss due to uncoordinated left ventricular contractions. *Am. J. Physiol. - Hear. Circ. Physiol.*, vol. 305, 996–1003 (2013).

[67] Urheim S., Rabben S.I., Skulstad H., Lyseggen E., Ihlen H., and Smiseth O.A. Regional myocardial work by strain Doppler echocardiography and LV pressure: A new method for quantifying myocardial function. *Am. J. Physiol. - Hear. Circ. Physiol.*, vol. 288, 2375–2380 (2005).

[68] Galli E., Leclercq C., Fournet M., Hubert A., Bernard A., Smiseth O.A., Mabo P., Samset E., Hernandez A., and Donal E. Value of Myocardial Work Estimation in the Prediction of Response to Cardiac Resynchronization Therapy. *J. Am. Soc. Echocardiogr.*, vol. 31, 220–230 (2018).

[69] Hubert A., Le Rolle V., Leclercq C., Galli E., Samset E., Casset C., Mabo P., Hernandez A., and Donal E. Estimation of myocardial work from pressure–strain loops analysis: an experimental evaluation. *Eur. Heart J. Cardiovasc. Imaging*, vol. 19, 1372–1379 (2018).

[70] Giorgino T. Computing and visualizing dynamic time warping alignments in R: The dtw package. *J. Stat. Softw.*, vol. 31, 1–24 (2009).

[71] Russel S. and Norvig P. *Artificial intelligence—a modern approach 3rd Edition* (2012).

[72] Noble W.S. What is a support vector machine? *Nat. Biotechnol.*, vol. 24, 1565–1567 (2006).

[73] Eddy S.R. What is Bayesian statistics? *Nat. Biotechnol.*, vol. 22, 1177–1178 (2004).

[74] Kingsford C. and Salzberg S.L. What are decision trees? *Nat. Biotechnol.*, vol. 26, 1011–1012 (2008).

[75] Fix E. and Hodges J.L. Discriminatory Analysis. Nonparametric Discrimination: Consistency Properties. *Int. Stat. Rev. / Rev. Int. Stat.*, vol. 57 (1989).

[76] Pollard A. What are neural networks? *Sens. Rev.*, vol. 10, 115–116 (1990).

[77] BREIMAN L. Random Forests LEO. *Mach. Learn.*, vol. 45, 5–32 (2001).

[78] Hastie T., Rosset S., Zhu J., and Zou H. Multi-class AdaBoost. *Stat. Interface*, vol. 2 (2009).

[79] Friedman J.H. Greedy function approximation: A gradient boosting machine. *Ann. Stat.*, vol. 29 (2001).

[80] Chen T. and Guestrin C. XGBoost: A scalable tree boosting system. *Proc. ACM SIGKDD Int. Conf. Knowl. Discov. Data Min.*, vol. 13-17-Augu, 785–794 (2016).

[81] Barlow H. Unsupervised Learning. *Neural Comput.*, vol. 1, 295–311 (1989).

[82] Ziegel E.R., Fayyad U.M., Piatetski-Shapiro G., Smyth P., and Uthurusamy R. Advances in Knowledge Discovery and Data Mining. *Technometrics*, vol. 40 (1998).

[83] Ahmad A. and Dey L. A k-mean clustering algorithm for mixed numeric and categorical data. *Data Knowl. Eng.*, vol. 63 (2007).

[84] Rousseeuw P.J. Silhouettes: A graphical aid to the interpretation and validation of cluster analysis. *J. Comput. Appl. Math.*, vol. 20, 53–65 (1987).

[85] Murtagh F. and Contreras P. Algorithms for hierarchical clustering: an overview, II (2017).

[86] Geary D.N., McLachlan G.J., and Basford K.E. Mixture Models: Inference and Applications to Clustering. *J. R. Stat. Soc. Ser. A (Statistics Soc.*, vol. 152 (1989).

[87] Han E.H.S., Karypis G., Kumar V., and Mobasher B. Clustering Based on Association Rule Hypergraphs. *Work. Res. Issues Data Min. Knowl. Discov.* (1997).

[88] Ringnér M. What is principal component analysis? *Nat. Biotechnol.*, vol. 26, 303–304 (2008).

[89] Pedregosa F., Varoquaux G., Gramfort A., Michel V., Thirion B., Grisel O., Blondel M., Prettenhofer P., Weiss R., Dibourg V., Vanderplas J., Passos A., Cournapeau D., Brucher M., Perrot M., and Duchesnay E. Scikit-learn: Machine Learning in Python. *J. Mach. Learn. Res.*, vol. 12, 2825–2830 (2011).

Chapter

3 Model-based Analysis of Myocardial Strains in Left Bundle Branch Block

Left Bundle of Branch Block (LBBB), introduced in Section 1.3.1 is a common electrocardiographic abnormality that causes intra- and interventricular conduction delay and leads to uncoordinated contraction of the ventricle, alterations in LV mechanical activity and LV dysfunction [1]. Observational studies of patients with LBBB have shown a relation between strain curve morphologies, obtained by speckle-tracking echocardiography (STE), and responses to Cardiac Resynchronization Therapy (CRT) [2–4]. However, the regional distribution patterns of dyssynchrony in LBBB is highly heterogeneous, as it involves differently septal and lateral walls [5, 6]. Moreover, strain morphologies could also be affected by mechanical dysfunctions, such as those observed in ischemia [7]. Therefore, the assessment of dyssynchrony patterns in LBBB appears as particularly complex because strain morphologies reflect dynamics associated with both electrical conduction delays and mechanical cardiac activities. Previous studies have shown that only the mechanical dysfunction attributable to an electrical conduction delay can be corrected by CRT [8]. The possibility of using strain-derived data to disclose the complex interplay between electrical conduction delay and the specific mechanical substrate associated with LV dyssynchrony is particularly interesting and might have a pivotal role in the selection of CRT-candidates.

In this context, model-based approaches may provide a better understanding of myocardial deformations observed in LBBB, since these approaches explicitly represent the underlying physiological mechanisms. Indeed, computational modeling appears as efficient tool to integrate knowledge, concerning cardiac electrical activation, mechanical properties, and hemodynamic conditions, in the data processing. A variety of cardiac electromechanical models has been proposed in the literature, at many different levels of detail [9] and representing different physiological functions, including the cardiac electrical activity [10–12], the excitation-contraction coupling [13, 14], the mechanical activity [15] and the mechano-hydraulic coupling [16]. Most of the proposed cardiac models are based on the Finite Element (FE) method [17–27] for the simulation of cardiac mechanical activity, including a 3D mesh geometry. Some of them include multimodality imaging [28] or used atlases [29] to reduce the computational cost. However, these models require high computational resources, and they are still difficult to personalize. Moreover, dynamic loading conditions and interventricular interactions are usually not considered in these models and their integration is possible only at the expenses of an increasing amount of model complexity. Alternative approaches have been proposed to overcome this computational cost [30–35], by reducing drastically the patient anatomy representation with lower dimension models. These types of models allow for a better clinical translation [36] and incorporation of

components such as heart hemodynamics within the entire circulation. Although, these particular models' examples have been successfully used to propose keys to understand the CRT response with virtual or animal cohorts, efforts still have to be made in order to adapt these studies to non-invasive, patient-specific data.

In [37], our team has proposed the first model-based approach for the analysis of Tissue Doppler Imaging (TDI). Model parameters for the LV were estimated by minimizing an error computed between strain signals synthesized by the computational model and strain signals obtained through TDI from several myocardial segments in a patient-specific approach. Then this model was complete by Owashi et al. in [38] with the representation of the right ventricle, the atrium and the systemic and pulmonary circulations [39, 40].

This chapter will follow the work published in the journal *Frontiers in Applied Mathematics and Statistics* [41] and a previous study published as co-first author with Kimi Owashi in the *Journal of Cardiovascular Development and Disease* [42].

3.1 Experimental data

3.1.1 Study population

We prospectively included 10 healthy adults and 20 LBBB patients, including ischemic (n=10) and non-ischemic (n=10) cardiomyopathies. Table 3.1 summarizes patients' clinical characteristics. The study was carried out in accordance with the principles outlined in the Declaration of Helsinki on research in human subjects and received specific ethical approval from the local Medical Ethical Committee. All patients signed a written informed consent before the participation to the study protocol.

	Age *years old*	**Male sex** *N (%)*	**BSA** (body surface area)	**NYHA class** I/II/III	**QRS width** (ms)
LBBB ischemia (*n=10*)	72.1 $\pm$ 10.3	9 (90%)	1.84 $\pm$ 0.12	2/7/1	160 $\pm$ 25.4
LBBB non-ischemia (*n=10*)	68.2 $\pm$ 6.2	8 (80%)	1.83 $\pm$ 0.15	1/6/3	163 $\pm$ 13.0
Healthy (*n=10*)	48.8 $\pm$ 14.4	7 (70%)	1.88 $\pm$ 0.12	–	109 $\pm$ 9.9

Table 3.1: Population' clinical characteristics.

3.1.2 Echocardiography

All patients underwent a standard Trans-Thoracic Echocardiography (TTE) using a Vivid S6, E7 or E9 ultrasound system (General Electric Healthcare, Horten, Norway). Images were recorded on a remote station for off-line analysis by dedicated software (EchoPAC PC, version BT 202, General Electric Healthcare, Horten, Norway). The experimental dataset includes the measured regional

myocardial strain curves obtained by STE at transthoracic echocardiography in apical 4-chamber, 2-chamber, and 3-chamber views. Excel files of these 3 longitudinal strain view analyses were exported for a dedicated analysis performed in python language. Strain curves references were fixed at the onset of the QRS.

3.1.3 Cardiac magnetic resonance image (cMRI)

For 10 LBBB patients, the location of the scar was performed by cardiac magnetic resonance imaging (cMRI) and then confirmed by echocardiography. Prior to CRT implantation, cardiac magnetic resonance was performed on a 3-T clinical magnetic resonance system (Ingenia, Philips Medical Systems, Best, the Netherlands) with a 32-channel cardiovascular array coil. LGE images were acquired 10–15 minutes after intravenous administration of 0.2 mmol/kg of gadolinium (Gadoterate meglumine, Dotarem, Guerbet, Aulnay-sous-bois, France), using 2D breath-hold inversion-recovery and phase-sensitive inversion-recovery sequences in short-axis plane (spoiled gradient-echo, slice thickness 8 mm, repetition time 6.1 ms, echo time 2.9 ms, flip angle 25°, inversion time adjusted to null normal myocardium, typical breath-hold 11 seconds). The localization of myocardial scar was performed by a trained radiologist and the regional LGE extent was semi quantitatively assessed on a per-segment basis [43].

3.2 Model

The model of the cardiovascular system integrates four main sub-models and is illustrated in Figure 3.1:

1. The cardiac electrical system,
2. The right and left atria,
3. A multi-segment representation of the right and the left ventricles,
4. The systemic and pulmonary circulations.

The combined model is characterized by 44 state variables and 551 parameters. It was implemented using the Multiformalism Modeling and Simulation Library (M2SL) [44, 45] presented in Section 2.1.1. Supplementary information on parameters can be found in Appendix A (Table A.1, Table A.2).

3.2.1 Cardiac electrical system

The proposed model of the cardiac electrical activity, is based on a set of coupled automata, adapted from [37]. In order to perform comparisons between simulations and clinical data, the left ventricle wall was divided into 16 segments according to the standardized segmentation of the AHA [46] (see Figure 3.2). The base (Bas) and medium (Mid) layers are separated in six components:

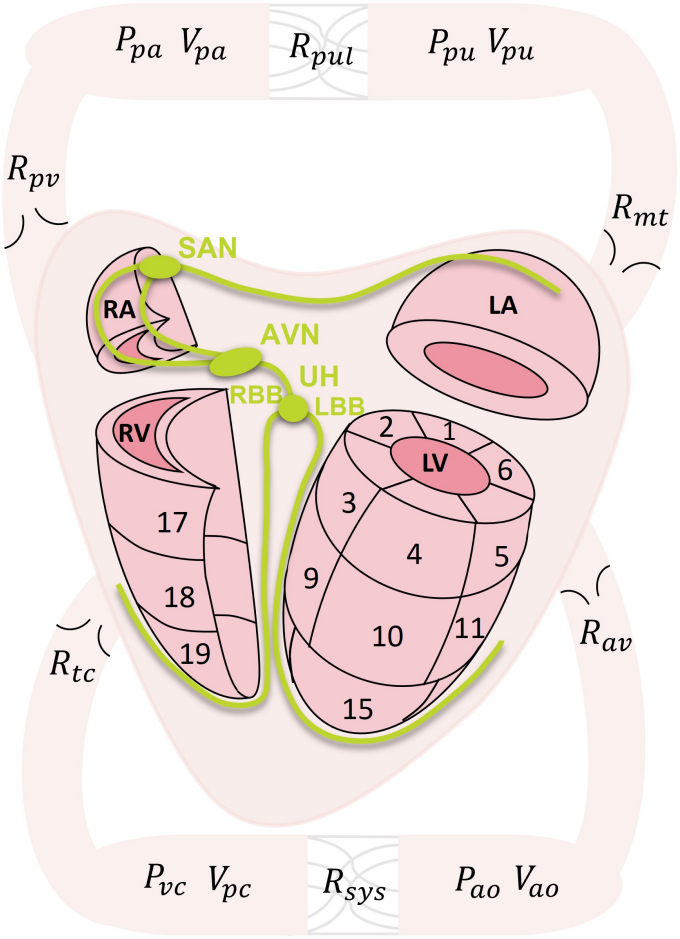

Figure 3.1: Physiological model representation with i) the electrical automata (SAN: sinoatrial node, AVN: atrioventricular node, UH: upper bundle of His, RBB: right bundle branch, LBB: left bundle branch), ii) right and left atria (RA, LA), iii) multi-segment right and left ventricle (RV, LV), and iv) systemic and pulmonary circulation (P: pressure, V: volume, R: resistance, pv: pulmonary valve, pa: pulmonary artery, pul: pulmonary, pu: pulmonary vein, mt: mitral valve, av: aortic valve, ao: aorta, sys: systemic, vc: vena cava, tc: tricuspid valve).

- anterior (Ant),
- anteroseptal (AntSep),
- inferoseptal (InfSep),
- inferior (Inf),
- inferolateral (InfLat)
- anterolateral (AntLat).

The apex (Ap) layer is divided in four components:

- anterior,
- septal,
- inferior,

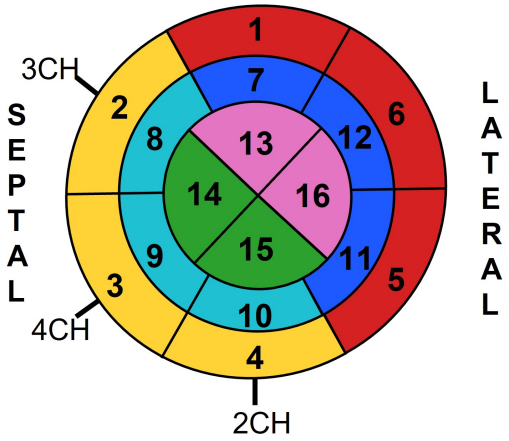

Figure 3.2: LV bull eye representation with electrical links between LV automata (1: basal anterior, 2: basal anteroseptal, 3: basal inferoseptal, 4: basal inferior, 5: basal inferolateral, 6: basal anterolateral, 7: mid anterior, 8: mid anteroseptal, 9: mid inferoseptal, 10: mid inferior, 11: mid inferolateral, 12: mid anterolateral, 13: apical anterior, 14: apical septal, 15: apical inferior, 16: apical lateral).

- lateral.

Right ventricle wall is divided into three layers (base, medium, and apex). The whole model consists of 26 automata representing:

- the SinoAtrial Node (SAN),
- the Right Atrium and Left Atrium (RA and LA),
- the AtrioVentricular Node (AVN),
- the Upper bundle of His (UH),
- the bundle branches (RBB and LBB),
- the 3 segments of Right Ventricle (RV),
- the 16 segments of Left Ventricle (LV).

The distribution of the electrical activation between automata is represented in Figure 3.3 . Each automaton represents the electrical activation state of a given myocardial tissue, covering the main electrophysiological activation periods (Figure 3.4):

- a Slow Diastolic Depolarization (SDD) or waiting period (Idle),
- an Upstroke Depolarization Period (UDP),
- an Absolute Refractory Period (ARP),
- a Relative Refractory Period (RRP).

The transitions between states happen spontaneously at the end of the phase. After the UDP period, each automaton transmits a stimulus to its neighboring segments. Each automaton is fully connected (antegrade and retrograde connections) to its neighbors. The connections between

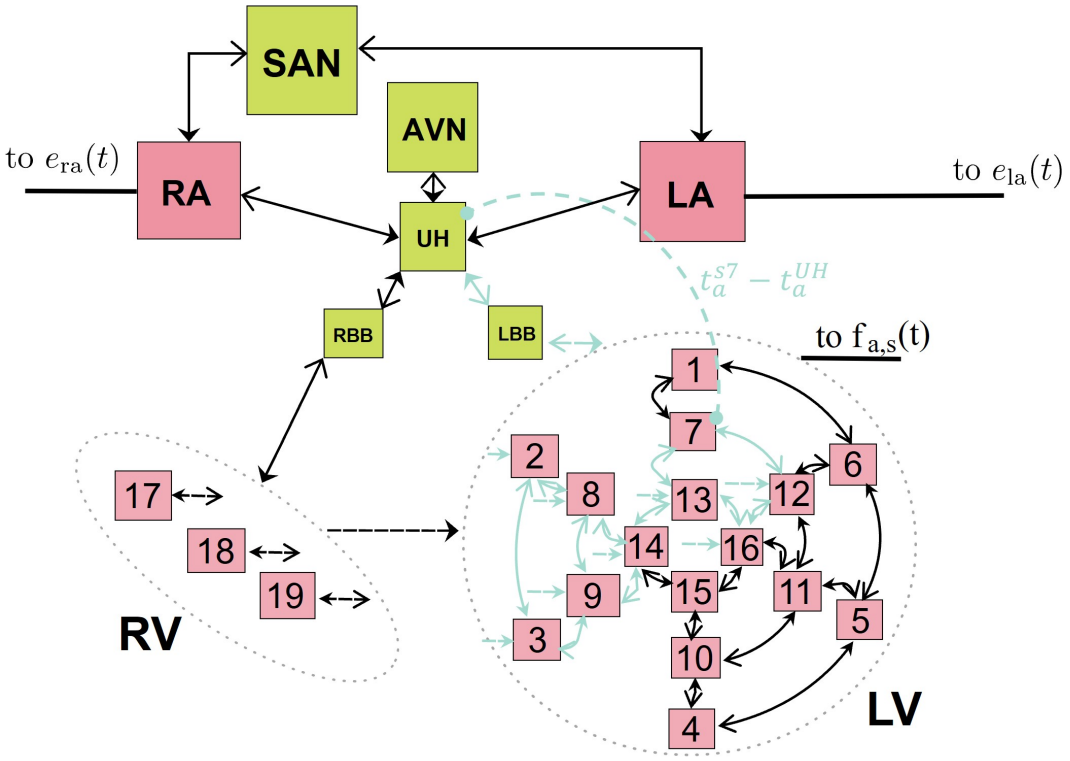

Figure 3.3: The whole electrical representation of the model, with the 26 cellular automata and their sequence of electrical activation. The nodal cells (*in green*): sinoatrial node (SAN), atrioventricular node (AVN), upper bundle of His (UH), right bundle branch (RBB), left bundle branch (LBB), and myocardial cells (*in pink*): right atria (RA), left atria (LA) and right and left ventricle (Figure 3.2 numbering) are represented and led by their own signal (Figure 3.4). The blue path is an illustration of the electrical activation time for the seventh LV segment ($s7$).

automaton are illustrated in Figure 3.3 where we can see that the excitation arrives from the LBB automaton and is propagated to the apex, through septal automata and the medium anterolateral automaton (segments numbered 2, 3, 8, 9, 12, 13, 14 and 16), then to the other segments in function of each automaton's parameter values (T_{UDP}, T_{ARP}, T_{RRP}, T_{SDD}).

The electrical activation time (EAT) associated with each ventricular segment could be defined by the time elapsed between the electrical activation of the UH automaton and the segmental one. An illustration of the EAT is proposed in Figure 3.3 for the seventh LV segment ($s7$). These delays of activation, accessible for each segment, will provide us a representation of the dyssynchrony. UH automaton activation also corresponds to the initialization of the simulated strain curves.

3.2.2 Right and left atria

To account for the mechanical function of the atria, the right and left atrial pressures (P_{ra} and P_{la}) are defined as linear functions of instantaneous volumes (V_{ra} and V_{la}) [40, 47]. These pressures are determined by their volumes intercept ($V_{ra,d}$ and $V_{la,d}$) and their elastances (E_{ra} and E_{la}),

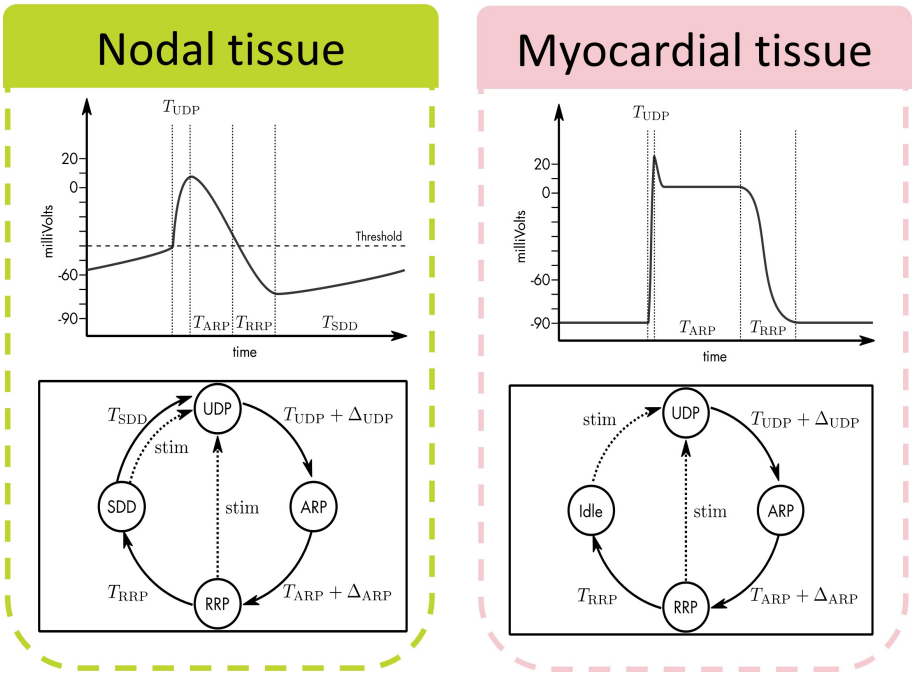

Figure 3.4: State diagram of the generalized automaton that represents nodal cells (*green, left*) and myocardial cells (*pink, right*) and diagrams showing the correspondence of the transition parameters with the myocardial action potential dynamics and their timing parameters: T_{UDP}, T_{ARP}, T_{RRP}, T_{SDD}.

which represent the elastic properties of the atrial wall and are bounded by $E_{x,min}$ and $E_{x,max}$:

$$P_x(V_x, t) = E_x \cdot (V_x(t) - V_{x,d}) \tag{3.1a}$$

$$E_x(t) = e_x(t) \cdot (E_{x,max} - E_{x,min}) + E_{x,min} \tag{3.1b}$$

where $x \in \{ra,la\}$ and $e_x(t)$ is a Gaussian driving function that cycles between atrial diastole and systole:

$$e_x(t) = A_x \cdot \exp\left(-B_x \cdot (t_a(t) - C_x)^2\right) \tag{3.2}$$

where t_a is the time elapsed since the atrial activation by the automata corresponding to the right and left atrium. Parameters A_x, B_x and C_x could be used to control the rise and peak of the atrial systole.

3.2.3 Right and left ventricles

Each LV and RV automaton triggers an Electro-Mechanical Driving Function (EMDF) [48, 49], which represents in a simplified manner, the complex processes involved in the electromechanical coupling at the tissue-level:

$$f_{a,s}(t_s) = \left[\frac{\left(\frac{t_s}{\alpha_{1,s}\cdot T}\right)^{n_{1,s}}}{1+\left(\frac{t_s}{\alpha_{1,s}\cdot T}\right)^{n_{1,s}}}\right] \cdot \left[\frac{1}{1+\left(\frac{t_s}{\alpha_{2,s}\cdot T}\right)^{n_{2,s}}}\right] \cdot A_{max} \tag{3.3}$$

The onset of the cardiac cycle, denoted t_s, is determined by the activation instant of the corresponding segment in the cardiac electrical model presented in the previous section. The first and second terms in Equation 3.3 represent ventricle segment contraction and relaxation presented after an electrical activation, respectively. T is the heart period, $\alpha_{1,s}$, $\alpha_{2,s}$ are shape parameters, and $n_{1,s}$, $n_{2,s}$ control the steepness of the curve. These four parameters ($\alpha_{1,s}$, $\alpha_{2,s}$, $n_{1,s}$, $n_{2,s}$) are assumed positive. A_{max} is the maximum EMDF value, and $s \in \{S_{lv}, S_{rv}\}$ with S_{lv} = {BasAnt, BasAntSep, BasInfSep, BasInf, BasInfLat, BasAntLat, MidAnt, MidAntSep, MidInfSep, MidInf, MidInfLat, MidAntLat, ApAnt, ApSep, ApInf, ApLat} (see Figure 3.2) and S_{rv} = {BasRV, MidRV, ApRV}.

Concerning each segment s, cardiac mechanical activity can be separated into active ($T_{s,act}$) and passive ($T_{s,pass}$) components:

$$T_s = T_{s,pass} + T_{s,act} \tag{3.4}$$

Passive myocardial tension depends on myocardial strain Equation 3.5.

$$\varepsilon_s = \frac{(l_s - l_{s,ref})}{l_{s,ref}} \tag{3.5}$$

And it is defined as follows according to [50]:

$$T_{s,pass} = K_{s,pass} \cdot T_{ref,pass} \cdot (36 \cdot max(0, \varepsilon_s - 0.1)^2 + 0.1(\varepsilon_s - 0.1) + 0.0025e^{10\varepsilon_s}) \tag{3.6}$$

where $K_{s,pass}$ is a parameter related to passive stiffness that is comprised between 0 and 1, $T_{ref,pass}$ is the reference passive tension at $\varepsilon_s = 1$, l_s and $l_{s,ref}$ are current and reference fiber lengths. Active myocardial tension is represented by a non-linear law inspired from [51]:

$$T_{s,act} = K_{s,act} \cdot T_{ref,act} \cdot (1 + \beta(\varepsilon_s - 1)) \cdot \frac{{f_{a,s}}^2}{f_{a,s}^2 + F_a^2} \tag{3.7}$$

where $K_{s,act}$ is a parameter related to myofiber contractility, $T_{ref,act}$ is the reference active tension at $\varepsilon_s = 1$, and β, F_a are constants related with the muscle kinetic. The relation between pressure P_s and tension T_s in each segment is approximated by the Laplace law (Equation 3.8)

$$P_s = e \cdot T_s \left(\frac{\cos(\theta_s)}{\varepsilon_s \cdot R_{m,s}} + \frac{\sin(\theta_s)}{\varepsilon_s \cdot R_{p,s}}\right) \tag{3.8}$$

In Equation 3.8, θ_s is the mean angle of the muscular fibers. $R_{m,s}$ and $R_{p,s}$ are the radii of curvature in the meridian and parallel directions, while e is the mean wall thickness. As the ventricle was assumed to be an ellipsoid of revolution, $R_{p,s}$ and $R_{m,s}$ could be calculated analytically. Length

variation is obtained by a power conservation:

$$P_s \cdot Q_s = F_s \cdot \frac{dl_s}{dt} \tag{3.9}$$

Where the force is:

$$F_s = T_s \cdot S_s \tag{3.10}$$

S_s is the area of each segment. The hydraulic behavior of the blood volume in contact with the wall segment are represented by its inertial (I_s) and resistive (R_s) effects:

$$P_y - P_s = I_s \frac{dQ_s}{dt} \tag{3.11a}$$

$$Q_s = \frac{P_y - P_s}{R_s} \tag{3.11b}$$

with $y \in$ {lv, rv} and $R_s \in \{R_{min}, R_{max}\}$ according to the mitral valve opening. Ventricular flow is calculated, taking into account the contribution of the flow of each one of the segments $Q_{s,y}$ and of the intraventricular cavity $Q_{c,y}$:

$$Q_y(t) = Q_{c,y}(t) + \sum_{s_y} Q_{s,y}(t) \tag{3.12}$$

where P_y and Q_y are respectively cavity center pressure and flow. Segments, associated with the septum, are treated separately since their pressure depends on the pressure gradient across the septal wall:

$$P_{sept} = P_{lv} - P_{rv} \tag{3.13}$$

3.2.4 Systemic and pulmonary circulations

The arteries, veins and capillaries of systemic and pulmonary circulations were included (Figure 3.1). The volume change, ΔV, of each compartment is computed from the integral of their respective net flow:

$$\Delta V_z(t) = \int (Q_{in} - Q_{out})\, \mathrm{d}t \tag{3.14}$$

with $z \in \{lv, rv, la, ra, pa, pu, ao, vc\}$, and in and $out \in \{la, ra, pa, pu, ao, vc, sys, pul, art, veins\}$, while the flow, Q, is defined by the pressure gradient, ΔP, across chambers and a resistance, R:

$$Q = \frac{\Delta P_z}{R} \tag{3.15}$$

$R \in \{R_{pul}, R_{sys}, R_{art}, R_{veins}, R_{la}, R_{ra}, R_{mt}, R_{av}, R_{tcv}, R_{pv}\}$. Pressures on venous and arterial vessels are defined as an elastance dependent relationship:

$$P_z = E_z \cdot (V_z - V_d) \tag{3.16}$$

$V_d \in \{V_{d,lv}, V_{d,rv}, V_{d,la}, V_{d,ra}, V_{d,pa}, V_{d,pv}, V_{d,ao}, V_{d,art}, V_{d,vc}, V_{d,veins}\}$, where E is the elastance and V_d refers to the dead volume. For example, these equations become:

$$\Delta V_{ao}(t) = \int (Q_{ao} - Q_{sys})\, \mathrm{d}t, \tag{3.17a}$$

$$Q_{sys} = \frac{P_{ao} - P_{vc}}{R_{sys}}, \tag{3.17b}$$

$$P_{ao} = E_{ao} \cdot (V_{ao} - V_{d,ao}) \tag{3.17c}$$

in the systemic part of the model (Figure 3.1 *bottom*). The same equations are applied all around the myocardial loop. The heart valves are modeled as perfect diodes.

3.3 Sensitivity analysis

The first step of patient-specific adaptation corresponds to the sensitivity analysis of the model in order to provide insight into the relation between parameters and outputs and to allow a characterization of the relative significance of each parameter. Using the Morris elementary effects method [52] presented in Section 2.1.2.

The analysis was applied to a total of 288 parameters, with 18 parameters for each of the 16 segments: one from the electrical automaton and the 16 other one from electromechanical coupling part of segmental sub-model equivalent. The circulatory parameters were previously studied in [40]. In this study, the analysis is focused on the LV desynchrony and especially on the influence of electromechanical parameters on strain morphologies. In order to preserve computational costs, we have decided to include only parameters associated with electromechanical activity of ventricles. For each parameter X_j, the range of possible values was selected from the nominal literature and previous work values $\pm$30% [39, 53, 54], except for the electrical depolarization time parameter (UDP) whose range was defined between 2 and 150 ms.

Analysis were performed with: $Y = \{\text{mean}(\varepsilon_{min,s}^{model}), \text{mean}(t(\varepsilon_{min,s}^{model})), \text{std}(\varepsilon_{min,s}^{model}), \text{std}(t(\varepsilon_{min,s}^{model}))\}$, where $\varepsilon_{min,s}^{model}$ and $t(\varepsilon_{min,s}^{model})$ correspond respectively to the minimum value of strain and the corresponding time for each segment s (Figure 3.5). Mean and standard-deviation values were calculated over the 16 strain signals.

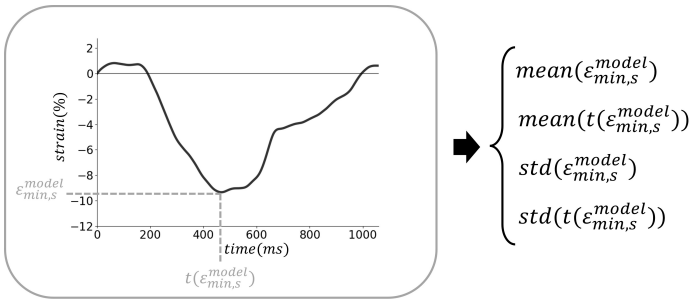

Figure 3.5: Outputs Y analyzed during the sensitivity analysis.

3.4 Model specification/parameters identification

The second step of the patient-specific adaptation is the identification of a set of parameters selected from the sensitivity analysis. Figure 3.6 illustrates the parameters' identification process.

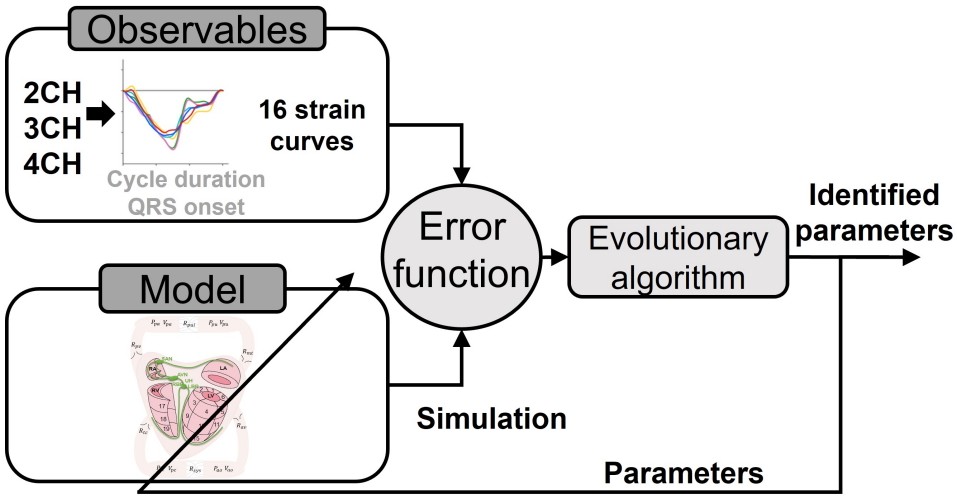

Figure 3.6: Parameters identification pipeline with the evolutionary algorithm and its error function (J_{error}) adapted from [41]. The observables of this parameter identification are the 6 strain curves of the 4- and 2- chamber views, the 4 strain curves of the 3-chamber view and the cycle duration.

3.4.1 Error function

For each healthy adult and LBBB patient, an error function J_{error} between simulation outputs and experimental strain curves was minimized in order to find patient-specific parameters:

$$J_{error} = \sum_{s=1}^{16} J_s \tag{3.18a}$$

$$J_s = \frac{1}{T}\sum_{t_e=0}^{T-1} \mid \varepsilon_s^{exp}(t_e) - \varepsilon_s^{model}(t_e) \mid + \mid \varepsilon_{s,min}^{exp} - \varepsilon_{s,min}^{model} \mid \tag{3.18b}$$

where ε_s^{exp} and ε_s^{model} are the myocardial strain signals obtained from available clinical data and simulated outputs, respectively. t_e corresponds to the time elapsed since the onset of the identification period and T is the duration of a cardiac cycle. To build this error function, experimental and simulated strain curves were synchronized on the onset of QRS of synthesized and clinical ECG.

3.4.2 Evolutionary algorithm

The error function J_{error} was minimized using Evolutionary Algorithm (EA) (see Section 2.1.3). These stochastic search methods are founded on theories of natural evolution, such as selection, crossover, and mutation [55]. In this study, a Differential Evolution algorithm (DE) algorithm [56] was applied to find the optimal set of parameters. In order to reduce the search space, values for parameters were bounded to the physiologically plausible intervals: $I_{K_{act}} = [0; 1]$, $I_{K_{pass}} = [0; 1]$, $I_{n_1} = [0.5; 2]$, $I_{n_2} = [5; 15]$, $I_{\alpha_1} = [0.2; 0.6]$, $I_{\alpha_2} = [0.2; 0.6]$, $I_{UDP} = [1; 200]$. These intervals were defined around parameter values used for the simulation of baseline conditions and are based on physiological knowledge on the electromechanical activities of the heart [37, 40, 42, 48–51, 53, 54]. DE was implemented with 200 individuals through 100 generations with crossover and mutation probabilities equals to 0.9 and 0.02 using the C++ library PAGMO [57].

3.4.3 Interpretable patient-specific features

After parameter identification, some output features will be specifically discussed in this study:

- $K_{s,act}$: myocardial contractility that describes ability of the heart muscle to contract,
- $K_{s,pass}$: myocardial stiffness, which plays a key role in diastolic LV function,
- EAT_s : electrical activation time (Figure 3.7), which corresponds to the activation of a segment automaton taking the upper bundle of His automaton as reference,

$K_{s,act}$ and $K_{s,pass}$ represent the tissue quality of each myocardial segment and were described in Equation 3.4. They were directly identified by the EA. Two other features were extracted from patient-specific simulations of the electromechanical activity.

3.4.4 Solution unicity

In order to evaluate the robustness of the method, we repeated 10 times the identification process on 5 patients. Two patients of the healthy and LBBB ischemic population and one in the LBBB non-ischemic population were randomly chosen for this evaluation. In fact, different set of parameters could give similar simulated strain curves. The 10 obtained sets of parameters were analyzed

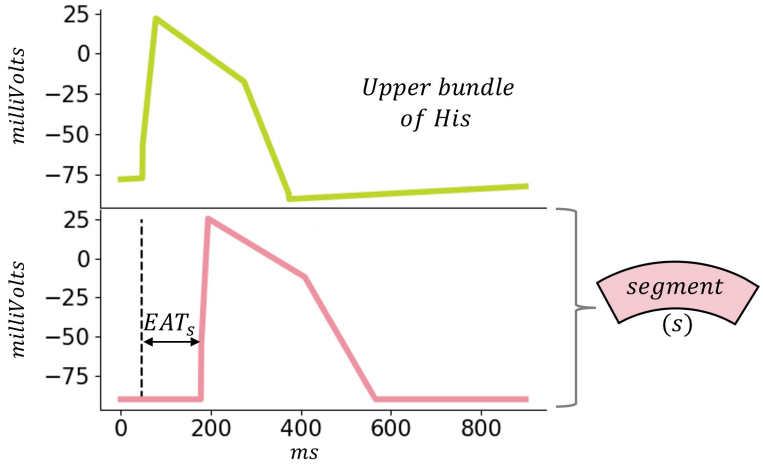

Figure 3.7: Representation of the electrical activation time (EAT_s) with the UH (*green*) and the segment s automaton activation (*pink*).

to justify the solution unicity of the identification process by comparing the distribution of each parameter p_i in its own value interval I_{p_i}. For each parameter, the ratio of the standard deviation over its value interval length was calculated. Then, the average was calculated over the 16 LV segments and expressed as percentage.

$$R^s_{p_i} = \frac{std(p_i^1, p_i^2, ..., p_i^9, p_i^{10})}{max(I_{p_i}) - min(I_{p_i})} \tag{3.19a}$$

$$R_{p_i} = \frac{100}{16} \sum_s R^s_{p_i} \tag{3.19b}$$

where $p_i \in \{ K^s_{act}, K^s_{pass}, n^s_1, n^s_2, \alpha^s_1, \alpha^s_2, UDP^s \}$ and $s \in$ {BasAnt, BasAntSep, BasInfSep, BasInf, BasInfLat, BasAntLat, MidAnt, MidAntSep, MidInfSep, MidInf, MidInfLat, MidAntLat, ApAnt, ApSep, ApInf, ApLat} .

3.4.5 Quantification of error between simulated and clinical data

In order to compare simulated and clinical strain curves, the Root-Mean-Square Error (RMSE) was calculated for each segment s :

$$RMSE_s = \sqrt{\frac{1}{T} \sum_{t_e=0}^{T-1} (\varepsilon_s^{exp}(t_e) - \varepsilon_s^{model}(t_e))^2} \tag{3.20}$$

A mean RMSE value, over the 16 segments, was calculated for each subject. Moreover, bull's eye plot was used to describe mean RMSE values calculated for each segment over each population: healthy, ischemic LBBB and non-ischemic LBBB patients.

3.5 Results

3.5.1 Baseline simulations

Figure 3.8 illustrates a simulation results' example from the proposed computational model with a set of parameters determined in previous work and literature (The set of parameter values are included in supplementary materials). Ventricular, aortic, and atrial pressures as well as ventricular volume are presented on the left of the figure. Myocardial strain signals corresponding to the 16 LV segments are presented on the right of the figure. The results are presented for a healthy case. Systolic LV pressure is equal to 120 mmHg and the aortic pressure varies between 45 and 120 mmHg. The LV volume varies between 85 and 120 mL. The strain signals present similar morphologies between all the segments due to the mechanical synchronicity between them. Generally, simulation results agree with the physiological values and behaviors of a healthy subject.

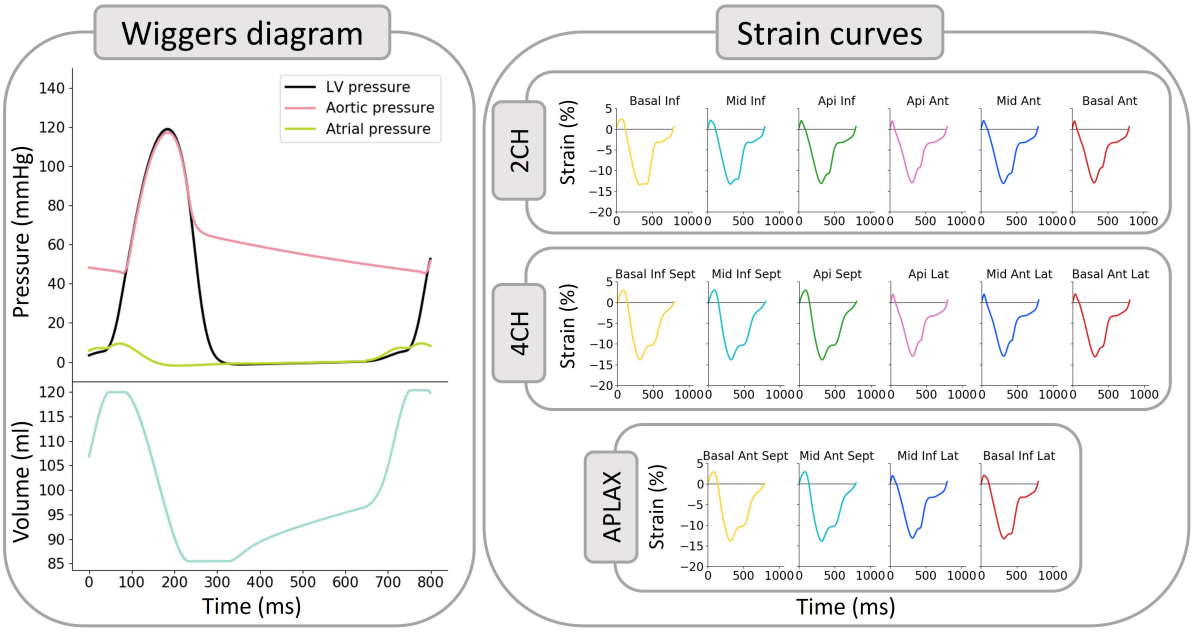

Figure 3.8: Model simulation example results in healthy conditions adapted from [41]. *Wigger diagram:* left ventricle (*black*), aortic (*pink*) and atrial pressure (*green*) and LV volume (*blue*). On the right, the *Strain curves:* 16 LV segments strain signals for the 3 views (2CH, 4CH and APLAX).

3.5.2 Simulations of desynchronization strain patterns by parameter variations

Figure 3.9 illustrates the simulated strain traces obtained in the septal and lateral walls for a digital healthy subject, LBBB with only electrical modification, LBBB with electrical modification and septal contractility reduction, LBBB with electrical modification and lateral contractility reduction. First, to induce an electrical modification, the electrical delay of all the LV segments were increased

as well as the electrical delay of the LBBB. Then, the septal and lateral hypocontractility were respectively induced by a reduction of the active components of the LV septal and lateral segments: K_{act}.

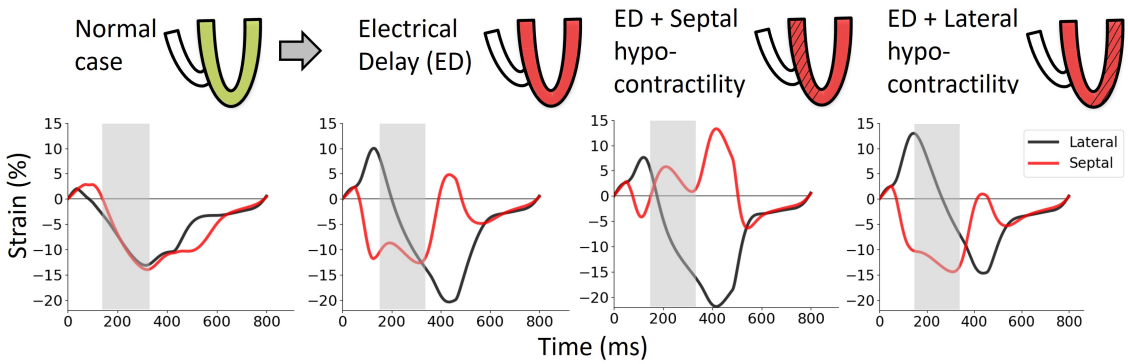

Figure 3.9: Simulated septal (*in red*) and lateral (*in black*) strain curves of a: healthy case, LBBB with only electrical modification, LBBB with electrical modification and septal contractility reduction, LBBB with electrical modification and global contractility reduction. Grey background indicates aortic valve opening to closure period. Figure adapted from [41]

In the case of LBBB with only electrical modification, simulations present a typical septo-to-lateral activation pattern. In this case, the pre-ejection contraction of the septal wall is followed by an immediate re-lengthening of the wall, which induces a septal rebound stretch. In the septal hypocontractility case, the rebound stretch effect increases. The lateral hypocontractility case is characterized by a modification of LV activation pattern and is associated with a significant reduction in lateral wall strain and a diminution of the septal rebound stretch. The simulations could be related with [6] experimental results where LBBB was induced in dogs with or without LV scar.

3.5.3 Sensitivity analysis

Figure 3.10 shows a Morris scheme where 100 of the most influential parameters are plotted in the $\mu^* - \sigma$ plane based on the D_j index. This representation highlights the parameters with negligible (*lower left-hand corner*), the linear without interaction (*bottom right*) and nonlinear or interaction (*top right*) impact on Y. Parameters α_2 and n_1 present a great recurrence impact on the sensitivity of the evaluated outputs Y. In fact, as α_1 and n_2, they are involved in the electromechanical coupling at the tissue-level (Equation 3.3) which causes modifications in mechanical contraction and, consequently, in the deformation of the LV segments. These parameters appear especially important for lateral and septal segments.

UDP, related with the electrical depolarization time, is also one of the most influential parameters. UDP is the time of the upstroke depolarization, it drives the activation of the neighbor's automata and affects the t_a and t_s value of Equation 3.2 and Equation 3.3. t_a is the time elapsed since

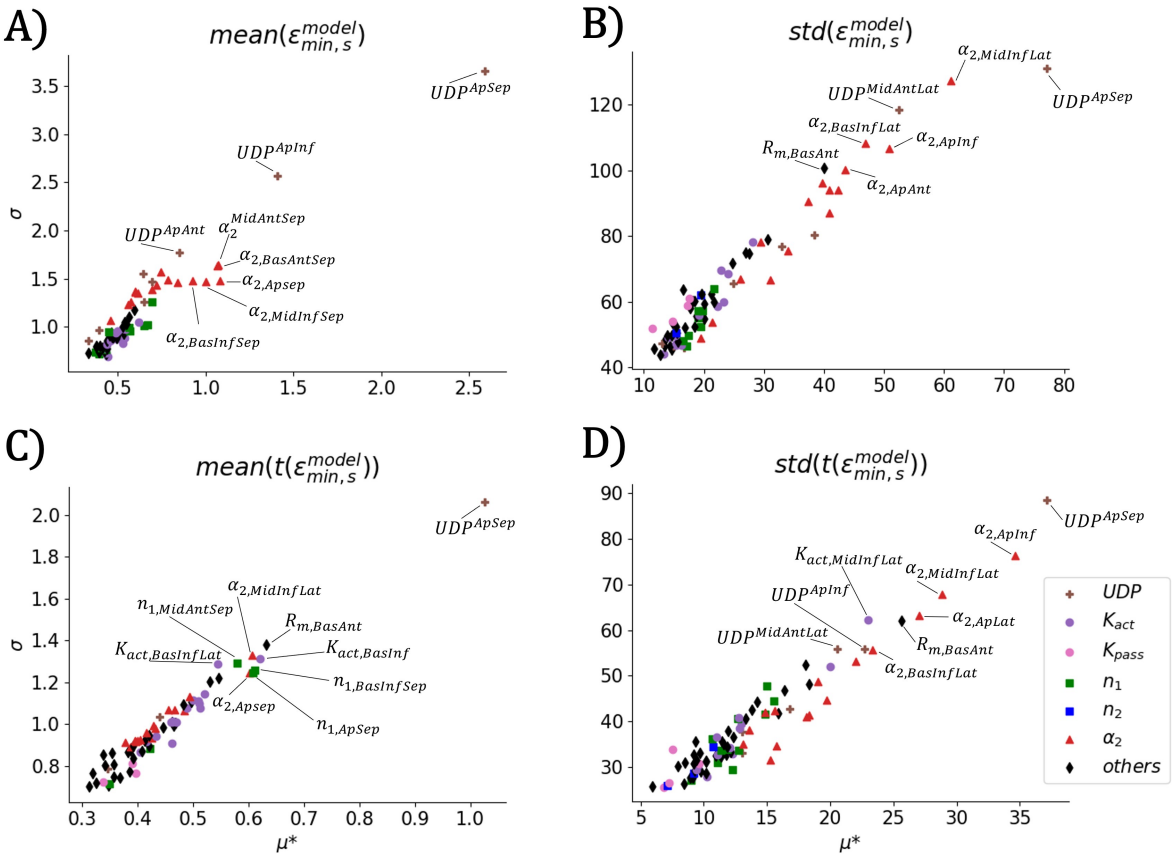

Figure 3.10: Most influential parameters on *A)* the average of the minimum peaks over all segments, *B)* the standard deviation of the minimum peaks over all segments, *C)* the average time associated to each minimum peak over all segments and *D)* the standard deviation of the time associated to each minimum peak over all segments (*bottom,right*); according to Morris sensitivity results. Only the first 100 parameters according to their distance D_j are plotted in the $\mu^* - \sigma$ plane. (Figure extracted from [41])

the beginning of the activation and t_s is initialized by the activation of the neighbors, so directly impact by the UDP times of the previous automata. If we look closer at the sensitivity analysis, we can notice that the UDP related to the apical segments have the highest influence on the mean and standard deviation of the minimum strain value as well as the corresponding time. This could be explained by the electrical path. Indeed, the electrical and mechanical activities are closely related, therefore the deformation of a segment is highly dependent on the occurrence of electrical depolarization. K_{act} and K_{pass}, respectively related with the active and passive components of the cardiac muscle, show also high sensitivity.

Results from the sensitivity analysis were used to select the 7 most significant model parameters to be identified for each segment: parameters related with the EMDF ($n_1, n_2, \alpha_1, \alpha_2$), the active ($K_{act}$) and passive ($K_{pass}$) components of the cardiac muscle and the electrical depolarization time (UDP). The electrical depolarization time of the left bundle branch (UDP^{LBB}) was also

added to the parameter identification list.

Complementary results of the sensitivity analysis as well as a sum up of the parameters and value intervals used in the study are gathered in Appendix A (Table A.4, Table A.5, Table A.6, Table A.7 and Table A.8).

3.5.4 Patient-specific simulations of segmental strain curves

Myocardial strain curves of the 16 LV segments acquired by experimental measurements and patient-specific simulations are presented in one representative healthy subject (Figure 3.11), an anterior ischemic and a non-ischemic (Figure 3.12) LBBB patient (All results are included in Appendix A).

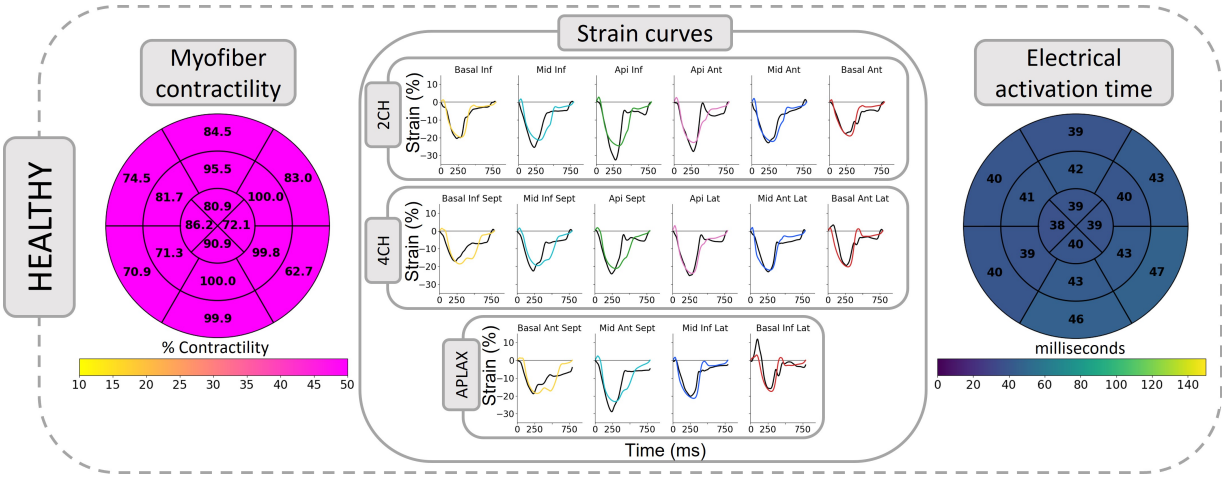

Figure 3.11: Patient-specific simulation results for a healthy subject. Experimental (*black*) and simulated (*colored*) strain curves corresponding to the 16 LV segments. Bull's-eye representations of segmental electrical activation time and segmental myofiber contractility. Color scale at the contractility bull's-eye plot set between 10 and 50% in order to highlight the segments with low contractility.

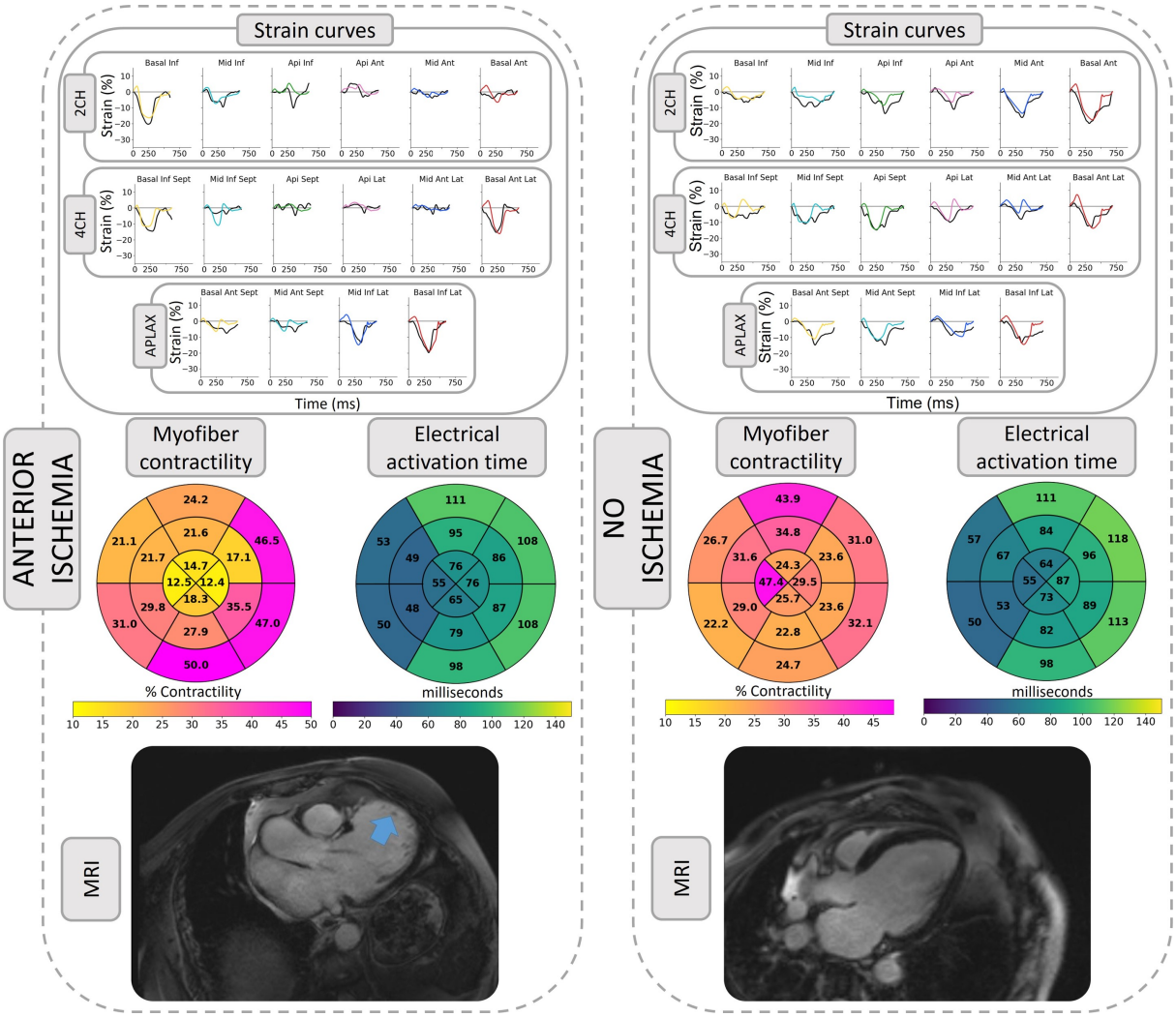

Figure 3.12: Patient-specific simulation results for a LBBB patient with an anterior ischemia (*left*) and no ischemia (*right*). Experimental (*black*) and simulated (*colored*) strain curves corresponding to the 16 LV segments. Bull's-eye representations of segmental electrical activation time and segmental myofiber contractility obtained by patient-specific simulations.The ischemia is localized on the cMRI (*blue arrow*).

For both healthy and LBBB cases, a good agreement was observed between clinical and simulated strain signals. The RMSE errors are similar through the 16 strain curves for each patient in both LBBB patient types. Concerning healthy cases, the strain curves present similar morphologies in all the segments due to the synchronization in all LV regions when the myocardium contracts, but we can notice some difficulties to well fit the basal anterior and lateral strain in some healthy patients. Figure 3.13 presents this RMSE average by regions for the three groups (the same RMSE bull's eye representation is included in supplementary materials for each patient).

Mean RMSE between estimated and observed strain signals in the healthy adults was equal to 5.04 ± 1.02 (Table 3.2).

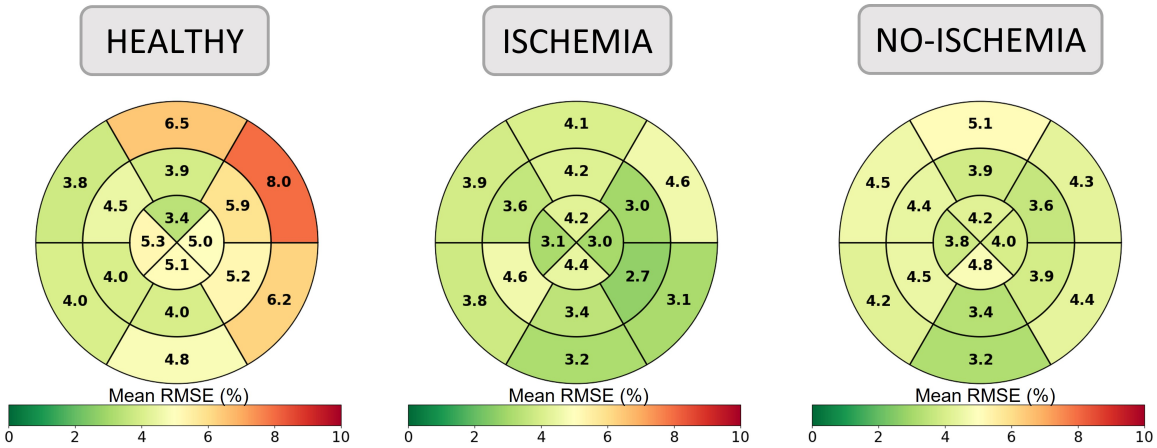

Figure 3.13: Mean RMSE by region for the 3 groups of patients: healthy, LBBB ischemia, LBBB no-ischemia

Healthy	Mean RMSE	LBBB (Isch)	Mean RMSE	LBBB (Non-isch)	Mean RMSE
Patient 1	4.91 ± 2.16	**Patient 1**	2.71 ± 1.13	**Patient 1**	3.47 ± 1.03
Patient 2	3.89 ± 1.08	**Patient 2**	2.88 ± 1.0	**Patient 2**	3.63 ± 0.82
Patient 3	4.77 ± 1.53	**Patient 3**	2.50 ± 0.56	**Patient 3**	5.03 ± 1.49
Patient 4	4.19 ± 1.13	**Patient 4**	1.96 ± 0.69	**Patient 4**	4.38 ± 2.06
Patient 5	5.41 ± 1.66	**Patient 5**	3.51 ± 1.1	**Patient 5**	3.73 ± 1.3
Patient 6	6.23 ± 12.45	**Patient 6**	4.50 ± 2.42	**Patient 6**	2.99 ± 1.0
Patient 7	3.43 ± 0.88	**Patient 7**	8.23 ± 3.42	**Patient 7**	5.71 ± 2.29
Patient 8	5.45 ± 1.84	**Patient 8**	1.99 ± 0.72	**Patient 8**	3.15 ± 1.48
Patient 9	6.72 ± 2.38	**Patient 9**	4.60 ± 2.50	**Patient 9**	4.36 ± 1.76
Patient 10	5.40 ± 2.30	**Patient 10**	3.72 ± 1.33	**Patient 10**	4.86 ± 2.06

Table 3.2: Mean RMSE between the 16 experimental and simulated LV strain curves of the study population with healthy, LBBB with ischemia (Isch) and LBBB without ischemia (Non-isch) patients.

In LBBB cases, mean RMSE was equal to 3.90 ± 1.40 % (Table 3.2). In these cases, the strain curves obtained in LBBB patients present dissimilar morphologies between the different segments. Particularly, the septum and the lateral wall segments of the ventricle present opposite curves, where the shortening of septal segments occurs at the same time as in the lengthening of lateral segments.

3.5.5 Bull's eye representations of the identified parameter

From patient-specific simulations, segmental electrical activation time (EAT_s) and the percentage of myofiber contractility ($K_{s,act}$) were represented on bull's-eye plots in Figure 3.11 and Figure 3.12,

for 3 representative cases: 1) Healthy adult, 2) LBBB patient with LV anterior ischemia and 3) Non-ischemic LBBB patient.

In LBBB cases, electrical activation bull's-eye shows a significant electrical activation delay between the lateral and the septal wall of the LV; while in the healthy case, all LV segments are activated almost synchronously. Furthermore, the LBBB patient with LV anterior ischemia presented reduced contractility in anterior segments of the Bull's eye representation (Figure 3.12).

3.5.6 Comparison with MRI

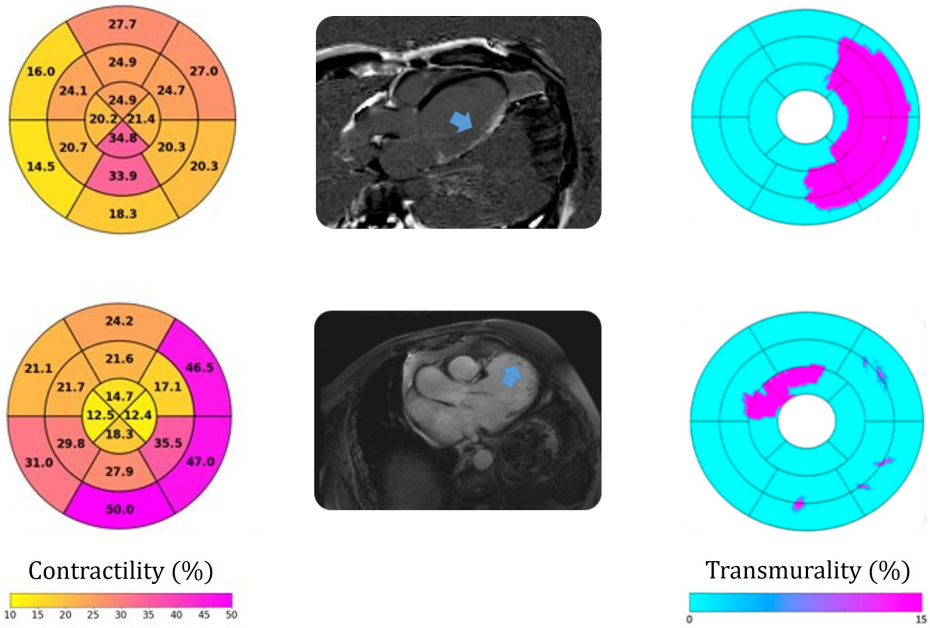

Figure 3.14: Identified contractility parameters (%) and transmurality degree (%) in two ischemic patients (*top*: lateral scar, *bottom*: antero septal scar) obtained by cMRI.

The model was able to reproduce regional modifications in LV contractility which are due to the LBBB, but also to local scarring. In the case of isolated LBBB, we observed increased contractility of the lateral wall compared to the septum. In the case of lateral scar, we observed a significant impairment in lateral contractility. In the case of anteroseptal scar, a higher reduction in contractility was observed in the septal and apical segments. As depicted in Figure 3.14, reduced contractility in ischemic patients corresponded to the areas of transmural distribution of late gadolinium enhancement observed with cMRI (Figure 3.14). A higher percentage of transmurality translates into larger fibrotic areas, which are associated with low contractility. Therefore, regional contractility levels allow distinction between ischemic and non-ischemic cases, where reduced contractility could be associated with damaged tissues. Half of the patient MRI are provided in Appendix A (Figure A.28: 10 with ischemia and 10 without).

3.5.7 Unicity evaluation

The ratio of the mean standard deviation over the interval length of each type of parameter is presented in Table 3.3.

Patients		K_{act}	K_{pass}	n_2	n_1	α_2	α_1	UDP	UDP^{LBB}
2	**LBBB ischemia**	16.32	2.17	9.39	2.74	1.84	3.45	2.60	0.47
		9.07	2.01	14.02	2.82	2.48	3.20	3.24	0.58
1	**LBBB no-ischemia**	12.96	2.00	10.44	3.18	1.82	3.21	2.85	0.49
2	**Healthy**	15.51	1.46	10.42	2.32	1.69	2.83	2.61	0.34
		12.66	1.47	9.80	2.18	1.42	3.10	2.34	0.44

Table 3.3: Mean ratio of the standard deviation over interval length for 10 identification repetitions over 5 patients (2 LBBB with ischemia, 1 LBBB without ischemia and 2 healthy)

The result of the repeated identification shows that the parameter values are gathered in the same part of the possible values of the interval. In fact, for all the parameter, this mean standard deviation is between 0.34 and 16.32% of their respective interval. Especially for the electrical parameter UDP^{LBB}, the ratio is less than 0.6%.

3.6 Discussion

This section presents a novel model-based approach that yields simulations of patient-specific strain curves in several LV regions for healthy adults and patients diagnosed with LBBB. It used *i)* an integrated model of the cardiovascular system coupled to multi-segment representations of ventricles (Section 3.2), proposed *ii)* the sensitivity analysis of model parameters on myocardial strains (Section 3.3), *iii)* the identification of model parameters to reproduce myocardial strain curves specifically to each patient (Section 3.4) and *iv)* the analysis of patient-specific identified parameters (Section 3.5).

The proposed CVS model is based on a functional integration of interacting physiological systems that takes into account the electromechanical coupling, the inter-ventricular interaction and a simplified representation of systemic and pulmonary circulations. The model includes the main cardiac properties required to tackle the problem under study, like the Frank-Starling law and the influence of preload and afterload. Results illustrate the model ability to simulate jointly the hemodynamic variables and myocardial deformations. Strain curves notably reflected typical characteristics associated with each phase of the cardiac cycle. In order to personalize models to patient-specific data, numerous simulations should be performed. In opposition to FEM representations [35], the proposed model requires limited computational resources, as the simulation of one cardiac cycle (1000 ms of simulation) takes about 0.5 seconds (Processor: 2,2 GHz Intel Core i7). The low computational cost is of primary importance to use cardiac modeling

in clinical practice and to adapt models to each patient.

The first step of patient-specific adaptation is the sensitivity analysis of model parameters, which highlights *i)* the close relationship between cardiac electrical and mechanical systems and *ii)* the importance of active and passive properties of the myocardium during cardiac contraction. The analysis results show that the electric stimulation timing between the different segment have a great importance in the variability between the strain curves. The sensitivity analysis also highlights the importance of parameters related to myocardial mechanical properties. In fact, a close relationship exists between excitation and contraction since a synchronous ventricular activation is a prerequisite for an adequate LV function, whereas the electrical activation time between opposite LV walls might lead to dyssynchronous ventricular contraction and LV failure [58]. Nevertheless, it has been shown that typical myocardial strain morphologies in LBBB could be modified by the presence of scar and low regional LV contractility. Figure 3.9 illustrates this point, by presenting different patterns though the modulation of parameters. Moreover, the parameters of the septal and lateral parts of the LV present highest influence on the strain curves' dyssynchrony. This is particularly interesting knowing the recent study on the importance of the septal variability in the contribution of the LV reverse modeling [6]. In this context, the ability of the model to disclose the relationship between electrical activation time and LV contractility has pivotal importance because it might ease the identification of myocardial substrates that are more prone to be associated with CRT-response.

In the second step of patient-specific adaptation, evolutionary algorithms were used to identify the most influential parameters in each patient. The error function was minimized based on experimental and simulated strain curves previously synchronized on the onset of QRS of synthesized and experimental ECG. Patient-specific simulations have shown satisfactory results, since we observed a good agreement between simulated and experimental myocardial strain curves given the reproducibility of strain signals [59, 60]. For healthy cases, morphologies of the myocardial strain curves were similar in all segments due to the synchronous contraction of the entire LV [43]. Associated bull-eyes show normal electrical activation times and elevated contractile levels.

In most patients with non-ischemic LBBB, the early activation of the LV septum, followed by the delayed activations of the LV wall [61, 62], causes a typical myocardial strain pattern. This pattern is characterized by an early marked shortening of the septum in the pre-ejection phase, known as "septal flash" [63] followed by an immediate re-lengthening of the septum, the "septal rebound stretch". Both the septal flash and septal rebound are known to be predictors of CRT response [4, 64].

In ischemic patients, the typical activation pattern induced by LBBB can be disrupted by the association of electrical delay and inhomogeneous LV contractility. In patients with LBBB and lateral scar, hypocontractile regions are localized in the lateral wall. In this case, deformation patterns are highly modified because the local impairment of contractility in the lateral wall caused

the loss of the rebound stretch in the septum [6]. On the contrary, the presence of anterior scar was associated with a reduced contractility of the corresponding myocardial segments and had less impact of septal deformation [6]. The strength of the model was therefore to reproduce the "atypical" strain patterns observed in patients with LBBB and ischemic cardiomyopathy thought the correct localization of the hypocontractile segments, which correspond to areas of myocardial scar identified by clinician based on cMRI.

There are several important consequences of the findings. First, results of the model-based approach underscore that septal motion and global strain morphologies are not only explained by electrical conduction delay, but also by the heterogeneity of contractile levels within the myocardium and suggest that the evaluation of LV dyssynchrony should consider both electrical delay and regional mechanical function. Second, the application of a model-based approach could bring additional information on the regional electrical and mechanical function of the LV from the simple analysis of echocardiographic data. This is particularly important because it can help to disclose the intrinsic complexity of LV mechanics in CRT candidates, and represents a step forwards the development of personalized LV modeling in the field of CRT. Third, one of the main strengths of the approach was to perform a parameter identification process for the patient-specific estimations of the segmental strain curves. In order to build the cost function, experimental and simulated strain curves were synchronized on QRS peaks of synthesized and experimental ECG. Model parameters were identified from the myocardial strain curves of the 16 LV segments acquired by STE. For both healthy and LBBB cases, a good agreement was observed between measured and estimated strain signals.

These results bode well for the model capacity to reproduce clinical measurements and could be promising in the LV function analyze for an individual patient and possibly in the prediction of optimal treatments.

Although several studies have successfully used computational models of the CVS to understand myocardial deformation patterns [19, 65, 66], or investigate the best CRT pacing location [19, 20, 67] this approach provides interesting advantages and original aspects. The multi-segment model of the LV allows not only the analysis of the deformation curves of the septal and lateral walls, but also the strain signals of all the ventricular regions. Therefore, the proposed model resolution was adapted to the standardized segmentation of the AHA, keeping a similar abstraction level as clinicians for the analysis of strain signals. It also uses data from 2D STE, highly accessible in clinical routine, with well-known strengths and limitation. Moreover, the proposed approach applies a parameter identification process, providing customized models specifically for each patient and allowing the recognition of hypocontractile areas that could be associated with the presence of fibrosis.

3.6.1 Limitations

The proposed model-based approach presents some limitations that should be mentioned. Several hypotheses were made in order to propose tissue-level representations of ventricles: *i)* the ventricular torsion was neglected, *ii)* the mechanical continuity between myocardial segments was not always assured because ventricles are represented by a set of sub-pumps controlled by a coordinated electrical activity and coupled in the hydraulic domain, *iii)* only mean myocardial fiber orientation was considered, and *iv)* electromechanical coupling was approximated by an analytic expression.

Despite these hypotheses, the model definition is in accordance with the problem under study and appears to be a useful tool to assist the interpretation of strain data. Moreover, in order to reduce computational costs, only a small sample of variables was selected for parameter identification. These parameters may have absorbed changes in other fixed parameters. For instance, septal segment parameters that may have been affected by RV variations. Thus, a wider range of parameters could be included in the future. Finally, this study is based on a small population of LBBB patients, an extension of the simulation on a larger clinical database and simulation repetitions should give us a better estimation of the reproducibility and the robustness of the method.

Moreover, as the results shown, the surface of the hypocontractile regions seems overestimated. That suggests a diffusion of the tissue quality in the parameter identification process. In the same way, a mismatch still exists between the experimental and simulated curves. Some efforts must still be made to reduce it, but the simplifications chosen in the model definition, as well as, the reduce number of parameters used in the patient specific identification explain it.

Nevertheless, this is the first work providing patient-specific simulations of strain curves in the case of LBBB in association with ischemia and the proposed approach is a step forward towards the integration of computational models in patient selection process before CRT procedures. The work presented in the next chapter will be dedicated to evaluating the proposed model-based indices, in a wider multi-parametric approach [68], for the prediction of CRT response.

3.7 Conclusion

In this chapter, we propose a novel model-based approach for the analysis of myocardial strains in LBBB patients. The global method is based on *i)* a physiological model of the cardiovascular system that integrates the electrical, mechanical, and hydraulic processes leading to ventricular contraction and *ii)* a parameter identification procedure for patient-specific simulations. The proposed model-based approach was evaluated with echocardiography data from 10 healthy individuals and 20 LBBB patients. Results show a close match between experimental and simulated strain curves in all the cases. Furthermore, the approach is able to reproduce electrical activation

delay and segmental myofiber contractility properly.

More extensive evaluations including a greater population of patients, as well as the analysis of a wider multi-parametric approach should be performed in the future. Nevertheless, this paper presents a first work towards the evaluation of myocardial strain signals and the assessment of certain echo-based parameters by patient-specific simulations based on computational models. The proposed personalized approach represents a promising tool for the LV mechanical dyssynchrony understanding and CRT responder identification.

BIBLIOGRAPHY

[1] Grines C.L., Bashore T.M., Boudoulas H., Olson S., Shafer P., and Wooley C.F. Functional abnormalities in isolated left bundle branch block. The effect of interventricular asynchrony. *Circulation*, vol. 79, 845–853 (1989).

[2] Risum N., Tayal B., Hansen T.F., Bruun N.E., Jensen M.T., Lauridsen T.K., Saba S., Kisslo J., Gorcsan J., and Sogaard P. Identification of Typical Left Bundle Branch Block Contraction by Strain Echocardiography Is Additive to Electrocardiography in Prediction of Long-Term Outcome after Cardiac Resynchronization Therapy. *J. Am. Coll. Cardiol.*, vol. 66, 631–641 (2015).

[3] De Boeck B.W., Teske A.J., Meine M., Leenders G.E., Cramer M.J., Prinzen F.W., and Doevendans P.A. Septal rebound stretch reflects the functional substrate to cardiac resynchronization therapy and predicts volumetric and neurohormonal response. *Eur. J. Heart Fail.*, vol. 11, 863–871 (2009).

[4] Stankovic I., Prinz C., Ciarka A., Daraban A.M., Kotrc M., Aarones M., Szulik M., Winter S., Belmans A., Neskovic A.N., Kukulski T., Aakhus S., Willems R., Fehske W., Penicka M., Faber L., and Voigt J.U. Relationship of visually assessed apical rocking and septal flash to response and long-term survival following cardiac resynchronization therapy (PREDICT-CRT). *Eur. Heart J. Cardiovasc. Imaging*, vol. 17, 262–269 (2016).

[5] Rao H.B., Krishnaswami R., Kalavakolanu S., and Calambur N. Ventricular dyssynchrony patterns in left bundle branch block, with and without heart failure. *Indian Pacing Electrophysiol. J.*, vol. 10, 115–121 (2010).

[6] Aalen J.M., Remme E.W., Larsen C.K., Andersen O.S., Krogh M., Duchenne J., Hopp E., Ross S., Beela A.S., Kongsgaard E., Bergsland J., Odland H.H., Skulstad H., Opdahl A., Voigt J.U., and Smiseth O.A. Mechanism of Abnormal Septal Motion in Left Bundle Branch Block: Role of Left Ventricular Wall Interactions and Myocardial Scar. *JACC Cardiovasc. Imaging*, vol. 12, 2402–2413 (2019).

[7] Hoit B.D. Strain and strain rate echocardiography and coronary artery disease. *Circ. Cardiovasc. Imaging*, vol. 4, 179–190 (2011).

[8] Lumens J., Tayal B., Walmsley J., Delgado-Montero A., Huntjens P.R., Schwartzman D., Althouse A.D., Delhaas T., Prinzen F.W., and Gorcsan J. Differentiating Electromechanical from Non-Electrical Substrates of Mechanical Discoordination to Identify Responders to Cardiac Resynchronization Therapy. *Circ. Cardiovasc. Imaging*, vol. 8 (2015).

[9] Trayanova N.A. and Rice J.J. Cardiac electromechanical models: From cell to organ. *Front. Physiol.*, vol. 2 AUG, 1–19 (2011).

[10] Tusscher K.H.W.J., Noble D., Noble P.J., and Panfilov A.V. A model for human ventricular tissue. *Am J Physiol Hear. Circ Physiol*, 1573–1589 (2003).

[11] Bartolucci C., Passini E., Hyttinen J., Paci M., and Severi S. Simulation of the Effects of Extracellular Calcium Changes Leads to a Novel Computational Model of Human Ventricular Action Potential With a Revised Calcium Handling. *Front. Physiol.*, vol. 11, 1–20 (2020).

[12] O'Hara T., Virág L., Varró A., and Rudy Y. Simulation of the undiseased human cardiac ventricular action potential: Model formulation and experimental validation. *PLoS Comput. Biol.*, vol. 7 (2011).

[13] Cortassa S., Aon M.A., O'Rourke B., Jacques R., Tseng H.J., Marbán E., and Winslow R.L. A computational model integrating electrophysiology, contraction, and mitochondrial bioenergetics in the ventricular myocyte. *Biophys. J.*, vol. 91 (2006).

[14] Dupuis L.J., Lumens J., Arts T., and Delhaas T. Mechano-chemical Interactions in Cardiac Sarcomere Contraction: A Computational Modeling Study. *PLoS Comput. Biol.*, vol. 12, 1–20 (2016).

[15] Regazzoni F., Dedè L., and Quarteroni A. Biophysically detailed mathematical models of multiscale cardiac active mechanics. *PLoS Comput. Biol.*, vol. 16 (2020).

[16] Pironet A., Desaive T., Kosta S., Lucas A., Paeme S., Collet A., Pretty C.G., Kolh P., and Dauby P.C. A multi-scale cardiovascular system model can account for the load-dependence of the end-systolic pressure-volume relationship. *Biomed. Eng. Online*, vol. 12 (2013).

[17] Sack K.L., Dabiri Y., Franz T., Solomon S.D., Burkhoff D., and Guccione J.M. Investigating the role of interventricular interdependence in development of right heart dysfunction during LVAD support: A patient-specific methods-based approach. *Front. Physiol.*, vol. 9, 1–13 (2018).

[18] Park J.I., Heikhmakhtiar A.K., Kim C.H., Kim Y.S., Choi S.W., Song K.S., and Lim K.M. The effect of heart failure and left ventricular assist device treatment on right ventricular mechanics: A computational study. *Biomed. Eng. Online*, vol. 17, 1–13 (2018).

[19] ichi Okada J., Washio T., Nakagawa M., Watanabe M., Kadooka Y., Kariya T., Yamashita H., Yamada Y., ichi Momomura S., Nagai R., Hisada T., and Sugiura S. Multi-scale, tailor-made heart simulation can predict the effect of cardiac resynchronization therapy. *J. Mol. Cell. Cardiol.*, vol. 108, 17–23 (2017).

[20] Crozier A., Blazevic B., Lamata P., Plank G., Ginks M., Duckett S., Sohal M., Shetty A., Rinaldi C.A., Razavi R., Smith N.P., and Niederer S.A. The relative role of patient physiology and device optimisation in cardiac resynchronisation therapy: A computational modelling study. *J. Mol. Cell. Cardiol.*, vol. 96, 93–100 (2016).

[21] Niederer S.A., Lamata P., Plank G., Chinchapatnam P., Ginks M., Rhode K., Rinaldi C.A., Razavi R., and Smith N.P. Analyses of the Redistribution of Work following Cardiac Resynchronisation Therapy in a Patient Specific Model. *PLoS One*, vol. 7, 1–9 (2012).

[22] Constantino J., Hu Y., and Trayanova N.A. A computational approach to understanding the cardiac electromechanical activation sequence in the normal and failing heart, with translation to the clinical practice of CRT. *Prog. Biophys. Mol. Biol.*, vol. 110, 372–379 (2012).

[23] Garcia-Blanco E., Ortigosa R., Gil A.J., Lee C.H., and Bonet J. A new computational framework for electro-activation in cardiac mechanics. *Comput. Methods Appl. Mech. Eng.*, vol. 348, 796–845 (2019).

[24] Aguado-Sierra J., Krishnamurthy A., Villongco C., Chuang J., Howard E., Gonzales M.J., Omens J., Krummen D.E., Narayan S., Kerckhoffs R.C., and McCulloch A.D. Patient-specific modeling of dyssynchronous heart failure: A case study. *Prog. Biophys. Mol. Biol.*, vol. 107, 147–155 (2011).

[25] Augustin C.M., Gsell M.A., Karabelas E., Willemen E., Prinzen F.W., Lumens J., Vigmond E.J., and Plank G. A computationally efficient physiologically comprehensive 3D–0D closed-loop model of the heart and circulation. *Comput. Methods Appl. Mech. Eng.*, vol. 386, page 114092 (2021).

[26] Zhang Y., Wang V.Y., Morgan A.E., Kim J., Ge L., Guccione J.M., Weinsaft J.W., and Ratcliffe M.B. A Novel MRI-Based Finite Element Modeling Method for Calculation of Myocardial Ischemia Effect in Patients With Functional Mitral Regurgitation. *Front. Physiol.*, vol. 11, 1–13 (2020).

[27] Oomen P.J., Phung T.K.N., Weinberg S.H., Bilchick K.C., and Holmes J.W. A rapid electromechanical model to predict reverse remodeling following cardiac resynchronization therapy. *Biomech. Model. Mechanobiol.*, vol. 21, 231–247 (2022).

[28] Pezzuto S., Prinzen F.W., Potse M., Maffessanti F., Regoli F., Caputo M.L., Conte G., Krause R., and Auricchio A. Reconstruction of three-dimensional biventricular activation based on the 12-lead electrocardiogram via patient-specific modelling. *Europace*, vol. 23, 640–647 (2021).

[29] Vincent K.P., Forsch N., Govil S., Joblon J.M., Omens J.H., Perry J.C., and McCulloch A.D. Atlas-based methods for efficient characterization of patient-specific ventricular activation patterns. *Europace*, vol. 23, I88–I95 (2021).

[30] Lumens J., Leenders G.E., Cramer M.J., De Boeck B.W., Doevendans P.A., Prinzen F.W., and Delhaas T. Mechanistic evaluation of echocardiographic dyssynchrony indices patient data combined with multiscale computer simulations. *Circ. Cardiovasc. Imaging*, vol. 5, 491–499 (2012).

[31] Willemen E., Schreurs R., Huntjens P.R., Strik M., Plank G., Vigmond E., Walmsley J., Vernooy K., Delhaas T., Prinzen F.W., and Lumens J. The left and right ventricles respond differently to variation of pacing delays in cardiac resynchronization therapy: A combined experimental-computational approach. *Front. Physiol.*, vol. 10, 1–13 (2019).

[32] van Everdingen W.M., Walmsley J., Cramer M.J., van Hagen I., De Boeck B.W., Meine M., Delhaas T., Doevendans P.A., Prinzen F.W., Lumens J., and Leenders G.E. Echocardiographic Prediction of Cardiac Resynchronization Therapy Response Requires Analysis of Both Mechanical Dyssynchrony and Right Ventricular Function: A Combined Analysis of Patient Data and Computer Simulations. *J. Am. Soc. Echocardiogr.*, vol. 30, 1012–1020.e2 (2017).

[33] Leenders G.E., De Boeck B.W., Teske A.J., Meine M., Bogaard M.D., Prinzen F.W., Doevendans P.A., and Cramer M.J. Septal rebound stretch is a strong predictor of outcome after cardiac resynchronization therapy. *J. Card. Fail.*, vol. 18, 404–412 (2012).

[34] Regazzoni F., Salvador M., Africa P.C., Fedele M., Dedè L., and Quarteroni A. A cardiac electromechanical model coupled with a lumped-parameter model for closed-loop blood circulation. *J. Comput. Phys.*, vol. 457, page 111083 (2022).

[35] Le Rolle V., Galli E., Danan D., El Houari K., Hubert A., Donal E., and Hernández A.I. Sensitivity Analysis of a Left Ventricle Model in the Context of Intraventricular Dyssynchrony. *Acta Biotheor.*, vol. 68, 45–59 (2019).

[36] Niederer S.A., Lumens J., and Trayanova N.A. Computational models in cardiology. *Nat. Rev. Cardiol.*, vol. 16, 100–111 (2019).

[37] Le Rolle V., Hernández A.I., Richard P.Y., Donal E., and Carrault G. Model-based analysis of myocardial strain data acquired by tissue Doppler imaging. *Artif. Intell. Med.*, vol. 44, 201–219 (2008).

[38] Owashi K.P. *Model-based analysis of myocardial strains for the evaluation of cardio- vascular function*. Ph.D. thesis, Université Rennes 1 (2021).

[39] Owashi K.P., Hubert A., Galli E., Donal E., Hernández A.I., and Rolle V.L. Model-based estimation of left ventricular pressure and myocardial work in aortic stenosis. *PLoS One*, vol. 15, 1–18 (2020).

[40] Calvo M., Le Rolle V., Romero D., Béhar N., Gomis P., Mabo P., and Hernández A.I. Model-based analysis of the autonomic response to head-up tilt testing in Brugada syndrome. *Comput. Biol. Med.*, vol. 103, 82–92 (2018).

[41] Taconné M., Owashi K.P., Galli E., Duchenne J., Hubert A., Donal E., Hernàndez A.I., and Le Rolle V. Model-based analysis of myocardial strains in left bundle branch block. *Front. Appl. Math. Stat.*, page 110 (2022).

[42] Owashi K., Taconné M., Courtial N., Simon A., Garreau M., Hernandez A., Donal E., Rolle V.L., and Galli E. Desynchronization Strain Patterns and Contractility in Left Bundle Branch Block through Computer Model Simulation. *J. Cardiovasc. Dev. Dis.*, vol. 9, page 53 (2022).

[43] Lang R.M., Badano L.P., Mor-Avi V., Afilalo J., Armstrong A., Ernande L., Flachskampf F.A., Foster E., Goldstein S.A., Kuznetsova T., Lancellotti P., Muraru D., Picard M.H., Rietzschel E.R., Rudski L., Spencer K.T., Tsang W., and Voigt J.U. Recommendations for cardiac chamber quantification by echocardiography in adults: An update from the American society of echocardiography and the European association of cardiovascular imaging. *Eur. Heart J. Cardiovasc. Imaging*, vol. 16, 233–271 (2015).

[44] Hernández A.I., Le Rolle V., Defontaine A., and Carrault G. A multiformalism and multiresolution modelling environment: Application to the cardiovascular system and its regulation. *Philos. Trans. R. Soc. A Math. Phys. Eng. Sci.*, vol. 367, 4923–4940 (2009).

[45] Hernández A.I., Le Rolle V., Ojeda D., Baconnier P., Fontecave-Jallon J., Guillaud F., Grosse T., Moss R.G., Hannaert P., and Thomas S.R. Integration of detailed modules in a core model of body fluid homeostasis and blood pressure regulation. *Prog. Biophys. Mol. Biol.*, vol. 107, 169–182 (2011).

[46] Cerqueira M.D., Weissman N.J., Dilsizian V., Jacobs A.K., Kaul S., Laskey W.K., Pennell D.J., Rumberger J.A., Ryan T.J., and Verani M.S. Standardized myocardial segmentation and nomenclature for tomographic imaging of the heart. *J. Cardiovasc. Magn. Reson.*, vol. 4, 203–210 (2002).

[47] Ugalde H.M.R., Ojeda D., Rolle V.L., Andreu D., Guiraud D., Bonnet J.L., Henry C., Karam N., Hag A., Mabo P., Carrault G., and Hern A.I. Model-Based Design and Experimental Validation of Control Modules for Neuromodulation Devices. *IEEE Trans. Biomed. Eng.*, vol. 63, 1551–1558 (2016).

[48] Stergiopulos N., Meister J.J., and Westerhof N. Determinants of stroke volume and systolic and diastolic aortic pressure. *Am. J. Physiol. - Hear. Circ. Physiol.*, vol. 270 (1996).

[49] Le Rolle V., Carrault G., Richard P.Y., Pibarot P., Durand L.G., and Hernández A.I. A tissue-level electromechanical model of the left ventricle: Application to the analysis of intraventricular pressure. *Acta Biotheor.*, vol. 57, 457–478 (2009).

[50] Lumens J., Delhaas T., Kirn B., and Arts T. Three-wall segment (TriSeg) model describing mechanics and hemodynamics of ventricular interaction. *Ann. Biomed. Eng.*, vol. 37, 2234–2255 (2009).

[51] Hunter P.J., Mcculloch A.D., and Keurs H.E.D.J. Modelling the mechanical properties of cardiac muscle. *Model. Mech. Prop. Card. muscle*, vol. 21, page 15 (1998).

[52] Morris M.D. Factorial sampling plans for preliminary computational experiments. *Technometrics*, vol. 33, 161–174 (1991).

[53] Guerrero G., Rolle V.L., and Hernandez A. Sensitivity Analysis of a Cardiorespiratory Model for the Study of Sleep Apnea. *Comput. Cardiol. (2010).*, vol. 2018-Septe, 18–21 (2018).

[54] Ojeda D., Le Rolle V., Harmouche M., Drochon A., Corbineau H., Verhoye J.P., and Hernandez A.I. Sensitivity analysis and parameter estimation of a coronary circulation model for triple-vessel disease. *IEEE Trans. Biomed. Eng.*, vol. 61, 1208–1219 (2014).

[55] Goldberg D.E. and Holland J.H. Genetic Algorithms and Machine Learning (1988).

[56] Storn R. and Price K. Differential Evolution – A Simple and Efficient Heuristic for Global Optimization over Continuous Spaces. *J. Glob. Optim.*, vol. 11, 341–359 (1997).

[57] Biscani F. and Izzo D. A parallel global multiobjective framework for optimization: pagmo. *J. Open Source Softw.*, vol. 5, page 2338 (2020).

[58] Nguyên U.C., Verzaal N.J., van Nieuwenhoven F.A., Vernooy K., and Prinzen F.W. Pathobiology of cardiac dyssynchrony and resynchronization therapy. *Europace*, vol. 20, 1898–1909 (2018).

[59] Cheng S., Larson M.G., McCabe E.L., Osypiuk E., Lehman B.T., Stanchev P., Aragam J., Benjamin E.J., Solomon S.D., and Vasan R.S. Reproducibility of speckle-tracking-based strain measures of left ventricular function in a community-based study. *J. Am. Soc. Echocardiogr.*, vol. 26 (2013).

[60] Armstrong A.C., Ricketts E.P., Cox C., Adler P., Arynchyn A., Liu K., Stengel E., Sidney S., Lewis C.E., Schreiner P.J., Shikany J.M., Keck K., Merlo J., Gidding S.S., and Lima J.A. Quality Control and Reproducibility in M-Mode, Two-Dimensional, and Speckle Tracking Echocardiography Acquisition and Analysis: The CARDIA Study, Year 25 Examination Experience. *Echocardiography*, vol. 32, 1233–1240 (2015).

[61] Gjesdal O., Remme E.W., Opdahl A., Skulstad H., Russell K., Kongsgaard E., Edvardsen T., and Smiseth O.A. Mechanisms of abnormal systolic motion of the interventricular septum during left bundle-branch block. *Circ. Cardiovasc. Imaging*, vol. 4, 264–273 (2011).

[62] De Boeck B.W., Kirn B., Teske A.J., Hummeling R.W., Doevendans P.A., Cramer M.J., and Prinzen F.W. Three-dimensional mapping of mechanical activation patterns, contractile dyssynchrony and dyscoordination by two-dimensional strain echocardiography: Rationale and design of a novel software toolbox. *Cardiovasc. Ultrasound*, vol. 6 (2008).

[63] Parsai C., Bijnens B., Sutherland G.R., Baltabaeva A., Claus P., Marciniak M., Paul V., Scheffer M., Donal E., Derumeaux G., and Anderson L. Toward understanding response to cardiac resynchronization therapy: Left ventricular dyssynchrony is only one of multiple mechanisms. *Eur. Heart J.*, vol. 30, 940–949 (2009).

[64] Doltra A., Bijnens B., Tolosana J.M., Borràs R., Khatib M., Penela D., De Caralt T.M., Castel M.Á., Berruezo A., Brugada J., Mont L., and Sitges M. Mechanical abnormalities detected with conventional echocardiography are associated with response and midterm survival in CRT. *JACC Cardiovasc. Imaging*, vol. 7 (2014).

[65] Walmsley J., Arts T., Derval N., Bordachar P., Cochet H., Ploux S., Prinzen F.W., Delhaas T., and Lumens J. Fast Simulation of Mechanical Heterogeneity in the Electrically Asynchronous Heart Using the MultiPatch Module. *PLoS Comput. Biol.*, vol. 11, 1–23 (2015).

[66] Albatat M., Arevalo H., Bergsland J., Strøm V., Balasingham I., and Odland H.H. Optimal pacing sites in cardiac resynchronization by left ventricular activation front analysis. *Comput. Biol. Med.*, vol. 128 (2021).

[67] Pluijmert M., Bovendeerd P.H., Lumens J., Vernooy K., Prinzen F.W., and Delhaas T. New insights from a computational model on the relation between pacing site and CRT response. *Europace*, vol. 18, iv94–iv103 (2016).

[68] Donal E., Hubert A., Le Rolle V., Leclercq C., Martins R., Mabo P., Galli E., and Hernandez A. New Multiparametric Analysis of Cardiac Dyssynchrony: Machine Learning and Prediction of Response to CRT. *JACC Cardiovasc. Imaging*, vol. 12, 1887–1888 (2019).

Chapter

4 Characterization of Responder Profiles for CRT Patient Selection

As mentioned before (Section 1.3.1), under some conditions, HF patients may benefit from CRT [1, 2]. However, the mechanisms of improvement of the left ventricle (LV) function with CRT are not yet elucidated. Around 20-30% of the eligible patients do not respond to this therapy [3–6]. Improvement of patient selection has been identified as an important factor associated with CRT response rate [1, 3, 7–9]. It is now recognized that a multiparametric approach, using Machine Learning (ML) algorithms based on a combination of echocardiographic and ECG features, could help to improve the identification of CRT responders [10–14]. Although ML provide good results, new tools are still required to assist feature selections, to optimize classification performances and to improve the interpretability of the approach while minimizing overfitting and limited robustness. In fact, LV strain curves reflect complex and multifactorial mechanisms that could be associated with electrical conduction delay, mechanical cardiac activity, and inter-regional interactions [15, 16]. Physiological models appear as efficient tools to integrate physiological knowledge, concerning mechanical properties, cardiac electrical activation, and blood circulation conditions.

The global methodology, presented in this chapter, is centered around an original explainable hybrid approach, combining in-silico and machine-learning models. First, a characterization of the CRT-eligible patient was proposed based on clinical and echocardiographic pre-implantation data. The obtained phenotypes have been improved by digital twins associated with the centroids. This study was presented at the *Computing in Cardiology* conference [17] with an oral presentation that won the *"Rosanna Degani Young Investigator"* first prize. Then another characterization of the CRT-eligible patient was proposed based on the physiological model-based parameters. On the third part of this chapter, CRT-response prediction was proposed, also based on hybrid approach, combining in-silico and machine-learning models.

This chapter is a good example of how we could combine a classical ML approaches based on data and signal processing with digital twin. This methodology adds physiological knowledge in one can consider as a black box approach.

4.1 Experimental data

Study population

The prospective database includes 250 patients from different centers in Europe (Belgium, Norway, France) who were eligible for CRT implantation based on current clinical guidelines. Clinical, electrocardiographic, and echocardiographic data were collected and systematically evaluated before CRT implantation and 6 months after implantation. Table 4.1 gathers the principal patient characteristics. Patients undergoing upgrades of pacemakers or implantable cardioverter-defibrillators were also included.

	Total *(N=250)*	**Responder** *(N=185)*	**Non-responder** *(N=65)*	**p-value**
Age	67.2 ± 10.9	67.2 ± 10.9	67.1 ± 10.8	0.96
Gender (male)	65.6%	60.0%	81.5%	0.002
Ischemic etiology	31.2%	23.2%	53.8%	< 0.001
Moderate to severe MR	9.6%	9.7%	9.2%	0.91
Diabetes mellitus	18.4%	15.7%	26.2%	0.07
Hypertension	30.8%	30.3%	32.3%	0.76
NYHA functional class	2.3 ± 0.7	2.3 ± 0.6	2.4 ± 0.8	0.26
Creatinine (μ mol)	92.2 ± 36.1	92.5 ± 33.5	91.5 ± 42.7	0.85
QRS duration (msec)	161 ± 23.0	163.7 ± 20.7	155.7 ± 27.7	0.015
LBBB	87.2%	91.4%	75.4 %	<0.001
Left atrial volume (mL/m2)	45.1 ± 16.1	43.8 ± 16.4	48.6 ± 14.9	0.04
LVEDV (mL)	216.2 ± 73.8	211.3± 75.6	230.1 ± 66.6	0.08
LVESV (mL)	156.8 ± 62.8	154.2 ± 63.7	164.2 ± 59.5	0.27
LVEF (%)	28.0 ± 6.6	27.9 ± 6.3	28.5 ± 7.3	0.51
SF	68.4%	82.7%	27.69%	<0.001
AR	65.2%	74.59%	38.46%	<0.001
E/e' ratio	13.9± 7.9	12.8 ± 7.7	17.1±7.8	<0.001
TAPSE	19.0 ± 5.1	19.6 ± 4.8	17.2± 5.5	<0.001
Right ventricular strain (%)	-15.5 ±10.1	-16.3±10.0	-13.1 ± 10.2	0.027
SPAP (mmHg)	21.6 ±20.6	21.7 ± 19.9	21.3 ± 22.6	0.90
GLS (%)	-8.6 ± 3.3	-9.0 ± 3.3	-7.3±2.7	<0.001
Dispersion (msec)	93.6 ± 49.0	96.6 ±46.0	85.1 ± 55.7	0.10

Table 4.1: Patient characteristics of the population (non-responders and responders). P-values from T-test and χ^2-test.

Responders were defined as having a $\geq$15% decrease in LV end-systolic volume at the 6-month follow-up, compared with baseline.

The study was carried out in accordance with the principles outlined in the Declaration of Helsinki and was approved by the local ethical committee of each center. All patients signed a written

informed consent before the participation to the study protocol.

Echocardiography

All patients underwent a standard Trans-Thoracic Echocardiography (TTE) using a Vivid S6, E7 or E9 ultrasound system (General Electric Healthcare, Horten, Norway). Images were recorded on a remote station for off-line analysis by dedicated software (EchoPAC PC, version BT 202, General Electric Healthcare, Horten, Norway). The experimental dataset includes the measured regional myocardial strain curves obtained by STE at transthoracic echocardiography in apical 4-chamber, 2-chamber, and 3-chamber views. Excel files of these 3 longitudinal strain view analyses were exported for a dedicated analysis performed in python language. Strain curve references were fixed at the onset of the QRS.

4.2 Feature extraction

Feature extraction was previously mentioned in Section 2.2.1 and was adapted from previous works of the team [18–20].

4.2.1 Clinical and echocardiographic features

Classical feature extraction was performed from clinical, electrocardiographic, and echocardiographic data, leading to a set of 26 features per patient :

- *gender, age,*
- *ischemic etiology, mitral regurgitation (moderate to severe), diabetes mellitus, hypertension, NYHA functional class, Creatinine,*
- *QRS duration, Left Bundle of Branch Block (LBBB),*
- *left atrial volume, LV end-diastolic volume, LV end-systolic volume, Left Ventricle Ejection Fraction (LVEF),*
- *septal flash, apical rocking,*
- *E/e' ratio, tricuspid annular plan systolic excursion (TAPSE), systolic pulmonary artery pressure (SPAP),*
- *right ventricular strain, global longitudinal strain (GLS), strain peak dispersion,*
- *global work, constructive work, wasted work, work efficiency.*

4.2.2 Feature extraction from strain curves

44 features were automatically extracted from longitudinal strain curves of the apical 4-chamber view only, according to the method defined by our team in [19]. Briefly, these features are based on estimation of the integral, or area under the curve, of each available segmental strain signal, on different time supports. To minimize the estimation error of these features, each strain curve

was up-sampled to 500 Hz. As performed in previous works, strain values between -5% and 5% were ignored from all calculations [10, 18, 21].

The first integral feature I^s_{avc} is calculated from the onset of the QRS to the instant of Aortic Valve Closure (AVC) of each segmental (s) strain curves. It represents a quantification of the cumulative strain developed by a given segment s, which effectively contributes to LV ejection. A second integral I^s_{peak} is calculated from the onset of the QRS to the strain peak. It represents the global cumulative strain developed by the contraction of the segment. The third integral is calculated as:

$$E^s = I^s_{peak} - I^s_{avc} \tag{4.1}$$

and corresponds thus to the integral between the strain peak and aortic valve closure. Negative values of this feature reflect a wasted cumulative strain, acting after AVC. This procedure (Figure 4.1) was applied to all segments of the 4-chamber view, for a total of 18 features. The onset of the QRS is used as reference for the calculation of all features.

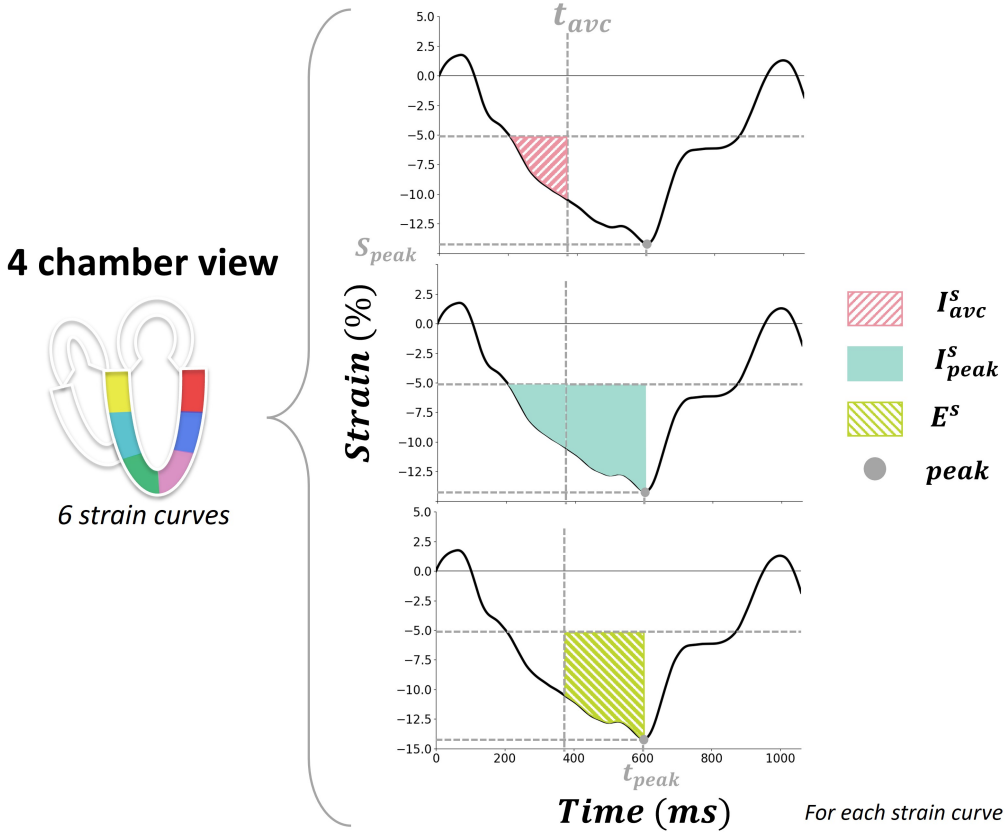

Figure 4.1: Strain integrals extraction on the 4-chamber view: I^s_{avc}, I^s_{peak} and its difference E^s delimited by the two timing: t_{avc} and t_{peak}.

Then, the mean of these different integrals ($Mean$) was calculated for each time support: I^{Mean}_{avc},

I_{peak}^{Mean} and E^{Mean}. The last set of features was based on the sums of integrals for the two walls, septal (S) and lateral (L): I_{avc}^{S}, I_{peak}^{S}, E^{S}, I_{avc}^{L}, I_{peak}^{L} and E^{L}. These features represent the cumulative strain from all segments of a given wall. The differences (D) of the cumulative strain of the two sides were then calculated:

$$I_{avc}^{D} = I_{avc}^{L} - I_{avc}^{S} \tag{4.2}$$

$$I_{peak}^{D} = I_{peak}^{L} - I_{peak}^{S} \tag{4.3}$$

$$E^{D} = E^{L} - E^{S} \tag{4.4}$$

Finally, the amplitude of the strain (S_{peak}^{s}), the time of the strain peak (t_{peak}^{s}) and their average on the 6 segmental strain curves were automatically extracted.

In a preprocessing phase, all the features were normalized with the standard score before the application of the clustering algorithm.

4.3 Patient-specific models

4.3.1 Model

The model presented in Chapter 3 was used in this work. As a reminder, it integrates four main sub-models:

1. The cardiac electrical system,
2. The right and left atria,
3. A multi-segment representation of the right and the left ventricles,
4. The systemic and pulmonary circulations.

This model has been validated on data from 20 LBBB and 10 healthy patients and fully described in Chapter 3.

4.3.2 Model specification/parameters identification

This identification was implemented with an EA. The same 113 parameters were involved, based on the previous model sensitivity analysis (Section 3.5.3). The EA chosen in this study was a Self-Adaptive Differential Evolution (SADE) algorithm [22] implemented with 4 islands, 15 individuals through 10 generations and 20 evolutions using the python library PyGMO (see Section 2.1.3). The EA process with the 4 islands is illustrated in Figure 4.2. The choice of parameters of crossover and mutation is directly integrated in the algorithm by an adaptive process [22].

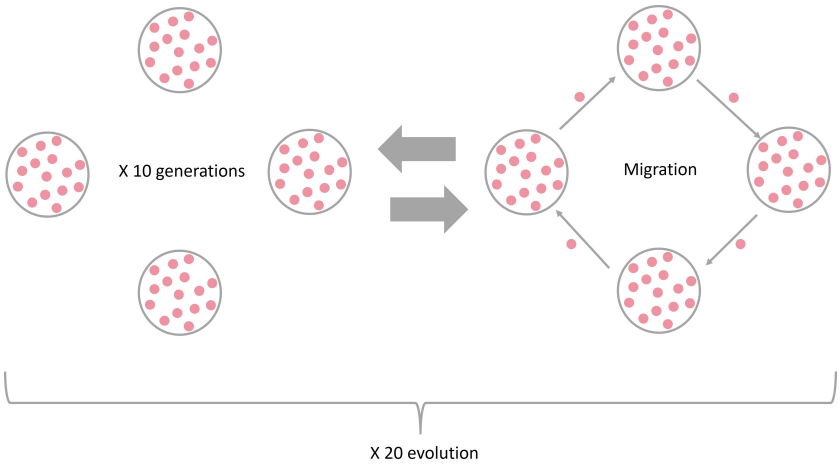

Figure 4.2: EA algorithm illustration with the 4 islands of 15 individuals and the 20 evolutions of 10 generations.

4.4 Characterization of responder profiles

In [18], our team proposed a multiparametric clustering method using clinical and echocardiographic data to group 250 CRT candidates based on their therapy response and outcomes. This approach identified specific CRT response subgroups and revealed how cardiac regional deformations, measured through strain integrals, may relate to response. However, interpreting the physiological implications of observed strain modifications remains challenging. Physiological model-based methods offer a promising solution to increase interpretability by providing parameters with direct physiological meaning.

In this section, we propose a method to improve the interpretability of the unsupervised clustering method previously proposed [18] through a digital twin approach, based on patient-specific model identification. Digital twins were proposed for the patients associated with cluster centroids, and the parameters reflecting physiological mechanisms were analyzed.

4.4.1 Method

i) Clustering analysis, based on clinical and echocardiographic pre-implantation data

The set of all features was clustered by applying the K-Means method [23]. This algorithm partition in K groups, named clusters based on common characteristics, and aim at minimizing within-cluster variances. The optimal number of clusters was determined using a Silhouette score and Inertia (defined in Section 2.3.2: Equation 2.12 and Equation 2.15). The algorithm was applied on the 250 patients with their 70 features. It was implemented in Python language using the Sklearn library [24].

Graphical representation: To visualize clustering results, a Principal Component Analysis (PCA) was performed after the clustering step. The PCA transforms the 70 dimensions space of the database in a 2 dimensions space to illustrate the different groups of patients.

Clusters analysis: A Wilcoxon test was applied to assess how the clusters differ from each other. The top-ranked features highlight the connection to the CRT response of a given cluster. These best ranked features were presented to underline the highest, medium, or lowest mean values compared to the rest of the database.

ii) Digital twin of patients associated with centroids

Personalized physiological models were proposed by identifying parameters for patients associated with centroids of each cluster. Parameters reflecting physiological mechanisms were analyzed and added to the cluster's profiles. Figure 4.3 illustrates this methodological approach.

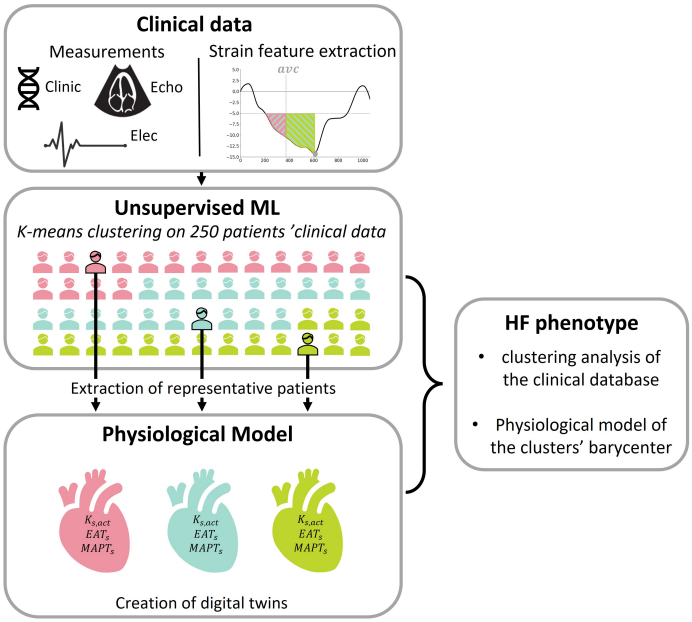

Figure 4.3: Methodological illustration of the digital twin patients associated with clusters' centroid.

Virtual patient representative: For each cluster, the proposed model was personalized to the patient closest to the cluster's centroid, which has the three-echo view available. Similarly to the previous chapter, the model personalizing was done by identifying model parameters. This identification was implemented with the same method presented in Section 4.3.2 with the same EA algorithm, error function (J_{error}), parameters identified and tuning.

Interpretable patient-specific features: The output features discussed in this study are the following:

- $K_{s,act}$ and $K_{s,pass}$: myocardial contractility and stiffness that describes quality of the myocardial tissue.
- EAT_s : electrical activation time.
- $MAPT_s$: mechanical activity peak time that is defined as the time of EMDF (Equation 3.3) curve maximum, considering the same bundle of His activation as reference.

The three first features were presented previously. The two first represented the tissue quality of each myocardial segment and were described in equations (Equation 3.4). They were directly identified by the EA. The two other features were extracted from patient-specific simulations of the electromechanical activity.

4.4.2 Results

i) Clustering analysis based on clinical and echocardiographic pre-implantation data

The clustering analysis was performed on the dataset of 70 features (26 classical clinical and echocardiographic features and 44 strain-extracted features) and 250 patients. The optimal number of clusters K=5 was obtained using the silhouette score and inertia (Figure 4.4). The optimal number of cluster must be in the elbow of these curves [25].

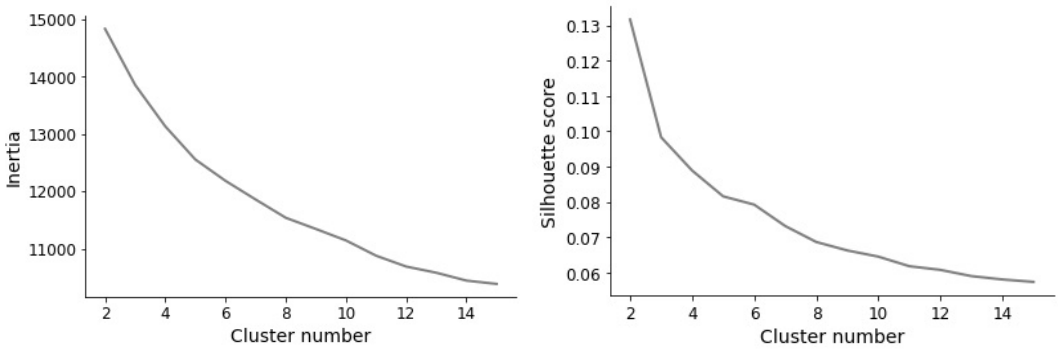

Figure 4.4: Inertia and silhouette score to choose the number of cluster K.

Table 4.2 gathers the responder rate ranging from 50% to 93% of CRT response and the most significant features of each cluster. Added to already known features for poor responder profile such as no septal flash or no apical rocking which are typical movement of the ventricle visible in echocardiography [1, 2, 26], the proposed integral features are noticeable in the main extracted features of the different clusters. For example, in most of the good responder phenogroups, the strain features associated with the lateral wall are discriminative: septal and mean minimum strain time, lateral integrals and integral difference ($t_{peak}^{...sept}$, t_{peak}^{Mean}, I_{avc}^{L}, I_{peak}^{L} , I_{avc}^{D}). This refers to the quality of the LV walls to provide enough work during systole despite the potential wall desynchronization.

Cluster 1 (50%)	**Cluster 2** (71%)	**Cluster 3** (72%)	**Cluster 4** (86%)	**Cluster 5** (93%)
$I_{avc}^{midinfsept}$	GLS	$I_{avc}^{midinfsept}$	t_{peak}^{Mean}	I_{avc}^{L}
I_{avc}^{D}	S_{peak}^{Mean}	I_{avc}^{S}	$t_{peak}^{midinfsept}$	I_{avc}^{D}
I_{peak}^{D}	I_{peak}^{Mean}	I_{avc}^{Mean}	$t_{peak}^{apiinfsept}$	$I_{avc}^{midantlat}$
$septal\ flash\ rate$	I_{peak}^{S}	$I_{peak}^{midinfsept}$	E^{Mean}	$I_{avc}^{apiantlat}$
I_{avc}^{L}	I_{avc}^{Mean}	I_{peak}^{S}	E^{S}	I_{peak}^{L}
$apical\ rocking\ rate$	$constructive\ work$	$I_{avc}^{basinfsep}$	$E^{midsept}$	$I_{avc}^{basantlat}$
I_{peak}^{L}	I_{avc}^{S}	S_{peak}^{Mean}	$E^{basinfsept}$	$I_{peak}^{midantlat}$
$I_{avc}^{midantlat}$	$I_{peak}^{midinfsept}$	$S_{peak}^{midinfsept}$	$male\ rate$	$S_{peak}^{midantlat}$

Table 4.2: Response rate (in %) for each of the five identified clusters and their most significant features, colored by relative value based on clusters analysis: High (green), medium (orange) and low (red).

Representation: Figure 4.5 represents the two first principal components of the PCA analysis of the database. These two first principal components explain 33.6% of the variance, with 23.4% for the first and 10.2% for the second. The five clusters of the study [18] are represented, as well as the CRT response of each patient. (The 5 clusters can already be distinguishing of the 2D PCA but even more in a 3D PCA with almost no overlapping, the 3D figure is provided in appendix file: Figure B.1).

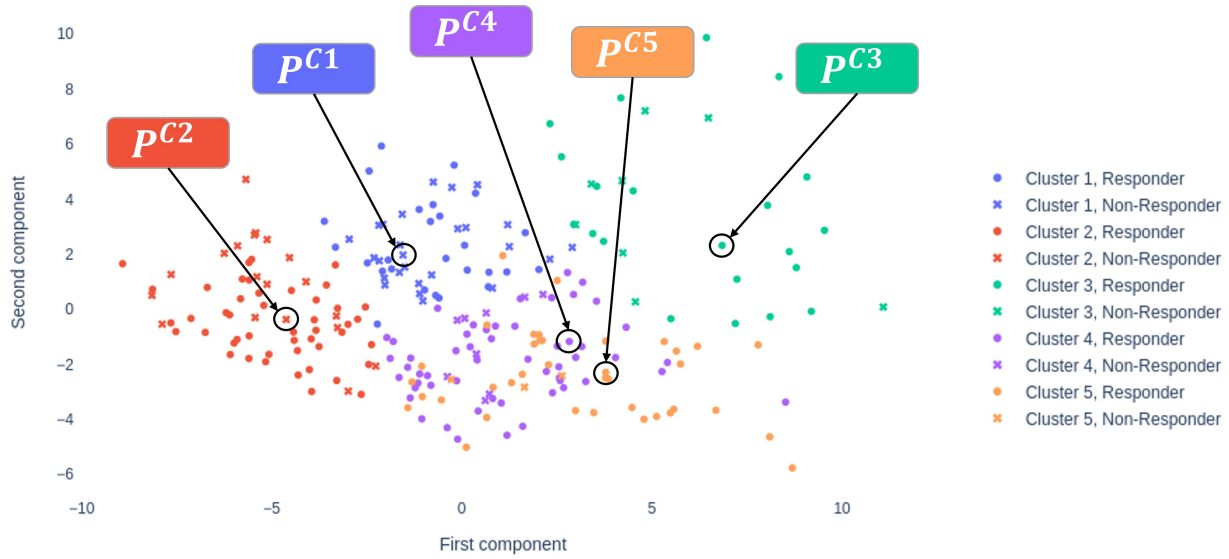

Figure 4.5: PCA visualization of the database of 250 patients colored by cluster and symbolized by their CRT responses (cross: non-responder, circle: responder). Patients closest to the centroids are circled in black.

Kaplan-Meier Analysis: Figure 4.6 displays Kaplan-Meier curves for event-free survival at 4 years. The overall adverse event rate was 22.8% and gathers events of death and hospitalization for heart failure. We can easily notice a difference of event rate between cluster 1 and 5 with

respectively 36.5% and 7.3% (p-value=0.003 between cluster 1 and 5 with a log-rank test) [18].

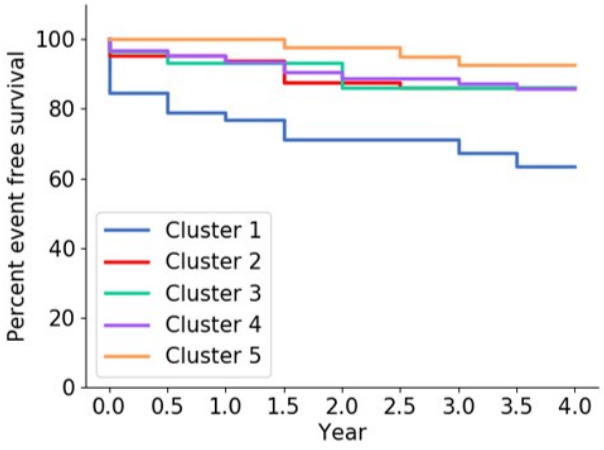

Figure 4.6: Kaplan-Meier survival curve at 4 years.

ii) Digital twin of patients associated with centroids

Parameters identifications and simulations

From the identification process, patient-specific model parameters were obtained for the 5 patients associated with each cluster centroid (circled in Figure 4.5). Patient-specific strain curves of these patients were simulated. Figure 4.7 presents the identified parameters and the comparison of experimental and simulated strain curves of the 16 LV segments. First, at the top of each patient box, the 16 experimental (*black*) and simulated (*colored*) strain curves are compared with a good fit. The mean mRMSE on the five patients is 3.97% ($\pm$ 1.74) and written on Figure 4.7 for the five patients with their mean identified contractility and electrical activation time. Although, for some patients, the strain morphologies are not completely reproduced for all the 16 curves, a close match was observed between the curve's patterns.

At the bottom, the interpretable patient-specific features, described in Section 4.4.1, are represented through bull-eyes diagrams (see Figure 3.2 numbering). Concerning the contractility, the 2 patients representing clusters with below-average rates (cluster 1 and 2) are associated with low values compared to other patients. Contractility values range are [13%; 45%], [11%; 47%] and [18%; 47%] respectively for the centroid patients of cluster 3, 4 and 5 who are responders to CRT. By comparison, the contractility of clusters 1 and 2 patients (non-responders) is clearly lower with range of [12%; 25%], [6%; 25%]. Low contractility in LV septal part could inhibit contraction mechanism and its propagation in the rest of the ventricle.

Larger stiffness was noticed in the cluster 1's patients with a mean value over the 16 segments equal to 64.0% compared to the cluster 2's patients with 60.5%. The increase of stiffness could generally be linked to degradation of the diastolic dysfunction. Cluster 3 and 4 present reduced

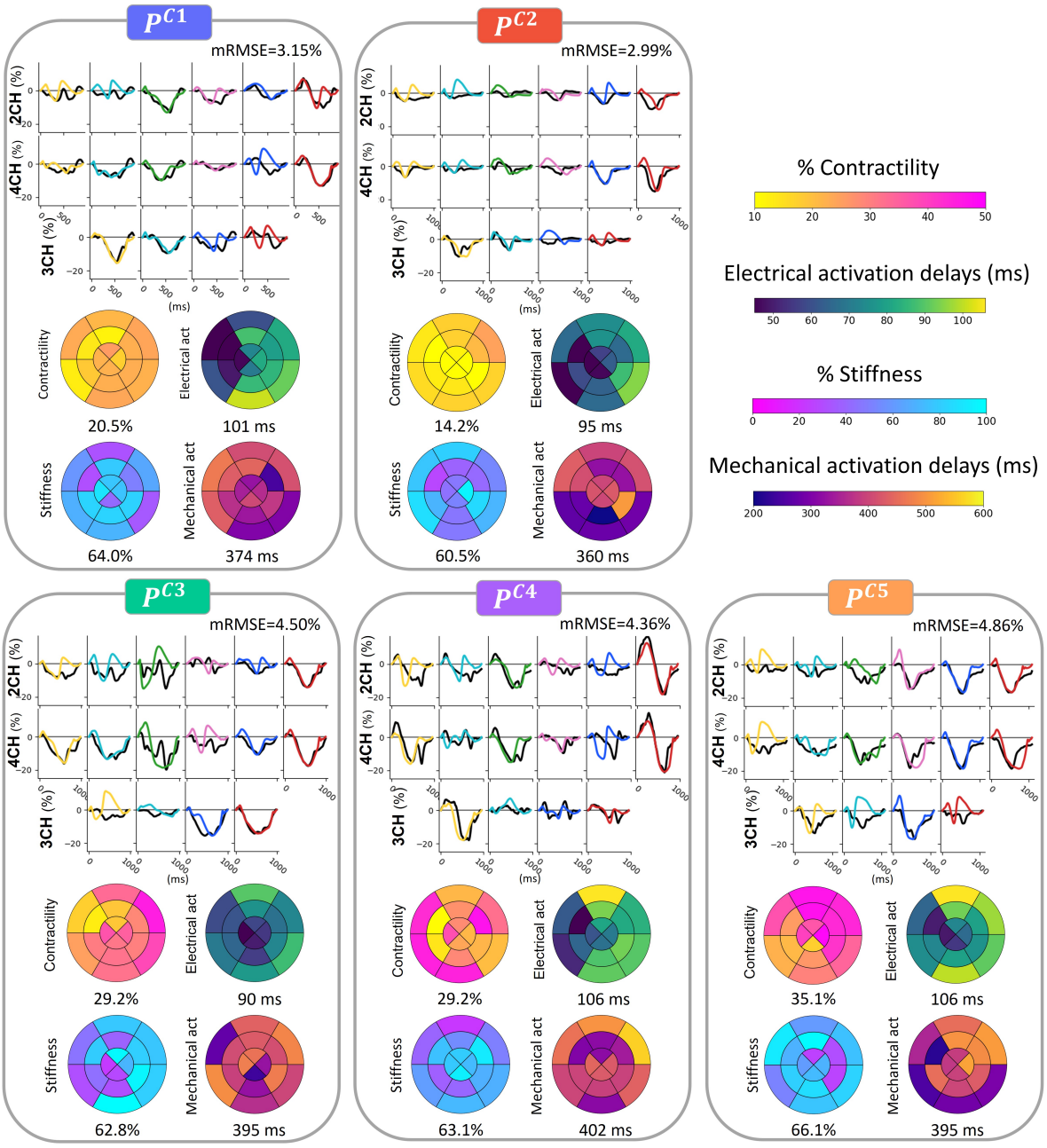

Figure 4.7: Comparison of the 16 experimental (*black*) and simulated (*colored*) strain curves for each of the 5 patients with the mRMSE on the 16 curves. The identified model parameters are represented in bull'eye: contractility (*yellow-pink*), electrical activation time (*blue-yellow*), stiffness (*pink-cyan*), and mechanical activation time (*purple-yellow*) with the mean value written below.

values (respectively 62.8% and 63.1%). Concerning specifically cluster 5, stiffness presents globally higher values (66.1%).

Concerning electrical activation times, clusters 4 and 5 show an earlier activation of the septal wall and an extended lateral activation compared to clusters 1, 2 and 3. LV electrical delays

associated with clusters 4 and 5 are also slightly higher than the other clusters with a maximum electrical activation time of 106 ms for these two clusters against 101, 95 and 90 ms for the cluster 1, 2 and 3 respectively.

The mechanical activity peak is slightly delayed in the three responder patient simulations with mean $MAPT_s$ equal to 395, 402 and 395 ms for the cluster 3, 4 and 5 respectively. In the two other clusters, the mean mechanical activity peak times are 374 and 360 ms for patient of cluster 1 and 2. For these patients, the septal segments' activation arrived later than the one located on the lateral part of the LV (mean septal $MAPT_s$ respectively equal to 410 ms and 362 ms), while an early septal mechanical activity peak was noticed for cluster 5: 332 ms.

4.4.3 Discussion

The main contribution of this work consists in combining unsupervised clustering and patient-specific physiological modeling for the analysis of response profiles to CRT. This original methodology was declined in different applications. First, five clusters, defining groups of below-average to excellent responders, were defined based on clinical and echocardiographic pre-implantation data. Then, patients associated with centroids of each cluster were considered to propose five patient-specific models. The identified parameters of these five digital twins provide a direct physiological interpretation of strain curve morphologies.

These study aims at providing characterization of CRT eligible patient by proposing different patient profiles with more or less risks of non-response.

i) Clustering analysis, based on clinical and echocardiographic pre-implantation data

In [18], our team has shown that unsupervised machine learning could be used to integrate echocardiographic, ECG and clinical data to phenotype HF patients and their responses to CRT. Results allows for the identification of groups of different response rates, ranging from below-average to above-average, in comparison with response rate described in the literature [6]. Cluster 1 and 2, which are the two groups with below-average rate, are associated with low strain integral values and work as well as a reduced proportion of septal flash and apical rocking. The other clusters with normal or elevated response rates present higher strain integral values, with strain with larger amplitudes. To be more specific, in the best cluster (cluster 5), strain morphology shows a typical LBBB activation pattern with early stretching of the lateral wall and early shortening of the septal wall. This characteristic pattern has been shown to be associated with an improved prognosis after CRT [27].

The advantage of using unsupervised ML is that, unless using hypothesis driven, as classically used, this approach is data driven and hypothesis free. In comparison to other clustering

approaches [14], the proposed method allows for the quantitative analysis of left ventricular mechanics, through the evaluation of strain integrals [18, 19]. Although these features could be related to myocardial contraction, direct physiological interpretation remains difficult only based on clustering results.

ii) Digital twin of patients associated with centroids

Added physiological based explanations with personalized models [28, 29] helps to provide a fine-tuned understanding of the cardiovascular behaviors associated with each cluster, by explicitly representing the underlying physiological mechanisms. In fact, identified parameters provide additional information on the regional electrical and mechanical LV functions. Electrical conduction delays, mechanical activity peak time, stiffness and contractile levels appears as particularly relevant to strain curves morphology. Contractility parameter is especially interesting because it could be associated to potential area of damaged tissues or scars.

Clusters 1 and 2, defined by below-average response rates to CRT, are associated with reduced myocardial contractility parameters, as illustrated on bull-eyes obtained from the model (Figure 4.7). In fact, total myocardial scar or located in the posterolateral wall are associated with non-response to CRT [30]. Aalen et al. in [31] also demonstrate that myocardial viability and particularly the septal viability is an indicator of CRT response.

Myocardial stiffness is more elevated in cluster 1 in comparison with cluster 2. A stiff heart links to degradation of the diastolic dysfunction [32] that was recently associated to worst-prognostic CRT candidate [33]. Concerning mechanical activation delays, late septum activations, compared to their lateral wall, were observed for these two clusters. In fact, several studies [34–36] have shown that septal and lateral activations, that differ from typical LBBB patterns, are mainly associated with bad CRT responses.

Patient-specific models of the other clusters present more elevated contractilities and elevated electrical activation delays, that better corresponds to pure electrical dyssynchrony. In responder patients (3, 4 and 5), early mechanical activation of the septal segments (added to a preserved contractility) was identified and represent typical LBBB pattern and/or presence of septal flash, well known to be a CRT response indicator [37]. Furthermore, this kind of impaired electromechanical substrate has been shown to be beneficial to CRT response [36, 38].

Concerning specifically the best responder (cluster 5), stiffness values appear as more elevated than other clusters. We hypothesize that myocardial stiffness is compensated by a well-preserved contractility and large electrical activation time resolved by CRT stimulation. In fact, [39] proved that E/e' ratio, a parameter used to estimate diastolic dysfunction, has a less predictive value on CRT response than others parameters such as SF and AR (usually associated with contractility) [34].

4.5 Characterization of responder profiles based on the digital twin database

Contrary to the previous clustering, based on clinical and echocardiographic pre-implantation data, this clustering was based on the model-based parameters. The physiological model parameters used to create each digital twin constituted a new database and were used as inputs of the clustering. Due to the lack of all the strain echo views, this characterization will be done on 162 of the 250 patients of this database.

4.5.1 Method

Figure 4.8 illustrates the methodological approach. 162 patients were involved in this study and a digital twin was created for each of them. The identified parameters of the digital twins were then used as inputs of the clustering

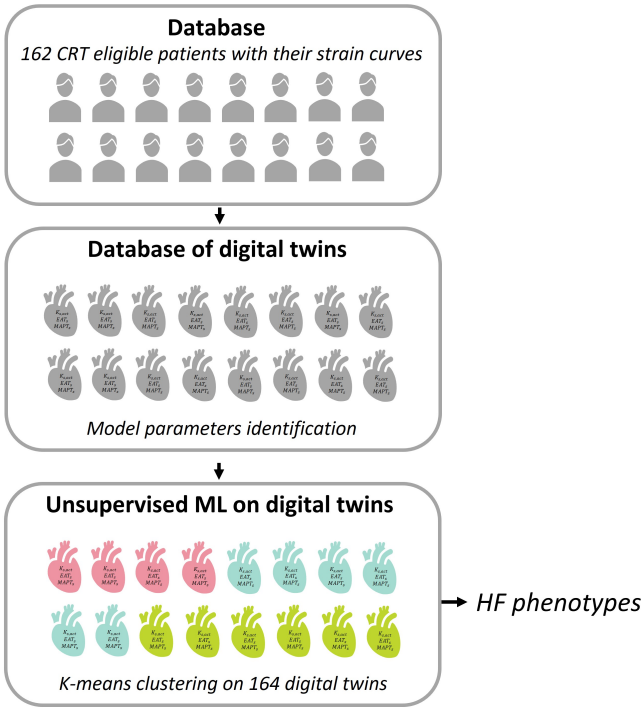

Figure 4.8: Methodological illustration of the clustering analysis on the physiological model-based parameters.

Parameter space

The database now contains 145 model-extracted features. The interpretable features: $K_{s,act}$, $K_{s,pass}$, EAT_s and $MAPT_s$, previously mentioned for each of the 16 segments (s) were used. Some more specific identified parameters were also extracted from the digital twins:

- The parameters involve in the EMDF (Equation 3.3) of each segment: $n_{1,s}$, $n_{2,s}$, $\alpha_{1,s}$, $\alpha_{2,s}$.

– The electrical depolarization time of each segment and the one of the LBB: UDP^{s} and UDP^{LBB}.

In order to visualize the distribution of the different interpretable parameters on each cluster, the average was calculated over all the patient of a same cluster, for each parameter type and for each segment. This computation provides four mean bull eyes for each cluster, one for each parameter type.

To visualized and extract variability of this data set of 145 model-extracted features, a Principal Component Analysis (PCA) was applied.

Clustering

The set of all model-extracted features was clustered by applying the K-Means method [23].

The optimal number of clusters was determined using a Silhouette score and Inertia (defined in Section 2.3.2: Equation 2.12 and Equation 2.15). As before, the clustering was performed before PCA to offer more interpretability and provide a comprehensive report on the role of the different features.

Clusters analysis: A Wilcoxon test was applied to assess how the clusters differ from each others. The top-ranked features highlight the connection to the CRT response of a given cluster.

4.5.2 Results

Model parameter identification and simulations

For each of the 162 patients, 113 parameters were identified to obtain a digital twin. Patient specific strain curves of these patients were simulated from these digital twins. Although, for some patients, the strain morphologies are not completely reproduced for all the 16 curves, a close match was observed between the curves patterns. The mean mRMSE between the 16 simulated and experimental strain curves on the 162 patients is 4.48% ($\pm$ 1.08). The 162 digital twin simulations, separated by cluster, are provided in Appendix B (Figure B.2, Figure B.3, Figure B.4, Figure B.5 and Figure B.6)

A statistical study of all the identified parameters was proposed in Table 4.3. For 17 of the 145 features, there is a significant difference between the population of responder and non-responder (p-value < 0.05).

– 7 are model parameters or extracted features involved in the EMDF (1 $MAPT_s$, 1 $\alpha_{2,s}$, 3 $n_{1,s}$, 2 $n_{2,s}$).
– 9 are tissue quality model parameters (6 $K_{s,act}$ and 3 $K_{s,pass}$).
– 1 are electrical model parameters or extracted features ($UDP^{BasalAntLat}$).

13 of these 17 features are segments of the 4-chamber view.

Parameters	Non-responder	Responder	p-value
$K_{ApiLat,pass}$	73.2%	56.8%	$<$0.001
$K_{ApiLat,act}$	20.9%	28.1%	$<$0.001
$K_{MidAntLat,act}$	21.5%	27.3%	$<$0.001
$K_{MidAntSept,act}$	18.2%	23.2%	0.004
$K_{BasalAntLat,pass}$	61.0%	49.2%	0.005
$K_{ApiSept,act}$	21.8%	27.0%	0.005
$\alpha_{2,BasalInfSept}$	0.44	0.40	0.01
$UDP^{BasalAntSept}$	13.0 ms	16.2 ms	0.01
$n_{1,ApiSept}$	1.32	1.15	0.02
$n_{2,MidAntLat}$	8.91	9.96	0.02
$n_{1,MidInfSept}$	1.31	1.16	0.02
$MAPT_{BasalInfSept}$	365 ms	332 ms	0.03
$K_{BasalInfLat,pass}$	68.2%	61.0%	0.04
$K_{ApiInf,act}$	26.3%	30.0%	0.04
$n_{1,ApiAnt}$	1.33	1.19	0.04
$K_{MidInf,act}$	25.4	28.6	0.04
$n_{2,MidAntSept}$	9.49	10.3	0.04

Table 4.3: T-test on the 145 identified and extracted features of the model over the 162 patients. Only the ones with a p-value $<$0.5 are presented here.

Clustering

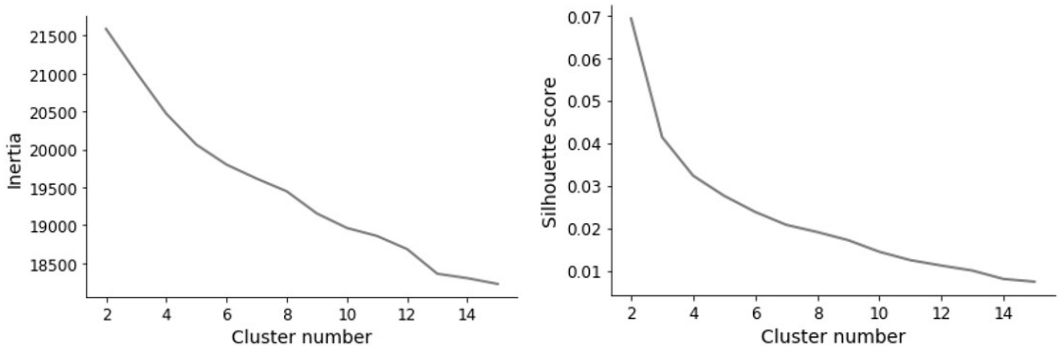

Figure 4.9: Inertia and silhouette score to choose the number of cluster K on the identified parameters' base.

The clustering analysis was performed on the identified parameter dataset of the 162 patients. The optimal number of clusters was also K=5, based on the silhouette score and inertia (Figure 4.9).

Figure 4.10 represents the three first principal components of the PCA analysis of the database. The five clusters of the study are represented, as well as the CRT response of each patient. A 3D

representation was preferred to better visualize the separation of the five clusters, less noticeable in 2D. The three first principal components represent 21.5% of the variance (12.0% for the first, 5.4% for the second and 4.1% for the third).

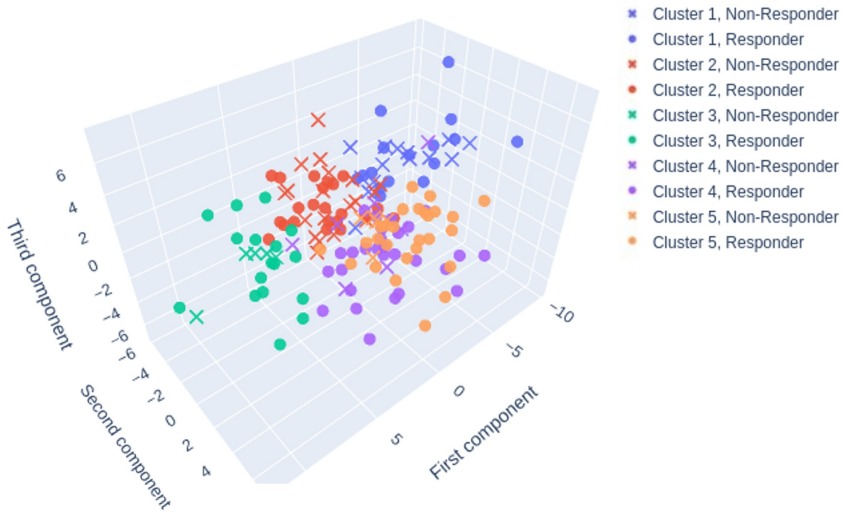

Figure 4.10: PCA visualization of the parameters' base of 162 patients colored by cluster and symbolized by their CRT response (cross: non-responder, circle: responder).

The responder rate ranges from 52% to 84% of CRT response (52%, 54%, 77%, 78% and 84%). Figure 4.11 presents the average interpretable patient-specific features in bull eyes representation for the five clusters.

Concerning the first row (K_{act}: contractility), the two "best" clusters in terms of CRT response present higher identified values. Their mean values over the 16 segments are 33.0% and 27.8%, respectively, for cluster 4 and 5. By comparison, the three cluster with the lower CRT response rate present smaller contractility values with 22.5%, 22.8% and 23.4% mean value for cluster 1, 2 and 3.

Larger electrical activation times were noticed in cluster 1 and 5 with means over the 16 segments of the average bull eye of 82.0 ms and 88.4 ms respectively. This confirms the hypothesis that not only the electrical behavior must be considered. A preserve myocardial tissue must be present to ensure effective stimulation of the CRT device. The three other cluster's bull eyes have mean value of 69.1 ms, 55.8 ms and, 69.2 ms for the second, third, and fourth respectively.

Concerning the stiffness, the mean of the average bull eye is similar over the five clusters: 62.4%, 62.4%, 61.7%, 56.4%, 61.2%.

The peak of the mechanical activity is well delayed for the cluster 1 and 5 with 450 ms and 387 ms. It is consistent with the electrical activation time also delayed for these two clusters. The cluster 3 mean $MAPT_s$ are extremely well-preserved and could explain the not so bad CRT response despite a damage contractility.

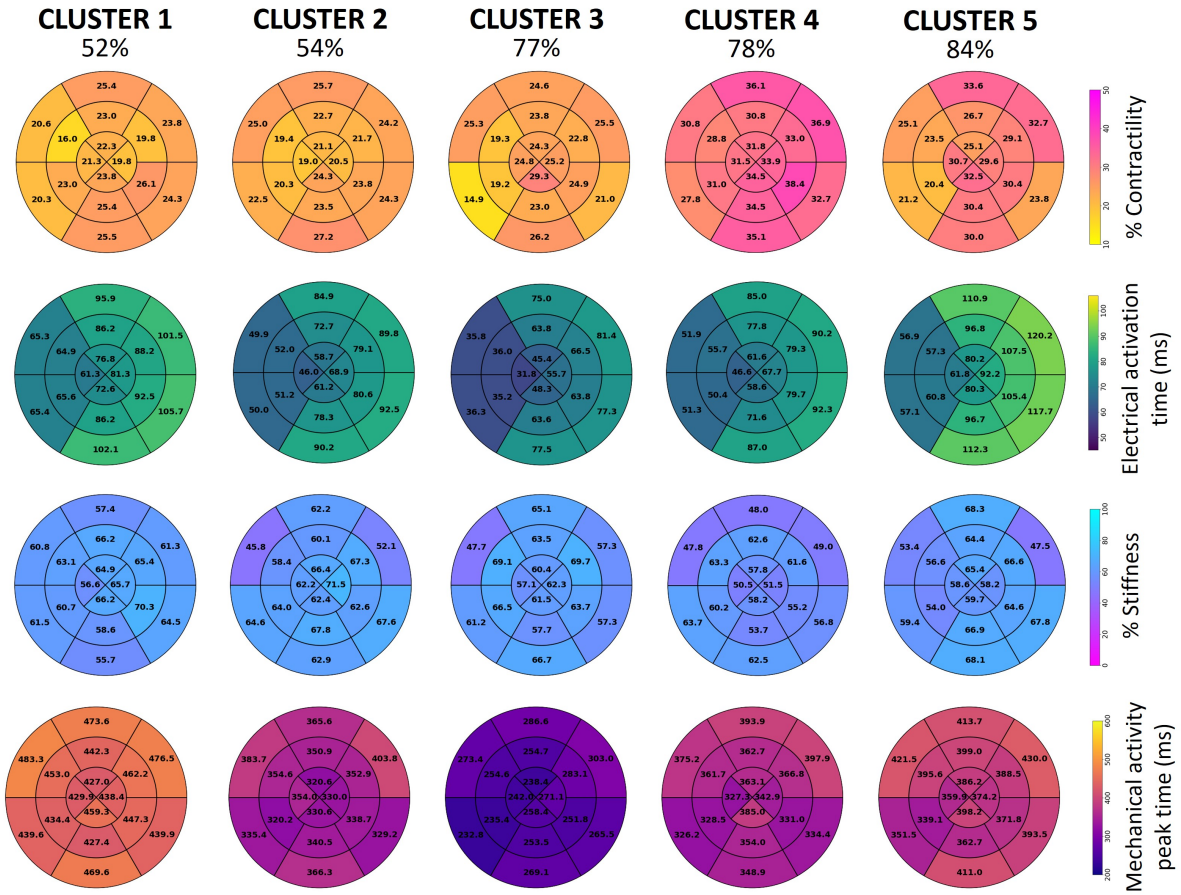

Figure 4.11: Average bull eyes of the interpretable patient-specific features of the five clusters: contractility (*yellow-pink*), electrical activation time (*blue-yellow*), stiffness (*pink-cyan*), and mechanical activation delay (*purple-yellow*) with their response rate.

4.5.3 Discussion

In this section, the process was brought further. CRT patient phenotyping, only based on the digital twins, were created thanks patient strains with hypothesis-free on CRT response markers. The two first clusters present a below average response rate and with the third one, they present low values of identified contractility. The two other clusters (cluster 4 and 5) with normal or elevated response rates present higher contractility values. Added to that, we can notice larger electrical activation time in the best cluster (cluster 5). This confirms that not only the electrical markers must be considered in the CRT selection. The quality of the tissue, well underlined by the identified parameters of the digital twins, must be considered as it is essential to an efficient CRT stimulation. In fact, if the CRT device leads are set on necrotic tissues/scar zones, the electrical signal could be impaired [40–42].

If we look at the statistics tests, we can notice that the features with the smallest p-value

are the one that described the tissue quality and the one involved in the electromechanical coupling. $K_{ApiLat,pass}$, $K_{ApiLat,act}$ and $K_{MidAntLat,act}$ present p-value $<$0.001 and represent active and passive ability of three lateral segments to contract (Table 4.3). The contractility parameters of the myocardium are better preserved for responder patients, and passivity parameters are also lower. In the same idea, the mechanical activity peak time $MAPT_s$ are also less delayed in responder patient. These model parameters and extracted features confirm that the contractile levels within the myocardium must be considered and are well link with the ischemic proportion of non-responder patient (p-value = 0.0001). In fact, A stiff heart links to degradation of the diastolic dysfunction [32] that was recently associated to a worst-prognostic CRT candidate [33]. Myocardial viability was demonstrated to be a CRT-response indicator in [31] and particularly the septal viability of the myocardium.

This second section aims at going deeper in the characterization of CRT eligible by providing understandable features to provide direct physiological interpretation of strain curve morphologies. The digital twin proposed could be a way to specifically understand the electromechanical coupling of the different LV regions of a patient. Then, referring to the clustering and/or this database, decide or not of the therapy given the CRT response of the closest neighbor(s) or cluster. To our knowledge, this is the first time ML approaches were applied on a digital twin database created thank to experimental strain curves. Recent studies proposed digital/virtual patient cohort, but without any patient experimental data [43, 44]

4.6 Prediction of response to CRT

A best selection of patients before implantation is essential to improve the individual quality of care and prevent the risk of non-justified complications. In the last years, significant research activities have been addressed at disclosing the biological, electrical, and mechanical aspect of CRT inefficiency, in order to improve patient selection and CRT response [1, 3, 7–9]. However, the selection of candidates for resynchronization therapy and the follow-up of implanted patients still remains challenging because it depends on several factors including clinical characteristics, typical ventricular conduction disturbances, and the evaluation of the specific electromechanical substrate responsible for LV discoordination. The objective of this section is to propose, a multiparametric evaluation, based on the combination of data-driven and model based features, to improve the prediction of response to CRT. First, a CRT response classifier train on pre-operative data was proposed. Then the same classifier was then trained on digital twin extracted features.

4.6.1 Method

The same part of the prospective database, including the 162 CRT eligible patients from two centers in Europe, were used. The same clinical, electrocardiographic, and echocardiographic data were collected as well as the strain extracted features. The creation of the digital twins was

performed thanks to a model parameter identification process, as described in Section 4.3.2. The same EA algorithm, error function (J_{error}), parameters identified and tuning were used.

Supervised machine learning algorithm

Feature selection: Feature selection is a preliminary step that measures the strength of the relationship of the variables with the event. It aims at keeping a reduced set of the most meaningful feature to build the final model. In this study, the feature selection was done using a 'Out-Of-Bag' (OOB) feature importance analysis on the random forest classifier with the "Gini" importance criteria [45].

Among the selected features, a high correlation was found between some features (correlation index > 0.7) and only the features presenting the highest relative importance were kept for further analysis after ensuring that it would not affect the model's performance by testing with and without it.

After this step, the features are ordered by importance and "redundant" features are removed. We can then iterate on the number of features to create the Random Forest (RF) model [46].

Ensemble classification algorithm: The classifier used in this study is a RF. It is an ensemble method that averages the independent prediction of numerous decision trees created on a subset of features. The number of trees is a hyperparameter of the algorithm that must be tuned [47].

Proposed approach

In this study, we wanted to propose a CRT response classifier. The same classification algorithm was applied on two categories of features : 1) The first one is clinical and echocardiographic pre-implantation data presented in the previous study with strain extracted features, 2) The second one is composed of model-extracted features (identified model parameters or feature extracted of the patient specific model simulation) of the 162 digital twins. Figure 4.12 presents the different step of the classifier creation. The global performance was assessed by a repetitive cross-validation method, which randomly selects at each round 80% of the population to be trained (training dataset) and 20% to be tested (test dataset).

4.6.2 Results

Supervised ML on features extracted from data

Feature selection

The 70 features extracted from data were included in the following process. First, they were order by importance (RF classifier feature importance or Gini importance). Then, the RF classifier

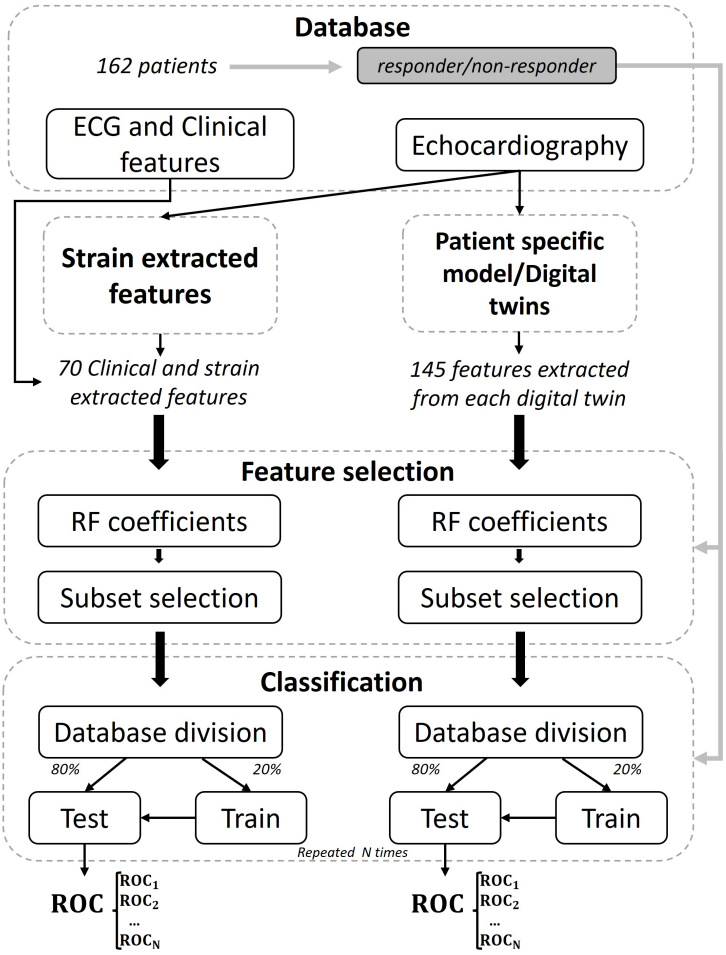

Figure 4.12: Methodological illustration of the CRT response prediction approach.

was iteratively test with the first i features (ordered by importance). The AUC results of these iterations are plotted in Figure 4.13. 9 features were selected to be used in the classifier.

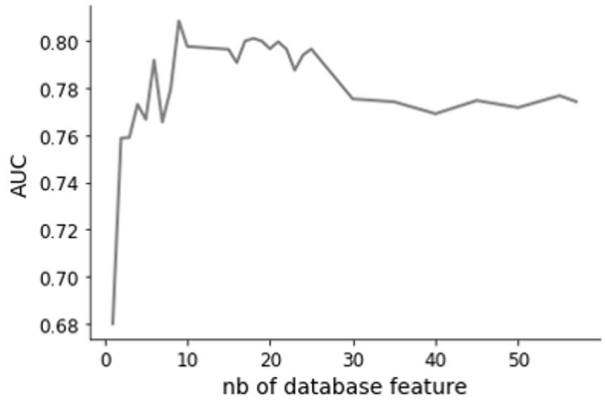

Figure 4.13: Choice of the number of features in the list of the feature importance from data. The AUC is computed on 200 repetitions of test datasets.

Figure 4.14 shows the 9 most important features selected after this features selection step:

- 7 are strain extracted features: integrals ($I^s_{peak/avc}$), strain maximum amplitude (S^s_{peak}) and strain peak time (t^s_{peak}),
- 2 are classic echocardiographic features.

Concerning the localization of the parameter segments, they are mostly features extracted from lateral and septal segments.

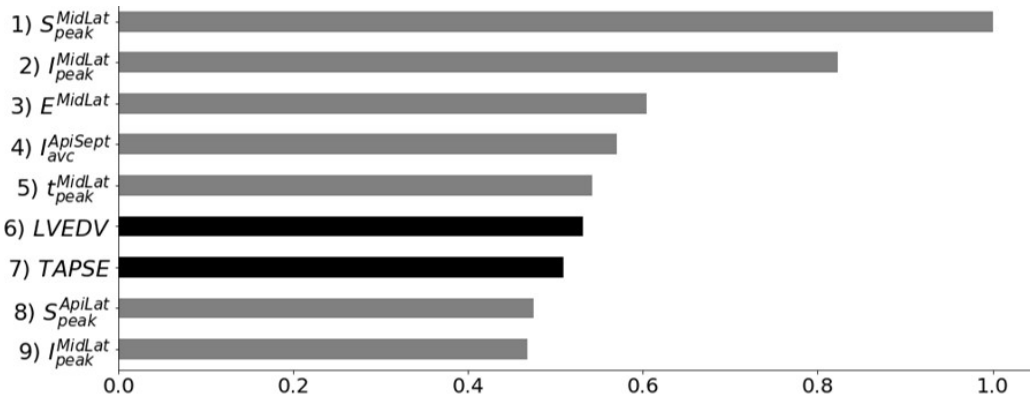

Figure 4.14: List of the 9 first features from data order by importance, the correlated features were removed. Color code: strain extracted features (*gray*) and classic echocardiographic features (*black*): Tricuspid Annular Plane Systolic Excursion (TAPSE) and Left ventricle End-Diastolic Volume (LVEDV).

Ensemble classification results

Figure 4.15 represent the process of RF hyperparameters choice. To choose the number of estimators (trees) to use in the classifier, the AUC value was computed for 2 to 550 estimators. Thus, 500 estimators were chosen for this study. The deepness of the tree was also tested, but the default mode was the best. The default parameterization of the tree deepness is to extend the nodes until all leaves are pure.

Figure 4.16 shows the Area Under Curve (AUC) for the prediction of response to the CRT. After 200 cross validation rounds, the predictive performance was good with a final AUC of 0.81 ± 0.07. The optimal threshold was taken to maximize the geometric mean of sensitivity and specificity (known as G-mean: Equation 2.11) with a sensitivity = 0.75 and a specificity = 0.72.

Supervised ML on model-based extracted features

Feature selection

From the identification process, as mentioned in Section 4.4, 145 model-based extracted features could be extracted from the 162 digital twins.

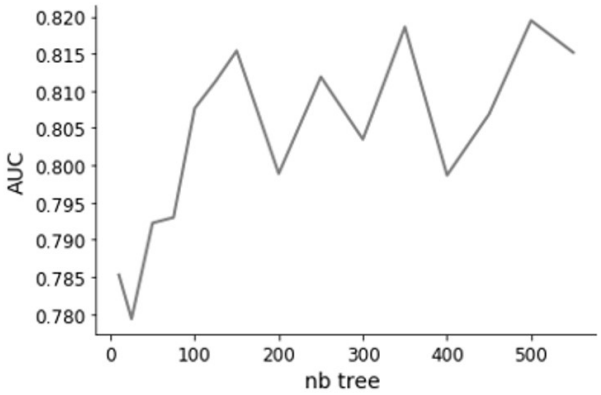

Figure 4.15: Choice of the number of trees/estimators. The AUC is computed on 200 repetitions of test datasets.

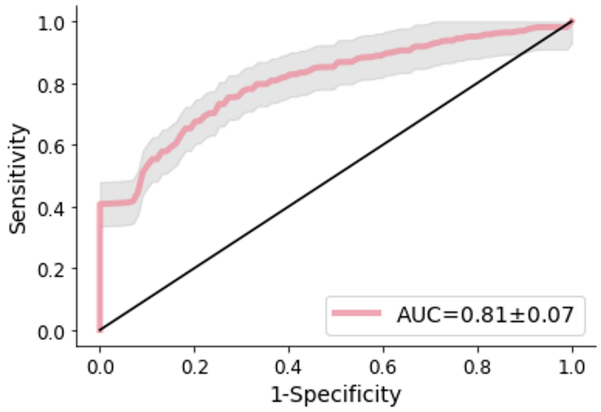

Figure 4.16: ROC curve of the RF classifier on features extracted from data with the 9 first features, 500 estimators and 200 cross-validation repeats. The AUC is computed on the 200 test datasets.

As already described, the number of features used in the classifier was determined by iteratively test i features, (order by importance). The AUC results of these iterations are plotted in Figure 4.17.

Figure 4.18 shows the 22 most important features selected after this features selection step:

- 10 are model parameters or extracted features involved in the EMDF,
- 9 are tissue quality model parameters,
- 3 are electrical model parameters or extracted features.

Concerning the localization of the parameter segments, they are mostly parameters or features extracted from lateral and septal segments. Moreover, the basal layer of the LV are more represented in these 22 selected features.

Ensemble classification results

Figure 4.19 represent the process of RF hyperparameters choice. The same process was applied, and 500 estimators were chosen for this study. The deepness of the tree was also tested, but the

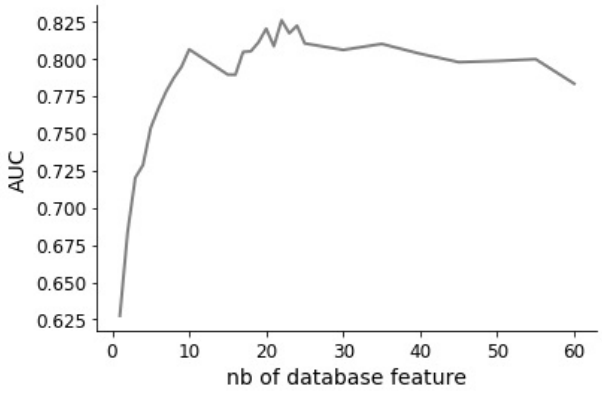

Figure 4.17: Choice of the number of features in the list of the feature importance from model. The AUC is computed on 200 repetitions of test datasets.

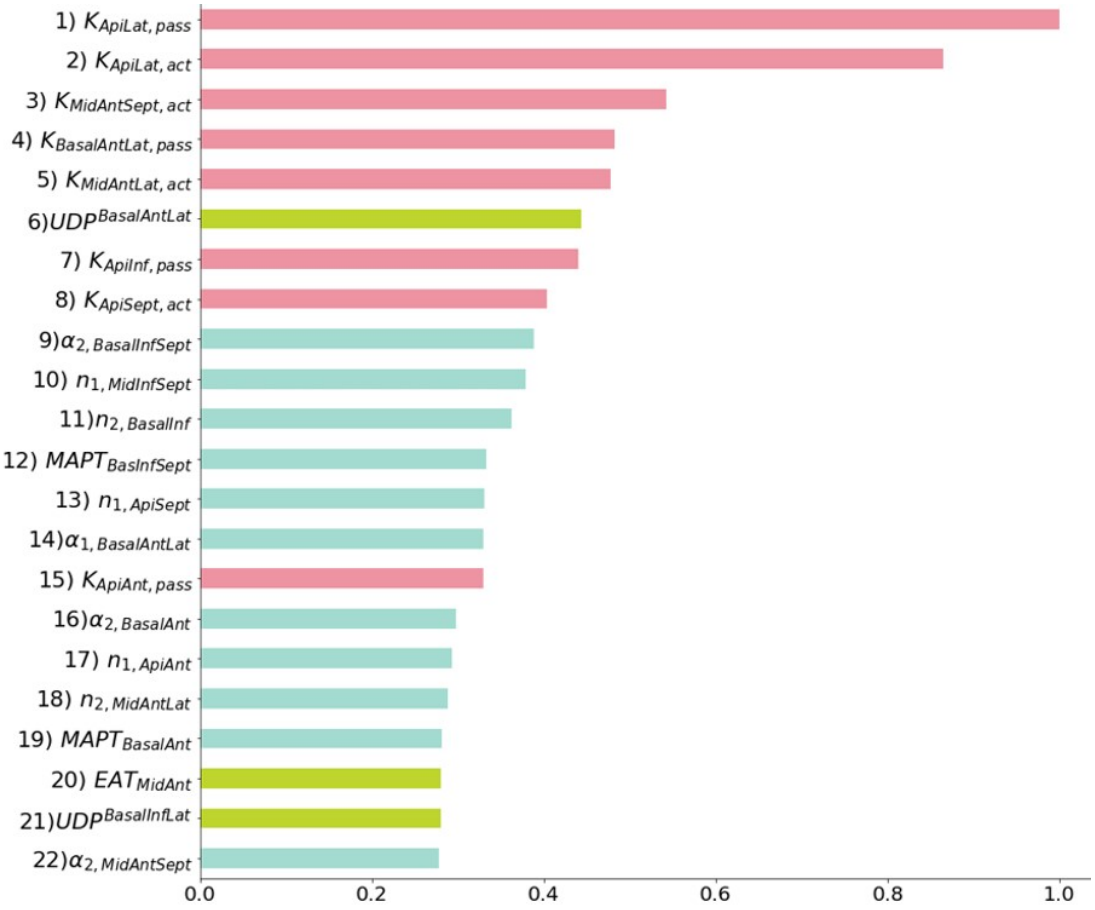

Figure 4.18: List of the 22 first model extracted features ordered by importance, the correlated features were removed. Color code: tissue quality parameters (*pink*), electrical parameters or extracted features (*green*) and parameters or extracted features involved in the EMDF (*blue*).

default mode was the best.

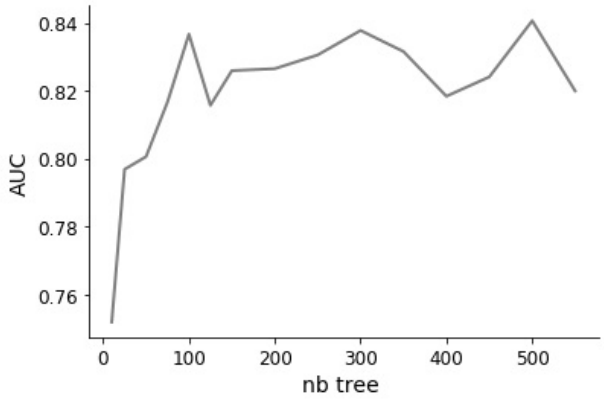

Figure 4.19: Choice of the number of trees/estimators. The AUC is computed on 200 repetitions of test datasets.

Figure 4.20 shows the Area Under Curve (AUC) for the prediction of response to the CRT. After 200 cross validation rounds, the predictive performance was excellent with a final AUC of 0.86 ± 0.07. The optimal threshold was taken to maximize the geometric mean of sensitivity and specificity (known as G-mean: Equation 2.11) with a sensitivity = 0.74 and a specificity = 0.82.

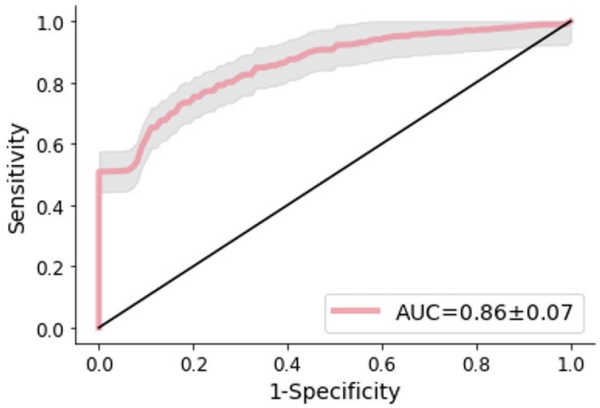

Figure 4.20: ROC curve of the RF classifier on model-extracted features with the 22 first features, 500 estimators and 200 cross-validation repeats. The AUC is computed on the 200 test datasets.

4.6.3 Discussion

The main contribution of this work is the analysis of the added-value of model-based features to predict CRT response. For this purpose, a complete digital twin database was created based on a clinical database of CRT candidates. A hybrid explainable pipeline, combining in-silico and supervised ML models, was proposed.

This classifier turned out to be more efficient than the one created based on the features extracted from clinical and echocardiographic pre-implantation data. Moreover, the strain extracted features

seems to have a positive effect on the prediction compare to the literature that are principally based on a reduce number of clinical available features [13, 21, 48, 49]. However, these predictor models are hard to compare due to the different data and features used as inputs and the criteria of CRT response or endpoint [50].

As an extension of the previous part, the following step was to predict the response of CRT eligible patients based on their digital twins. A classical machine learning classifier was put in place and provided very interesting result but in addition to the classification, the feature selection is an extra value. In fact, by providing the importance of the digital twin extracted features in the classification, this demonstrates the informative quality of the features. Electrical parameters, tissue quality parameters and parameters involved in the EMDF are all represented in the feature importance analyses and the statistical test. In the RF-based feature importance estimation, half of the twenty-two-first features are model parameters or simulation extracted features involved in the electromechanical coupling. These twenty-two features are not particularly correlated to each other (<0.6).

In this study, we can notice that lateral and septal segment are overrepresented in the most important features. This confirms the fact that these two walls analyzed thanks to the 4-chambers views in echocardiography must be prioritized during the selection of CRT eligible patients and specially their asynchrony [10, 51–53]. Cikes et al. [14] stated that individuals who do not respond to CRT typically exhibit low strain in the apical septal region. This observation aligns with the fact that the septal segments, tend to experience the highest rebound stretch. In simpler terms, the lack of effectiveness in myocardial systolic strain is most pronounced in these segments [54].

A combination of the clinical, strain-extracted and model-based features were tested as inputs of a RF classifier. No significant added value was observed compared to the model-based features only, presented before (Figure 4.20). Further work is needed to explore methods that could take advantage of these different type of features.

4.7 Conclusion

This chapter proposes combined approaches based on personalized cardiovascular modeling and ML algorithms. These original methods aim at improving the interpretability of the ML algorithms by explicitly integrates meaningful physiological knowledge through the proposed computational model. Moreover, they also bring the physiological model closer to the clinical practice by using a complete patient database and adapting its level of abstraction to the one provided by the experimental measurements.

Model-based approaches improve the understanding of LV mechanics and the assessment of heart function in patients undergoing CRT, and ML phenotyping helps in the characterization and classification of HF patient profiles and could prioritize particular patients to a CRT implantation.

These novel approaches have great potential clinical implications, suggesting personalization of patient care. They provide new strain-derived parameters to use in the selection of CRT candidate and fill the lack of mechanical analyses needed to understand the non-response of 30% of the implanted patients [55].

BIBLIOGRAPHY

[1] Ponikowski P., Voors A.A., Anker S.D., Bueno H., Cleland J.G., Coats A.J., Falk V., González-Juanatey J.R., Harjola V.P., Jankowska E.A., Jessup M., Linde C., Nihoyannopoulos P., Parissis J.T., Pieske B., Riley J.P., Rosano G.M., Ruilope L.M., Ruschitzka F., Rutten F.H., Van Der Meer P., Sisakian H.S., Isayev E., Kurlianskaya A., Mullens W., Tokmakova M., Agathangelou P., Melenovsky V., Wiggers H., Hassanein M., Uuetoa T., Lommi J., Kostovska E.S., Juilliere Y., Aladashvili A., Luchner A., Chrysohoou C., Nyolczas N., Thorgeirsson G., Weinstein J.M., Lenarda A.D., Aidargaliyeva N., Bajraktari G., Beishenkulov M., Kamzola G., Abdel-Massih T., Celutkiene J., Noppe S., Cassar A., Vataman E., AbirKhalil S., van Pol P., Mo R., Straburzynska-Migaj E., Fonseca C., Chioncel O., Shlyakhto E., Zavatta M., Otasevic P., Goncalvesova E., Lainscak M., Molina B.D., Schaufelberger M., Suter T., Yilmaz M.B., Voronkov L., and Davies C. 2016 ESC Guidelines for the diagnosis and treatment of acute and chronic heart failure. *Eur. Heart J.*, vol. 37, 2129–2200m (2016).

[2] Bristow M.R., Saxon L.A., Boehmer J., Krueger S., Kass D.A., De Marco T., Carson P., DiCarlo L., DeMets D., White B.G., and Others. Cardiac-Resynchronization Therapy with or without an Implantable Defibrillator in Advanced Chronic Heart Failure. *Congest. Hear. Fail.*, vol. 10, 257–258 (2004).

[3] Zareba W., Klein H., Cygankiewicz I., Hall W.J., McNitt S., Brown M., Cannom D., Daubert J.P., Eldar M., Gold M.R., Goldberger J.J., Goldenberg I., Lichstein E., Pitschner H., Rashtian M., Solomon S., Viskin S., Wang P., and Moss A.J. Effectiveness of cardiac resynchronization therapy by QRS morphology in the multicenter automatic defibrillator implantation trial-cardiac resynchronization therapy (MADIT-CRT). *Circulation*, vol. 123, 1061–1072 (2011).

[4] Cleland J.G., Abraham W.T., Linde C., Gold M.R., Young J.B., Claude Daubert J., Sherfesee L., Wells G.A., and Tang A.S. An individual patient meta-analysis of five randomized trials assessing the effects of cardiac resynchronization therapy on morbidity and mortality in patients with symptomatic heart failure. *Eur. Heart J.*, vol. 34 (2013).

[5] W illiam T. A braham , M.D., W estby G. F isher , M.D., A ndrew L. S mith , M.D., D avid B. D elurgio M., A ngel R. L eon , M.D., E van L oh , M.D., D usan Z. K ocovic , M.D., M ilton P acker , M.D., A lfredo L. C avell , M.D., D avid L. H ayes , M.D., M yrvin E llestad , M.D., and J ohn M essenger , M.D. F.T.M.S.T.G.R.., and A. CARDIAC RESYNCHRONIZATION IN CHRONIC HEART FAILURE W. *N. Engl. J. Med.*, vol. 346, 305–310 (2002).

[6] Daubert C., Behar N., Martins R.P., Mabo P., and Leclercq C. Avoiding non-responders to cardiac resynchronization therapy: A practical guide. *Eur. Heart J.*, vol. 38, 1463–1472 (2017).

[7] Glikson M., Nielsen J.C., Kronborg M.B., Michowitz Y., Auricchio A., Barbash I.M., Barrabés J.A., Boriani G., Braunschweig F., Brignole M., Burri H., Coats A.J., Deharo J.C., Delgado V., Diller G.P., Israel C.W., Keren A., Knops R.E., Kotecha D., Leclercq C., Merkely B., Starck C., Thylén I., Tolosana J.M., Leyva F., Linde C., Abdelhamid M., Aboyans V., Arbelo E., Asteggiano R., Barón-Esquivias G., Bauersachs J., Biffi M., Birgersdotter-Green U., Bongiorni M.G., Borger M.A., Celutkienė J., Cikes M., Daubert J.C., Drossart I., Ellenbogen K., Elliott P.M., Fabritz L., Falk V., Fauchier L., Fernández-Avilés F., Foldager D., Gadler F., De Vinuesa P.G.G., Gorenek B., Guerra J.M., Hermann Haugaa K., Hendriks J., Kahan T., Katus H.A., Konradi A., Koskinas K.C., Law H., Lewis B.S., Linker N.J., Løchen M.L., Lumens J., Mascherbauer J., Mullens W., Nagy K.V., Prescott E., Raatikainen P., Rakisheva A., Reichlin T., Ricci R.P., Shlyakhto E., Sitges M., Sousa-Uva M., Sutton R., Suwalski P., Svendsen J.H., Touyz R.M., Van Gelder I.C., Vernooy K., Waltenberger J., Whinnett Z., Witte K.K., Kronborg M.B., Michowitz Y., Auricchio A., Barbash I.M., Barrabés J.A., Boriani G., Braunschweig F., Brignole M., Burri H., Coats A.J., Deharo J.C., Delgado V., Diller G.P., Israel C.W., Keren A., Knops R.E., Kotecha D., Leclercq C., Merkely B., Starck C., Thylén I., and Tolosana J.M. 2021 ESC Guidelines on cardiac pacing and cardiac resynchronization therapy. *Eur. Heart J.*, vol. 42, 3427–3520 (2021).

[8] Chung E.S., Leon A.R., Tavazzi L., Sun J.P., Nihoyannopoulos P., Merlino J., Abraham W.T., Ghio S., Leclercq C., Bax J.J., Yu C.M., Gorcsan J., Sutton M.S.J., Sutter J.D., and Murillo J. Results of the predictors of response to crt (prospect) trial. *Circulation*, vol. 117, 2608–2616 (2008).

[9] Duchenne J. Finding New Insights in Cardiac Resynchronization Therapy and the Pathophysiology behind Left Ventricular Dyssynchrony. *J. Clin. Med.*, 10–12 (2022).

[10] Gallard A., Galli E., Hubert A., Bidaut A., Le Rolle V., Smiseth O., Voigt J.U., Donal E., and Hernández A.I. Echocardiographic view and feature selection for the estimation of the response to CRT. *PLoS One*, vol. 16, page e0252857 (2021).

[11] Kalscheur M.M., Kipp R.T., Tattersall M.C., Mei C., Buhr K.A., Demets D.L., Field M.E., Eckhardt L.L., and Page C.D. Machine Learning Algorithm Predicts Cardiac Resynchronization Therapy Outcomes: Lessons from the COMPANION Trial. *Circ. Arrhythmia Electrophysiol.*, vol. 11, 1–11 (2018).

[12] Tokodi M., Schwertner W.R., Kovács A., Tosér Z., Staub L., Sárkány A., Lakatos B.K., Behon A., Boros A.M., Perge P., Kutyifa V., Széplaki G., Gellér L., Merkely B., and Kosztin A. Machine learning-based mortality prediction of patients undergoing cardiac resynchronization therapy: The SEMMELWEIS-CRT score. *Eur. Heart J.*, vol. 41, 1747–1756 (2020).

[13] Feeny A.K., Rickard J., Patel D., Toro S., Trulock K.M., Park C.J., Labarbera M.A., Varma N., Niebauer M.J., Sinha S., Gorodeski E.Z., Grimm R.A., Ji X., Barnard J., Madabhushi A., Spragg D.D., and Chung M.K. Machine Learning Prediction of Response to Cardiac Resynchronization Therapy: Improvement Versus Current Guidelines. *Circ. Arrhythmia Electrophysiol.*, vol. 12, 1–12 (2019).

[14] Cikes M., Sanchez-Martinez S., Claggett B., Duchateau N., Piella G., Butakoff C., Pouleur A.C., Knappe D., Biering-Sørensen T., Kutyifa V., Moss A., Stein K., Solomon S.D., and Bijnens B. Machine learning-based phenogrouping in heart failure to identify responders to cardiac resynchronization therapy. *Eur. J. Heart Fail.*, vol. 21, 74–85 (2019).

[15] Voigt J.U. and Cvijic M. 2- and 3-Dimensional Myocardial Strain in Cardiac Health and Disease. *JACC Cardiovasc. Imaging*, vol. 12, 1849–1863 (2019).

[16] Mada R.O., Duchenne J., and Voigt J.U. Tissue Doppler, strain and strain rate in ischemic heart disease "How I do it". *Cardiovasc. Ultrasound*, vol. 12, 1–9 (2014).

[17] Taconne M., Rolle V.L., Gallard A., Owashi K.P., Wazzan A., Voigt J.U., Duchenne J., Smiseth O., Donal E., and Hernandez A. Model-based and Unsupervised Machine-learning Approaches for the Characterization of Responder Profiles for Cardiac Resynchronization Therapy. *Comput. Cardiol. (2010).*, 3–6 (2022).

[18] Gallard A., Bidaut A., Hubert A., Sade E., Marechaux S., Sitges M., Separovic-Hanzevacki J., Le Rolle V., Galli E., Hernandez A., and Donal E. Characterization of Responder Profiles for Cardiac Resynchronization Therapy through Unsupervised Clustering of Clinical and Strain Data. *J. Am. Soc. Echocardiogr.*, vol. 34, 483–493 (2021).

[19] Bernard A., Donal E., Leclercq C., Schnell F., Fournet M., Reynaud A., Thebault C., Mabo P., Daubert J.C., and Hernandez A. Impact of cardiac resynchronization therapy on left ventricular mechanics: Understanding the response through a new quantitative approach based on longitudinal strain integrals. *J. Am. Soc. Echocardiogr.*, vol. 28, 700–708 (2015).

[20] Bernard A. *Réponse à la Resynchronisation Cardiaque : Au-delà des Asynchronismes*. Ph.D. thesis, Université de Rennes 1 (2014).

[21] Gallard A., Hubert A., Smiseth O., Voigt J.U., Le Rolle V., Leclercq C., Bidaut A., Galli E., Donal E., and Hernandez A.I. Prediction of response to cardiac resynchronization therapy using a multi-feature learning method. *Int. J. Cardiovasc. Imaging*, vol. 37, 989–998 (2020).

[22] Brest J., Greiner S., Bošković B., Mernik M., and Zumer V. Self-adapting control parameters in differential evolution: A comparative study on numerical benchmark problems. *IEEE Trans. Evol. Comput.*, vol. 10, 646–657 (2006).

[23] Lloyd S.P. Least Squares Quantization in PCM. *IEEE Trans. Inf. Theory*, vol. 28, 129–137 (1982).

[24] Pedregosa F., Varoquaux G., Gramfort A., Michel V., Thirion B., Grisel O., Blondel M., Prettenhofer P., Weiss R., Dibourg V., Vanderplas J., Passos A., Cournapeau D., Brucher M., Perrot M., and Duchesnay E. Scikit-learn: Machine Learning in Python. *J. Mach. Learn. Res.*, vol. 12, 2825–2830 (2011).

[25] Thorndike R.L. Who belongs in the family? *Psychometrika*, vol. 18, 267–276 (1953).

[26] Kemp C.D. and Conte J.V. The pathophysiology of heart failure. *Cardiovasc. Pathol.*, vol. 21, 365–371 (2012).

[27] Vaillant C., Martins R.P., Donal E., Leclercq C., Thébault C., Behar N., Mabo P., and Daubert J.C. Resolution of left bundle branch block-induced cardiomyopathy by cardiac resynchronization therapy. *J. Am. Coll. Cardiol.*, vol. 61, 1089–1095 (2013).

[28] Owashi K., Taconné M., Courtial N., Simon A., Garreau M., Hernandez A., Donal E., Rolle V.L., and Galli E. Desynchronization Strain Patterns and Contractility in Left Bundle Branch Block through Computer Model Simulation. *J. Cardiovasc. Dev. Dis.*, vol. 9, page 53 (2022).

[29] Taconné M., Owashi K.P., Galli E., Duchenne J., Hubert A., Donal E., Hernàndez A.I., and Le Rolle V. Model-based analysis of myocardial strains in left bundle branch block. *Front. Appl. Math. Stat.*, page 110 (2022).

[30] Bleeker G.B., Kaandorp T.A., Lamb H.J., Boersma E., Steendijk P., De Roos A., Van Der Wall E.E., Schalij M.J., and Bax J.J. Effect of posterolateral scar tissue on clinical and echocardiographic improvement after cardiac resynchronization therapy. *Circulation*, vol. 113, 969–976 (2006).

[31] Aalen J.M., Donal E., Larsen C.K., Duchenne J., Lederlin M., Cvijic M., Hubert A., Voros G., Leclercq C., Bogaert J., Hopp E., Fjeld J.G., Penicka M., Linde C., Aalen O.O., Kongsgård E., Galli E., Voigt J.U., and Smiseth O.A. Imaging predictors of response to cardiac resynchronization therapy: Left ventricular work asymmetry by echocardiography and septal viability by cardiac magnetic resonance. *Eur. Heart J.*, vol. 41, 3813–3823 (2020).

[32] Nagueh S.F., Smiseth O.A., Appleton C.P., Byrd B.F., Dokainish H., Edvardsen T., Flachskampf F.A., Gillebert T.C., Klein A.L., Lancellotti P., Marino P., Oh J.K., Popescu B.A., and Waggoner A.D. Recommendations for the evaluation of left ventricular diastolic function by echocardiography: An update from the American society of echocardiography and the European association of cardiovascular imaging. *Eur. Heart J. Cardiovasc. Imaging*, vol. 17, 1321–1360 (2016).

[33] Galli E., Smiseth O.A., Aalen J.M., Larsen C.K., Sade E., Hubert A., Anilkumar S., Penicka M., Linde C., Le Rolle V., Hernandez A., Leclercq C., Duchenne J., Voigt J.U., and Donal E. Prognostic utility of the assessment of diastolic function in patients undergoing cardiac resynchronization therapy. *Int. J. Cardiol.*, vol. 331, 144–151 (2021).

[34] van Everdingen W.M., Walmsley J., Cramer M.J., van Hagen I., De Boeck B.W., Meine M., Delhaas T., Doevendans P.A., Prinzen F.W., Lumens J., and Leenders G.E. Echocardiographic Prediction of Cardiac Resynchronization Therapy Response Requires Analysis of Both Mechanical Dyssynchrony and Right Ventricular Function: A Combined Analysis of Patient Data and Computer Simulations. *J. Am. Soc. Echocardiogr.*, vol. 30, 1012–1020.e2 (2017).

[35] Risum N., Tayal B., Hansen T.F., Bruun N.E., Jensen M.T., Lauridsen T.K., Saba S., Kisslo J., Gorcsan J., and Sogaard P. Identification of Typical Left Bundle Branch Block Contraction by Strain Echocardiography Is Additive to Electrocardiography in Prediction of Long-Term Outcome after Cardiac Resynchronization Therapy. *J. Am. Coll. Cardiol.*, vol. 66, 631–641 (2015).

[36] Lumens J., Tayal B., Walmsley J., Delgado-Montero A., Huntjens P.R., Schwartzman D., Althouse A.D., Delhaas T., Prinzen F.W., and Gorcsan J. Differentiating Electromechanical from Non-Electrical Substrates of Mechanical Discoordination to Identify Responders to Cardiac Resynchronization Therapy. *Circ. Cardiovasc. Imaging*, vol. 8, 1–12 (2015).

[37] Aalen J.M., Remme E.W., Larsen C.K., Andersen O.S., Krogh M., Duchenne J., Hopp E., Ross S., Beela A.S., Kongsgaard E., Bergsland J., Odland H.H., Skulstad H., Opdahl A., Voigt J.U., and Smiseth O.A. Mechanism of Abnormal Septal Motion in Left Bundle Branch Block: Role of Left Ventricular Wall Interactions and Myocardial Scar. *JACC Cardiovasc. Imaging*, vol. 12, 2402–2413 (2019).

[38] Leenders G.E., De Boeck B.W., Teske A.J., Meine M., Bogaard M.D., Prinzen F.W., Doevendans P.A., and Cramer M.J. Septal rebound stretch is a strong predictor of outcome after cardiac resynchronization therapy. *J. Card. Fail.*, vol. 18, 404–412 (2012).

[39] Galli E., Le Rolle V., Smiseth O.A., Duchenne J., Aalen J.M., Larsen C.K., Sade E.A., Hubert A., Anilkumar S., Penicka M., Linde C., Leclercq C., Hernandez A., Voigt J.U., and Donal E. Importance of Systematic Right Ventricular Assessment in Cardiac Resynchronization Therapy Candidates: A Machine Learning Approach. *J. Am. Soc. Echocardiogr.*, vol. 34, 494–502 (2021).

[40] Dauw J., Martens P., and Mullens W. CRT Optimization: What Is New? What Is Necessary? *Curr. Treat. Options Cardiovasc. Med.*, vol. 21 (2019).

[41] Sade L.E., Saba S., Marek J.J., Onishi T., Schwartzman D., Adelstein E.C., Soman P., and Gorcsan J. The association of left ventricular lead position related to regional scar by speckle-tracking echocardiography with clinical outcomes in patients receiving cardiac resynchronization therapy. *J. Am. Soc. Echocardiogr.*, vol. 27 (2014).

[42] Kydd A.C., Khan F.Z., Watson W.D., Pugh P.J., Virdee M.S., and Dutka D.P. Prognostic benefit of optimum left ventricular lead position in cardiac resynchronization therapy: Follow-up of the TARGET study cohort (targeted left ventricular lead placement to guide cardiac resynchronization therapy). *JACC Hear. Fail.*, vol. 2, 205–212 (2014).

[43] Akdeniz M., Manetti C.A., Koopsen T., Mirar H.N., Snare S.R., Aase S.A., Lumens J., Sprem J., and McLeod K.S. Deep Learning for Multi-Level Detection and Localization of Myocardial Scars Based on Regional Strain Validated on Virtual Patients. *IEEE Access*, vol. 11, 15 788–15 798 (2023).

[44] Lumens J., Leenders G.E., Cramer M.J., De Boeck B.W., Doevendans P.A., Prinzen F.W., and Delhaas T. Mechanistic evaluation of echocardiographic dyssynchrony indices patient data combined with multiscale computer simulations. *Circ. Cardiovasc. Imaging*, vol. 5, 491–499 (2012).

[45] BREIMAN L. Random Forests LEO. *Mach. Learn.*, vol. 45, 5–32 (2001).

[46] Genuer R., Poggi J.M., and Tuleau-Malot C. Variable selection using random forests. *Pattern Recognit. Lett.*, vol. 31, 2225–2236 (2010).

[47] Probst P., Wright M.N., and Boulesteix A.L. Hyperparameters and tuning strategies for random forest. *Wiley Interdiscip. Rev. Data Min. Knowl. Discov.*, vol. 9, 1–15 (2019).

[48] Cai C., Tafti A.P., Ngufor C., Zhang P., Xiao P., Dai M., Liu H., Noseworthy P., Chen M., Friedman P.A., and Cha Y.M. Using ensemble of ensemble machine learning methods to predict outcomes of cardiac resynchronization. *J. Cardiovasc. Electrophysiol.*, vol. 32, 2504–2514 (2021).

[49] Hu S.Y., Santus E., Forsyth A.W., Malhotra D., Haimson J., Chatterjee N.A., Kramer D.B., Barzilay R., Tulsky J.A., and Lindvall C. Can machine learning improve patient selection for cardiac resynchronization therapy? *PLoS One*, vol. 14, 1–13 (2019).

[50] Tokodi M., Schwertner W.R., Kovács A., Tosér Z., Staub L., Sárkány A., Lakatos B.K., Behon A., Boros A.M., Perge P., Kutyifa V., Széplaki G., Gellér L., Merkely B., and Kosztin A. Machine learning-based mortality prediction of patients undergoing cardiac resynchronization therapy: The SEMMELWEIS-CRT score. *Eur. Heart J.*, vol. 41, 1747–1756 (2020).

[51] Marcus G.M., Rose E., Viloria E.M., Schafer J., De Marco T., Saxon L.A., and Foster E. Septal to posterior wall motion delay fails to predict reverse remodeling or clinical improvement in patients undergoing cardiac resynchronization therapy. *J. Am. Coll. Cardiol.*, vol. 46, 2208–2214 (2005).

[52] Pitzalis M.V., Iacoviello M., Romito R., Massari F., Rizzon B., Luzzi G., Guida P., Andriani A., Mastropasqua F., and Rizzon P. Cardiac resynchronization therapy tailored by echocardiographic evaluation of ventricular asynchrony. *J. Am. Coll. Cardiol.*, vol. 40, 1615–1622 (2002).

[53] Yu C.M., Fung W.H., Lin H., Zhang Q., Sanderson J.E., and Lau C.P. Predictors of left ventricular reverse remodeling after cardiac resynchronization therapy for heart failure secondary to idiopathic dilated or ischemic cardiomyopathy. *Am. J. Cardiol.*, vol. 91, 684–688 (2003).

[54] Galli E., Leclercq C., Fournet M., Hubert A., Bernard A., Smiseth O.A., Mabo P., Samset E., Hernandez A., and Donal E. Value of Myocardial Work Estimation in the Prediction of Response to Cardiac Resynchronization Therapy. *J. Am. Soc. Echocardiogr.*, vol. 31, 220–230 (2018).

[55] Galli E., Galand V., Rolle V.L., Taconne M., Wazzan A.A., Hernandez A., Leclercq C., and Donal E. The saga of dyssynchrony imaging : Are we getting to the point. 1–15 (2023).

Chapter

5 Myocardial Work Estimation in Aortic Stenosis Case

Aortic stenosis (AS) is the most common primary valvular heart disease, leading to an intervention with growing prevalence due to the aging population [1]. Current recommendations state that Aortic Valve Replacement (AVR) is a class I indication in cases of symptoms or reduced left ventricular ejection fraction (LVEF, <50%). Whatever, LVEF is preserved in many patients with AS even when symptoms develop. Stratification of pre-operative and post-operative risk of each patient is currently challenging. Unfortunately, valvular parameters such as Aortic Valve Area (AVA) and transvalvular gradient did not permit an ideal risk stratification [2, 3]. Several studies suggest the additional value of Global Longitudinal Strain (GLS) to better stratify this population. Magne et al.[4] demonstrated in a meta-analysis that GLS <14, 7% with preserved LVEF increased with an OR of 2.6 risk of death. Despite these results, GLS is not widely used in clinical routine. A possible explanation is the after-load dependence of GLS [5]. Indeed, GLS decreases with the increasing LV after-load, that is why an after-load independent feature to better describe LV function would be necessary.

Myocardial Work (MW) is a very promised new tool to assess more precisely LV function [6, 7] taking into account LV after-load. Its efficiency in patient's stratification has already been suggested in cardiac resynchronization therapy [8, 9], hypertrophic cardiomyopathies [10], and mitral regurgitation [11]. However, in order to calculate the MW, an accurate estimation of the pressure curve is needed. Russell et al. [6, 12] have proposed a non-invasive method for the estimation LV pressure based on a black-box non-linear method that fits a reference waveform to the duration of the isovolumic and ejection phases of a given patient, as measured by echocardiographic timing of aortic and mitral valve events. Peak LV pressure was estimated from a non-invasive cuff-based measurement of the brachial artery pressure [13]. Thanks to this pressure curve estimation, a MW computation tool was developed for these patients with normal or subnormal afterload [6]. However, this pressure estimation method could not be applied in the case of AS, where high pressure gradients could be observed between LV and the aorta. Fortuni et al [14]. have adapted the pressure estimation method by calculating peak LV pressure as the sum of mean aortic transvalvular gradient and aortic systolic pressure to calculate MW for this type of patient. On the other side, our team recently proposed a novel model-based approach to assess non-invasively LV pressure and MW in AS patients [15].

The objective of this chapter is to improve the model-based approach to assess non-invasively LV pressure proposed in our team [15, 16], and then compare and evaluate the LV pressure estimation

with the adapted method of Russel et al. [6, 12] by Fortuni et al. [17]. As the essential part of the MW determination is the estimation of LV pressure, pressure curves calculated with each method were compared with the invasively computed in severe and moderate AS patients.

This chapter follows the work published in *the European Heart Journal* [18] and preliminary studies presented in two conferences, with an oral presentation and a conference paper for the first [19], and a poster for the second [20].

5.1 Data

5.1.1 Population

Sixty-seven adults (>18 years old) with severe (AVA < 1 cm^2, n=62) and moderate (n=5) AS, who underwent a coronary angiography with Left Heart Catheterization (LHC), were prospectively included. Ten patients were excluded from the final analysis because of atrial fibrillation, concomitant significant aortic regurgitation, or incomplete set of images for getting robust GLS measurements. The study was carried out in accordance with the principles outlined in the Declaration of Helsinki on research in human subjects and received specific ethical approval from the local Medical Ethics Committee. All patients were informed, and a consent was obtained.

5.1.2 Echocardiography

All patients underwent a standard Trans-Thoracic Echocardiography (TTE) using a Vivid S70 or E95 ultrasound system (General Electric Healthcare, Horten, Norway). Images were recorded on a remote station for off-line analysis by dedicated software (EchoPAC PC, version BT 202, General Electric Healthcare, Horten, Norway). Aortic and mitral valve events were manually evaluated in apical long-axis view: mitral valve closure (MVC), aortic valve opening (AVO), aortic valve closure (AVC), and mitral valve opening (MVO). Standard speckle tracking strain analysis was applied in order to extract regional myocardial strain curves. The AVA (cm^2) and mean pressure gradient were also quantified according to current recommendations.

5.1.3 Invasive ventricular pressure

The LHC was performed via retrograde access from the radial artery with a 5 French Judkin R4 catheter (ICU Medical, San Clemente, CA, USA) placed at the mid LV cavity using fluoroscopic screening. It has been performed with cautious to optimize the quality of the recording but using the catheter people are used to. Before coronary angiography, transducers were calibrated, with a 0-level set at the mid-axillary line. In a second time, a catheter was placed in the thoracic ascendant aorta to measure aortic pressure. The experimental invasive data set includes the measured ventricular pressure P_{lv}^{exp}, the systolic and diastolic arterial pressures.

5.1.4 Patient characteristics

The baseline characteristics of the population are depicted in Table 5.1. The continuous variables are presented as mean ± standard deviation in the case of normal distribution, as median (interquartile range) in the non-normal distribution case, categorical variable as absolute frequencies and percentage.

Variables	Overall (N)
Age (years)	82 (79, 85)
Male (%)	38 (57%)
NYHA > I and II	28 (42%)
AF (%)	14 (31%)
HB (mmol/L)	12.2 ± 1.5
Previous MI (%)	33 (49%)
Creatinine (μmol/L)	101 (74.0, 102)
BMI (kg.m^2)	26.8 ± 4.3
BSA (m^2)	1.78 ± 0.18
DBP (mmHg)	59.5 ± 22.5
LV mass (g.m^{-2})	153 ± 61
V max (m.s^{-1})	3.68 ± 0.84
LV root diameter (m^2)	21.9 ± 1.8
LVEDV(ml/m^2)	46.6 ± 27.7
LVEF (%)	59 (52, 68)
LV GLS (%)	-15.0 ± 4.0
LV SVi (mL/m^2)	12.7 ± 3.2
Mean E/e'>14 (%)	35 (52%)
AV mean gradient (mmHg)	49.8 ± 14.8
AVA (cm^2)	0.769 ± 0.236
SPAP (mmHg)	43.2 ± 16.0

Table 5.1: Clinical and echocardiographic characteristic for the overall population. NYHA: New-York Heart Association, AF: atrial fibrilation, HB: hemoglobin, MI: myocardial infraction, BMI: body mass index, BSA: body surface area, DBP; diastolic blood pressure, LV: left ventricle, V: velocity, LVEDV: LV end-diastolic volume, LVEF: Left Ventricle Ejection Fraction, GLS: global longitudinal strain, SVi: systolic volume index, AV: aortic valve, AVA: Aortic Valve Area, SPAP: Systolic Pulmonary Artery Pressure.

The population had a mean age of 82 years. The majority of patients was males (57%), with 58% of NYHA class I– II and 42% of NYHA class III–IV. All the patients suffering from severe (93%) or moderate AS with a mean AVA equal to 0.77 cm^2.The LV pressure and work indices extracted from invasive measurement are summarized in Table 5.2. The overall population presents a mean GWW higher than normal [21] (459 mmHg.%) and a mean GWE reduce (83%).

Variables	Overall (N)
Invasive LV SBP (mmHg)	184 (164, 205)
Aortic DBP (mmHg)	72.7 (55.0, 81.5)
Aortic SBP (mmHg)	144 (119, 166)
GWI (mmHg.%)	1273 $\pm$ 1128
GCW (mmHg.%)	2357$\pm$ 913
GWW (mmHg.%)	459 (207, 610)
GWE (-)	0.823 (0.744, 0.917)

Table 5.2: LV pressure and work indices computed with invasive LV pressure (SBP: systolic blood pressure, DBP: diastolic blood pressure).

5.2 Method

Two method of LV pressure estimation will be compared to the invasive one. These two estimated LV pressure curves will be used and compared in the computation of myocardial indices previously described (Section 2.2.2) to the one computed with the experimental pressure curve.

5.2.1 Model

The first method used a model to simulate the LV pressure curve of each patient. In this subsection the model will be described as well as the process of specification for each AS patient.

Model description

Four main sub-models, based on previous works of our team [22, 23], were coupled:

1. Cardiac electrical system,
2. Elastance-based cardiac cavities,
3. Systemic and pulmonary circulations
4. Heart valves.

The proposed model (Figure 5.2) and the equations have been described in detail in the article of Owashi et al. [15]. To sum up:

Cardiac electrical system: A set of interconnected cellular automata, adapted from [22, 23] represents the cardiac electrical activity of the model. Each automaton represents different cardiac regions that cycle between four electrical activation states:

- slow diastolic depolarization (SDD),
- upstroke depolarization period (UDP),
- absolute refractory period (ARP),

– relative refractory period (RRP).

Figure 5.1 represents the nine automata:

– the sinoatrial node (SAN),
– the right and left atria (RA and LA),
– the atrioventricular node (AVN),
– the upper bundle of His (UH),
– the bundle branches (RBB and LBB),
– the two ventricles (RV and LV).

The electrical activation of the automata is used to synthesize an Electrocardiogram (ECG), from which the QRS peak was extracted to synchronize the experimental and simulated signals.

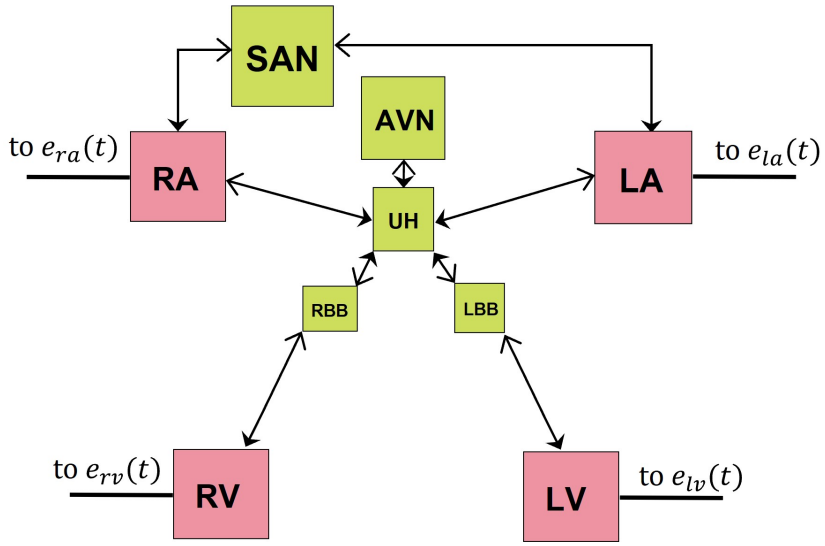

Figure 5.1: Cardiac electrical system with the sinoatrial node (SAN), the right and left atria (RA and LA), the atrioventricular node (AVN), the upper bundle of His (UH), the bundle branches (RBB and LBB), and the two ventricles (RV and LV).

Elastance-based cardiac cavities: The ventricular (v) pressure is represented by a combination of end-systolic (es) and end-diastolic (ed) pressure-volume relationships [24, 25]. These relations are driven by time-varying elastances E_{es} and E_{ed} that represent contraction and relaxation phases.

$$P_{es}(V) = E_{es}(V - V_d) \tag{5.1a}$$

$$P_{ed}(V) = P_0(e^{\lambda(V-V_0)} - 1) \tag{5.1b}$$

$$P(V) = e(t)P_{es}(V) + (1 - e(t))P_{ed}(V) \tag{5.1c}$$

For the atrium (a):

$$P_a(V_a, t) = E_a(t) \cdot (V_a(t) - V_{d,a}) \tag{5.2a}$$

$$E_a(t) = E_{a,max} \cdot (e_a(t) + \frac{E_{a,min}}{E_{a,max}}) \tag{5.2b}$$

For the right and left ventricles (v), a "double Hill" driving function e was selected [26] with parameters n_1, n_2, α_1, α_2 and k, while a Gaussian function was used for right and left atria (a) with parameter C and B:

$$e_v(t_s) = k \cdot \left[\frac{\left(\frac{t_s}{\alpha_1 \cdot T}\right)^{n_1}}{1 + \left(\frac{t_s}{\alpha_1 \cdot T}\right)^{n_1}}\right] \cdot \left[\frac{1}{1 + \left(\frac{t_s}{\alpha_2 \cdot T}\right)^{n_2}}\right] \tag{5.3a}$$

$$e_a(t_s) = exp(-B_{la} \cdot (t - C_{la})^2) \tag{5.3b}$$

The onset of the cardiac cycle, denoted t_s, is determined by the activation instant of the corresponding segment in the cardiac electrical model presented in the previous section. The first and second terms in Equation 5.3a represent ventricle segment contraction and relaxation presented after an electrical activation, respectively. T is the heart period, α_1, α_2 are shape parameters, and n_1, n_2 control the steepness of the curve. These four parameters (α_1, α_2, n_1, n_2) are assumed positive.

Systemic and pulmonary circulations: The model integrates the pulmonary and systemic arteries, capillaries, and veins [27]. Arteries and veins compartments pressure P is calculated using a linear relationship between its volume P and its elastance E. The volume of each cardiac or vessel chamber is computed from the net flow $Q_{int} - Q_{out}$:

$$\Delta V(t) = \int (Q_{int} - Q_{out}) dt \tag{5.4}$$

The pressures are then used to calculate blood flow between two chambers as:

$$Q = \frac{\Delta P}{R} \tag{5.5}$$

where ΔP is the pressure gradient between the chambers and R the corresponding resistance.

Cardiac valves: A detailed model of heart valves (mitral, aortic, tricuspid and pulmonary) was integrated [28]. Briefly, the relation between the pressure gradient ΔP and the fluid flow Q across an open valve is approximated by the Bernoulli equation:

$$\Delta P = Bq|q| + L\frac{dq}{dt}, \quad \text{with} \quad L = \rho\frac{l_{eff_{ao}}}{A_{eff}} \tag{5.6}$$

The cardiac valve model integrates the effective cross-sectional area of the valve A_{eff} with its dynamic ξ:

$$A_{eff}(t) = (A_{eff,max} - A_{eff,min})\xi(t) + A_{eff,min} \tag{5.7}$$

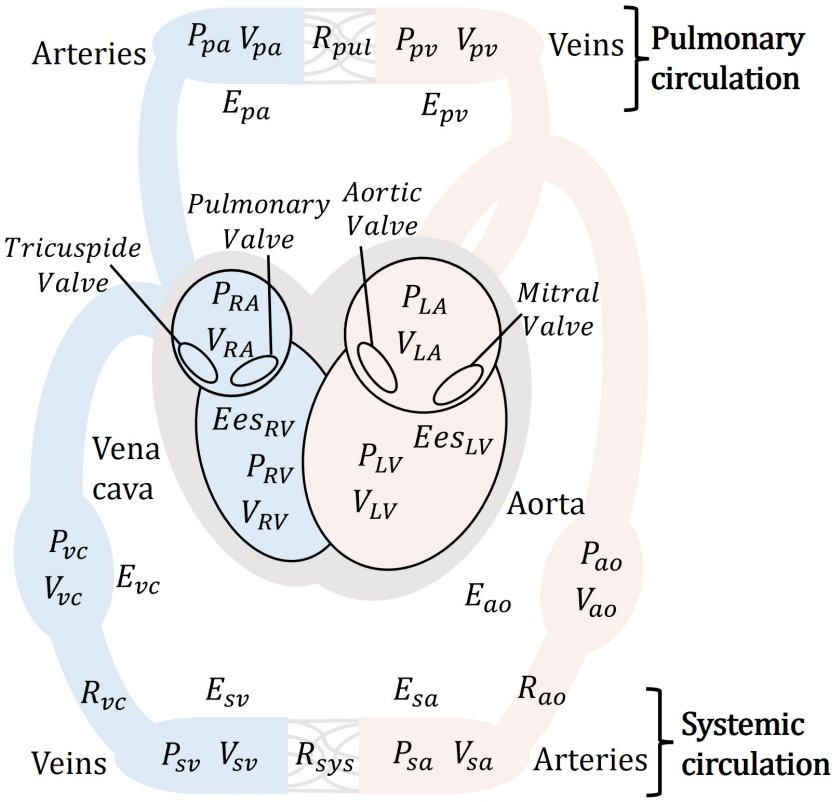

Figure 5.2: Cardiovascular model for AS patients with the pressures (P) and volumes (V), resistances (R) and elastances (E) for the pulmonary arteries (pa), pulmonary veins (pv), aorta (ao), systemic arteries (sa), systemic veins (sv), vena cava (vc), left atrium (LA), left ventricle (LV); right atrium (RA) and right ventricle (RV)

where

$$A_{eff,max} = Mst_{ao}.Aann_{ao} \tag{5.8a}$$

$$A_{eff,min} = Mrg_{ao}.Aann_{ao} \tag{5.8b}$$

They correspond respectively to the maximum and minimum valve areas and $Aann_{ao}$ to the estimation of the aortic valve area. And the rate of opening ξ describes the dynamic of the valve position in response to ΔP.

$$\frac{d\xi}{dt} = \begin{cases} (1-\xi) \cdot K_{vo} \cdot \Delta P & \text{if} \Delta P \geq 0 \\ \xi \cdot K_{vc} \cdot \Delta P & \text{else.} \end{cases} \tag{5.9}$$

K_{vo} and K_{vc} are the rate coefficients for valve opening and closure, respectively.

A sum up of the parameters and their baseline values is proposed in Appendix C (Table C.1).

Sensitivity analysis

Sensitivity analysis through the Morris 'screening method [29] was performed to determine the most influential parameters of two model outputs: LV pressure gradient (ΔP) and Stroke Volume (SV). The method was introduced in Section 2.1.2 consists in generating several random trajectories through the parameter space. Each trajectory is associated with an estimation of the Elementary Effects EE_i, defined for a parameter x_j:

$$EE_j^* = \left| \frac{Y([x_0, \dots, x_j, \dots]) - Y([x_0, \dots, X_j + \Delta, \dots])}{\Delta} \right| \tag{5.10}$$

where Y is an output of the model and Δ is a predefined variation such as $\Delta = \frac{p}{2(p-1)}$. The parameter p and the number of trajectories r were equal respectively to 6 and 30. EE_j are calculated r times, and the mean of absolute value μ_j* and standard deviation σ_j of these r realizations are then computed for each parameter j. D_i index gathered this two-sensitivity measure. The different index computations were described in Section 2.1.2. In this study the sensitivity analyses were applied on 80 parameters with ranges selected from previous work and literature $\pm$30%.

Model specification and LV pressure estimation

Based on the results of the sensitivity analyses, a set of parameters is selected for patient-specific model identification. This identification was implemented with an Evolutionary Algorithm (EA). This type of algorithm consists of making evolve a population of set of parameter values X in order to minimize an error function J_{error} by selecting, crossing and mutating the population through generations. A more detailed presentation of the EA and its implementation was proposed in Section 2.1.3. The function J_{error} was redefined after several tests, including the addition of computed LV volume and flow curves (thank the echocardiographic speckle tracking images of the LV and the measurement by Doppler imaging of the blood velocity through the aortic valve). The final J_{error} function aims at minimizing the error between LV systolic and diastolic pressures $P_{ao,sys}$ and $P_{ao,dias}$ as well as the mean aortic valve pressure gradient ΔP from experimental (exp) measurements and simulated by the model ($model$):

$$J_{error} = |P_{ao,sys}^{exp} - P_{ao,sys}^{model}| + |P_{ao,dias}^{exp} - P_{ao,dias}^{model}| + |\Delta P^{exp} - \Delta P^{model}| \tag{5.11}$$

Two model parameters are fixed for each patient:

- T is the duration of a cardiac cycle measured in ECG.
- The Aortic Valve Area (AVA) measured in TTE

Other error functions J_{error} were explored during this thesis. Some used the entire invasive LV pressure curve, other not ΔP and exploratory research tried to used LV volume. The computation

of the LV volume was done using a technique developed in the team [30] using the 2- and 4-chamber echo-views and reconstruct the volume using the speckle tracking of these 2D views.

5.2.2 Template-based method of LV pressure estimation

As suggested by Russel et al. [6], valvular timings (MVC, AVO, AVC and MVO) obtained from TTE may be used to estimate a normalized, patient-specific LV pressure curve. A predefined LV pressure curve template, calculated from the average of observed data in previous works of the group, is temporally adjusted and scaled in amplitude so as to fit the observed valvular timings and non-invasive systolic pressure value of a given patient. Mean aortic valve pressure gradient, estimated with echocardiography, was added to the instantaneous systolic pressure value to scale the normalized AS patient-specific LV pressure curve [14]. This method leads to a template-based estimate of a patient-specific LV pressure curve $P_{lv}^{template}$ which was directly extracted from the echocardiography workstation (EchoPAC version 202, General Electric Healthcare, Horten, Norway). The method is summarized in the top right part of Figure 5.3.

5.2.3 MW computation

As previously introduced in Section 2.2.2 MW indices were calculated from strains and LV pressure, as proposed by Russell et al. [12]: The instantaneous power was first obtained by multiplying the strain-rate, obtained by differentiating the strain curve, and the instantaneous LV pressure. Then, segmental MW was calculated by integrating the power over time, during the cardiac cycle from MVC until MVO (Figure 5.3). From each segmental MW curve, Global Positive (GPW), Negative (GNW), Constructive (GCW), Wasted (GWW) MW, Global Work Index (GWI), and Global Work Efficiency (GWE) parameters were calculated. Detailed description of MW indices could be found in [13, 15]. GPW(respectively GNW) is defined as the shortening (respectively lengthening) between MVC and MVO. GCW represents segmental shortening during the systole, i.e. effective energy for blood ejection, and lengthening during IVR, whereas GWW corresponds to segmental stretching during the systole, i.e. energy loss for blood ejection and shortening during the isovolumic relaxation phase. GWE is defined as the global work efficiency as explain in Section 2.2.2:

$$GWE = \frac{GCW}{GCW + GWW} \tag{5.12}$$

And Global Work Index (GWI) is defined as the amount of work performed by the left ventricle during systole:

$$GWI = GPW + GNW \tag{5.13}$$

The MW indices were calculated from experimental and simulated LV pressure, in order to obtain:

- **Model-based indices:** GCW^{model}, GWW^{model}, GWE^{model}, GPW^{model}, GNW^{model}, and GWI^{model}.

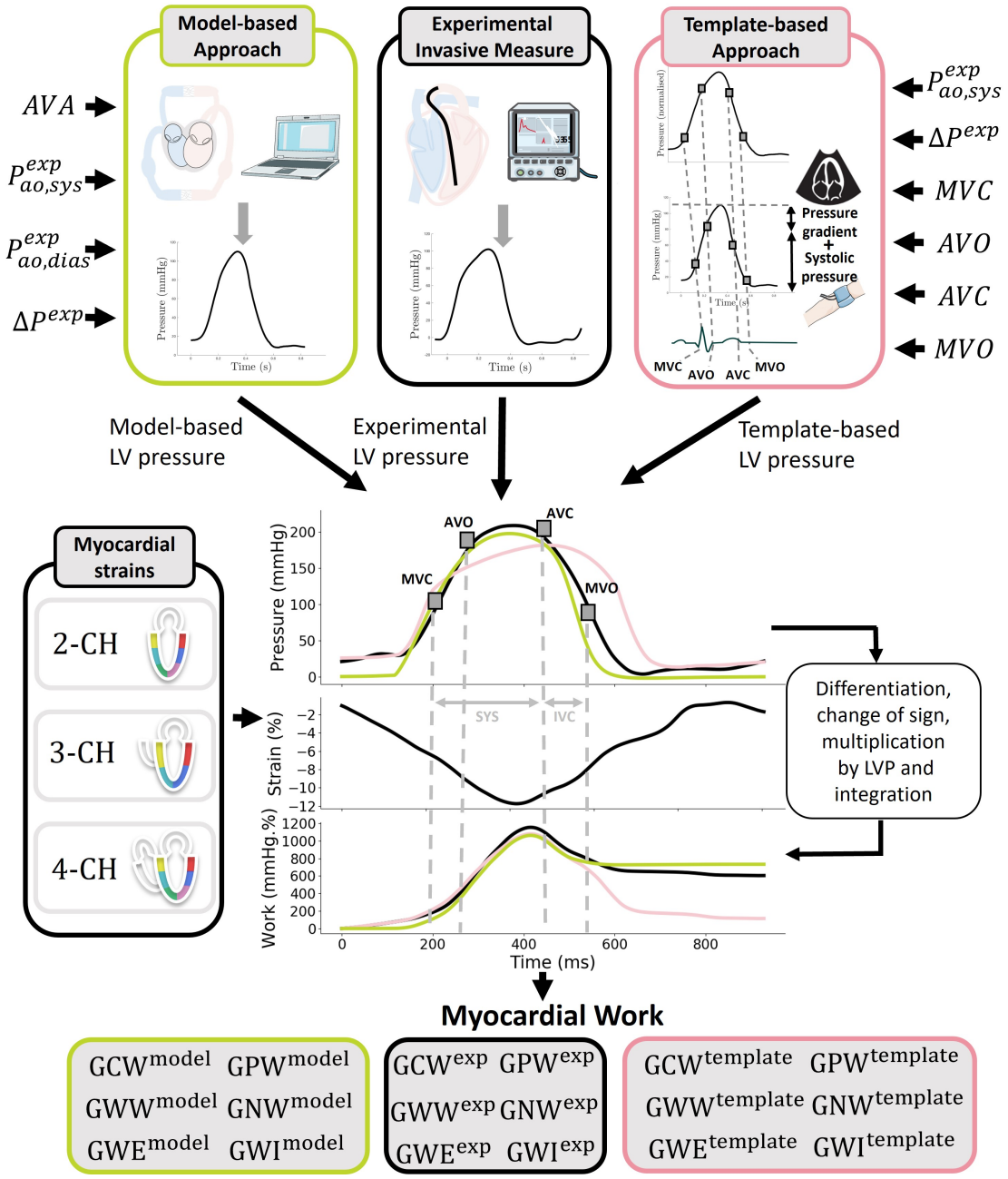

Figure 5.3: Myocardial work evaluation from model-based, template-based approaches and experimental invasive measure. On the left, the model-based method with the Aortic Valve Area (AVA), the mean aortic valve pressure gradient (ΔP^{exp}), the LV systolic and diastolic pressures ($P^{exp}_{ao,sys}$ and $P^{exp}_{ao,dias}$) as inputs. On the right, the template-based method with the LV systolic pressure ($P^{exp}_{ao,sys}$), the mean aortic valve pressure gradient (ΔP^{exp}) and the valve timings: Mitral Valve Closure (MVC), Aortic Valve Opening (AVO), Aortic Valve Closure (AVC), and Mitral Valve Opening (MVO). At the end (*bottom*), we can compare the six MW indices (GCW, GWW, GWE, GPW, GNW and GWI) of the model and the template with the experimental ones (exp)

– **Template-based indices:** $GCW^{template}$, $GWW^{template}$, $GWE^{template}$, $GPW^{template}$, $GNW^{template}$, and $GWI^{template}$.
– **experimental indices:** GCW^{exp}, GWW^{exp}, GWE^{exp}, GPW^{exp}, GNW^{exp}, and GWI^{exp}.

5.3 Result

5.3.1 Model

Baseline simulations

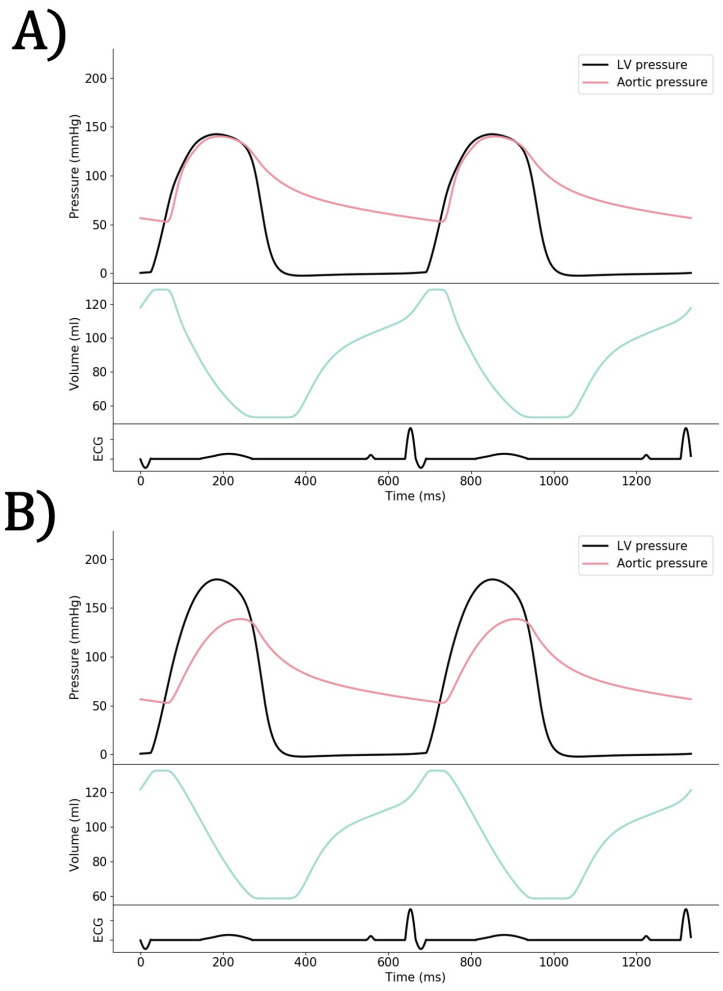

Figure 5.4: Simulation examples provided in a Wigger diagram format of a) a healthy subject and b) an aortic stenosis patient.

Figure 5.4 illustrates the hemodynamic simulation results of the proposed computational model in a Wigger diagram format. Concerning the healthy subject, systolic LV pressure is equal to 145 mmHg, and the aortic pressure varies between 50 and 145 mmHg. AS was represented as a

decrease in the $A_{eff,max}$ parameter (from 2.5 to 0.75 cm^2). We can observe an important gradient pressure between LV and aorta, characteristic of an AS patient, in which the narrowing of the aortic valve opening evokes an LV pressure overload.

Sensitivity analysis

Concerning sensitivity analysis results (Figure 5.5), the most influential parameters of ΔP were mainly related to the aortic valve sizes and the LV elastance, which underline the direct impact of the aortic narrowing of this pathology on the gradient pressure [28]. In fact, $l_{eff_{ao}}$ and $Aann_{ao}$ correspond to the aortic valve length and area, modulated by Mst_{ao} and used in the valve dynamics computations (Equation 5.6, Equation 5.7). In addition, parameter such as α_2, n_1 and λ_{LV} are used in the computation of LV pressure through the driving function and end-diastolic pressure. Modification of these parameters not only change the maximum value of the LV elastance but also its timing and pattern.

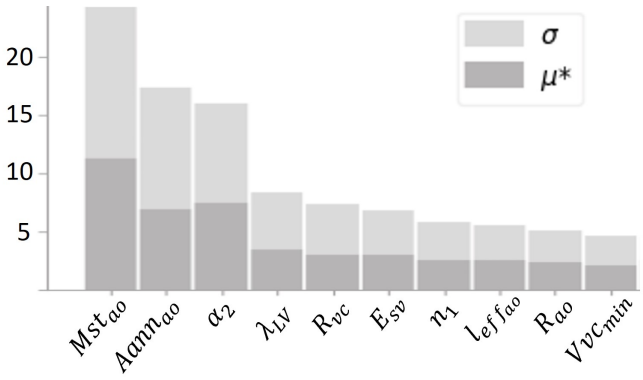

Figure 5.5: Sensitivity analysis on ΔP. The ten most influential parameters are presented and ordered based on their D_j value.

The parameters with the highest sensitivities were selected for parameter identification.

5.3.2 LV pressure estimation

Model-based

Figure 5.6 presents the comparison between model-based (P_{lv}^{model}) and invasive (P_{lv}^{exp}) pressures obtained for the 67 AS patients. The mean correlation coefficient (r^2) was equal to 0.81 (min: 0.23; max: 0.99). Mean slope and intercept of the regression line between the simulated and the measured pressure data were 0.94 (min: 0.49, max: 1.27) and -8.30 mmHg (min:-42.4, max: 21.9), respectively. The mean RMSE was equal to 33.9 mmHg (min: 9.15, max: 90.4).

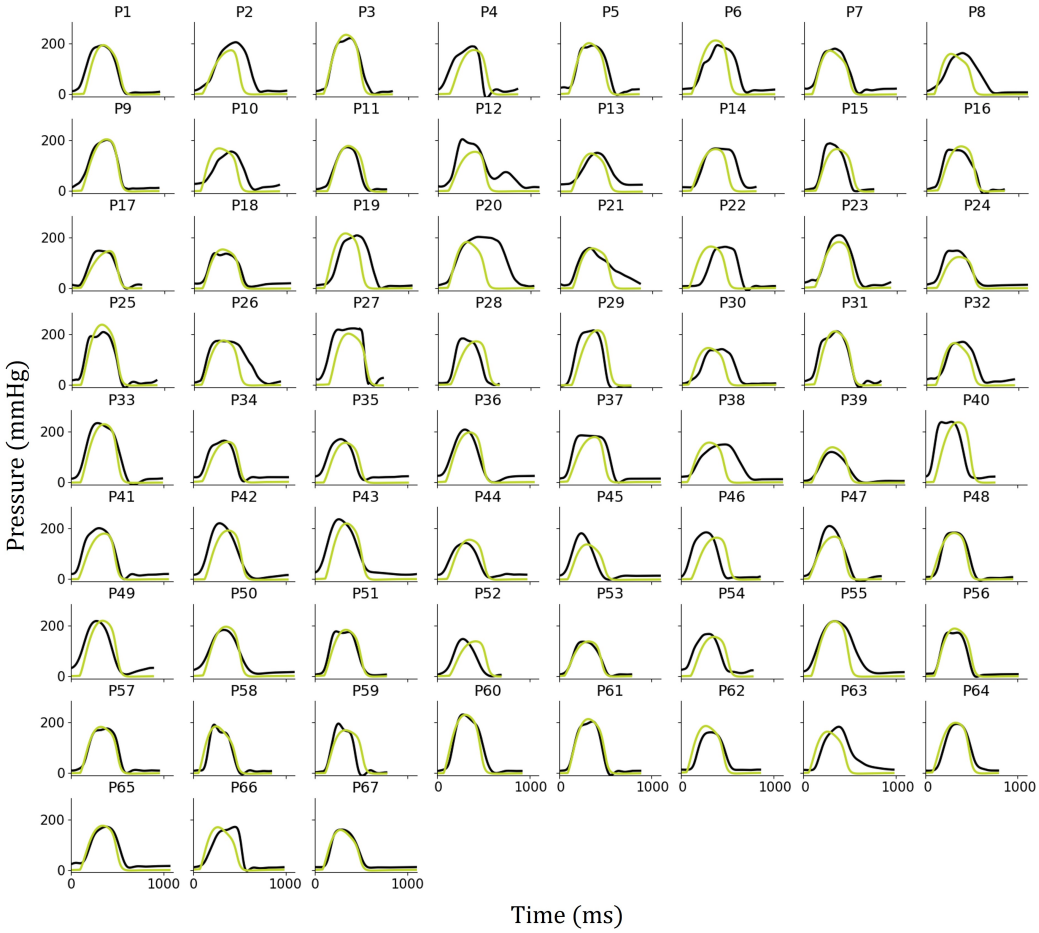

Figure 5.6: Model-based LV pressure curves comparison of 67 patients: experimental (*black*), and simulated (*green*) curves.

Template-based

Similarly, a comparison was performed between template-based estimation ($P_{lv}^{template}$) and experimental pressure (P_{lv}^{exp}) and provides in Figure 5.7. Mean RMSE was equal to 40.4 mmHg (min: 14.0, max: 89.2), mean r^2 is 0.72 (min: 0.25, max: 0.99), mean slope and mean intercept to 0.84 (min: 0.45, max: 1.21) and 23.8 (min: 5.87, max: 64.1), respectively. Despite results are slightly better for the model-based LV pressure estimation, the difference is not significant to conclude for a superior method.

5.3.3 MW comparison

Model-based

Model-based MW Scatter and Bland-Altman plots for GCW, GWW, GWE, GPW, GNW and GWI indices are presented in Figure 5.8. Concerning constructive work, slope and intercept of the

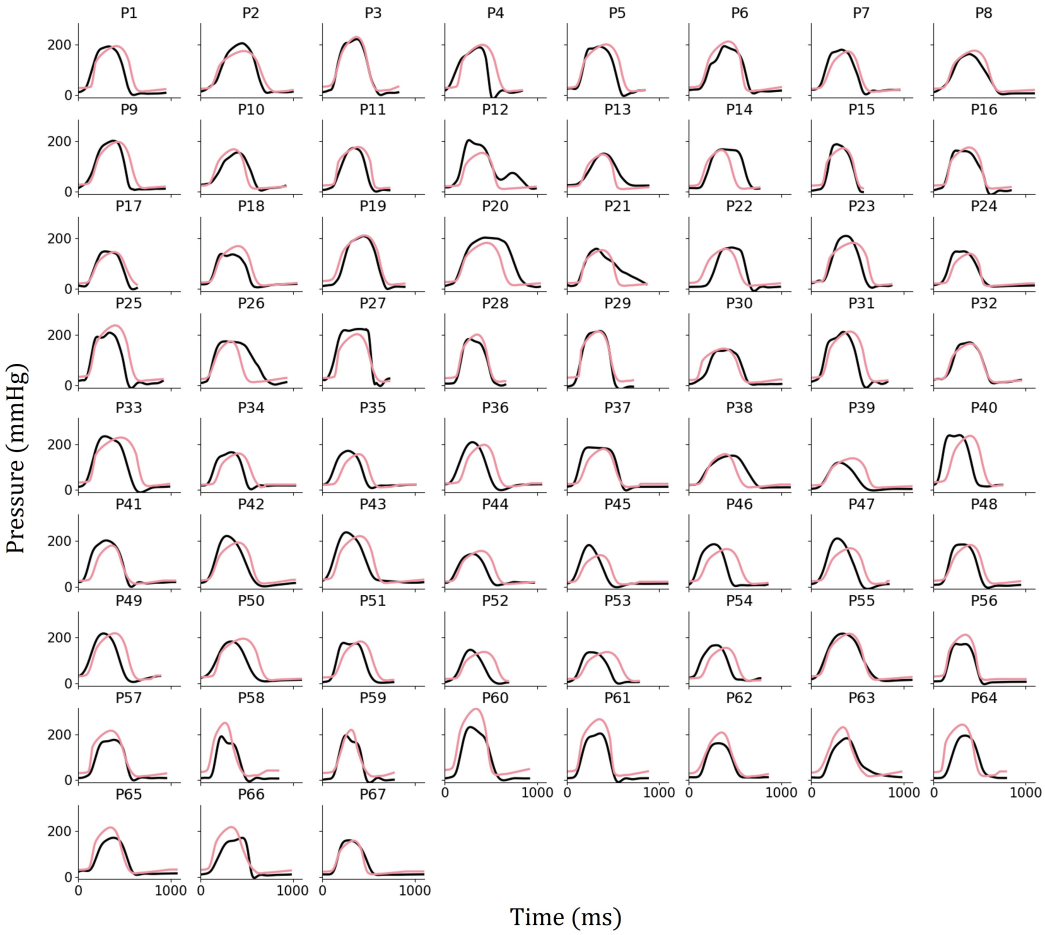

Figure 5.7: Template-based LV pressure curves comparison of 67 patients: experimental (*black*), and estimated (*pink*) curves.

regression line between estimations and measures were 0.79 and 251 mmHg.%, and r^2=0.81. In Bland-Altman analysis, the mean bias of estimation is −251 mmHg.%. For wasted work, slope and intercept of the regression line between estimations and measures are 0.84 and −39.3 mmHg.% and r^2=0.91. In Bland-Altman analysis, the mean bias of estimation is -32. 0mmHg.%. For work efficiency, slope and intercept of the regression line between estimations and measures are 1.00 and −0.003 and r^2=0.92. In Bland-Altman analysis, the mean bias of estimation was -0.007. For GCW, GWW, and GWI the slope and intercept were 0.74 and 327 mmHg.%, 0.83 and 59.6 mmHg.%, 0.77 and 148 mmHg.%, r^2 were 0.76 , 0.80 , and 0.77 and the mean bias were −214 mmHg.%, −70.0 mmHg.%, and −144 mmHg.%, respectively. The negative mean bias observed on all the Bland-Altman analyses could be explained by an under-estimation of MW indices due to a slight advance observed in LV estimated pressure curves in most of the patients with this method.

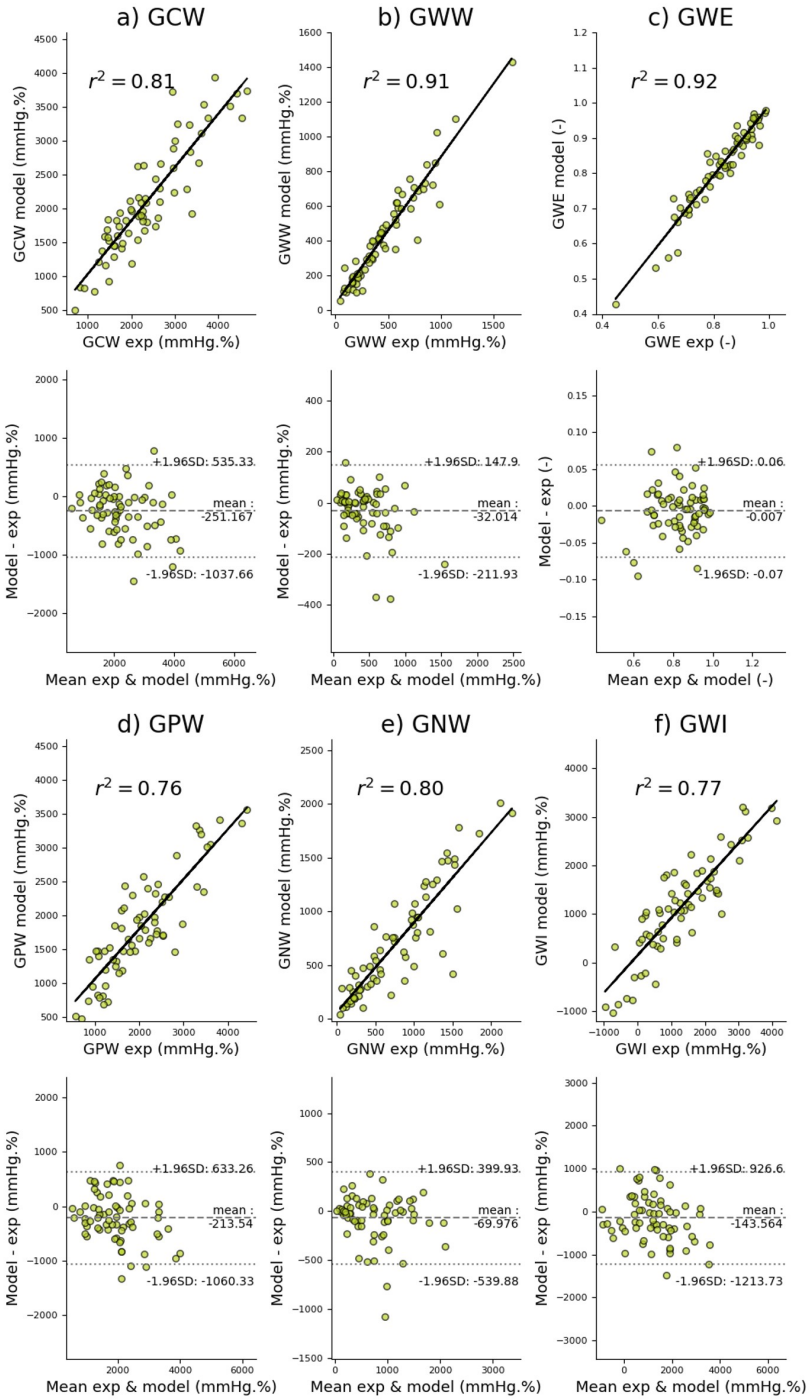

Figure 5.8: Results of global work indices' comparison, on all patients for model-based method. Scatter plots and Bland-Altman analysis of: a) Global Constructive Work (GCW), b) Global Wasted Work (GWW), c) Global Work Efficiency (GWE), d) Global Positive Work (GPW), e) Global Negative Work (GNW), f) Global Work Index (GWI).

Template-based

Template-based MW Figure 5.9 presents the comparison between template-based and invasive indices. Despite an overestimation of all the indices, the quality of the result is similar, with a good correlation coefficient. For GCW, GWW, GWE, GPW, GNW and GWI, slope and intercept of the regression line between estimations and measures were 0.86 and 413 mmHg.%, 0.90 and 103 mmHg.%, 0.89 and 0.08, 0.71 and 576 mmHg.%, 0.88 and 251 mmHg.%, 0.69 and 216 mmHg.% with r^2=0.66, r^2=0.93, r^2=0.93, r^2=0.60, r^2=0.82, and r^2=0.72, respectively. In Bland-Altman analyses the mean bias were 76.8 mmHg.%, 57.4 mmHg.%, −0.013, −19.2 mmHg.%, 156mmHg.%, and −175 mmHg.%, respectively, for the six indices. The bias, here, could be explained by larger pattern of the LV pressure curve in some patients.

In order to propose another error computation and better understand the results, we also calculate for each patient and each MW indices, the relative error:

$$\frac{X^{exp} - X^{estimated}}{X^{exp}}, \quad \text{for} \quad X \in \{GCW, GWW, GWE, GPW, GNW, GWI\} \tag{5.14}$$

These results are gathered with the regression line summary in Table 5.3 for the two methods. We can notice that GCW, GWW and GWE, where the bias is lower, have reasonable relative error (in %) with 14.77%, 16.51%, and 3.10% for the model-based method and 18.38%, 26.70%, and 2.97% for the template-base method, respectively, for these three indices.

5.4 Discussion

A model-based and template-based method were evaluated against invasive hemodynamic assessment of LV-pressure in a prospective cohort and results shown the validity of the estimations made in patients with an AS, combining the mean pressure gradient to the software currently commercially available. MW indices can thus be easily applied in routine clinical practice.

5.4.1 Estimation of LV pressure and MW indices

Concerning the evaluation of LV pressure, both methods show a good agreement between estimated and measured pressure waveforms. To our knowledge, our study is the first to provide a quantitative comparison between two estimated LV pressures and invasively measured curves in the context of AS on such a database. Moreover, myocardial indices calculated with the two estimation methods were compared with indices calculated with invasive pressures. Model-based method allows for the in-silico assessment of MW indices, while integrating physiological knowledge. This method has the advantage of requiring only AVA, pressure gradient evaluated in echocardiography, systolic and diastolic pressure values. The computational model directly integrates a representation of the pathophysiology of the aortic valves and takes into account

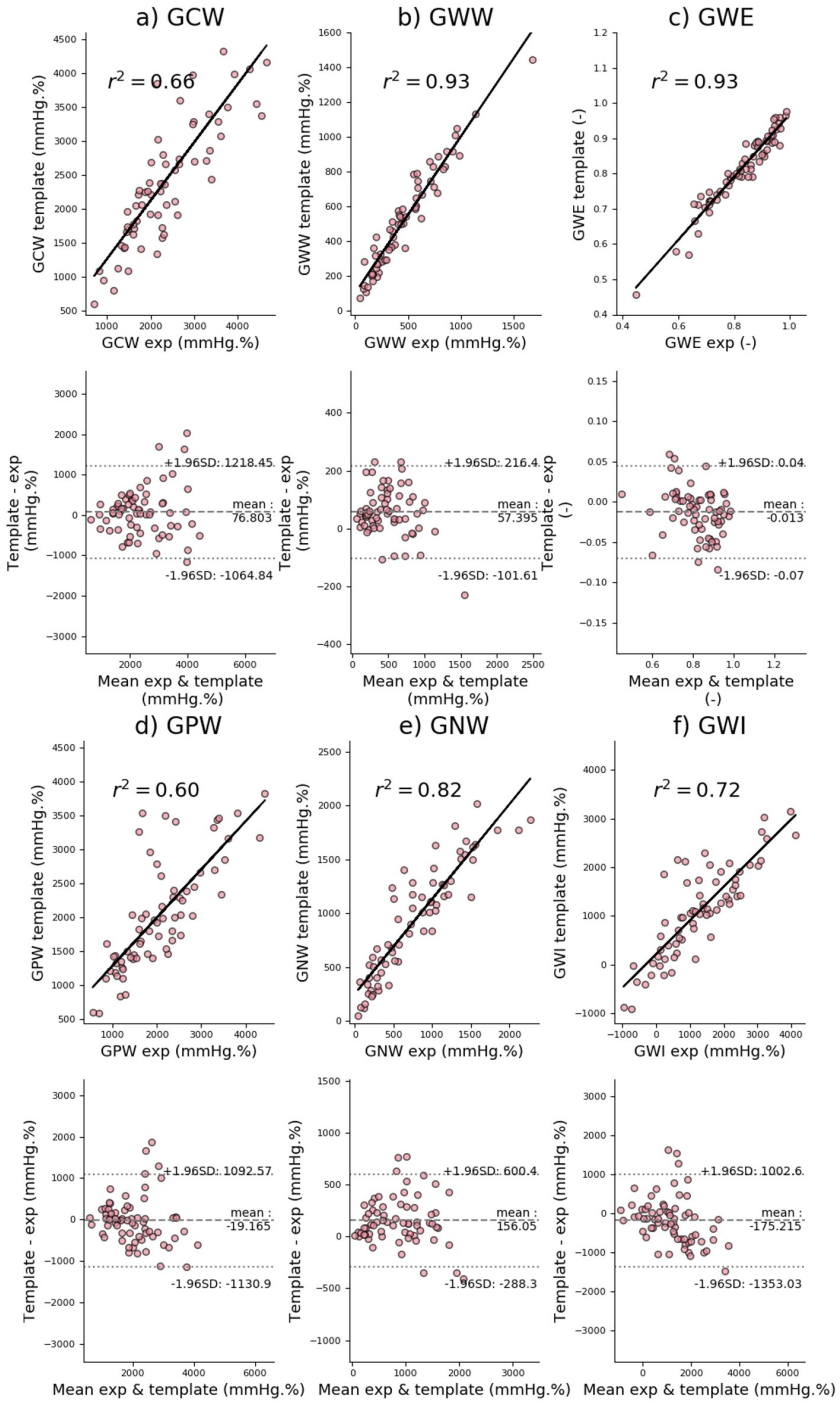

Figure 5.9: Results of global work indices' comparison, on all patients for template-based method. Scatter plots and Bland-Altman analysis of: a) Global Constructive Work (GCW), b) Global Wasted Work (GWW), c) Global Work Efficiency (GWE), d) Global Positive Work (GPW), e) Global Negative Work (GNW), f) Global Work Index (GWI).

Indices		Model-based	Template-based
GCW	Slope	0.79	0.86
	Intercept	250.71	413.05
	r^2	0.81	0.66
	Relative error	14.77	18.38
GWW	Slope	0.84	0.9
	Intercept	39.30	103.26
	r^2	0.91	0.93
	Relative error	16.51	26.70
GWE	Slope	1.00	0.89
	Intercept	0.00	0.08
	r^2	0.92	0.93
	Relative error	3.10	2.97
GPW	Slope	0.74	0.71
	Intercept	326.95	575.93
	r^2	0.76	0.60
	Relative error	19.82	21.13
GNW	Slope	0.83	0.88
	Intercept	59.57	250.92
	r^2	0.80	0.82
	Relative error	29.04	46.24
GWI	Slope	0.77	0.69
	Intercept	147.56	216.36
	r^2	0.77	0.72
	Relative error	85.21	65.89

Table 5.3: Results of the six myocardial work indices line regressions between computation with invasive and estimate LV pressure curves for the model-based and template-based methods.

characteristics associated with the subject and pathology. Compared with model-based approach, template-based estimations require additional information related to aortic and MVO and closure, which should be manually identified on apical 3-chamber view and pulsed wave Doppler recordings. Consequently, evaluations of valve timings could be cumbersome. Despite the manual evaluation of valvular events, the template-based method appears to be more appropriate in a clinical context. In fact, LV pressure and work indices could be directly extracted from the echocardiography workstation, whereas the model-based method implies an off-line procedure associated with a computational cost. Although template-based method could be privileged in clinical practice, model-based approach could be interesting for the evaluation of retrospective databases that do not integrate valve timings.

5.4.2 Work estimation

Despite the imprecise evaluation of LV pressure in both cases, the estimation of LV work indices strongly correlates with invasive measurements [13]. Model-based and template-based approaches appear as accurate methods for the estimation of MW in AS. This good correlation of all the works indices despite the imperfect estimation of LV pressure curves could be explained by different points. First, the temporal integration during the work computation induces a smoothing of the error between experimental and estimated work in both methods. Moreover, the computation of the indices uses only the pressure curve between AVO and AVC. This issue of using LV pressure estimation in order to analyze the MW could be avoided by using other indices based only on strain curves [31].

5.4.3 Myocardial function for AS patients

Current guidelines recommend surgical AVR in patients with Severe AS who have symptoms, or those who have reduced LVEF. The LVEF considered up to now was 50%, but recent papers clearly showed that already for LVEF reaching 55–60%, patient prognosis is already dismal [32, 33]. The severity of AS is not assessed merely by gradient and valve area, but also resides in the interplay between increased LV-after-load of a stenotic valve and its deleterious effects on the myocardium. In a subpopulation of patients with long-standing AS that does not improve after intervention, with increased morbidity and mortality, adverse and irreversible LV-remodeling has often been implicated [34]. Prior meta-analysis revealed that asymptomatic severe AS patients who were treated with a watchful-waiting strategy had a 3.5-fold higher rate of all-cause mortality at 4 years, compared with those who underwent early AVR [4]. Also, Taniguchi et al.[35] demonstrated in a propensity score-matched analysis that patients treated with the initial AVR strategy had a lower risk of all-cause death and heart failure requiring hospitalization, than patients treated with a conservative strategy. Several studies underscore the relevance of a precise assessment of the myocardial consequences of the severe AS. Load is a key factor that impacts parameters quantifying LV systolic function. MW provides a unique opportunity to assess, with much less load dependent, LV systolic function in AS patients [36, 37]. The classic 'pressure–volume' loop, from invasive hemodynamics, has formed the basis of our understanding of the contributions of preload, after-load, and contractility to LV systolic function. The 'area' within this loop is referred to as LV stroke work and was the first way to conceptualize MW. It was followed by 'pressure–strain' loop and the MW indices that offer a complementary picture of LV systolic function. Also, Jain et al. [38] underline that LV function do not fully recover in days and months following Transcatheter Aortic Valve Replacement. (TAVR). By comparing this index pre- and post-TAVR, they demonstrated that GLS improved as MW reduced in patients treated with TAVR for severe AS. Strain indices and MW appear particularly promising, providing a sensitive evaluation of LV function that could guide for potential earlier-TAVR for pauci-symptomatic patients. One limitation of this paper is to treat almost only patient with severe AS. Still large randomized trials

are needed for confirming the value of echo-parameter and to demonstrate that currently, we might propose valve replacement at a late timing according to the heart consequences of the chronic increase in afterload related to the AS.

5.5 Conclusion

The two non-invasive methods of LV pressure estimation and the work indices computation correlate with invasive measurements and computations for as patients. Although the model-based approach requires less information and is associated with slightly better performances, the implementation of template-based method is easier and seems more appropriate in a clinical practice.

In both cases, it permits to provide an effective tool to assess more precisely LV function and help in the patient stratification of this particular population.

BIBLIOGRAPHY

[1] Falk V., Baumgartner H., Bax J.J., De Bonis M., Hamm C., Holm P.J., Iung B., Lancellotti P., Lansac E., Muñoz D.R., Rosenhek R., Sjögren J., Tornos Mas P., Vahanian A., Walther T., Wendler O., Windecker S., and Zamorano J.L. 2017 ESC/EACTS Guidelines for the management of valvular heart disease. *Eur. J. Cardiothorac. Surg.*, vol. 52, 616–664 (2017).

[2] Hachicha Z., Dumesnil J.G., Bogaty P., and Pibarot P. Paradoxical low-flow, low-gradient severe aortic stenosis despite preserved ejection fraction is associated with higher afterload and reduced survival. *Circulation*, vol. 115, 2856–2864 (2007).

[3] Garcia D., Pibarot P., Dumesnil J.G., Sakr F., and Durand L.G. Assessment of aortic valve stenosis severity: A new index based on the energy loss concept. *Circulation*, vol. 101, 765–771 (2000).

[4] Magne J., Cosyns B., Popescu B.A., Carstensen H.G., Dahl J., Desai M.Y., Kearney L., Lancellotti P., Marwick T.H., Sato K., Takeuchi M., Zito C., Casalta A.C., Mohty D., Piérard L., Habib G., and Donal E. Distribution and Prognostic Significance of Left Ventricular Global Longitudinal Strain in Asymptomatic Significant Aortic Stenosis: An Individual Participant Data Meta-Analysis. *JACC Cardiovasc. Imaging*, vol. 12, 84–92 (2019).

[5] Donal E., Bergerot C., Thibault H., Ernande L., Loufoua J., Augeul L., Ovize M., and Derumeaux G. Influence of afterload on left ventricular radial and longitudinal systolic functions: A two-dimensional strain imaging study. *Eur. J. Echocardiogr.*, vol. 10, 914–921 (2009).

[6] Russell K., Eriksen M., Aaberge L., Wilhelmsen N., Skulstad H., Remme E.W., Haugaa K.H., Opdahl A., Fjeld J.G., Gjesdal O., Edvardsen T., and Smiseth O.A. A novel clinical method for quantification of regional left ventricular pressurestrain loop area: A non-invasive index of myocardial work. *Eur. Heart J.*, vol. 33, 724–733 (2012).

[7] ran Wang R., Tian T., qiang Li S., ping Leng X., and wei Tian J. Assessment of Left Ventricular Global Myocardial Work in Patients With Different Degrees of Coronary Artery Stenosis by Pressure-Strain Loops Analysis. *Ultrasound Med. Biol.*, vol. 47, 33–42 (2021).

[8] Galli E., Leclercq C., Hubert A., Bernard A., Smiseth O.A., Mabo P., Samset E., Hernandez A., and Donal E. Role ofmyocardial constructive work in the identification of responders to CRT. *Eur. Heart J. Cardiovasc. Imaging*, vol. 19, 1010–1018 (2018).

[9] Galli E., Leclercq C., Fournet M., Hubert A., Bernard A., Smiseth O.A., Mabo P., Samset E., Hernandez A., and Donal E. Value of Myocardial Work Estimation in the Prediction of Response to Cardiac Resynchronization Therapy. *J. Am. Soc. Echocardiogr.*, vol. 31, 220–230 (2018).

[10] Galli E., Vitel E., Schnell F., Le Rolle V., Hubert A., Lederlin M., and Donal E. Myocardial constructive work is impaired in hypertrophic cardiomyopathy and predicts left ventricular fibrosis. *Echocardiography*, vol. 36, 74–82 (jan 2019).

[11] Hubert A., Galli E., Leurent G., Corbineau H., Auriane B., Guillaume L., Leclercq C., and Donal E. Left ventricular function after correction of mitral regurgitation: Impact of the clipping approach. *Echocardiography*, vol. 36, 2010–2018 (2019).

[12] Russell K., Eriksen M., Aaberge L., Wilhelmsen N., Skulstad H., Gjesdal O., Edvardsen T., and Smiseth O.A. Assessment of wasted myocardial work: A novel method to quantify energy loss due to uncoordinated left ventricular contractions. *Am. J. Physiol. - Hear. Circ. Physiol.*, vol. 305, 996–1003 (2013).

[13] Hubert A., Le Rolle V., Leclercq C., Galli E., Samset E., Casset C., Mabo P., Hernandez A., and Donal E. Estimation of myocardial work from pressure–strain loops analysis: an experimental evaluation. *Eur. Heart J. Cardiovasc. Imaging*, vol. 19, 1372–1379 (2018).

[14] Fortuni F., Butcher S.C., van der Kley F., Lustosa R.P., Karalis I., de Weger A., Priori S.G., van der Bijl P., Bax J.J., Delgado V., and Ajmone Marsan N. Left Ventricular Myocardial Work in Patients with Severe Aortic Stenosis. *J. Am. Soc. Echocardiogr.*, vol. 34, 257–266 (2020).

[15] Owashi K.P., Hubert A., Galli E., Donal E., Hernández A.I., and Rolle V.L. Model-based estimation of left ventricular pressure and myocardial work in aortic stenosis. *PLoS One*, vol. 15, 1–18 (2020).

[16] Owashi K.P. *Model-based analysis of myocardial strains for the evaluation of cardio- vascular function*. Ph.D. thesis, Université Rennes 1 (2021).

[17] Fortuni F., Butcher S.C., van der Kley F., Lustosa R.P., Karalis I., de Weger A., Priori S.G., van der Bijl P., Bax J.J., Delgado V., and Ajmone Marsan N. Left ventricular myocardial work in patients with severe aortic stenosis Federico. *J. Am. Soc. Echocardiogr.*, page 124658 (2020).

[18] Taconne M., Le Rolle V., Panis V., Hubert A., Auffret V., Galli E., Hernandez A., and Donal E. How myocardial work could be relevant in patients with an aortic valve stenosis? *Eur. Hear. J. - Cardiovasc. Imaging*, vol. 23, 1–11 (2022).

[19] Taconne M., Le Rolle V., Owashi K.P., Panis V., Hubert A., Auffret V., Galli E., Hernandez A., and Donal E. Sensitivity Analysis and Parameter Identification of a Cardiovascular Model in Aortic Stenosis. In *Comput. Cardiol. (2010).*, vol. 2021-Septe, page 2 (2021).

[20] Taconne M., Le Rolle V., Panis V., Hubert A., Auffret V., Galli E., Hernandez A., and Donal E. How myocardial work could be relevant in patients with an aortic valve stenosis? *Eur. Hear. J. - Cardiovasc. Imaging*, vol. 23, page 2022 (2022).

[21] Manganaro R., Marchetta S., Dulgheru R., Ilardi F., Sugimoto T., Robinet S., Cimino S., Go Y.Y., Bernard A., Kacharava G., Athanassopoulos G.D., Barone D., Baroni M., Cardim N., Hagendorff A., Hristova K., López-Fernández T., De La Morena G., Popescu B.A., Penicka M., Ozyigit T., Rodrigo Carbonero J.D., Van De Veire N., Von Bardeleben R.S., Vinereanu D., Zamorano J.L., Rosca M., Calin A., Moonen M., Magne J., Cosyns B., Galli E., Donal E., Carerj S., Zito C., Santoro C., Galderisi M., Badano L.P., Lang R.M., Oury C., and Lancellotti P. Echocardiographic reference ranges for normal non-invasive myocardial work indices: Results from the EACVI NORRE study. *Eur. Heart J. Cardiovasc. Imaging*, vol. 20, 582–590 (2019).

[22] Hernández A.I., Carrault G., and Mora F. Model-based interpretation of cardiac beats by evolutionary algorithms. *Comput. Cardiol.*, vol. 29, 93–96 (2002).

[23] Le Rolle V., Hernández A.I., Richard P.Y., Donal E., and Carrault G. Model-based analysis of myocardial strain data acquired by tissue Doppler imaging. *Artif. Intell. Med.*, vol. 44, 201–219 (2008).

[24] Chung D.C., Niranjan S.C., Clark J.W., Bidani A., Johnston W.E., Zwischenberger J.B., and Traber D.L. A dynamic model of ventricular interaction and pericardial influence. *Am. J. Physiol. - Hear. Circ. Physiol.*, vol. 272 (1997).

[25] Calvo M., Le Rolle V., Romero D., Béhar N., Gomis P., Mabo P., and Hernández A.I. Recursive model identification for the analysis of the autonomic response to exercise testing in Brugada syndrome. *Artif. Intell. Med.*, vol. 97, 98–104 (2019).

[26] Stergiopulos N., Meister J.J., and Westerhof N. Determinants of stroke volume and systolic and diastolic aortic pressure. *Am. J. Physiol. - Hear. Circ. Physiol.*, vol. 270 (1996).

[27] Ojeda D., Le Rolle V., Harmouche M., Drochon A., Corbineau H., Verhoye J.P., and Hernandez A.I. Sensitivity analysis and parameter estimation of a coronary circulation model for triple-vessel disease. *IEEE Trans. Biomed. Eng.*, vol. 61, 1208–1219 (2014).

[28] J. P. Mynard , M.R.Davidson3 D. and Smolich J.J. A simple, versatile valve model for use in lumped parameter and one-dimensional cardiovascular models. *Training*, vol. 4179, page 53 (2012).

[29] Morris M.D. Factorial sampling plans for preliminary computational experiments. *Technometrics*, vol. 33, 161–174 (1991).

[30] Hubert A., Le Rolle V., Galli E., Bidaud A., Hernandez A., and Donal E. New expectations for diastolic function assessment in transthoracic echocardiography based on a semi-automated computing of strain–volume loops. *Eur. Heart J. Cardiovasc. Imaging*, vol. 21, 1366–1371 (2020).

[31] Menet A., Bernard A., Tribouilloy C., Leclercq C., Gevaert C., Guyomar Y., Guerbaai R.A., Delelis F., Castel A.L., Graux P., Ennezat P.V., Donal E., and Maréchaux S. Clinical significance of septal deformation patterns in heart failure patients receiving cardiac resynchronization therapy. *Eur. Heart J. Cardiovasc. Imaging*, vol. 18, 1388–1397 (2017).

[32] Dahl J.S., Magne J., Pellikka P.A., Donal E., and Marwick T.H. Assessment of Subclinical Left Ventricular Dysfunction in Aortic Stenosis. *JACC Cardiovasc. Imaging*, vol. 12, 163–171 (2019).

[33] Bohbot Y., de Meester de Ravenstein C., Chadha G., Rusinaru D., Belkhir K., Trouillet C., Pasquet A., Marechaux S., Vanoverschelde J.L., and Tribouilloy C. Relationship Between Left Ventricular Ejection Fraction and Mortality in Asymptomatic and Minimally Symptomatic Patients With Severe Aortic Stenosis. *JACC Cardiovasc. Imaging*, vol. 12, 38–48 (2019).

[34] Bridonneau V., Galli E., Auffret V., Lederlin M., Campion M., Le Breton H., Boulmier D., Hubert A., Lenz P.A., Leclercq C., Oger E., and Donal E. Management of aortic valve replacement according to the gradient across symptomatic aortic valve stenosis and its prognostic impact. *Echocardiography*, vol. 36, 2136–2144 (2019).

[35] Taniguchi T., Morimoto T., Shiomi H., Ando K., Kanamori N., Murata K., Kitai T., Kawase Y., Izumi C., Miyake M., Mitsuoka H., Kato M., Hirano Y., Matsuda S., Nagao K., Inada T., Murakami T., Takeuchi Y., Yamane K., Toyofuku M., Ishii M., Minamino-Muta E., Kato T., Inoko M., Ikeda T., Komasa A., Ishii K., Hotta K., Higashitani N., Kato Y., Inuzuka Y., Maeda C., Jinnai T., Morikami Y., Sakata R., and Kimura T. Initial Surgical Versus Conservative Strategies in Patients with Asymptomatic Severe Aortic Stenosis. *J. Am. Coll. Cardiol.*, vol. 66, 2827–2838 (2015).

[36] Jain R., Khandheria B.K., and Tajik A.J. Myocardial Work in Aortic Stenosis: It Does Work! *J. Am. Soc. Echocardiogr.*, vol. 34, 267–269 (2021).

[37] Roemer S., Jaglan A., Santos D., Umland M., Jain R., Tajik A.J., and Khandheria B.K. The Utility of Myocardial Work in Clinical Practice. *J. Am. Soc. Echocardiogr.*, 1–12 (2021).

[38] Jain R., Bajwa T., Roemer S., Huisheree H., Allaqaband S.Q., Kroboth S., Perez Moreno A.C., Tajik A.J., and Khandheria B.K. Myocardial work assessment in severe aortic stenosis undergoing transcatheter aortic valve replacement. *Eur. Heart J. Cardiovasc. Imaging*, vol. 22, 715–721 (2021).

Chapter

6 Sudden Cardiac Death Prediction in Hypertrophic Cardiomyopathy Patients

As mentioned in Section 1.3.3, Hypertrophic CardioMyopathy (HCM) represents a major cause of Sudden Cardiac Death (SCD), particularly in the young people, with a risk of about 1% per year [1, 2]. Hypertrophied myocardial areas are characterized by myocardial disarray, interstitial and focal fibrosis constituting the substrate of ventricular arrhythmias which classically occurs in addition to an excess of sympathetic tone (e.g. exercise, stress) and/or ischemia (e.g. functional ischemia, specific small vessel disease) [3, 4].

Primary prevention of SCD is based on Implantable Cardiac Defibrillator (ICD) with good effectiveness but at the cost of an invasive procedure and device complications including infection and inappropriate shocks [5]. Identification of patients at risk of SCD is still a major clinical challenge. Current international guidelines rely on retrospective evaluations of old HCM cohorts and are based on limited and pre-selected clinical and imaging predictor variables to select patients at risk of SCD [6, 7]. As a consequence, the European Society of Cardiology (ESC) five years risk of SCD score demonstrates relatively weak performance, with a C-index of 0.69 to identify SCD [6]. In comparison to classical statistical analysis, machine learning allows a hypothesis-free and data-driven approach, processing a larger amount of various parameters to generate dynamic self-learning models [8, 9]. In this context, left ventricle global longitudinal strain (LV-GLS) is a promising tool that has already shown relevance in the detection of ventricular arrhythmias in HCM patients [10].

Cardiac magnetic resonance imaging reveals the presence of myocardial fibrosis and disarray in HCM patients, which is linked to a higher likelihood of ventricular arrhythmias. These findings align with a mechanical decrease and temporal delay in the segmental LV longitudinal strain of affected regions [10–14]. This suggests that the excessive mechanical and temporal heterogeneity in the deformation of the left ventricular myocardial wall could indicate significant histological and electrophysiological remodeling at high arrhythmogenic potential.

In this chapter, we sought to investigate whether a machine learning model using heterogeneous data: clinical and imaging variables in addition to left ventricular longitudinal strain information could be relevant for the prediction of SCD risk in HCM patients. It is also a perfect example of the use of signal and data processing in a complete machine learning process and could be placed on the right part of our methodological thesis illustration.

This chapter follows the work submitted as co-first author with Adrien Al Wazzan and presented at *EACVI* congress [15]

6.1 Data

6.1.1 Population

535 consecutive patients with HCM established according to current guidelines [16] were retrospectively enrolled between 2008 and 2019 from two tertiary centers: the University Hospital of Rennes, France and the University Hospital of Oslo, Norway. The exclusion criteria were as follows: lack of a complete echocardiographic assessment, insufficient image quality enabling the analysis of echo data, age < 18 years, history of Acute Coronary Syndrome (ACS) and significant Coronary Artery Disease (CAD). 434 patients were left. The study was conducted according to the Declaration of Helsinki and approved by internal review boards of each center. All patients provided informed consent for the conduction of the study.

6.1.2 Clinical and Imaging data

All patients underwent a standard and 2D-speckle-tracking transthoracic echocardiography at baseline using a Vivid 7, E9, or E95 ultrasound system (GE Healthcare, Horten, Norway). The 2D, color Doppler, pulsed-wave, and continuous-wave Doppler data were stored on a dedicated workstation (EchoPAC v204; GE Healthcare, Horten, Norway) and offline analysis was made according to the recommendations [17]. An apical aneurysm was defined as a discrete thin-walled dyskinetic or akinetic segment [17]. All the echographic measurements were performed blind to clinical data and events. Clinical data were collected from electronic health records. Other initial investigations included a 12-lead electrocardiogram (ECG), a 48 hours Holter monitoring, an exercise stress test, a CMR with Late Gadolinium Enhancement (LGE) sequences, and a genetic testing for sarcomeric mutations. 12-lead ECGs were analyzed according to recommendations [18] with automatic measurements for interval, duration and axis and visual assessment for repolarization abnormalities. Cardiac magnetic resonance imaging was performed within 2 years after baseline inclusion. The presence or absence of LGE was assessed qualitatively. Exercise testing was made on a bicycle ergometer with stepped increasing load and continuous ECG recording. Maximal predicted heart rate was calculated with 220-age formula and predicted peak work from the Cooper and Storer formula [19].

6.1.3 Outcome and follow-up

Endpoint for ventricular arrhythmias included:

— history of Aborted Cardiac Arrest (ACA),

- history of Sustained Ventricular Tachycardia (SVT),
- history of appropriate ICD therapy,
- SVT during follow-up,
- appropriate ICD therapy during follow-up,
- aborted cardiac arrest during follow-up,
- suspected SCD.

All patients underwent follow-up in accordance with the recommendations, including repetitive 24-48 hours Holter monitoring and ICD interrogation looking for ventricular arrhythmias and/or appropriate shocks if applicable [16]. Non-Sustained Ventricular Tachycardia (NSVT) was defined as runs of ventricular beats with duration between $\geq$3 beats and 30s with heart rate >100 bpm [20].

Data for events were collected from electronic patient records and from information provided by the referring cardiologists if available. The risk of SCD was evaluated according to the 2020 AHA/ACC Guideline for the diagnosis and Treatment of HCM [7] and with the 5 years-risk of SCD score (HCM risk-SCD) of the 2014 HCM guidelines by the European Society of Cardiology (ESC) [16].

6.1.4 2D LV strain analysis

Left ventricle longitudinal strain by speckle tracking echocardiography was obtained from 2D apical 2-, 3-, and 4- chamber views at a frame rate of at least 60 m/s, each view containing 6 segments. Endocardial borders were semi-automatically defined and manually adjusted if needed. Visual assessment for good quality of wall tracking was done and patients were excluded in case of insufficient or aberrant tracking. Region of interest was automatically defined between the endocardial and epicardial borders and adjusted to fit the myocardial thickness. The temporal window of strain collection was between two R-waves on ECG, R-waves used as zero-reference. Aortic Valve Closure (AVC) time was automatically defined from the 3ch view. Figure 6.1 presents three patients strain curves with their three echo-views.

6.2 Method

6.2.1 Feature extraction

The calculated longitudinal strain curves were exported from the EchoPAC software in raw files containing strain times series and AVC time for each of the 18 segments of the LV, allowing a virtual reconstruction of LV strain curves for each patient. A standardization consisting of an upsampling to 500 Hz of the strain curves and elimination of the strain values between 5% and -5% was applied. From these files, automatic extraction of the strain features was performed as

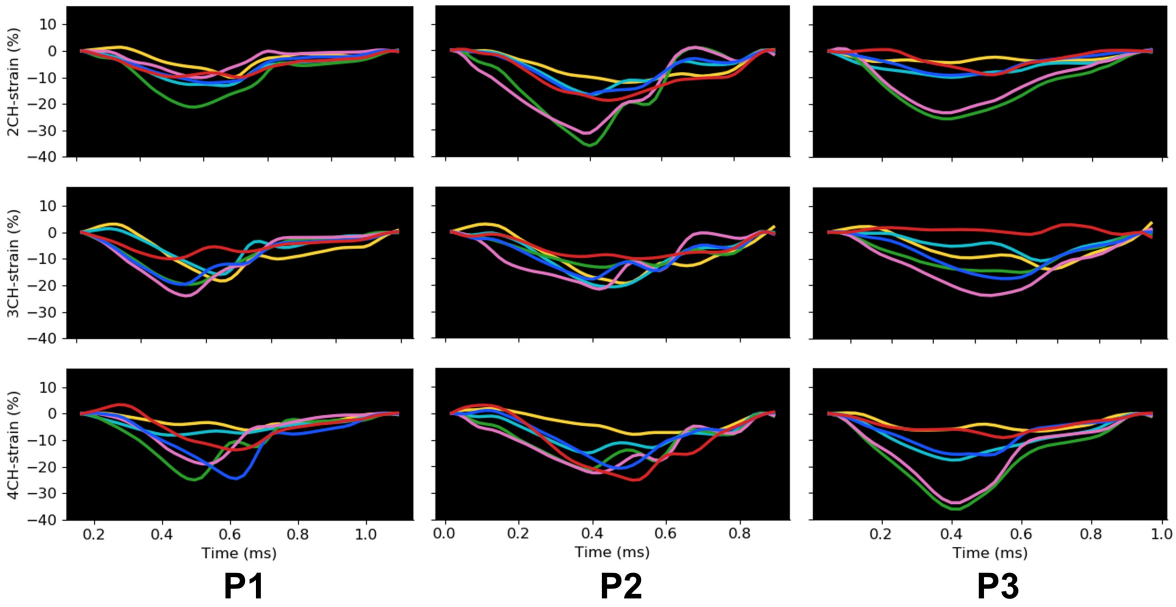

Figure 6.1: Strain curves of 3 HCM patients (*P1*, *P2*, *P3*) separated in 3 echo-views:
2-chamber: basal inferior (*yellow*), mid inferior (*cyan*), apical inferior (*green*), apical anterior (*pink*), mid anterior (*blue*), basal anterior (*red*).
3-chamber : basal anteroseptal (*yellow*), mid anteroseptal (*cyan*), apical anteroseptal (*green*), apical inferolateral (*pink*), mid inferolateral (*blue*), basal inferolateral (*red*).
4-chamber: basal inferoseptal (*yellow*), mid inferoseptal (*cyan*), apical inferoseptal (*green*), apical anterolateral (*pink*), mid anterolateral (*blue*), basal anterolateral (*red*).

shown in Figure 6.2 and already fully described in Section 2.2.1. R-wave was used as a reference for the calculation of all features.

The first comparative step was to compare these strain parameters using different levels of comparison in order to highlight all potential levels of temporal and/or mechanical heterogeneity in LV deformation. Thus, LV has been subdivided as follows: segmental (18 segments : s), regional (each segment s with the four or three segments surrounding it), LV-walls (e.g. anteroseptal AS), LV pole (basal and apical) and apical chamber views (2-, 3-, 4- chamber views) (Figure 6.2). Strain minimum value (S_{min}) and timing (t_{min}) as well as strain value and timing at the Aortic Valve Closure (AVC) were extracted (Savc, Tavc) from the curves. The difference between these values were then computed ($S_{peak} - S_{avc}$, $t_{peak} - t_{avc}$). Estimation of strain integrals during different time support (I^s_{peak}, I^s_{avc} and the difference E^s) were automatically extracted from these 18 strain curves as described in previous work [21, 22]. Comparisons were made by calculating the standard deviation for each parameter at each level.

The second step was to compare the shape of the strain curve considered over the entire cardiac

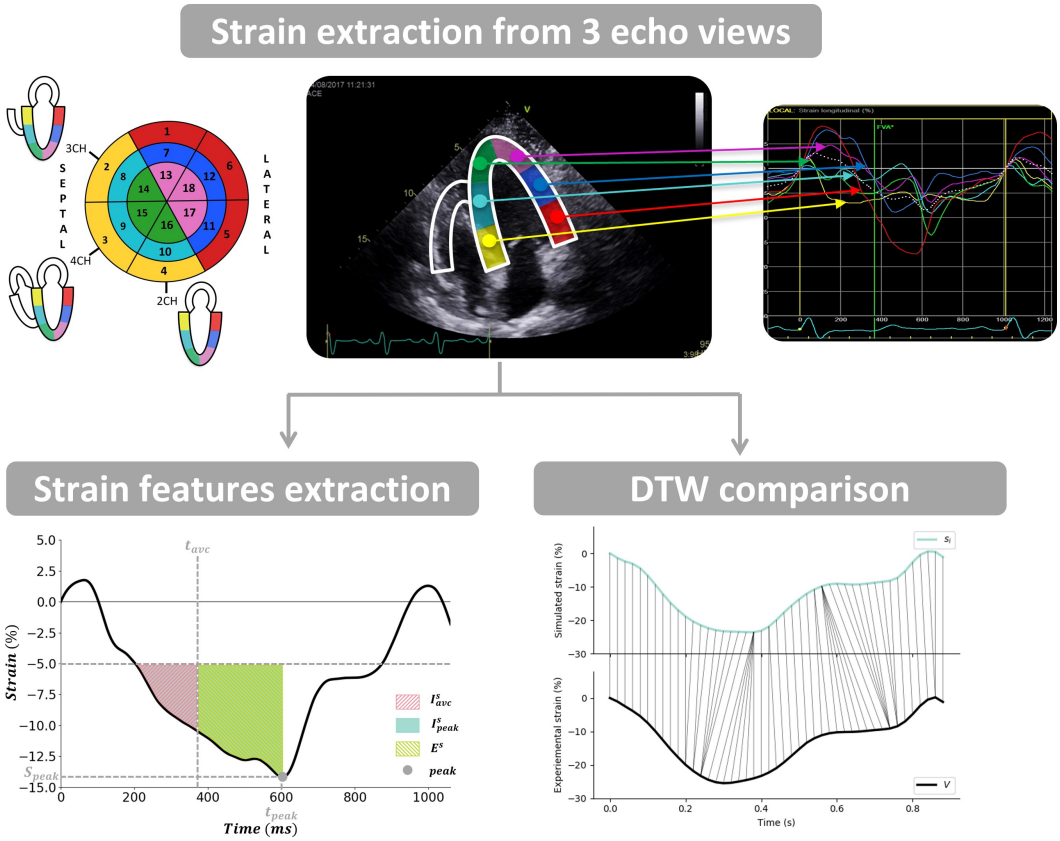

Figure 6.2: LV longitudinal strain features extraction and strain shape comparison with DTW (Dynamic Time Warping) method. For the strain features extraction step, 3 types of parameters were extracted from each segmental strain curve to be subsequently used in the model:
- temporal parameters (ms): time to peak of strain (t_{peak}), time to AVC (t_{avc}), difference between these two ($t_{peak} - t_{avc}$).
- mechanical parameters (% of strain): peak value of strain (S_{peak}), strain value at AVC (S_{avc}), difference between these two ($S_{peak} - S_{avc}$).
- integration of the first two parameters (area under the curve): integral to peak (I_{peak}), integral to AVC (I_{avc}), difference between these two (E).
Dynamic time warping (DTW) method compare similarity between two temporal sequences with different activation time but the same curve shape. At the bottom right, an example with a segmental LV strain with the average LV strain of the corresponding view.

cycle. In order to highlight only shape differences regardless of time sequence activation, a Dynamic Time Warping (DTW) method was used to overcome physiological time lag in the onset of the contraction between LV regions (e.g. base vs apex) (Figure 6.2). Strain curves distance comparison was performed between each segmental curve (s_i) and the average curve of the corresponding apical view (DTW^{s_i}) after applying DTW method.

6.2.2 Feature selection

By combining clinical and imaging information with extracted strain features, a dataset of 287 parameters was created. Figure 6.3 illustrates the ML pipeline. Features selection is a preliminary step that measures the strength of the relationship of variables with the event in order to keep a reduced set of the most meaningful feature to build the final model. The most effective method of feature selection was the estimation of coefficients for each variable by a "Ridge Regression" method. Among the selected features, a high correlation was found between some of the strain features (correlation index > 0.7) and only the features presenting the highest relative importance were kept for further analysis after ensuring that it would not affect the model's performance.

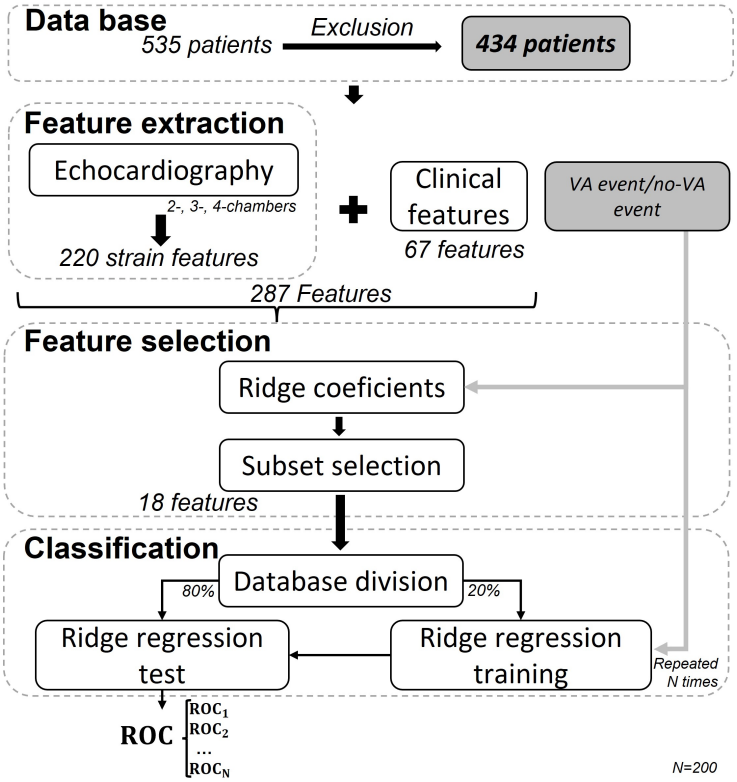

Figure 6.3: Machine learning pipeline. Clinical information and data extracted from LV longitudinal strain curves were collected for 434 HCM patients. Among the 287 features extracted (220 strain-derived), a sub-selection of the most discriminating features was made according to ridge coefficient order. Finally, the final performance of the model is obtained after a repeated cross validation step.

6.2.3 Machine Learning algorithm

The final model was based on a "Ridge Regression" algorithm, which is particularly suitable when the dataset is highly unbalanced (only 7.8% of the patients with an event in our cohort) and /or when there are correlations between predictor variables. The ridge regression was trained

using the reduced sample of the database. The global performance was assessed by a repetitive cross-validation method, which randomly selects at each round 80% of the population to be trained (training dataset) and 20% to be tested (test dataset). After N training rounds, based on N different training and test data sets, the ROC curve and the corresponding AUC of the final model were estimated (Figure 6.3).

Oversampling and undersampling of the database

Another test was applied on this study, the training set was oversampled and undersampled. The testing set was unchanged, and this process was also repeated in cross validation 200 times.

The oversampling process is a technique that creates new synthetic points (patients) of the minority class to better balance the training dataset. The oversampling technique use here was an Adaptive synthetic sampling (ADASYN) [23]. ADASYN is a technique that generate new synthetic "patients" depending on an estimate of the local distribution of the class to be oversampled: the patient with event.

On the other hand, the undersampling process aims at balancing the class distribution for a classification dataset that has a skewed class distribution. The undersampling used here was a random undersampling algorithm. For these two resampling, a ratio (α) must be chosen. It is the number of samples in the minority class over the number of samples in the majority class after resampling:

$$\alpha = N_{rm}/N_M \tag{6.1}$$

where N_{rm} is the number of samples in the minority class after resampling and N_M is the number of samples in the majority class.

6.2.4 HCM Risk computation

ESC risk score

ESC risk score is a probability of SCD at 5 years [6]. It is calculated using a derived Cox proportional hazard model:

$$P_{SCD} = 1 - 0.998e^{Prognostic_{Index}} \tag{6.2}$$

with $Prognostic_{Index}$ = 0.15939858 · Maximal wall thickness (mm) - 0.00294271 · Maximal wall thickness^2 (mm^2) + 0.0259082 · Left atrial diameter (mm) + 0.00446131 · Maximal left ventricular outflow tract gradient (mmHg) + 0.4583082 · Family history SCD + 0.82639195 · NSVT + 0.71650361 · Unexplained syncope - 0.01799934 · Age at clinical evaluation (years).

The value 0.998 is the average survival probability at 5 years).

AHA risk index

AHA risk index [7] is positive if at least one of the following features is true:

- family history of SCD,
- Massive LV hypertrophy,
- Unexplained syncope,
- Apical aneurysm,
- LVEF $\leq$ 50%.

6.2.5 Statistical and machine-learning analysis

A custom-made methods and algorithms, developed in the *Python* language, were used to analyze and extract strain features from the strain times series files. Ridge regression algorithm was implemented using the *Sklearn Python* library [24]. The regularization parameter was automatically chosen by the algorithm. DTW analysis was made using a *fastDTW* algorithm [25]. The clinical and echocardiographic parameters were statistically analyzed. Quantitative variables were expressed as mean ± standard deviation, and qualitative variables were given in numbers and percentages. Univariate analysis was used to identify markers of ventricular arrhythmias by unpaired t-test or Pearson χ^2 where appropriate. Intrinsic performances (Sensitivity, Specificity), corresponding AUC and extrinsic performances (positive and negative predictive value) have been calculated for each of the three models (ESC risk score, AHA risk model, and machine-leaning model) using a threshold of $\geq$ 4%/5 years (ESC risk score) and $\geq$ 1 risk factors (AHA risk model) as positive test and occurrence of the composite endpoint as the event. The threshold for ML-based model was chosen to maximize the geometric mean of the sensitivity and specificity.

6.3 Result

6.3.1 Study population and outcome

From an eligible population of 535 patients, a total of 434 patients with HCM were finally included from both centers (201 patients from Rennes and 233 patients from Oslo). 71 patients were excluded for insufficient image quality, 18 for a history of CAD or ACS, and 12 for technical issues. Clinical and demographic characteristics of the population are displayed in Table 6.2. The mean follow-up duration was 6 years. 34 patients (7.8%) experienced VA, mainly during follow-up (11 SVT, 9 suspected SCD, 2 appropriate ICD therapy, and 1 ACA during follow-up, and 5 previous SVT and 5 previous ACA). The annual incidence of VA was 0.9%/years. Results of the baseline work-up are shown in Table 6.1.

Figure 6.4 presents the predicted by the ESC risk score and the observed outcome of the population.

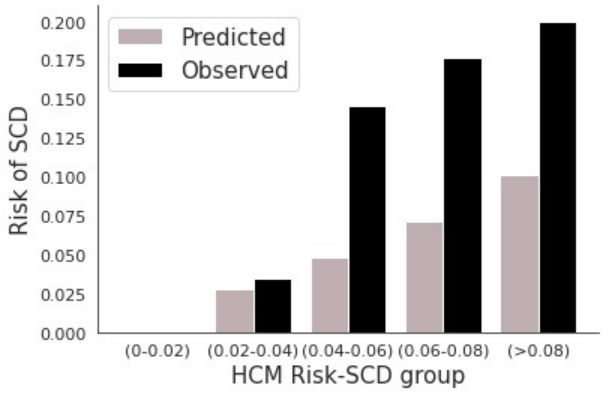

Figure 6.4: ESC risk prediction.

6.3.2 Feature selection

Figure 6.5 shows the 18 most important features selected after the feature selection phase:

- 7 derived from LV longitudinal strain analysis,
- 2 clinical (unexplained syncope, female gender),
- 6 echocardiographic (LVEF < 50%),
- apical aneurysm,
- apical hypertrophy,
- E/A ratio,
- mean E/e' ratio,
- left atrial volume),
- 1 electrocardiographic (NSVT),
- 2 from exercise test (work peak, maximal heart rate).

Among the strain features set, the two most important features were DTW^{MI} and DTW^{MS}, representing the difference in curve shape between LV mid-inferior segment and the 2-chamber view average strain curve and between LV mid-inferoseptal and the 4-chamber view average strain curve, respectively. Other strain features retained in the feature selection were:

- $S_{peak} - S_{avc}$ for the apical anterolateral ($apiantlat$), the apical anterior ($apiant$) and the mid inferior ($midinf$) segments: $S_{peak}^{apiantlat} - S_{avc}^{apiantlat}$, $S_{peak}^{apiant} - S_{avc}^{apiant}$ and $S_{peak}^{midinf} - S_{avc}^{midinf}$ (which represent the difference between strain value at peak and strain value at AVC for the corresponding segments),
- E for the apical anterolateral segment: E^{apiant} (difference between integral to peak and integral to AVC for the apical anterolateral segment)
- DTW for the mid anterolateral ($midantlat$) segment: $DTW^{midantlat}$.

Variables	Overall (N=434)	Non-event group (N=400)	Event group (N=34)	p value
Age (years)	56 .29±14.88	56.23±14.94	56.91±14.06	0.799
Male (%)	65.44%	66%	58.82%	0.511
BMI (%)	26.80±4.30	26.79±4.02	26.93±5.29	0.86
HR (bpm)	69.14±58.47	69.57±60.67	64.04±16.96	0.597
SBP (mmHg)	136.63±73.4	137.52±76.24	126.17±19.17	0.388
DBP (mmHg)	78.74±11.51	78.84±11.57	77.47±10.67	0.506
Genetic mutations	44.24%	44.5%	41.18%	0.864
- MYBC3	26.50%	26.5%	26.47%	0.843
- MYH7	11.29%	11.25%	11.76%	0.848
- TNNI3	1.15%	1.25%	0%	0.856
- TNNT2	3.00%	3%	2.94%	0.614
HCM family history	41.24%	41.75%	35.29%	0.580
SCD family history	11.98%	12%	11.76%	0.815
ICD implantation	11.75%	8.75%	41.18%	4.94E-8
Myomectomie/SRT	14.29%	15%	5.88%	0.229
NYHA				0.081
- NYHA 1	25.8%	26.75%	14.71%	
- NYHA 2	44.24%	42.25%	67.65%	
- NYHA 3-4	16.82%	17.5%	8.82%	
Palpitations	24.19%	24.25%	23.53%	0.909
Unexplained syncope	12.44%	11.75%	20.59%	0.219
Arterial hypertension	27.42%	28.75%	11.76%	0.054
Beta-blocker	70.51%	69.75%	79.41%	0.322
Calcium-blocker	13.82%	13.75%	14.71%	0.917

Table 6.1: Baseline work-up characteristics in the overall population and in patients with and without ventricular arrhythmia.

All the ordered features are provided in Appendix D (Table D.1).

6.3.3 Ventricular arrhythmias prediction

Figure 6.6 shows the area under the Area Under Curve (AUC) for the prediction of ventricular arrhythmia for each of the three risk models. After N=200 cross-validation rounds, the study's risk model has the highest predictive performance with a final AUC of 0.83 $\pm$ 0.08 (sensitivity 0.77 $\pm$ 0.17, specificity 0.8 $\pm$ 0.1). In comparison, ESC risk score (for $\geq$ 4%/5 years risk of SCD) and AHA/ACC (for $\geq$ 1 risk factor of SCD) model exhibit AUC of 0.56 (sensitivity 0.38, specificity 0.83) and 0.61 (sensitivity 0.47, specificity 0.74) respectively (Figure 11). Our model showed a

Variables	Overall *(N=434)*	Non-event group *(N=400)*	Event group *(N=34)*	p value
Echocardiography				
MWT (mm)	19.06±4.26	19.02±4.26	19.59±4.16	0.452
Peak LVOT (mmHg)	24.62±31.02	25.28±31.76	16.85±18.84	0.129
LVH localisation				
- Septal	34.56%	35.25%	26.47%	0.353
- Septal + other	46.77%	46.25%	52.94%	0.568
- Apical	12.67%	11.75%	23.53%	0.097
Apical aneurysm	0.92%	0.25% 8.82%	4.36E-5	
LVEDD (mm)	45.39±7.66	45.08±7.52	49.03±8.4	0.0038
LVEDD (mm)	30.76±7.44	30.50±7.07	33.79±10.40	0.013
MR				
- mild	37.10%	36.5%	44.12%	0.485
- moderate	17.97%	18%	17.65%	0.856
- severe	2.53%	2.75%	0%	0.681
E/A ratio	1.33±1.29	1.27±0.92	2.00±3,36	0.0016
EDT (ms)	226.0±79.84	227.24±78.14	211.88±96.54	0.283
E/e' mean	12.96±7.15	12.74±6.89	15.58±9.36	0.026
LA diameter (mm)	43.0±7	42.99±7.57	43.44±8.45	0.743
LAV (ml/m^2)	43.46±18.43	42.82±17.57	51.06±23.35	0.012
LVEDV (mL)	98.45±37.39	97.54±36.50	109.21±45.24	0.081
LV-EF (%)	65.25±10.32	65.54±9.87	61.82±14.17	0.044
LV-EF (<50%)	5.99%	4.25%	23.53%	3.92E-5
LV-GLS (%)	-15.3 (17.6;12.5)	-15.3 (17.6;12.7)	-14.4 (16.78;10)	0.171
Exercise testing				
Peak work (% pred)	87.85±82.71	91.14±62.54	49.15±199.19	0.004
THR (%)	80.80±12.06	81.03±12.08	78.12±11.43	0.178
Holter-monitoring				
NSVT history	16.82%	16.00%	26.47%	0.184
ECG				
- Q-wave or PRWP	12.21%	12%	14.71%	0.849
- ST changes	11.75%	11.5%	14.71%	0.780
- T-wave inversion	57.14%	56.75%	61.76%	0.700
MRI				
LV-LGE	73.50%	72.75%	82.35%	0.402

Table 6.2: Main clinical characteristics in the overall population and in patients with and without ventricular arrhythmia.

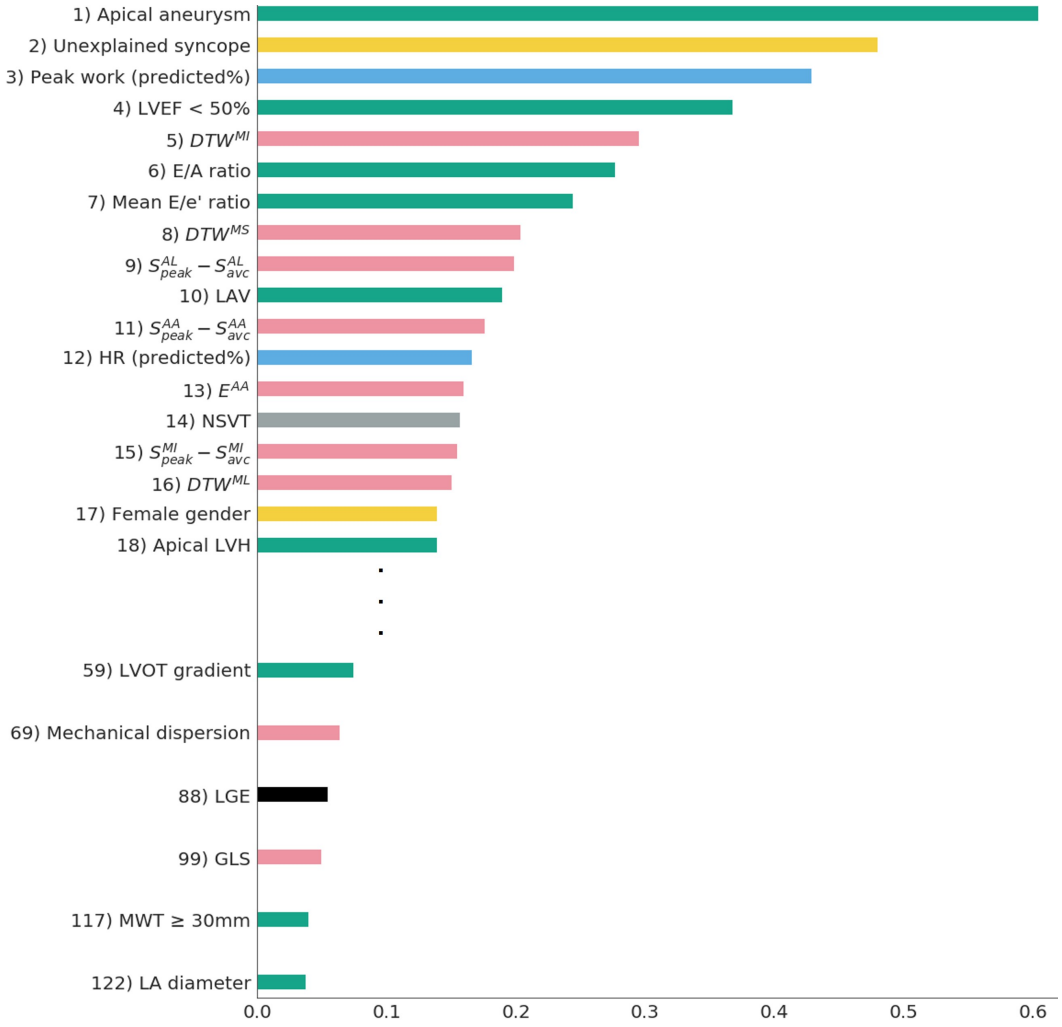

Figure 6.5: Subset of 18 selected features. Features are classed by decreasing Ridge coefficients importance. 7 derived from LV longitudinal strain analysis (*pink bars*), 2 clinical (*yellow bars*), 6 echocardiographic (*green bars*), 1 electrocardiographic (*gray bar*), 2 from exercise test (*blue bars*). The lower part of the figure shows the place of other known risk factors that were not included in the model (MRI indices in *black*). Mechanical dispersion was defined as the standard deviation of t_{min} in the 18 segments.

predictive positive value of 0.27 $\pm$ 0.13 and a negative predictive value of 0.98 $\pm$ 0.02. ESC risk score and AHA/ACC model showed a predictive positive value of 0.16 and 0.14, respectively, and the same negative predictive value of 0.94.

Only clinical features

An AUC of 0.83$\pm$0.8 was found for the same algorithm with the same selected features except the strain extracted features which were deleted to illustrate their contribution.

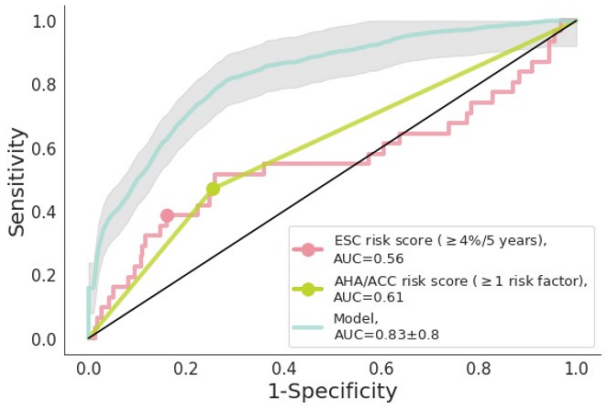

Figure 6.6: ROC curves for prediction of VA events in HCM patients. *Pink* curve shows the 2014 ESC risk score, *green* curve represents the 2020 AHA/ACC risk model and *blue* curve represent the ML-based model.

Oversampling and undersampling

The oversampling and undersampling were applied only on the training set during 200 cross validation evaluations. The ADASYN ratio was put at 0.5 and the random undersampling ratio was put at 0.6. This addition provides a better training for the algorithm that results in a 0.89±0.07 AUC (Figure 6.7). These two resampling reduce the unbalance characteristic of our original dataset by "creating" new positive patients (oversampling) and better balance the training set by selecting only a part of the non-training set (undersampling).

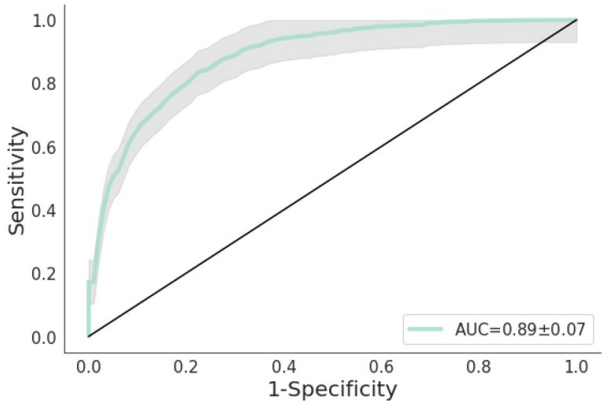

Figure 6.7: ROC curve with oversampling and undersampling of the database.

6.4 Discussion

In this study, we developed a performing prediction method of SCD risk in HCM patients using Machine Learning (ML). The computational approach allowed an automatic extraction and comparison of physiological parameters from LV longitudinal strain curves and their utilization

along with clinical and imaging parameters in a ML-based algorithm. In this bi-centric cohort, the predictive performance of our model was superior to the currently recommended risk score for SCD prediction, with an AUC of 0.83.

6.4.1 Justification of the methods

The most effective ML approach was based on a Ridge regression for both feature selection and model building. Other less successful methods were tested, including Random Forest. We avoided Deep Learning (DL) approach, which needs massive datasets and would expose us to a high risk of overfitting. Moreover, DL methods lack interpretability and would not allow the identification of new predictive features. The use of a DTW algorithm is an original approach that, to our knowledge, has never been used to compare the similarity of LV strain temporal sequences of HCM patients. This strain curve shape comparison resulted in the extraction of the two most important strain parameters in our model. Also, the other strain features were never tested in the field of HCM patients.

6.4.2 Features selection

DTW^{midinf} was, by far, the most useful LV strain parameter for the algorithm. The inferior wall is not usually involved by hypertrophy, the inferior extension of adverse remodeling could indicate a high burden of fibrosis and/or disarray with rhythmic over-risk. The other strain parameters were mainly related to the LV apex, highlighting the mechanical and temporal disarray of the apical segments. This is consistent with the fact that apical remodeling is an important poor prognostic factor in HCM patients [26, 27] which was also found in our model since apical aneurysm was the most powerful predictive factor. Despite having implemented dispersion parameters at different levels of comparison, the individual segmental strain parameters were, with the strain shape comparison, the only strain parameters used by the algorithm. This may result from the interesting properties of the DTW distance that catch the similarities between two curves in their entirety without penalize acceleration or deceleration in the signal. Diastolic parameters were also well represented with E/A ratio, E/e' ratio, and left atrium volume. Diastolic dysfunction and LA dilatation are associated with a known increased risk of SCD in HCM patients [28, 29]. In contrast to left atrium volume, the LA diameter, which is included in the ESC algorithm, was not selected by our model [7, 16]. Both the peak work and the percentage of predicted maximal heart rate were found as predictive factors in our model in an uncorrelated manner. Exercise capacity limitation is a well-identified prognostic factor in HCM patients, and chronotropic incompetence might be associated with an increased risk of SCD [30, 31]. Even though it has a relatively low coefficient in our model, it has also been shown that the female gender is associated with poorer survival in HCM patients [32]. Other selected features including apical aneurysm, LVEF < 50%, NSVT, and unexplained syncope are well-known risk factors of SCD already included in the current recommended risk models. The presence or absence of LGE was not relevant for the prediction

model. This may be explained by the lack of fibrosis quantification, not enabling the identification of high-risk patients with extensive fibrosis as defined by Chan et al. [13]. On the other hand, we know that LGE sequences fail to detect interstitial fibrosis and that strain imaging might be better for the detection of both interstitial and replacement fibrosis [33]. Together with strain imaging, interstitial fibrosis detection by T1-mapping sequences could be a promising tool in the future [34].

6.4.3 Resampling

The oversampling technique used in this study have to be discussed. Unless it helps to improve the model performance on unbalance data as this database, there are some limits. By creating synthetic patients, it could lead to overfitting or create unrealistic synthetic patients that do not represent the true distribution of the minority class. In this study, the ADASYN ratio was put at 0.5 to not create too many synthetic patients with event and reduce the presented risks.

6.4.4 Implications

There is a growing interest in exploiting multimodal data by machine learning-based algorithms to predict adverse outcomes in many cardiac diseases, including HCM patients with predictive performance outperforming current recommendations risk models [35, 36]. However, this is the first study to apply a machine learning algorithm to both conventional data and automatically extracted LV longitudinal strain parameters to predict sustained ventricular arrhythmias and SCD in HCM patients. By providing an automatic extraction method for strain, this study emphasizes the potential of exploiting mechanical, temporal, and positional information from segmental ventricular strain curves beyond the simple use of the GLS. However, there are still challenges. It seems essential to develop automated and centralized collection systems for patient data to allow their longitudinal implementation straight into dynamic machine learning-based predictive algorithms [37].For LV strain measurement, even if automation is on the right track [38], we already know that there are some discrepancies between acquisitions technique used by different manufacturers, especially for segmental function assessment [39]. However, the use of strain shape comparison more than the absolute value in our study could have limited manufacturer-dependent results [39].

6.4.5 Limitations

The number of events was insufficient to build the model on one center cohort with an external validation on the other. However, the use of a Ridge regression algorithm and the bi-centric international population probably reduced the risk of overfitting inherent to machine learning methods and improved the generalization of the model. Future external validation studies on larger cohorts are needed. The included patients were referred to tertiaries care centers, which

may introduce a selection bias with more severe patients included in our cohort. Patients were mainly excluded because of insufficient image quality, which may introduce selection bias. We did not exclude patients with septal reduction therapy, which could have introduced a confounding bias by changing the septal strain pattern. However, almost all strain parameters selected by the model did not include septal segments. Further investigations of this method including extended comparison are planned for the future.

6.5 Conclusion

A machine-learning-based algorithm combining heterogeneous data: clinical, imaging, and LV strain parameters was found to have a higher predictive value for sustained VA and SCD prediction in HCM patients than conventional risk models. The computational method allows automated extraction and comparison of new promising strain parameters.

BIBLIOGRAPHY

[1] Maron B.J., Olivotto I., Spirito P., Casey S.A., Bellone P., Gohman T.E., Graham K.J., Burton D.A., and Cecchi F. Epidemiology of Hypertrophic Cardiomyopathy–Related Death. *Circulation*, vol. 102, 858–864 (2000).

[2] Maron B.J., Shirani J., Poliac L.C., Mathenge R., Roberts W.C., and Mueller F.O. Sudden death in young competitive athletes: Clinical, demographic, and pathological profiles. *JAMA*, vol. 276 (1996).

[3] Varnava A.M., Elliott P.M., Sharma S., McKenna W.J., and Davies M.J. Hypertrophic cardiomyopathy: The interrelation of disarray, fibrosis and small vessel disease. *Heart*, vol. 84 (2000).

[4] Moore B., Semsarian C., Chan K.H., and Sy R.W. Sudden Cardiac Death and Ventricular Arrhythmias in Hypertrophic Cardiomyopathy (2019).

[5] Lin G., Nishimura R.A., Gersh B.J., Phil D., Ommen S.R., Ackerman M.J., and Brady P.A. Device complications and inappropriate implantable cardioverter defibrillator shocks in patients with hypertrophic cardiomyopathy. *Heart*, vol. 95 (2009).

[6] O'Mahony C., Jichi F., Pavlou M., Monserrat L., Anastasakis A., Rapezzi C., Biagini E., Gimeno J.R., Limongelli G., McKenna W.J., Omar R.Z., Elliott P.M., Ortiz-Genga M., Fernandez X., Vlagouli V., Stefanadis C., Coccolo F., Sandoval M.J.O., Pacileo G., Masarone D., Pantazis A., Tome-Esteban M., Dickie S., Lambiase P.D., and Rahman S. A novel clinical risk prediction model for sudden cardiac death in hypertrophic cardiomyopathy (HCM Risk-SCD). *Eur. Heart J.*, vol. 35, 2010–2020 (2014).

[7] Ommen S.R., Mital S., Burke M.A., Day S.M., Deswal A., Elliott P., Evanovich L.L., Hung J., Joglar J.A., Kantor P., Kimmelstiel C., Kittleson M., Link M.S., Maron M.S., Martinez M.W., Miyake C.Y., Schaff H.V., Semsarian C., and Sorajja P. 2020 AHA/ACC Guideline for the Diagnosis and Treatment of Patients With Hypertrophic Cardiomyopathy: A Report of the American College of Cardiology/American Heart Association Joint Committee on Clinical Practice Guidelines. *J. Am. Coll. Cardiol.*, vol. 76, e159–e240 (2020).

[8] Shameer K., Johnson K.W., Glicksberg B.S., Dudley J.T., and Sengupta P.P. Machine learning in cardiovascular medicine: Are we there yet? *Heart*, vol. 104, 1156–1164 (2018).

[9] Trayanova N.A. Learning for Prevention of Sudden Cardiac Death. *Circ. Res.*, vol. 128, 185–187 (2021).

[10] Haland T.F., Almaas V.M., Hasselberg N.E., Saberniak J., Leren I.S., Hopp E., Edvardsen T., and Haugaa K.H. Strain echocardiography is related to fibrosis and ventricular arrhythmias in hypertrophic cardiomyopathy. *Eur. Heart J. Cardiovasc. Imaging*, vol. 17, 613–621 (2016).

[11] Galli E., Vitel E., Schnell F., Le Rolle V., Hubert A., Lederlin M., and Donal E. Myocardial constructive work is impaired in hypertrophic cardiomyopathy and predicts left ventricular fibrosis. *Echocardiography*, vol. 36, 74–82 (jan 2019).

[12] Tseng W.Y.I., Dou J., Reese T.G., and Van Wedeen J. Imaging myocardial fiber disarray and intramural strain hypokinesis in hypertrophic cardiomyopathy with MRI. *J. Magn. Reson. Imaging*, vol. 23, 1–8 (2006).

[13] Chan R.H., Maron B.J., Olivotto I., Pencina M.J., Assenza G.E., Haas T., Lesser J.R., Gruner C., Crean A.M., Rakowski H., Udelson J.E., Rowin E., Lombardi M., Cecchi F., Tomberli B., Spirito P., Formisano F., Biagini E., Rapezzi C., De Cecco C.N., Autore C., Cook E.F., Hong S.N., Gibson C.M., Manning W.J., Appelbaum E., and Maron M.S. Prognostic value of quantitative contrast-enhanced cardiovascular magnetic resonance for the evaluation of sudden death risk in patients with hypertrophic cardiomyopathy. *Circulation*, vol. 130, 484–495 (2014).

[14] Ariga R., Tunnicliffe E.M., Manohar S.G., Mahmod M., Raman B., Piechnik S.K., Francis J.M., Robson M.D., Neubauer S., and Watkins H. Identification of Myocardial Disarray in Patients With Hypertrophic Cardiomyopathy and Ventricular Arrhythmias. *J. Am. Coll. Cardiol.*, vol. 73 (2019).

[15] Al Wazzan A., Taconne M., Le Rolle V., Forsaa Inngjerdingen M., Hermann Haugaa K., Galli E., Hernandez A., Edvarsen T., and Donal E. Machine learning model including left ventricular strain analysis for sudden cardiac death prediction in hypertrophic cardiomyopathy. *Arch. Cardiovasc. Dis.*, vol. 15, 253–257 (2023).

[16] Perry M. Elliott* (Chairperson) (UK) Aris Anastasakis (Greece), Michael A. Borger (Germany), Martin Borggrefe (Germany), FrancoCecchi (Italy), Philippe Charron (France), Albert Alain Hagege (France), Antoine Lafont (France), GiuseppeLimongelli (Italy), He H.U. 2014 ESC guidelines on diagnosis and management of hypertrophic cardiomyopathy: The task force for the diagnosis and management of hypertrophic cardiomyopathy of the European Society of Cardiology (ESC). *Eur. Heart J.*, vol. 35, 2733–2779 (2014).

[17] Lang R.M., Badano L.P., Mor-Avi V., Afilalo J., Armstrong A., Ernande L., Flachskampf F.A., Foster E., Goldstein S.A., Kuznetsova T., Lancellotti P., Muraru D., Picard M.H., Rietzschel E.R., Rudski L., Spencer K.T., Tsang W., and Voigt J.U. Recommendations for cardiac chamber quantification by echocardiography in adults: An update from the American society of echocardiography and the European association of cardiovascular imaging. *Eur. Heart J. Cardiovasc. Imaging*, vol. 16, 233–271 (2015).

[18] Kligfield P., Gettes L.S., Bailey J.J., Childers R., Deal B.J., Hancock E.W., van Herpen G., Kors J.A., Macfarlane P., Mirvis D.M., Pahlm O., Rautaharju P., and Wagner G.S. Recommendations for the Standardization and Interpretation of the Electrocardiogram. *J. Am. Coll. Cardiol.*, vol. 49 (2007).

[19] Storer T., DAVIS J.A., and CAIOZZO V. Accurate prediction of VO2max in cycle ergometry (1990).

[20] Pedersen C.T., Kay G.N., Kalman J., Borggrefe M., Della-Bella P., Dickfeld T., Dorian P., Huikuri H., Kim Y.H., Knight B., Marchlinski F., Ross D., Sacher F., Sapp J., Shivkumar K., Soejima K., Tada H., Alexander M.E., Triedman J.K., Yamada T., Kirchhof P., and Peachey H. EHRA/HRS/APHRS expert consensus on ventricular arrhythmias (2014).

[21] Gallard A., Bidaut A., Hubert A., Sade E., Marechaux S., Sitges M., Separovic-Hanzevacki J., Le Rolle V., Galli E., Hernandez A., and Donal E. Characterization of Responder Profiles for Cardiac Resynchronization Therapy through Unsupervised Clustering of Clinical and Strain Data. *J. Am. Soc. Echocardiogr.*, vol. 34, 483–493 (2021).

[22] Bernard A., Donal E., Leclercq C., Schnell F., Fournet M., Reynaud A., Thebault C., Mabo P., Daubert J.C., and Hernandez A. Impact of cardiac resynchronization therapy on left ventricular mechanics: Understanding the response through a new quantitative approach based on longitudinal strain integrals. *J. Am. Soc. Echocardiogr.*, vol. 28, 700–708 (2015).

[23] He H., Bai Y., Garcia E.A., and Li S. ADASYN: Adaptive synthetic sampling approach for imbalanced learning. *Proc. Int. Jt. Conf. Neural Networks*, 1322–1328 (2008).

[24] Pedregosa F., Varoquaux G., Gramfort A., Michel V., Thirion B., Grisel O., Blondel M., Prettenhofer P., Weiss R., Dibourg V., Vanderplas J., Passos A., Cournapeau D., Brucher M., Perrot M., and Duchesnay E. Scikit-learn: Machine Learning in Python. *J. Mach. Learn. Res.*, vol. 12, 2825–2830 (2011).

[25] Salvador S. and Chan P. Toward accurate dynamic time warping in linear time and space. *Intell. Data Anal.*, vol. 11, 561–580 (2007).

[26] Maron M.S., Finley J.J., Bos J.M., Hauser T.H., Manning W.J., Haas T.S., Lesser J.R., Udelson J.E., Ackerman M.J., and Maron B.J. Prevalence, clinical significance, and natural history of left ventricular apical aneurysms in hypertrophic cardiomyopathy. *Circulation*, vol. 118 (2008).

[27] Klarich K.W., Attenhofer Jost C.H., Binder J., Connolly H.M., Scott C.G., Freeman W.K., Ackerman M.J., Nishimura R.A., Tajik A.J., and Ommen S.R. Risk of death in long-term follow-up of patients with apical hypertrophic cardiomyopathy. *Am. J. Cardiol.*, vol. 111 (2013).

[28] Biagini E., Spirito P., Rocchi G., Ferlito M., Rosmini S., Lai F., Lorenzini M., Terzi F., Bacchi-Reggiani L., Boriani G., Branzi A., Boni L., and Rapezzi C. Prognostic Implications of the Doppler Restrictive Filling Pattern in Hypertrophic Cardiomyopathy. *Am. J. Cardiol.*, vol. 104 (2009).

[29] Debonnaire P., Thijssen J., Leong D.P., Joyce E., Katsanos S., Hoogslag G.E., Schalij M.J., Atsma D.E., Bax J.J., Delgado V., and Marsan N.A. Global longitudinal strain and left atrial volume index improve prediction of appropriate implantable cardioverter defibrillator therapy in hypertrophic cardiomyopathy patients. *Int. J. Cardiovasc. Imaging*, vol. 30 (2014).

[30] Rodrigues T., Raposo S.C., Brito D., and Lopes L.R. Prognostic relevance of exercise testing in hypertrophic cardiomyopathy. A systematic review. *Int. J. Cardiol.*, vol. 339 (2021).

[31] Magri D., Agostoni P., Sinagra G., Re F., Correale M., Limongelli G., Zachara E., Mastromarino V., Santolamazza C., Casenghi M., Pacileo G., Valente F., Morosin M., Musumeci B., Pagannone E., Maruotti A., Uguccioni M., Volpe M., and Autore C. Clinical and prognostic impact of chronotropic incompetence in patients with hypertrophic cardiomyopathy. *Int. J. Cardiol.*, vol. 271 (2018).

[32] Geske J.B., Ong K.C., Siontis K.C., Hebl V.B., Ackerman M.J., Hodge D.O., Miller V.M., Nishimura R.A., Oh J.K., Schaff H.V., Gersh B.J., and Ommen S.R. Women with hypertrophic cardiomyopathy have worse survival. *Eur. Heart J.*, vol. 38 (2017).

[33] Almaas V.M., Haugaa K.H., Strøm E.H., Scott H., Smith H.J., Dahl C.P., Geiran O.R., Endresen K., Aakhus S., Amlie J.P., and Edvardsen T. Noninvasive assessment of myocardial fibrosis in patients with obstructive hypertrophic cardiomyopathy. *Heart*, vol. 100 (2014).

[34] Qin L., Min J., Chen C., Zhu L., Gu S., Zhou M., Yang W., and Yan F. Incremental Values of T1 Mapping in the Prediction of Sudden Cardiac Death Risk in Hypertrophic Cardiomyopathy: A Comparison With Two Guidelines. *Front. Cardiovasc. Med.*, vol. 8 (2021).

[35] Bhattacharya M., Lu D.Y., Kudchadkar S.M., Greenland G.V., Lingamaneni P., Corona-Villalobos C.P., Guan Y., Marine J.E., Olgin J.E., Zimmerman S., Abraham T.P., Shatkay H., and Abraham M.R. Identifying Ventricular Arrhythmias and Their Predictors by Applying Machine Learning Methods to Electronic Health Records in Patients With Hypertrophic Cardiomyopathy (HCM-VAr-Risk Model). *Am. J. Cardiol.*, vol. 123, 1681–1689 (2019).

[36] Kochav S.M., Raita Y., Fifer M.A., Takayama H., Ginns J., Maurer M.S., Reilly M.P., Hasegawa K., and Shimada Y.J. Predicting the development of adverse cardiac events in patients with hypertrophic cardiomyopathy using machine learning. *Int. J. Cardiol.*, vol. 327, 117–124 (2021).

[37] Dey D., Slomka P.J., Leeson P., Comaniciu D., Shrestha S., Sengupta P.P., and Marwick T.H. Artificial Intelligence in Cardiovascular Imaging: JACC State-of-the-Art Review (2019).

[38] Salte I.M., Østvik A., Smistad E., Melichova D., Nguyen T.M., Karlsen S., Brunvand H., Haugaa K.H., Edvardsen T., Lovstakken L., and Grenne B. Artificial Intelligence for Automatic Measurement of Left Ventricular Strain in Echocardiography. *JACC Cardiovasc. Imaging*, vol. 14, 1918–1928 (2021).

[39] Mirea O., Pagourelias E.D., Duchenne J., Bogaert J., Thomas J.D., Badano L.P., Voigt J.U., Badano L.P., Thomas J.D., Hamilton J., Pedri S., Lysyansky P., Hansen G., Ito Y., Chono T., Vogel J., Prater D., Park S., Lee J.Y., Houle H., Georgescu B., Baumann R., Mumm B., Abe Y., and Gorissen W. Variability and Reproducibility of Segmental Longitudinal Strain Measurement. *JACC Cardiovasc. Imaging*, vol. 11 (2018).

Conclusion

The assessment of the cardiac function of HF patients is essential to diagnose, choose the appropriate treatment, predict risk, and ensure follow up. Strain curves-derived parameters, added to the ECG, could provide essential information on the complex and multifactorial mechanisms involves [1]. Recently, computational modeling and machine learning have become increasingly popular in biomedical research, particularly in the fields of disease prediction, diagnosis, and risk stratification, as well as in the development of personalized therapies. Both approaches, despite different philosophies, have proved valuable in helping to unravel the complex interactions that underlie multifactorial diseases. Modeling stands out to integrate physiological knowledge into the data processing chain. Machine learning, on its side, by its data driven conception ensure hypothesis free studies and permit large and multimodal database analyses. The thesis was focused on the assessment of the cardiac function based on methodological frameworks that include computational models and machine learning algorithms. These different frameworks were adapted to different phenotypes of heart failure.

The first contribution was **the development and validation of computational models on two clinical cases**: Left Bundle of Branch Block (LBBB) and Aortic Stenosis (AS) (Chapter 3 and Chapter 5). In fact, a first model of the cardiovascular system was proposed by coupling a multi-segment representation of LV and right ventricle, atria, systemic, and pulmonary circulations. This model was used to interpret different patterns of LV contraction observed in different cases of LBBB and was evaluated on data obtained from 10 healthy subjects and 20 patients with LBBB with underlying ischemic (n=10) and non-ischemic (n=10) cardiomyopathies to create patient digital twin. A close match was observed between estimated and observed strain signal of the 20 LBBB and 10 healthy patients. The analysis of model parameters show that septal motion and global strain morphologies are not only explained by electrical conduction delay but also by the heterogeneity of contractile levels within the myocardium. A second model was then used for a different objective: to obtain myocardial work indices in the case of AS with a noninvasive estimation of the LV pressure. A model identification process was applied on 67 AS patients. The objective was to improve the model-based approach to assess non-invasively LV pressure proposed in our team [2, 3]. Then, compare and evaluate the LV pressure estimation with the adapted method of Russel et al. [4, 5] by Fortuni et al. [6]. As the essential part of the MW determination is the estimation of LV pressure, pressure curves calculated with each method were compared with the invasively computed in severe and moderate AS patients. Both methods present good concordance with the MW indices computed with invasive pressure. Assessing regional myocardial work could hold significant importance in predicting the prognosis of patients

with severe asymptomatic AS without LV dysfunction. This is especially crucial as the optimal timing and criteria for surgical intervention of these patients continue to be a topic of debate.

The second contribution concern **the proposition of machine learning pipelines applied to two distinct databases of HF patients: CRT eligible patients and HCM patients** (Chapter 4 and Chapter 6). Supervised algorithms were applied on both of the database to provide a classification of these patients. In the first case, the classification aimed to predict the response to CRT, while in the second case, it aimed to identify at-risk patients. In both instances, the prediction results surpassed those of the current methods and risk scores. Furthermore, the feature selection process conducted to develop the classifier highlighted the most predictive features. Additionally, for CRT eligible patients, a characterization was proposed using an unsupervised ML algorithm. Five profiles were extracted with different response rate to the CRT. The findings emphasized the importance of regional myocardial contractility and electrical activation times in predicting CRT response. This characterization and classification of heart failure patient profiles were based on a combination of traditional and novel interpretable features extracted from strain data.

The final contribution introduced **a hybrid approach that combined in-silico models and machine learning to analyze strain curves in patients eligible for CRT** (Chapter 4). The different steps of the approaches were developed, as well as their different combinations/declinations. First, five digital representative patients were added to a 250 CRT-eligible patients' clustering. These digital twins provided supplementary understandable features to the five distinct phenogroup created based on their clinical and strain data. This combined approach appears as a promising tool to improve the understanding of LV mechanics and the assessment of heart function in patients undergoing CRT. Then, the proposed in-silico model was integrated in a complete ML pipeline to improve the interpretability of the approach. A database, composed of 164 CRT candidates, was analyzed with the proposed hybrid pipeline. The unsupervised ML was applied, and clusters were defined, associated with groups of below-average to excellent responders. Patient digital twins bring additional information on the regional electrical and mechanical function of the LV from the analysis of echocardiographic data. Finally, a supervised ML was applied to parameters extracted from digital twins to create a CRT-response classifier. This classifier was compared to a more classic classifier based on clinical and echocardiographic pre-implantation data. Results show that digital twins approach helps to improve the prediction of the response to CRT, while improving understanding of LV mechanics in patients undergoing CRT.

This thesis employs promising approaches that combine computational modeling and machine learning. The aim was to improve the interpretation of echocardiography strain curves by integrating physiological knowledge with models. The proposed methods enhanced physiological indices by providing personalized interpretation and additional information compared to traditional measures. Overall, this approach represents a step towards integrating explicit knowledge for evaluating cardiac function and improving the understanding of patient-specific indicators extracted from echocardiography.

The proposed approaches present some limitations that should be mentioned. First, medium-size populations of patients were used in this study. The analysis of wider populations should be performed in the future in order to strengthen and improve our results. Addressing this concern is crucial for ensuring reliable ML algorithms. Moreover, the two proposed models include some simplifications concerning the electrical and mechanical behaviors such as fiber, torsion or a complete mechanical continuity. Another limitation is related to the identification process, which was applied to reduce a global error. Enhancements could be made to overcome this limitation.

In future works, the proposed hybrid modeling approach, which combines in-silico and ML models, should be evaluated clinically for the prediction of each patient response to a CRT intervention and to support the medical decision process for implanting or not a patient. This hybrid classifier should be embedded in a novel Decision Support System (DSS) and used in inference mode to propose a new multivariate score, associated with an estimation of the probability of response. This approach will require the development of a technical architecture integrating all the available patient data and the calculation of a patient-specific probability of response in a timely manner.

Concerning the proposed estimation of work indices in the cases of AS, the methodology could be translated to tricuspid regurgitation patient. The treatment decision for these patients using clips is still questioning, and the impact on the right heart remodeling and outcomes are not yet fully understood. The evaluation of the right ventricle is currently a topic of growing interest, but there is limited research available on the analysis of its strain curves.

Similarly, the proposed characterization of the CRT eligible patients in Chapter 4 could be adapted to the HCM database to provide different patients profiles more or less at risk of SCD or ventricular arrhythmia. This phenotyping added to the predictive features underlined by the classification process could provide help in the identification of more at-risk patient and provide adapted management and follow-up.

This study also opens interesting perspectives for the use of digital twins in cardiology. In the future, the proposed cardiovascular models could be applied to the optimization of the design stages of medical devices, as proposed in the previous work of our team [7]. The model-based approach, defined in my thesis, can be used to conduct virtual experiments and test new diagnostic hypotheses (implantable device, ...), as a preliminary step to clinical or preclinical investigations. The advantages of such "virtual prototyping" are multiple (cost reduction, minimization of development time, etc.). This work therefore opens the way to new methods of processing and analyzing clinical data in the context of cardiology,

BIBLIOGRAPHY

[1] Galli E., Galand V., Rolle V.L., Taconne M., Wazzan A.A., Hernandez A., Leclercq C., and Donal E. The saga of dyssynchrony imaging : Are we getting to the point. *Frontiers in Cardiovascular Medicine*, 1–15 (2023).

[2] Owashi K.P., Hubert A., Galli E., Donal E., Hernández A.I., and Rolle V.L. Model-based estimation of left ventricular pressure and myocardial work in aortic stenosis. *PLoS One*, vol. 15, 1–18 (2020).

[3] Owashi K.P. *Model-based analysis of myocardial strains for the evaluation of cardio- vascular function*. Ph.D. thesis, Université Rennes 1 (2021).

[4] Russell K., Eriksen M., Aaberge L., Wilhelmsen N., Skulstad H., Remme E.W., Haugaa K.H., Opdahl A., Fjeld J.G., Gjesdal O., Edvardsen T., and Smiseth O.A. A novel clinical method for quantification of regional left ventricular pressurestrain loop area: A non-invasive index of myocardial work. *Eur. Heart J.*, vol. 33, 724–733 (2012).

[5] Russell K., Eriksen M., Aaberge L., Wilhelmsen N., Skulstad H., Gjesdal O., Edvardsen T., and Smiseth O.A. Assessment of wasted myocardial work: A novel method to quantify energy loss due to uncoordinated left ventricular contractions. *Am. J. Physiol. - Hear. Circ. Physiol.*, vol. 305, 996–1003 (2013).

[6] Fortuni F., Butcher S.C., van der Kley F., Lustosa R.P., Karalis I., de Weger A., Priori S.G., van der Bijl P., Bax J.J., Delgado V., and Ajmone Marsan N. Left ventricular myocardial work in patients with severe aortic stenosis Federico. *J. Am. Soc. Echocardiogr.*, page 124658 (2020).

[7] Ugalde H.M.R., Ojeda D., Rolle V.L., Andreu D., Guiraud D., Bonnet J.L., Henry C., Karam N., Hag A., Mabo P., Carrault G., and Hern A.I. Model-Based Design and Experimental Validation of Control Modules for Neuromodulation Devices. *IEEE Trans. Biomed. Eng.*, vol. 63, 1551–1558 (2016).

List of publications

International Journal Papers

[1] Galli E., Galland V., Le Rolle V., **Taconné M.**, Al Wazzan A., Hernández A., Leclercq C. and Donal E. The saga of dyssynchrony imaging: Are we getting to the point. *Frontiers in Cardiovascular Medicine*, Cardiovascular Imaging section, vol. 10, page 1-15 (2023).

[2] Quinio L., **Taconné M.**, Le Rolle V., Curtis L., Auffret V., Boulmier D., Leurent G., Le Breton H., Galli E., Oger E. and Donal E. Evolution of non-invasive myocardial work variables after transcatheter aortic valve implantation in patients with severe aortic stenosis. *Archives of Cardiovascular Diseases*, vol. 116, page 192–201 (2023).

[3] **Taconné M.**†, Owashi K. †, Galli E., Duchenne J., Hubert A., Donal E., Hernández A. and Le Rolle V. Model-based analysis of myocardial strains in left bundle branch block. *Frontiers in Applied Mathematics and Statistics*, Mathematical Biology section, vol. 8, page 1-18 (2022).

[4] **Taconné M.**†, Le Rolle V. †, Panis V., Hubert A., Auffret V., Galli E., Hernández A. and Donal E. How myocardial work could be relevant in patients with an aortic valve stenosis? *European Heart Journal Cardiovascular Imaging*, vol. 24, no 1, page 1-11 (2022).

[5] Owashi K. †, **Taconné M.**†, Courtial N., Simon A., Garreau M., Hernández A., Donal E., Le Rolle V. and Galli E. Desynchronization Strain Patterns and Contractility in Left Bundle Branch Block through Computer Model Simulation. *Journal of Cardiovascular Development and Disease*, vol. 9, no 2, page 53 (2022).

Submitted Paper

[6] **Taconné M.**, Le Rolle V., Galli E., Gallard A., Owashi K., Al Wazzan A., Donal E. and Hernández A. Characterization of Cardiac Resynchronization Therapy Response through Unsupervised Clustering and Digital Twins.

[7] Al Wazzan A. †, **Taconné M.**†, Inngjerdingen Forsa M., Le Rolle V., Hermann Haugaa K., Galli E., Hernández A., Edvardsen T. and Donal E. Machine learning model combining clinical and imaging information with left ventricular longitudinal strain analysis for a better prediction of sudden cardiac death in hypertrophic cardiomyopathy patients.

† These authors have contributed equally to this work and share first authorship.

International Conferences

Presentations and Peer-reviewed Papers

[1] **Taconné M.**, Le Rolle V., Gallard A., Owashi K., Al Wazzan A., Galli E., Voigt J., Duchenne J., Smiseth O., Donal E. and Hernández A. Model-based and Unsupervised Machine-learning Approaches for the Characterization of Responder Profiles for Cardiac Resynchronization Therapy. *CinC*, Tampere, Finland (2022).

[2] **Taconné M.**, Le Rolle V., Owashi K., Panis V., Hubert A., Auffret V., Galli E., Hernández A. and Donal E. Sensitivity Analysis and Parameter Identification of a Cardiovascular Model in Aortic Stenosis. *CinC*, Brno, Czech Republic (2021).

Presentation and Abstract

[3] **Taconné M.**, Le Rolle V., Galli E., Gallard A., Owashi K., Al Wazzan A., Voigt J., Duchenne J., Smiseth O., Donal E. and Hernández A. Characterization of responder profiles for cardiac resynchronisation therapy based on explainable machine-learning and virtual patient approaches. *EACVI*, Barcelona, Spain (2023).

Posters and Abstracts

[4] Al Wazzan A., **Taconné M.**, Le Rolle V., Hermann Haugaa K., Galli E., Hernández A., Edvardsen T. and Donal E. Identification of new ventricular arrythmias risks profiles in hypertrophic cardiomyopathy through clustering analysis including left ventricular strain data. *ESC*, Amsterdam, Netherlands (2023).

[5] Al Wazzan A., **Taconné M.**, Le Rolle V., Inngjerdingen Forsa M., Hermann Haugaa K., Galli E., Hernández A., Edvardsen T. and Donal E. Machine learning model including left ventricular strain analysis for sudden cardiac death prediction in hypertrophic cardiomyopathy. *EACVI*, Barcelona, Spain (2023).

[6] **Taconné M.**, Le Rolle V., Panis V., Hubert A., Auffret V., Galli E., Hernández A. and Donal E. How Myocardial work could be relevant in patients with an Aortic Valve Stenosis? *EuroEcho*, Berlin, Germany (online) (2021).

Editorials or Letter

[1] Hubert A. **Taconné M.**, Popescu B. Donal E. Diastolic function and its non-invasive assessment. The quest for the Holy Grail continues. *International Journal of Cardiology (editorial)*, vol.382, page 96-97 (2023).

[2] Donal E., **Taconné M.**, Le Rolle V., Galli E. Tips and tricks for the non-invasive assessment of myocardial work: the good, the bad and the ugly. *European Heart Journal (editorial)*, vol. 00, 1-3 (2022).

[3] Donal E., **Taconné M.**, Hubert A., Le Rolle V. The future of the diastolic function assessment will take advantage of the past and of the automatization. *European Heart Journal (letter)*, vol. 22, 599-600 (2021).

Prize

[1] **Rosanna Degani Young Investigators'Award** for the presentation and paper: Model-based and Unsupervised Machine-learning Approaches for the Characterization of Responder Profiles for Cardiac Resynchronization Therapy. *CinC*, Tampere, Finland (2022).

List of Figures

List of Tables

Appendix

A Sensitivity analysis and parameter identification of the LBBB model

Symbols	Descriptions	Values	Units
	Cardiac electrical system		
T^{s}_{UDP}	Upstroke depolarization of the segments	to identify	ms
T^{s}_{ARP}	Absolute refractory of the segments	230	ms
T^{s}_{RRP}	Relative refractory of the segments	140	ms
T^{s}_{SDD}	Slow diastolic depolarization of the segments	inf	ms
$T^{LBB/RBB}_{UDP}$	Upstroke depolarization of LBB and RBB	2500	ms
$T^{LBB/RBB}_{ARP}$	Absolute refractory of LBB and RBB	10	ms
$T^{LBB/RBB}_{RRP}$	Relative refractory of LBB and RBB	120	ms
$T^{LBB/RBB}_{SDD}$	Slow diastolic depolarization of LBB and RBB	120	ms
$T^{UH/NAV}_{UDP}$	Upstroke depolarization of UH and NAV	2000	ms
$T^{UH/NAV}_{ARP}$	Absolute refractory of UH and NAV	20	ms
$T^{UH/NAV}_{RRP}$	Relative refractory of UH and NAV	200	ms
$T^{UH/NAV}_{SDD}$	Slow diastolic depolarization of UH and NAV	100	ms
T^{SAN}_{UDP}	Upstroke depolarization of SAN	to define $*$	ms
T^{SAN}_{ARP}	Absolute refractory of SAN	10	ms
T^{SAN}_{RRP}	Relative refractory of SAN	120	ms
T^{SAN}_{SDD}	Slow diastolic depolarization of SAN	60	ms
$T^{LA/RA}_{UDP}$	Upstroke depolarization of LA and RA	inf	ms
$T^{LA/RA}_{ARP}$	Absolute refractory of LA and RA	30	ms
$T^{LA/RA}_{RRP}$	Relative refractory of LA and RA	230	ms
$T^{LA/RA}_{SDD}$	Slow diastolic depolarization of LA and RA	100	ms
	Right and left atria		
$E_{ra,max}$	Maximum systolic elastance of the right atrium	0.5	$mmHg/ml$
$E_{ra,min}$	Diastolic elastance of the right atrium	0.01	$mmHg/ml$
$E_{la,max}$	Maximum systolic elastance of the left atrium	0.5	$mmHg/ml$
$E_{la,min}$	Diastolic elastance of the right atrium	0.01	$mmHg/ml$
$V_{ra,d}$	Unstressed volume of the right atrium	3	ml
$V_{la,d}$	Unstressed volume of the left atrium	3	ml
A_{ra}	Constant controlling the rise and peak of the right atrial systole	1	$-$

B_{ra}	Constant controlling the rise and peak of the right atrial systole	120	$1/s^2$
C_{ra}	Constant controlling the rise and peak of the right atrial systole	0.2	s
A_{la}	Constant controlling the rise and peak of the left atrial systole	1	–
B_{la}	Constant controlling the rise and peak of the left atrial systole	120	$1/s^2$
C_{la}	Constant controlling the rise and peak of the left atrial systole	0.2	s
	Right and left ventricles		
n_1	Constant controlling the steepness of the electro-mechanical coupling	to identify	–
n_2	Constant controlling the steepness of the electro-mechanical coupling	to identify	–
α_1	Shape parameter of the electro-mechanical coupling	to identify	–
α_2	Shape parameter of the electro-mechanical coupling	to identify	–
$l_{s,ref}$	Reference fiber lenghs	0.95	cm
$T_{ref,pass}$	Reference passive tension	52.504	$mmHg$
$T_{ref,act}$	Reference active tension	375.0319	$mmHg$
K_{pass}	Parameter related to passive stiffness	to identify	-
K_{act}	Parameter related to myofiber contractility	to identify	-
β	Constant related with muscle kinetic	10	–
F_a	Constant related with muscle kinetic	5.33	–
θ	Mean angle of the muscular fibers	$\pi/12$	rad
e	Mean wall thickness	0.7	cm
R_m	Radii of curvature in the meridian directions	2.1548	cm
R_p	Radii of curvature in the parallel directions	4.5985	cm
S_s	Segmental area	8.8909	cm^2
I_s	Segmental inertia	0.0003	$mmHgs/ml$
R_s	Segmental resistance	0.5	$mmHgs/ml$
$P_{0,lv}$	Left ventricule gradient pressure	1.2751	$mmHgs$
λ_{lv}	Left ventricule curvature	0.015	$1/ml$
$V_{0,lv}$	Left ventricule volume intercept	5	ml
$P_{0,rv}$	Right ventricule gradient pressure	1.2001	$mmHgs$
λ_{rv}	Right ventricule curvature	0.015	$1/ml$
$V_{0,v}$	Right ventricule volume intercept	5	ml
	Systemic and pulmonary circulationss		
E_{lv}	Elastance of the left ventricle	3.4053	$mmHg/ml$

E_{rv}	Elastance of the right ventricle	0.6526	$mmHg/ml$
E_{pa}	Elastance of the pulmonary artery	0.3375	$mmHg/ml$
E_{pu}	Elastance of pulmonary vein	0.0062	$mmHg/ml$
E_{ao}	Elastance of the aorta	3.2906	$mmHg/ml$
E_{sa}	Elastance of the systemic arteries	0.7881	$mmHg/ml$
E_{vc}	Elastance of the vena cava	0.0154	$mmHg/ml$
E_{sv}	Elastance of the systemic veins	0.010	$mmHg/ml$
$V_{d,la}$	Unstressed volume of the left atrium	3	ml
$V_{d,ra}$	Unstressed volume of the right atrium	3	ml
$V_{d,pa}$	Unstressed volume of the pulmonary artery	160	ml
$V_{d,pu}$	Unstressed volume of the pulmonary vein	200	ml
$V_{d,ao}$	Unstressed volume of the aorta	196.5625	ml
$V_{d,art}$	Unstressed volume of the systemic arteries	520.6199	ml
$V_{d,vc}$	Unstressed volume of the vena cava	1907.7	ml
$V_{d,veins}$	Unstressed volume of the systemic veins	1648	ml
R_{pul}	Pulmonary resistance	0.1425	$mmHgs/ml$
R_{sys}	Systemic resistance	1.0501	$mmHgs/ml$
R_{la}	Left atrium resistance	0.2	$mmHgs/ml$
R_{ra}	Right atrium resistance	0.8	$mmHgs/ml$
R_{mt}	Mitral valve resistance	0.01	$mmHgs/ml$
R_{av}	Aortic valve resistance	0.0105	$mmHgs/ml$
R_{tcv}	Tricuspid valve resistance	0.01	$mmHgs/ml$
R_{pv}	Pulmonary valve resistance	0.0105	$mmHgs/ml$
R_{art}	Arteries resistance	0.2915	$mmHgs/ml$
R_{veins}	Veins resistance	0.1935	$mmHgs/ml$

Table A.1: Parameters, descriptions and values of the LBBB model.

$*$ to define with patient heart rate.

Parameters	value
K_{act}	1.5
K_{pass}	1
n_1	1.3
n_2	10
α_1	0.4
α_2	0.4
R_{lv}	0.3
I_{lv}	0.001

$f_{a,s}$	5
e	0.6
$Area$	8.890875
β	10
K_{cont}	1.5
θ	$\pi/12$
R_m	2.9
R_p	4.59
R_{min}	0.05
R_{max}	0.3
$l_{s,ref}$	0.9
$T_{ref,pass}$	52.5044632
$T_{ref,act}$	375.03188
C_a	5.33

Table A.2: Baseline simulation parameters values for all the segments.

Parameters
K_{act}
K_{pass}
n_1
n_2
α_1
α_2
R_{lv}
I_{lv}
$f_{a,s}$
$Area$
β
K_{cont}
θ
R_m
R_p
R_{min}
R_{max}
UDP

Table A.3: Lists of the 18 parameters for each of the 16 segments used in the sensitivity analysis.

order	Parameter i	Di	σ_i	μ_i^*
0	$ApiSept : T_{UDP}$	2.800832	3.657845	2.588772
1	$ApiInf : T_{UDP}$	1.822312	2.565196	1.406503
2	$ApiAnt : T_{UDP}$	1.255750	1.774345	0.850037
3	$MidAntSept : \alpha_2$	1.214396	1.643248	1.071249
4	$BasalAntSept : \alpha_2$	1.208903	1.637048	1.064982
5	$ApiSept : \alpha_2$	1.150119	1.473622	1.081045
6	$BasalInfLat : \alpha_2$	1.112731	1.571514	0.744877
7	$ApiLat : T_{UDP}$	1.112468	1.551048	0.643783
8	$MidInfSept : \alpha_2$	1.105292	1.468762	1.001812
9	$BasalInfSept : \alpha_2$	1.079997	1.480997	0.927203
10	$BasalAntLat : \alpha_2$	1.051284	1.484177	0.785716
11	$BasalInf : \alpha_2$	1.042726	1.458456	0.838153
12	$MidInf : T_{UDP}$	1.041634	1.470951	0.695768
13	$MidInfLat : \alpha_2$	1.011751	1.430819	0.718470
14	$BasalAnt : \alpha_2$	0.982837	1.389928	0.691827
15	$ApiInf : \alpha_2$	0.976932	1.371102	0.600590
16	$MidInf : \alpha_2$	0.970307	1.361894	0.596926
17	$MidAntLat : \alpha_2$	0.956434	1.347078	0.612480
18	$MidAntSept : n_1$	0.894065	1.257175	0.696066
19	$MidAntLat : T_{UDP}$	0.891784	1.260525	0.650467
20	$ApiAnt : \alpha_2$	0.889551	1.253713	0.574878
21	$ApiLat : \alpha_2$	0.872696	1.229430	0.560637
22	$BasalInfSept : R_m$	0.834149	1.179625	0.594655
23	$MidInfLat : R_m$	0.779722	1.102495	0.561690
24	$MidAnt : \alpha_2$	0.758697	1.062697	0.457326
25	$BasalInfSept : n_1$	0.756683	1.021062	0.670665
26	$ApiInf : K_{act}$	0.754266	1.050463	0.617918
27	$ApiSept : n_1$	0.743200	1.012439	0.647339
28	$BasalAntSept : R_m$	0.739187	1.044784	0.539868
29	$ApiSept : R_m$	0.730942	1.031352	0.550554
30	$BasalInfLat : R_m$	0.711927	1.005275	0.530483

Table A.4: Sensitivity analysis results on $Y = mean(\varepsilon_{min,s}^{model})$: 30 first.

order	Parameter i	Di	σ_i	μ_i^*
0	$ApiSept : T_{UDP}$	94.169699	131.151512	77.142361

1	$MidInfLat : \alpha_2$	90.151477	127.390870	61.138889
2	$MidAntLat : T_{UDP}$	84.291760	118.452881	52.534722
3	$BasalInfLat : \alpha_2$	77.160297	108.173815	46.913194
4	$ApiInf : \alpha_2$	75.519879	106.689813	50.906250
5	$BasalAnt : R_m$	72.718862	100.724433	39.986111
6	$ApiAnt : \alpha_2$	71.563015	100.332492	43.534483
7	$BasalAntLat : \alpha_2$	68.984097	96.135461	39.767361
8	$MidAnt : \alpha_2$	67.154357	94.172821	40.944444
9	$ApiLat : \alpha_2$	66.718162	93.910003	42.385057
10	$BasalAnt : \alpha_2$	65.007358	90.565887	37.381466
11	$BasalInf : \alpha_2$	61.604235	86.961352	40.840278
12	$MidInfLat : K_{act}$	57.395764	78.171241	28.156250
13	$BasalAnt : \beta$	57.208297	78.941972	30.614583
14	$ApiSept : \alpha_2$	56.995363	78.229849	29.406250
15	$ApiInf : T_{UDP}$	56.831360	80.291756	38.354167
16	$MidInfLat : \beta$	55.082331	75.012959	27.004310
17	$ApiAnt : T_{UDP}$	54.953418	76.925254	32.934028
18	$MidInfLat : R_m$	54.743105	74.834528	27.500000
19	$MidInf : \alpha_2$	53.652708	75.514977	34.059028
20	$BasalInfLat : R_m$	53.110847	71.746412	24.760417
21	$BasalInfSept : K_{act}$	52.061443	69.636420	22.864583
22	$BasalInfLat : K_{act}$	50.599550	68.582387	24.079861
23	$BasalInf : \beta$	50.066813	63.787891	16.527778
24	$MidInfSept : \alpha_2$	48.519706	66.974024	26.023707
25	$MidInf : T_{UDP}$	47.638787	65.507702	24.885417
26	$BasalInfSept : n_1$	47.613641	64.070217	21.677443
27	$MidAntLat : \alpha_2$	47.270718	66.699396	31.100694
28	$MidInfLat : Area$	47.077126	62.382640	19.562500
29	$BasalAnt : K_{pass}$	46.876239	60.980704	17.489224
30	$BasalAntLat : n_2$	46.800047	62.042148	19.496528

Table A.5: Sensitivity analysis results on $Y = std(\varepsilon_{min,s}^{model})$: 30 first.

order	Parameter i	Di	σ_i	μ_i^*
0	$ApiSept : T_{UDP}$	1.457107	2.060644	1.026232
1	$BasalAntLat : R_m$	0.978841	1.379305	0.630958
2	$MidInfLat : \alpha_2$	0.943565	1.329271	0.606176

3	$BasalInf : K_{act}$	0.929282	1.312275	0.620560
4	$BasalInfLat : K_{act}$	0.920971	1.287218	0.544307
5	$MidAntSept : n_1$	0.917034	1.290298	0.579893
6	$BasalInfSept : n_1$	0.888404	1.255933	0.610981
7	$ApiSept : n_1$	0.882080	1.247060	0.607957
8	$ApiSept : \alpha_2$	0.881197	1.245450	0.601085
9	$BasalInfLat : R_m$	0.866749	1.219197	0.546220
10	$BasalInf : R_m$	0.855847	1.201929	0.529699
11	$BasalAnt : K_{act}$	0.812760	1.144603	0.519762
12	$BasalAntLat : \alpha_2$	0.804895	1.129501	0.494145
13	$MidInfLat : K_{act}$	0.793131	1.115572	0.499451
14	$ApiInf : K_{act}$	0.787341	1.109771	0.509553
15	$MidAntLat : \beta$	0.787123	1.107416	0.497240
16	$MidAntLat : K_{act}$	0.778634	1.098491	0.510967
17	$MidInfLat : R_m$	0.777799	1.092469	0.482100
18	$BasalAntLat : K_{act}$	0.765447	1.077906	0.489109
19	$BasalInfLat : \alpha_2$	0.763800	1.068678	0.455745
20	$BasalInfSept : K_{act}$	0.762354	1.076831	0.511948
21	$MidAntLat : \alpha_2$	0.761666	1.068508	0.466137
22	$BasalInf : \alpha_2$	0.755750	1.064415	0.483896
23	$ApiInf : T_{UDP}$	0.738672	1.033042	0.438904
24	$MidAnt : K_{act}$	0.720263	1.014882	0.463930
25	$ApiLat : K_{act}$	0.717180	1.010595	0.462309
26	$BasalAnt : R_m$	0.716019	1.009091	0.462406
27	$MidInf : K_{act}$	0.715333	1.007729	0.459461
28	$ApiAnt : K_{act}$	0.715088	1.008909	0.469797
29	$BasalAnt : \beta$	0.711077	1.003266	0.467285
30	$MidInfSept : \alpha_2$	0.708872	0.993231	0.428628

Table A.6: Sensitivity analysis results on $Y = mean(t(\varepsilon_{min,s}^{model}))$: 30 first.

order	**Parameter** i	Di	σ_i	μ_i^*
0	$ApiSept : T_{UDP}$	63.314830	88.410263	37.113573
1	$ApiInf : \alpha_2$	54.207923	76.331412	34.612065
2	$MidInfLat : \alpha_2$	48.543849	67.897829	28.877045
3	$MidInfLat : K_{act}$	45.568638	62.324141	22.965989

4	$ApiLat : \alpha_2$	45.133891	63.180365	27.052077
5	$BasalAnt : R_m$	44.490573	62.009295	25.673852
6	$MidAntLat : T_{UDP}$	40.816545	55.829728	20.583047
7	$ApiInf : T_{UDP}$	40.132132	55.799369	22.713007
8	$BasalInfLat : \alpha_2$	39.877837	55.666332	23.312569
9	$MidInfLat : \beta$	38.878583	52.468498	18.016204
10	$ApiAnt : \alpha_2$	38.101594	53.118466	22.034535
11	$BasalAnt : K_{act}$	37.738394	52.012763	20.026305
12	$BasalInfLat : n_1$	36.078403	47.787494	14.954258
13	$BasalAnt : \alpha_2$	35.330446	48.796820	19.028327
14	$BasalAnt : \beta$	35.074114	48.244956	18.360291
15	$BasalInfLat : R_m$	34.632636	46.887555	16.365710
16	$ApiAnt : \beta$	33.257811	44.296484	14.242777
17	$ApiLat : n_1$	32.825736	44.469228	15.572300
18	$MidInfLat : R_m$	31.918237	42.566901	13.773346
19	$MidInf : \alpha_2$	31.814783	44.678591	19.684848
20	$BasalInfSept : \alpha_2$	30.936813	42.310554	15.587742
21	$ApiAnt : T_{UDP}$	30.919302	42.758283	16.803780
22	$ApiSept : \alpha_2$	30.914302	41.949573	14.818054
23	$BasalAntSept : K_{act}$	30.814696	40.789841	12.725504
24	$MidInfLat : n_1$	30.741691	40.671138	12.655047
25	$ApiInf : n_1$	30.550654	41.542536	14.836148
26	$MidAntLat : R_m$	30.430949	41.850560	15.909905
27	$BasalAntLat : \beta$	30.408687	40.663054	13.333447
28	$BasalInfLat : K_{act}$	29.540547	39.513039	12.974050
29	$MidAnt : \alpha_2$	29.509688	41.452105	18.309115
30	$BasalInf : \alpha_2$	29.208043	41.031786	18.138280

Table A.7: Sensitivity analysis results on $Y = std(t(\varepsilon_{min,s}^{model}))$: 30 first.

Parameter		Range
Segments	K_{act}	$[0.1; 1.5]$
	K_{pass}	$[0.1; 10]$
	n_1	$[0.5; 2]$
	n_2	$[5; 15]$
	α_1	$[0.2; 0.6]$
	α_2	$[0.2; 0.6]$
	UDP	$[1; 30]$
LBB	UDP	$[1; 200]$

Table A.8: Parameters list and range used in the parameters identifications for LBBB patients

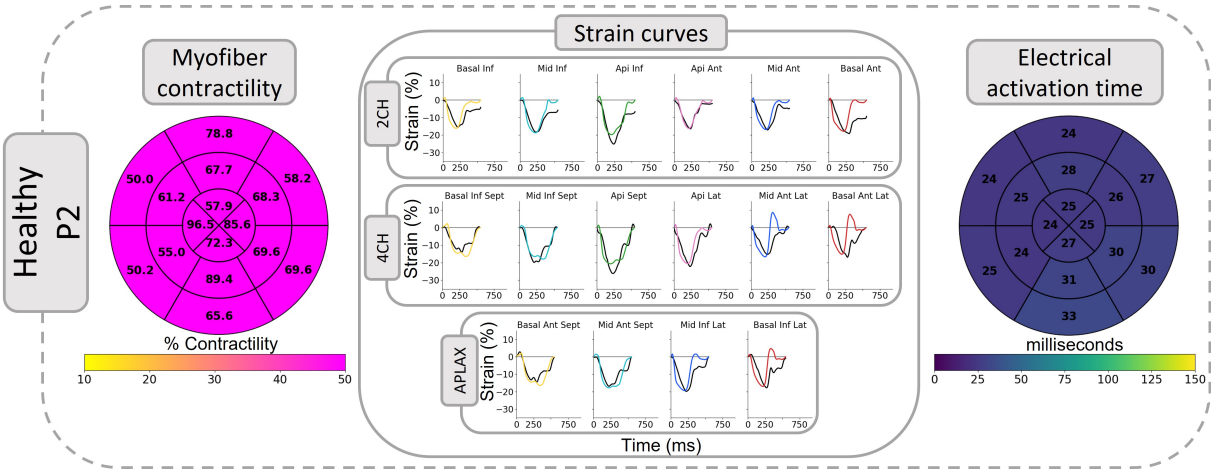

Figure A.1: Patient-specific simulation results for an other healthy subject. Experimental (*black*) and simulated (*colored*) strain curves corresponding to the 16 LV segments. Bull's-eye representations of segmental electrical activation delay and segmental myofiber contractility. Color scale at the contractility bull's-eye plot set between 10 and 50% in order to highlight the segments with low contractility.

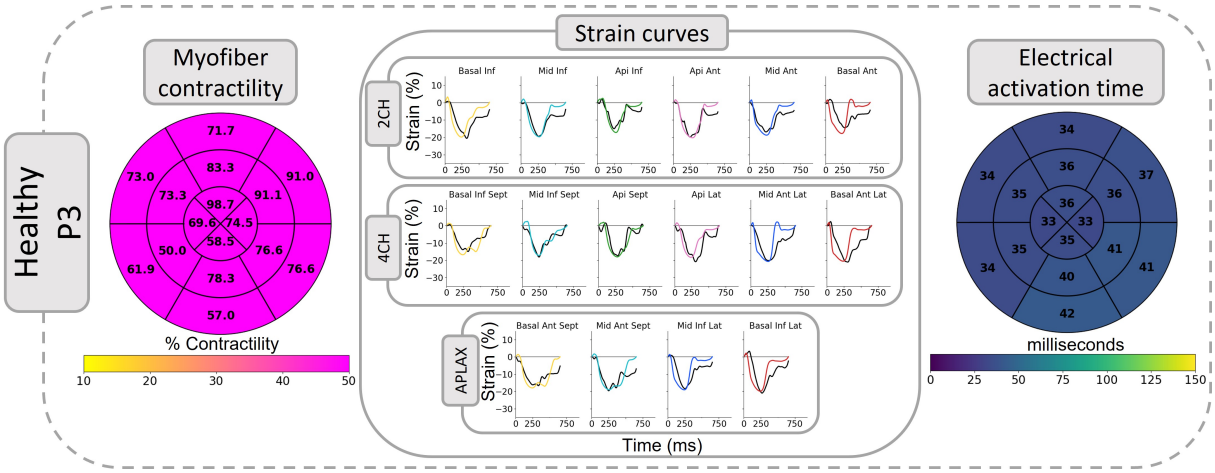

Figure A.2: Patient-specific simulation results for an other healthy subject. Experimental (*black*) and simulated (*colored*) strain curves corresponding to the 16 LV segments. Bull's-eye representations of segmental electrical activation delay and segmental myofiber contractility. Color scale at the contractility bull's-eye plot set between 10 and 50% in order to highlight the segments with low contractility.

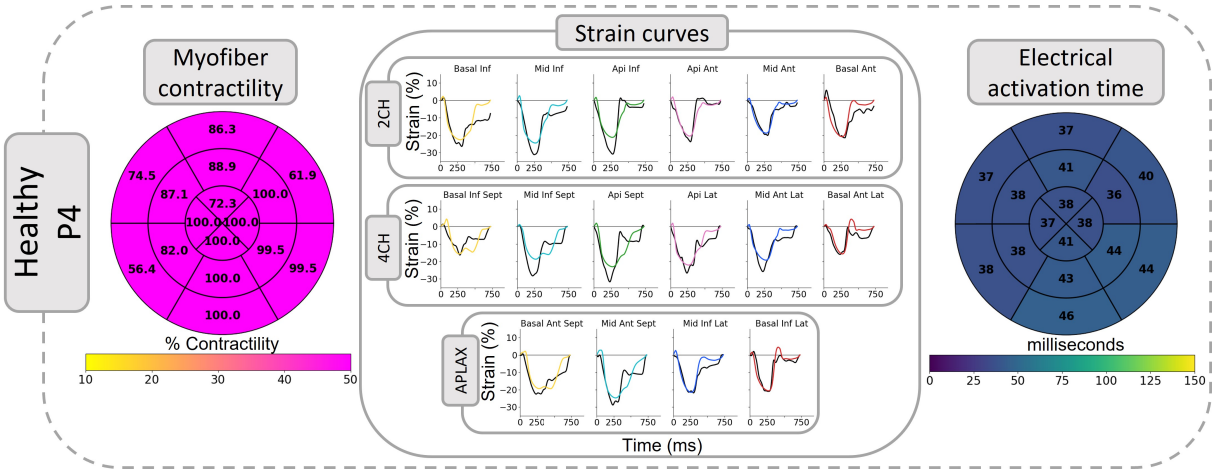

Figure A.3: Patient-specific simulation results for an other healthy subject. Experimental (*black*) and simulated (*colored*) strain curves corresponding to the 16 LV segments. Bull's-eye representations of segmental electrical activation delay and segmental myofiber contractility. Color scale at the contractility bull's-eye plot set between 10 and 50% in order to highlight the segments with low contractility.

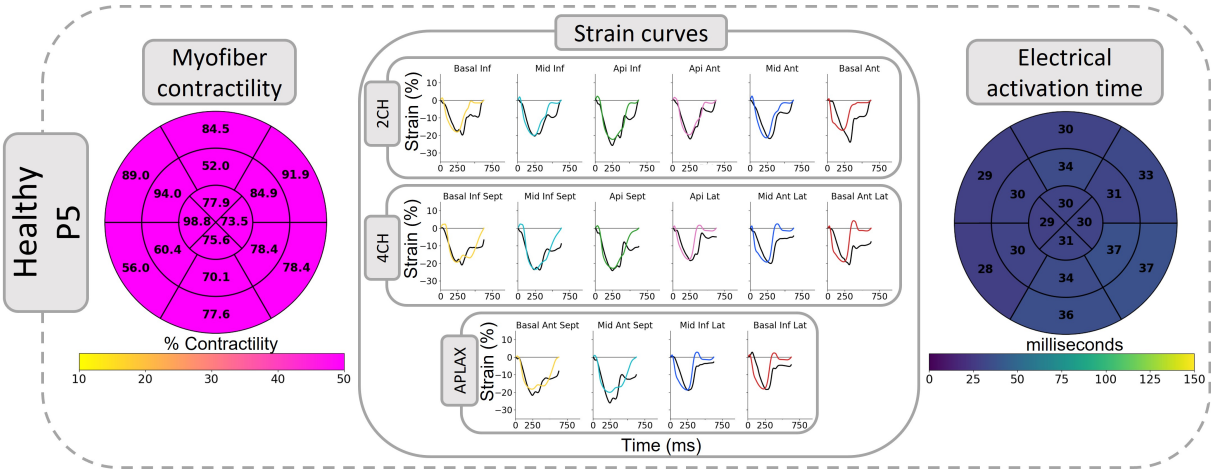

Figure A.4: Patient-specific simulation results for an other healthy subject. Experimental (*black*) and simulated (*colored*) strain curves corresponding to the 16 LV segments. Bull's-eye representations of segmental electrical activation delay and segmental myofiber contractility. Color scale at the contractility bull's-eye plot set between 10 and 50% in order to highlight the segments with low contractility.

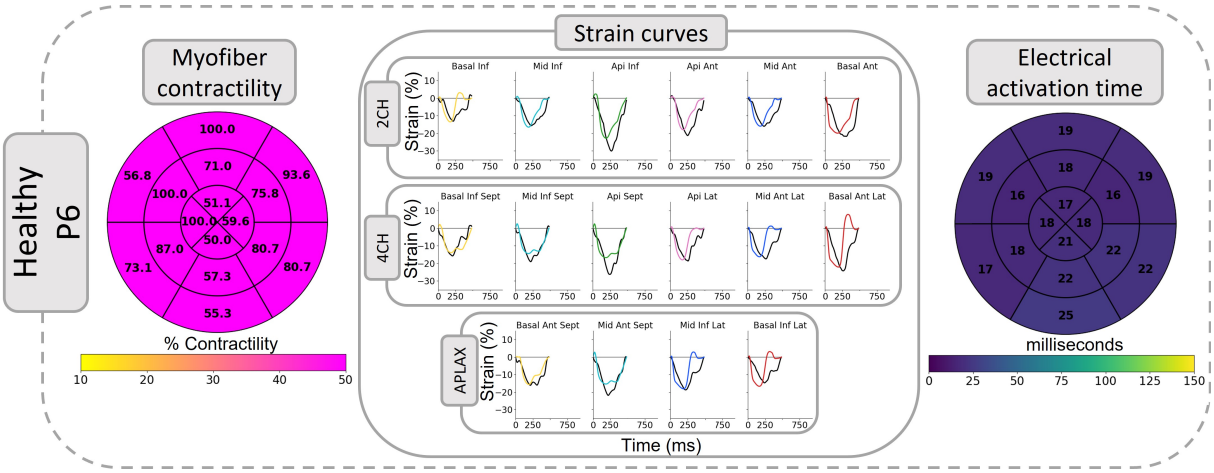

Figure A.5: Patient-specific simulation results for an other healthy subject. Experimental (*black*) and simulated (*colored*) strain curves corresponding to the 16 LV segments. Bull's-eye representations of segmental electrical activation delay and segmental myofiber contractility. Color scale at the contractility bull's-eye plot set between 10 and 50% in order to highlight the segments with low contractility.

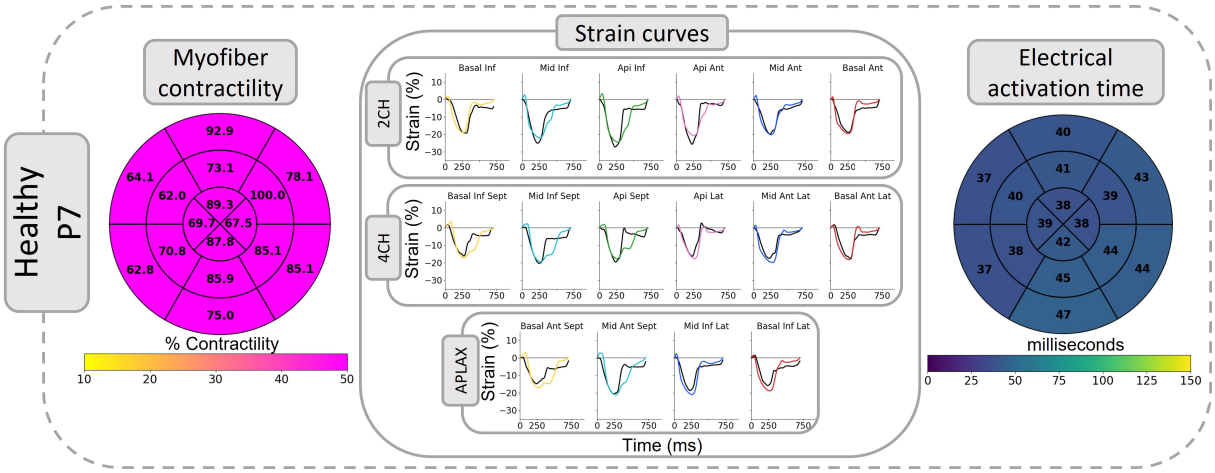

Figure A.6: Patient-specific simulation results for an other healthy subject. Experimental (*black*) and simulated (*colored*) strain curves corresponding to the 16 LV segments. Bull's-eye representations of segmental electrical activation delay and segmental myofiber contractility. Color scale at the contractility bull's-eye plot set between 10 and 50% in order to highlight the segments with low contractility.

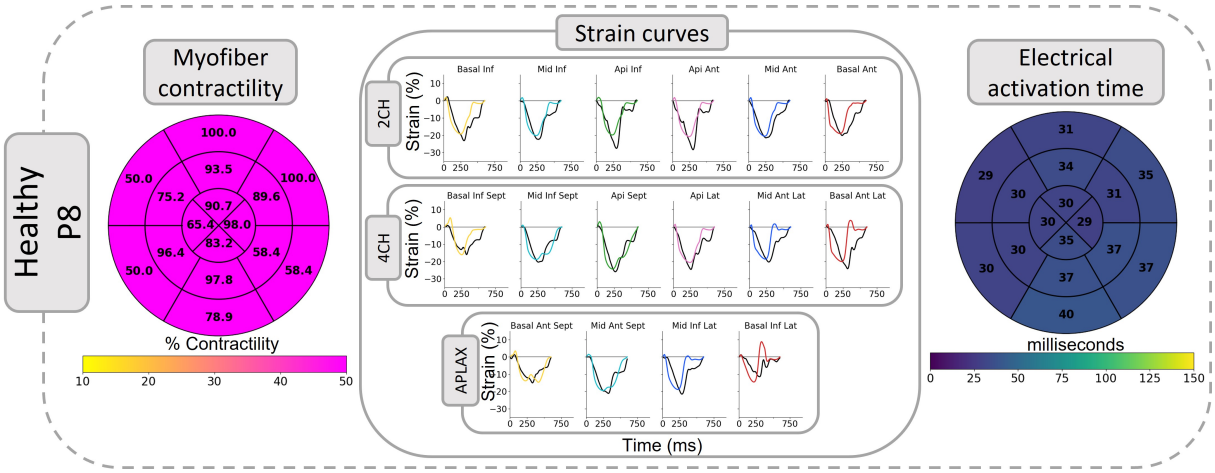

Figure A.7: Patient-specific simulation results for an other healthy subject. Experimental (*black*) and simulated (*colored*) strain curves corresponding to the 16 LV segments. Bull's-eye representations of segmental electrical activation delay and segmental myofiber contractility. Color scale at the contractility bull's-eye plot set between 10 and 50% in order to highlight the segments with low contractility.

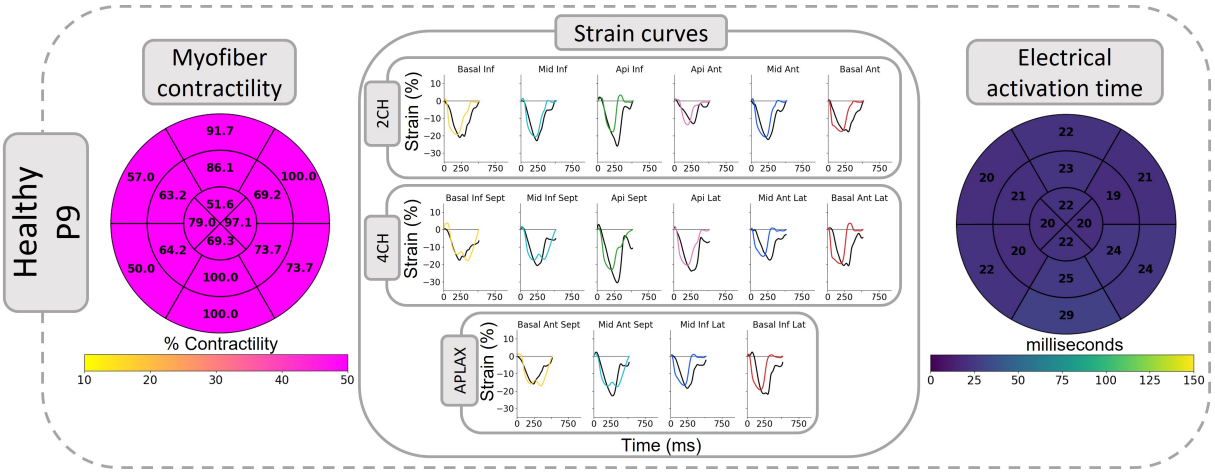

Figure A.8: Patient-specific simulation results for an other healthy subject. Experimental (*black*) and simulated (*colored*) strain curves corresponding to the 16 LV segments. Bull's-eye representations of segmental electrical activation delay and segmental myofiber contractility. Color scale at the contractility bull's-eye plot set between 10 and 50% in order to highlight the segments with low contractility.

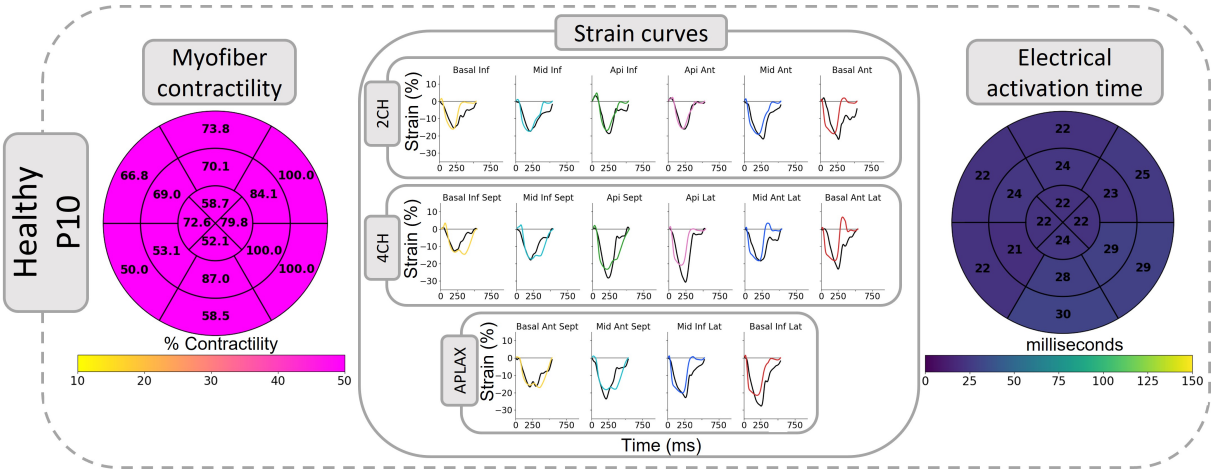

Figure A.9: Patient-specific simulation results for an other healthy subject. Experimental (*black*) and simulated (*colored*) strain curves corresponding to the 16 LV segments. Bull's-eye representations of segmental electrical activation delay and segmental myofiber contractility. Color scale at the contractility bull's-eye plot set between 10 and 50% in order to highlight the segments with low contractility.

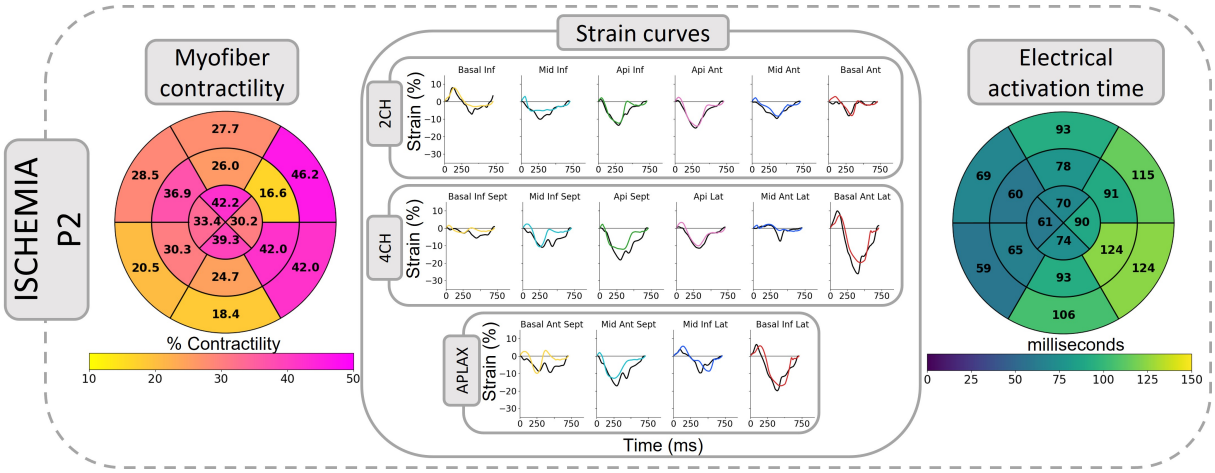

Figure A.10: Patient-specific simulation results for an ischemic LBBB patient. Experimental (*black*) and simulated (*colored*) strain curves corresponding to the 16 LV segments. Bull's-eye representations of segmental electrical activation delay and segmental myofiber contractility.

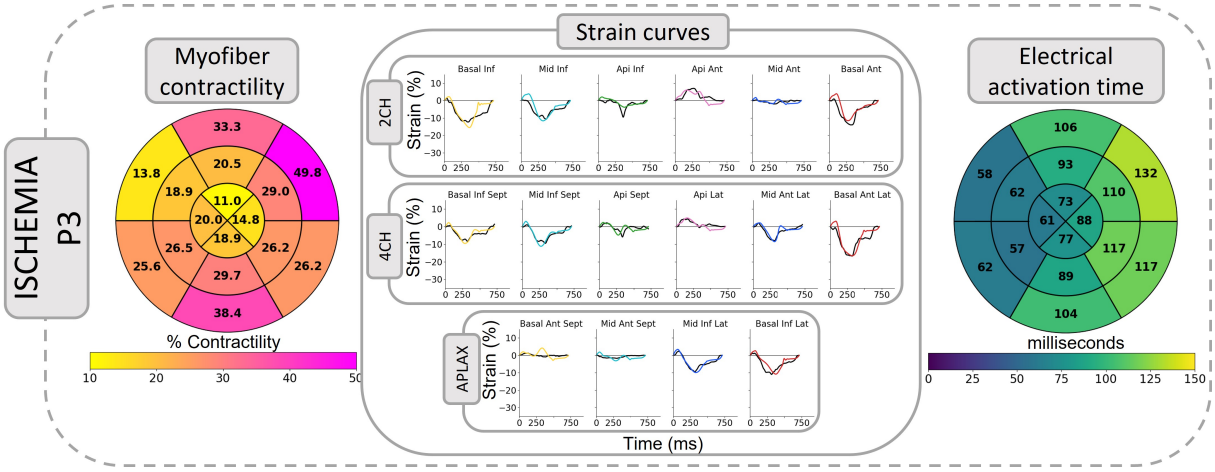

Figure A.11: Patient-specific simulation results for an ischemic LBBB patient. Experimental (*black*) and simulated (*colored*) strain curves corresponding to the 16 LV segments. Bull's-eye representations of segmental electrical activation delay and segmental myofiber contractility.

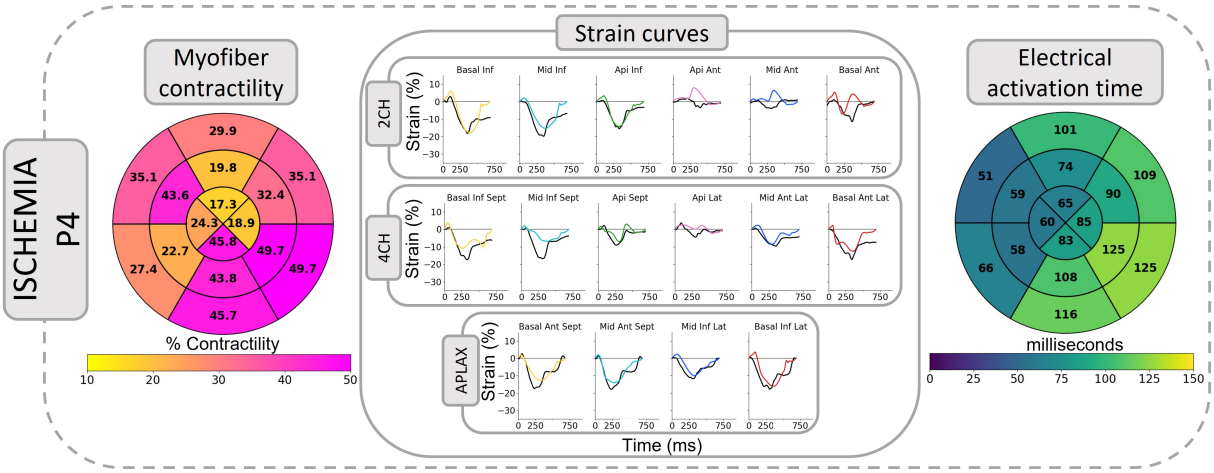

Figure A.12: Patient-specific simulation results for an ischemic LBBB patient. Experimental (*black*) and simulated (*colored*) strain curves corresponding to the 16 LV segments. Bull's-eye representations of segmental electrical activation delay and segmental myofiber contractility.

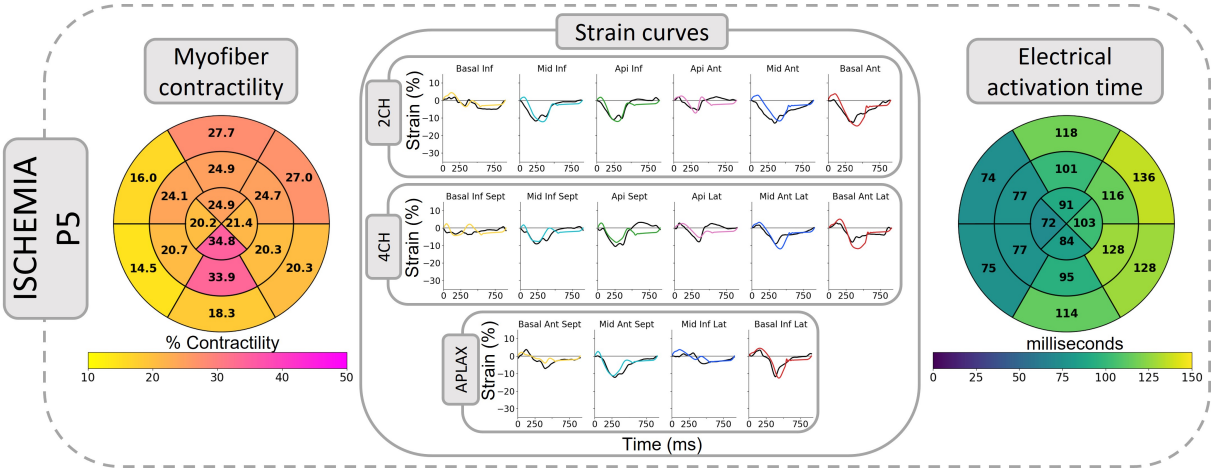

Figure A.13: Patient-specific simulation results for an ischemic LBBB patient. Experimental (*black*) and simulated (*colored*) strain curves corresponding to the 16 LV segments. Bull's-eye representations of segmental electrical activation delay and segmental myofiber contractility.

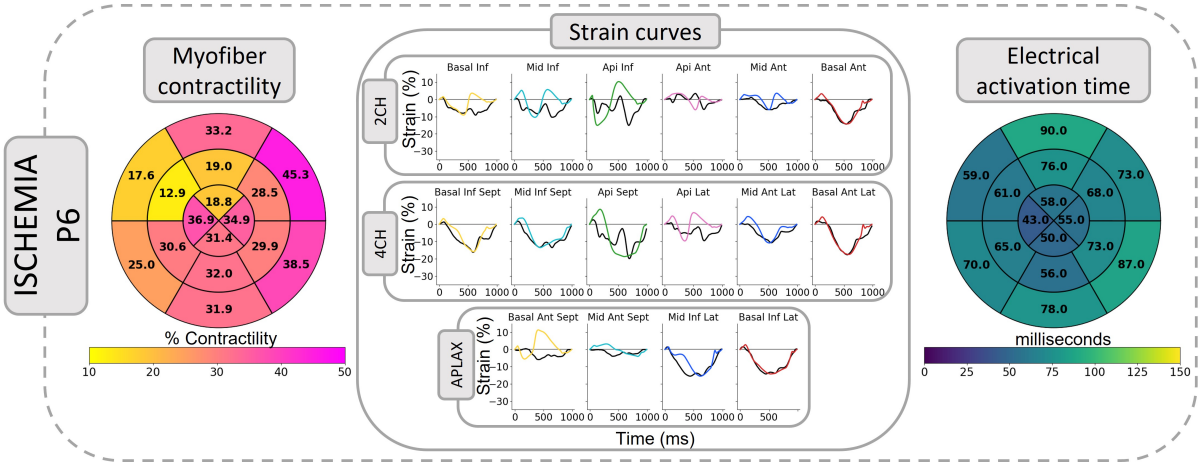

Figure A.14: Patient-specific simulation results for an ischemic LBBB patient. Experimental (*black*) and simulated (*colored*) strain curves corresponding to the 16 LV segments. Bull's-eye representations of segmental electrical activation delay and segmental myofiber contractility.

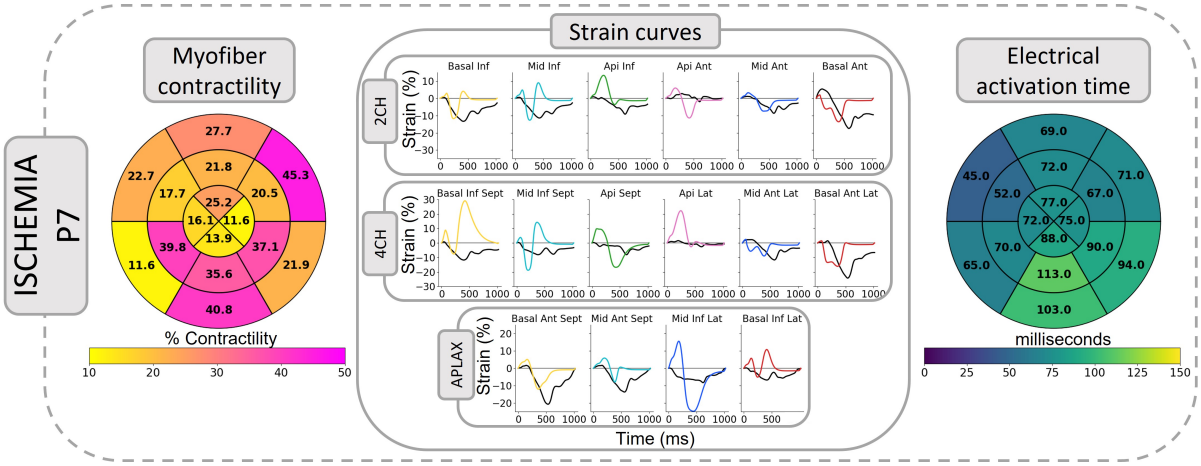

Figure A.15: Patient-specific simulation results for an ischemic LBBB patient. Experimental (*black*) and simulated (*colored*) strain curves corresponding to the 16 LV segments. Bull's-eye representations of segmental electrical activation delay and segmental myofiber contractility.

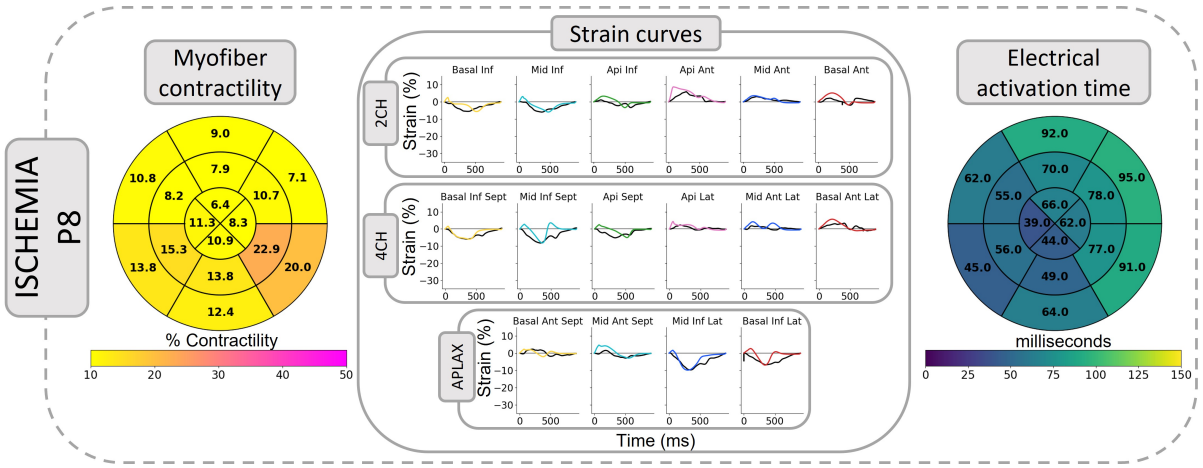

Figure A.16: Patient-specific simulation results for an ischemic LBBB patient. Experimental (*black*) and simulated (*colored*) strain curves corresponding to the 16 LV segments. Bull's-eye representations of segmental electrical activation delay and segmental myofiber contractility.

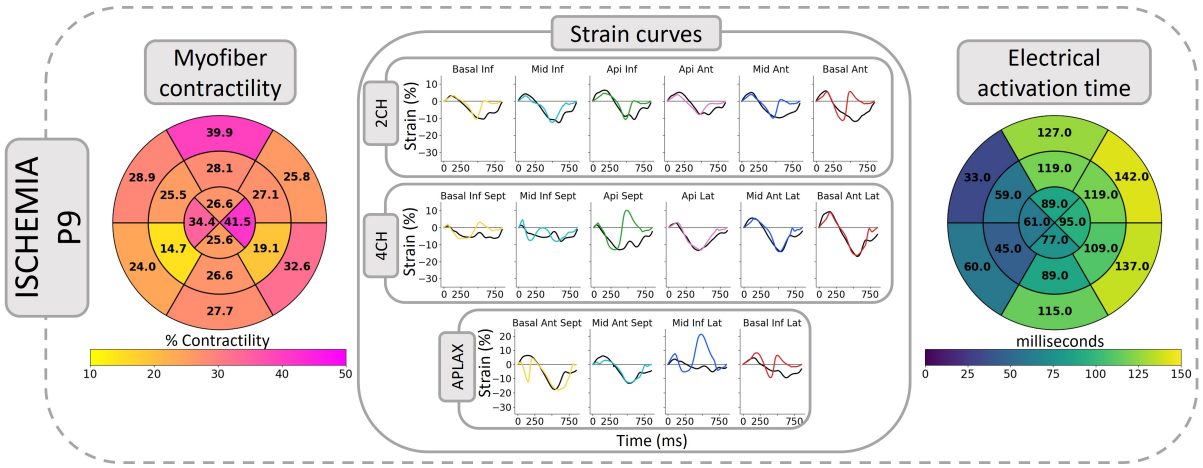

Figure A.17: Patient-specific simulation results for an ischemic LBBB patient. Experimental (*black*) and simulated (*colored*) strain curves corresponding to the 16 LV segments. Bull's-eye representations of segmental electrical activation delay and segmental myofiber contractility.

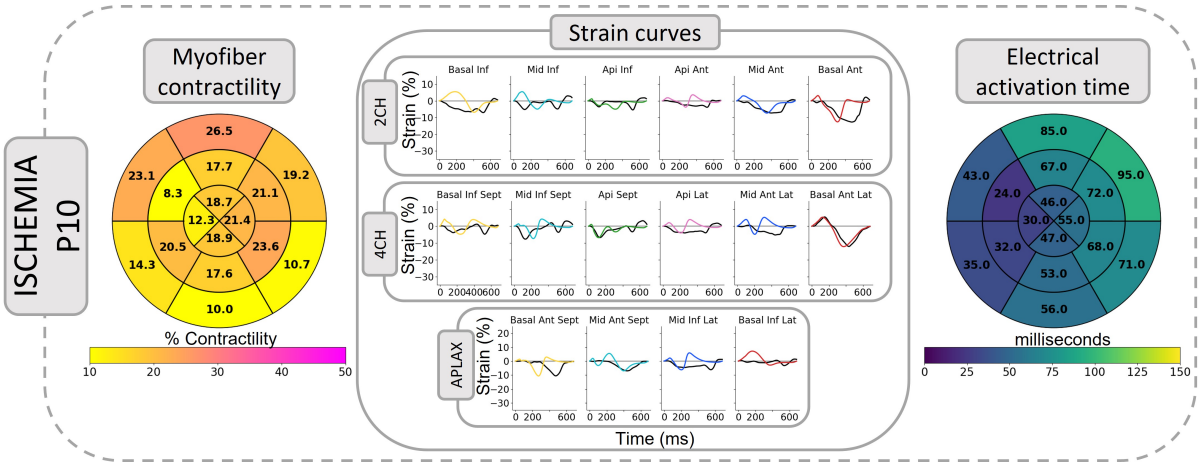

Figure A.18: Patient-specific simulation results for an ischemic LBBB patient. Experimental (*black*) and simulated (*colored*) strain curves corresponding to the 16 LV segments. Bull's-eye representations of segmental electrical activation delay and segmental myofiber contractility.

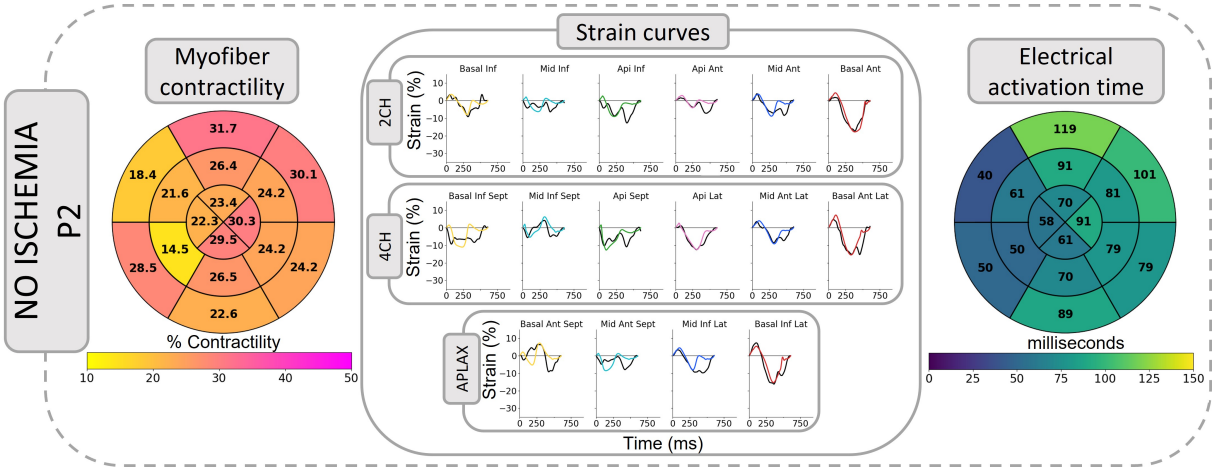

Figure A.19: Patient-specific simulation results for a non-ischemic LBBB patient. Experimental (*black*) and simulated (*colored*) strain curves corresponding to the 16 LV segments. Bull's-eye representations of segmental electrical activation delay and segmental myofiber contractility.

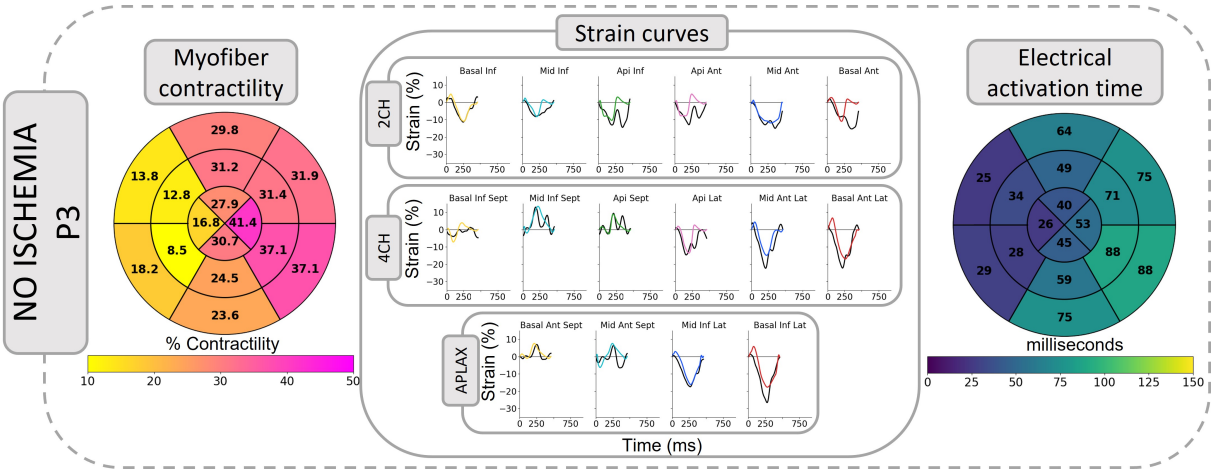

Figure A.20: Patient-specific simulation results for a non-ischemic LBBB patient. Experimental (*black*) and simulated (*colored*) strain curves corresponding to the 16 LV segments. Bull's-eye representations of segmental electrical activation delay and segmental myofiber contractility.

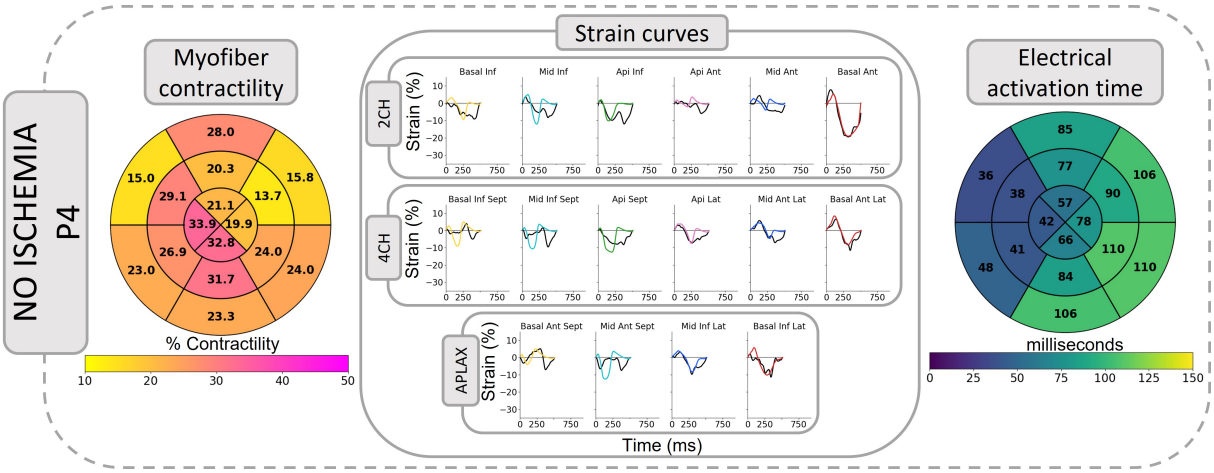

Figure A.21: Patient-specific simulation results for a non-ischemic LBBB patient. Experimental (*black*) and simulated (*colored*) strain curves corresponding to the 16 LV segments. Bull's-eye representations of segmental electrical activation delay and segmental myofiber contractility.

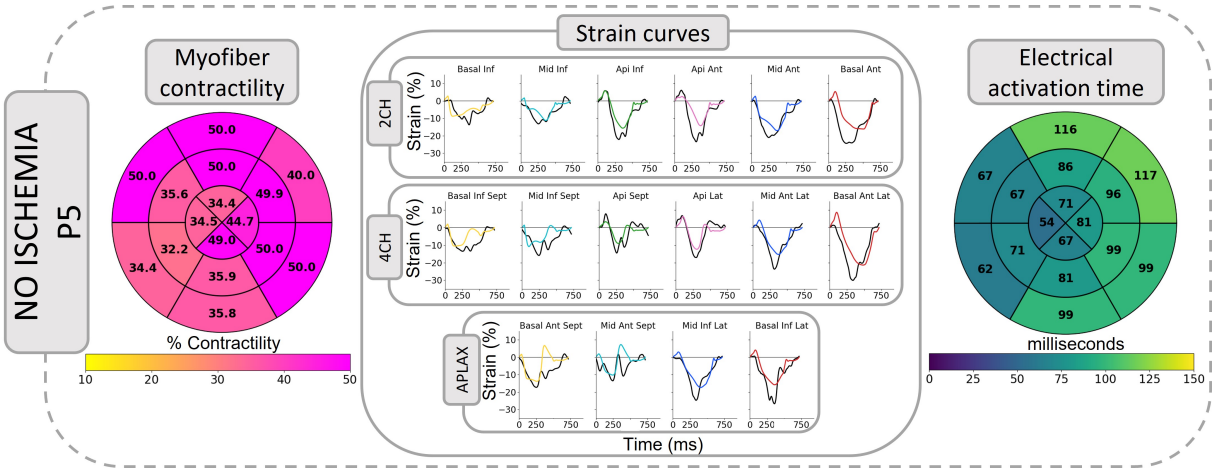

Figure A.22: Patient-specific simulation results for a non-ischemic LBBB patient. Experimental (*black*) and simulated (*colored*) strain curves corresponding to the 16 LV segments. Bull's-eye representations of segmental electrical activation delay and segmental myofiber contractility.

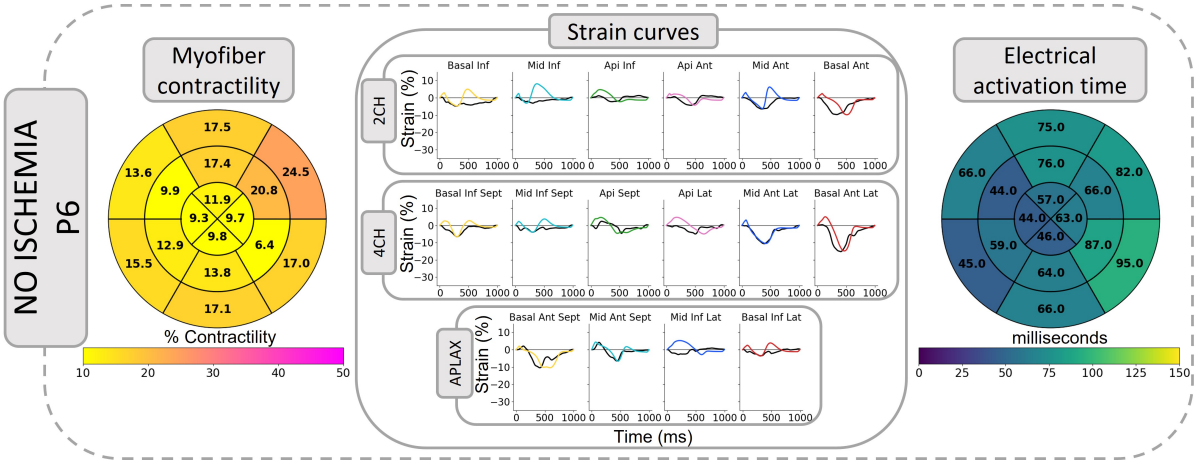

Figure A.23: Patient-specific simulation results for a non-ischemic LBBB patient. Experimental (*black*) and simulated (*colored*) strain curves corresponding to the 16 LV segments. Bull's-eye representations of segmental electrical activation delay and segmental myofiber contractility.

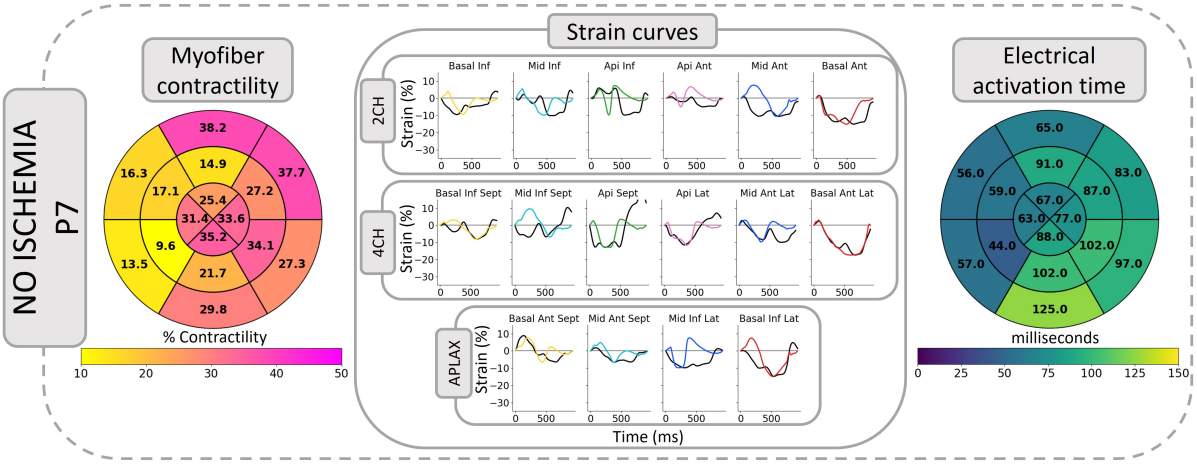

Figure A.24: Patient-specific simulation results for a non-ischemic LBBB patient. Experimental (*black*) and simulated (*colored*) strain curves corresponding to the 16 LV segments. Bull's-eye representations of segmental electrical activation delay and segmental myofiber contractility.

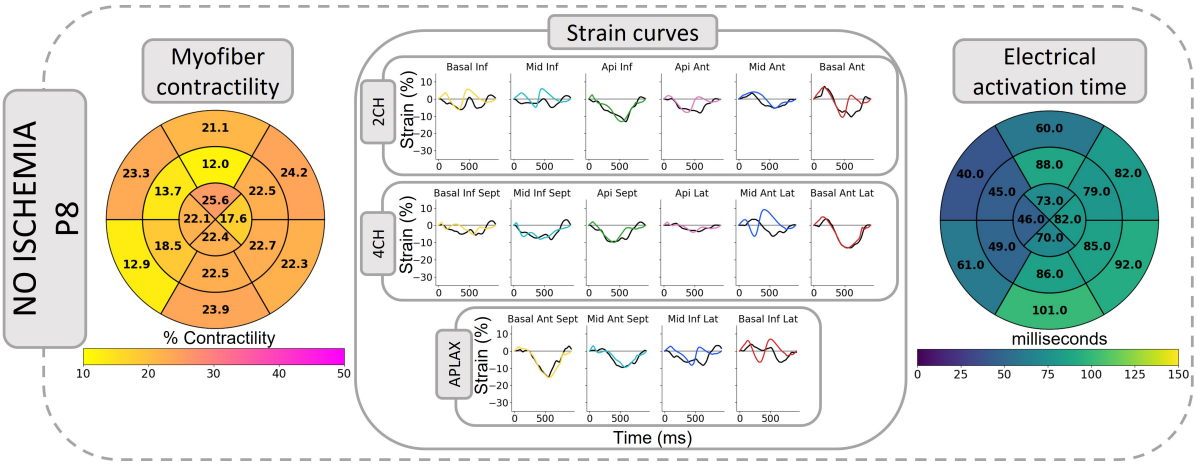

Figure A.25: Patient-specific simulation results for a non-ischemic LBBB patient. Experimental (*black*) and simulated (*colored*) strain curves corresponding to the 16 LV segments. Bull's-eye representations of segmental electrical activation delay and segmental myofiber contractility.

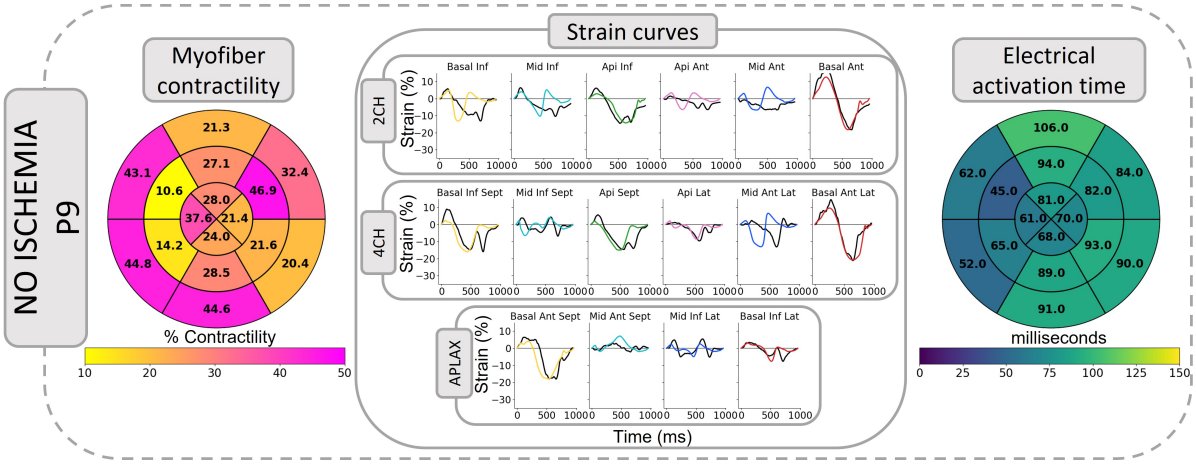

Figure A.26: Patient-specific simulation results for a non-ischemic LBBB patient. Experimental (*black*) and simulated (*colored*) strain curves corresponding to the 16 LV segments. Bull's-eye representations of segmental electrical activation delay and segmental myofiber contractility.

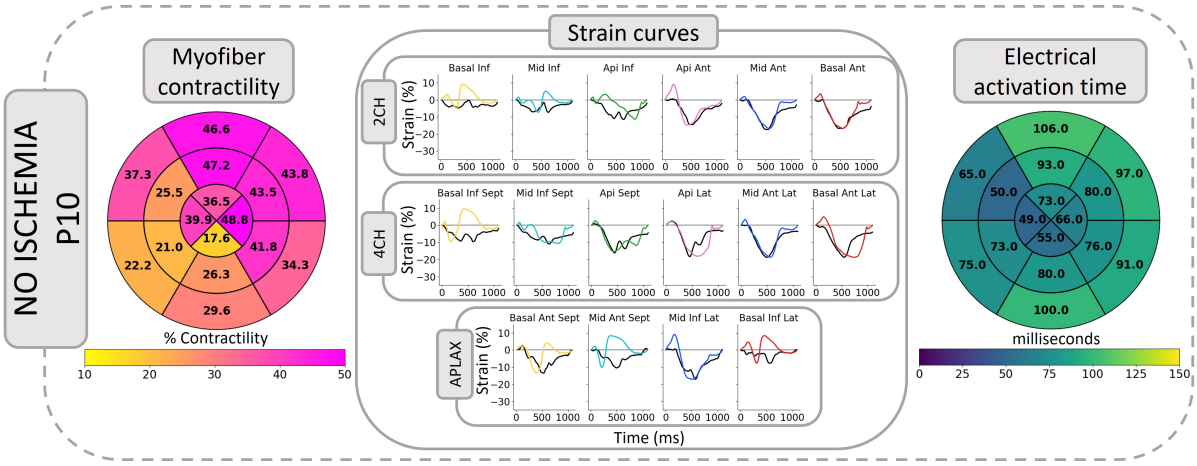

Figure A.27: Patient-specific simulation results for a non-ischemic LBBB patient. Experimental (*black*) and simulated (*colored*) strain curves corresponding to the 16 LV segments. Bull's-eye representations of segmental electrical activation delay and segmental myofiber contractility.

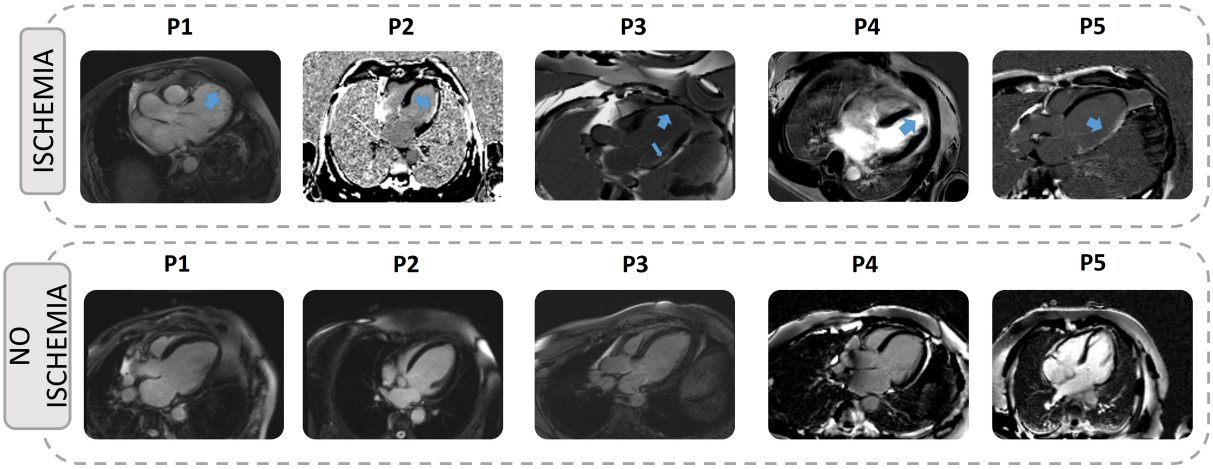

Figure A.28: MRI of 10 first LBBB patients with scar localization in the case of ischemia

Appendix

B Identified model parameters, clustering and digital twin simulations

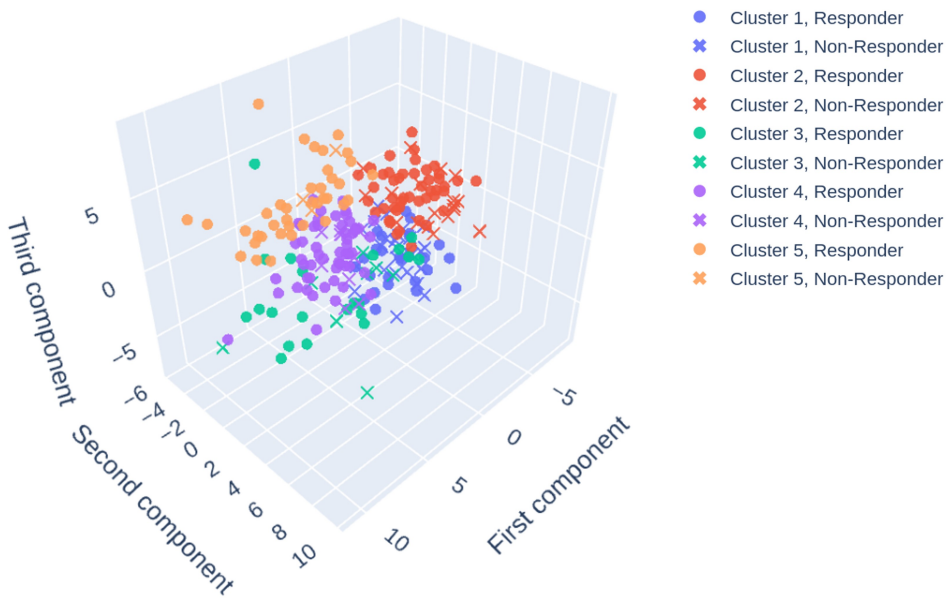

Figure B.1: PCA visualization of the database of 250 patients colored by cluster and symbolized by their CRT responses (cross: non-responder, circle: responder) in 3D.

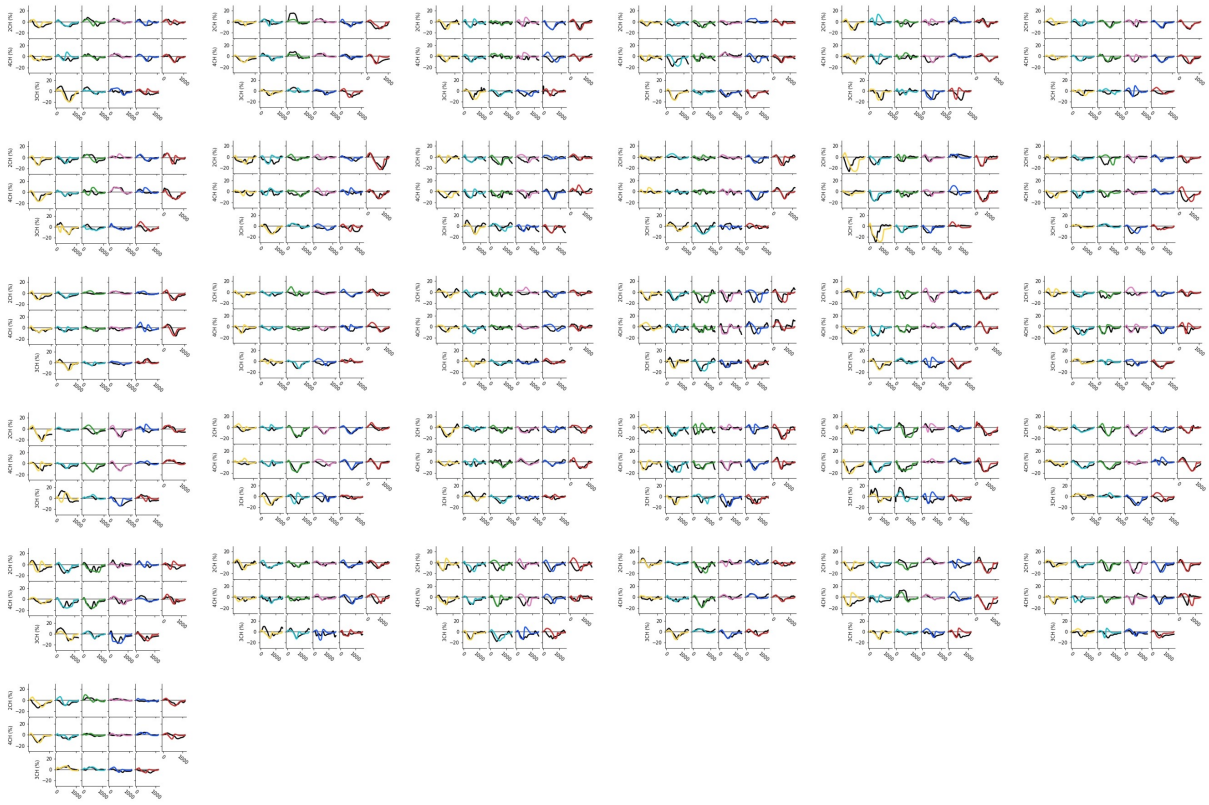

Figure B.2: Digital twin simulation of the 31 patients of the cluster 1.

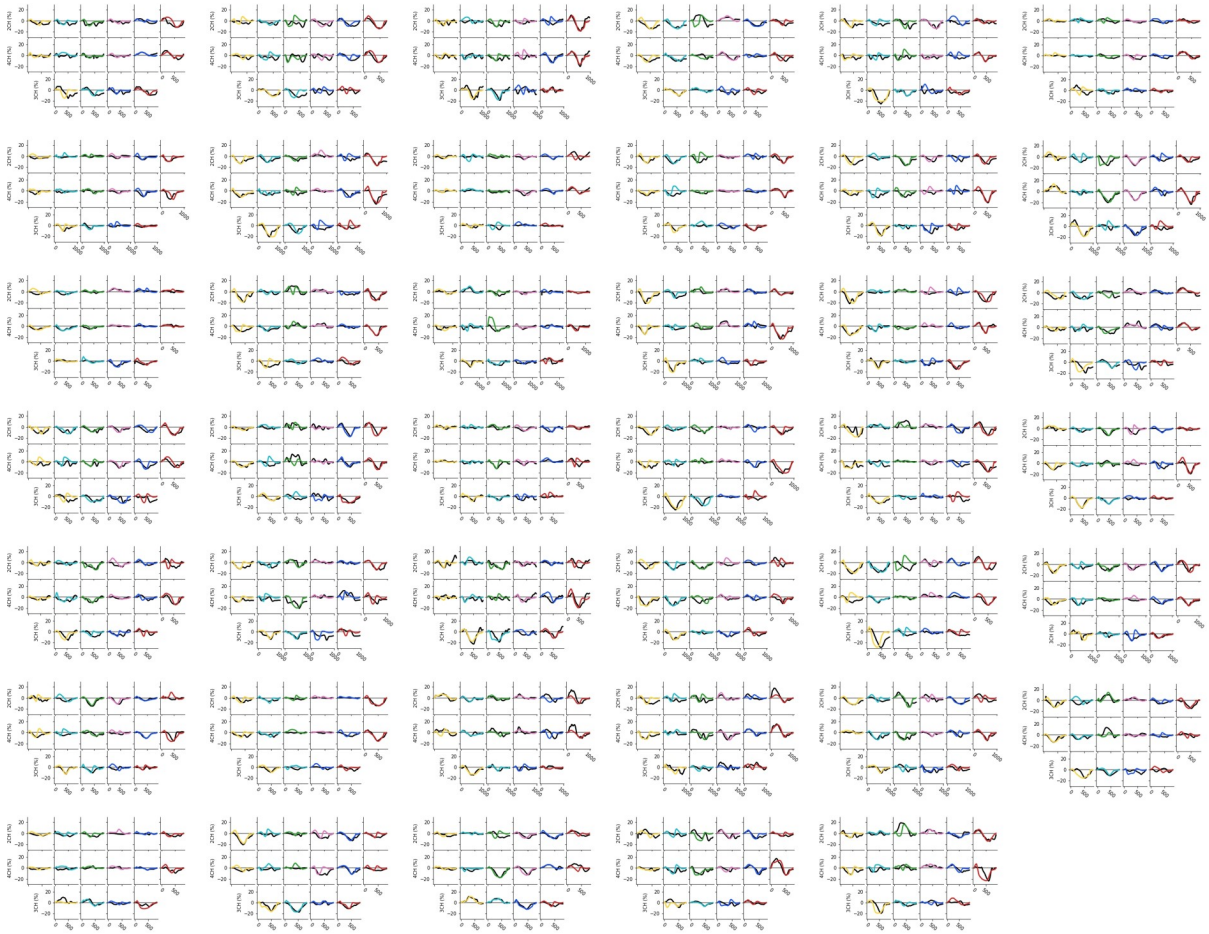

Figure B.3: Digital twin simulation of the 46 patients of the cluster 2.

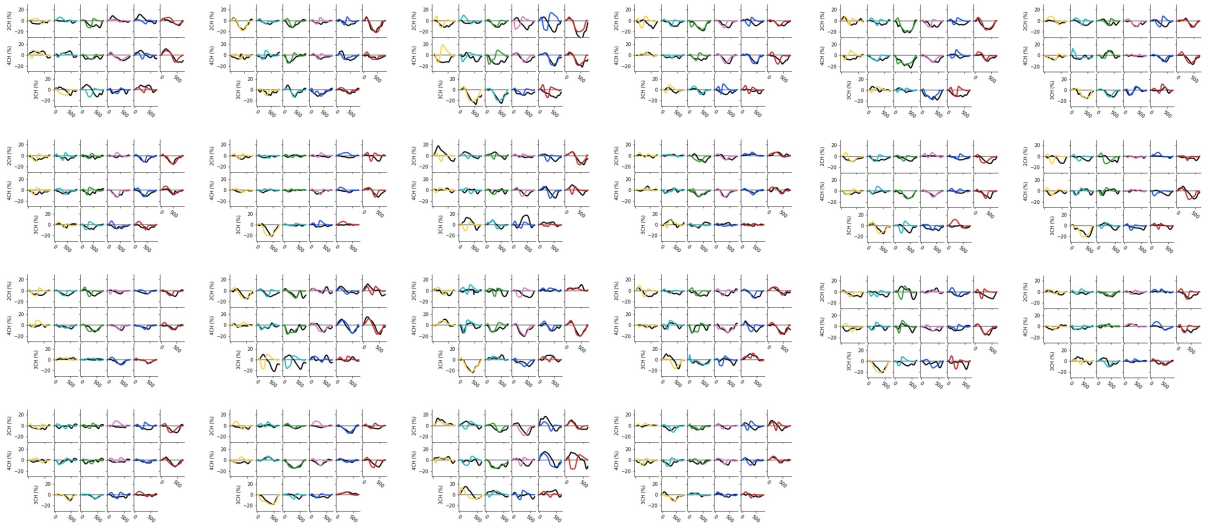

Figure B.4: Digital twin simulation of the 22 patients of the cluster 3.

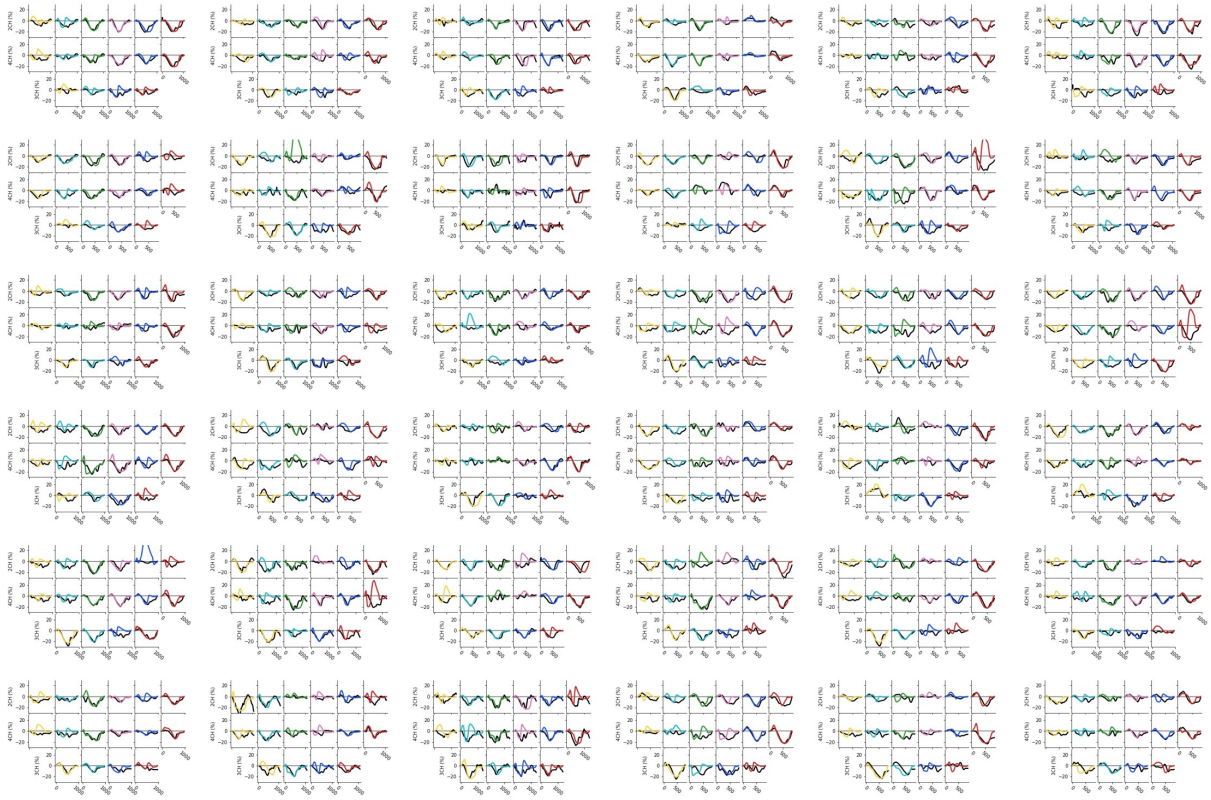

Figure B.5: Digital twin simulation of the 41 patients of the cluster 4.

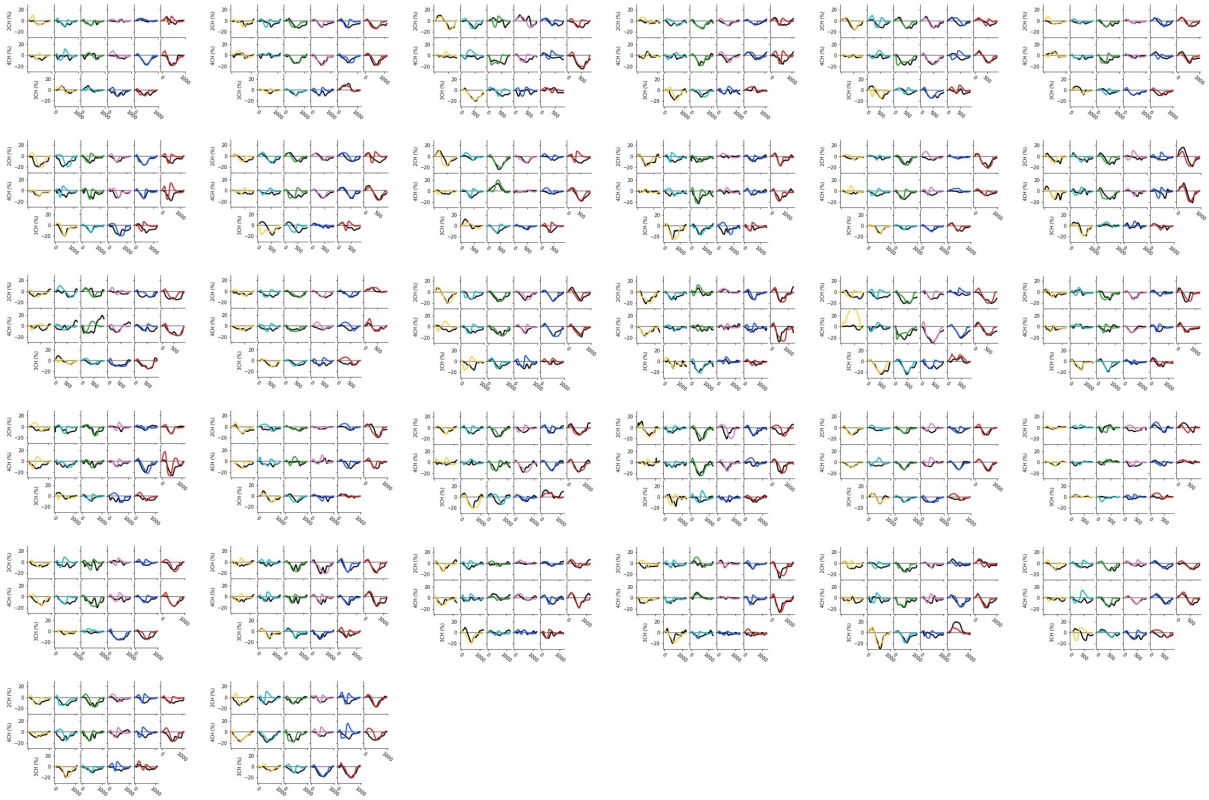

Figure B.6: Digital twin simulation of the 37 patients of the cluster 5.

Appendix

C Parameters of the AS model

Symbols	Descriptions	Values	Units
	Elastance-based cardiac cavities		
$E_{ra,max}$	Maximum systolic elastance of the right atrium	1.6	$mmHg/ml$
$E_{ra,min}$	Diastolic elastance of the right atrium	0.1	$mmHg/ml$
$E_{la,max}$	Maximum systolic elastance of the left atrium	1.6	$mmHg/ml$
$E_{la,min}$	Diastolic elastance of the right atrium	0.1	$mmHg/ml$
$V_{0,lv}$	Left ventricle volume intercept	10	ml
$V_{0,rv}$	Right ventricle volume intercept	10	ml
λ_{lv}	Curvature	0.014	$1/ml$
λ_{rv}	Curvature	0.013	$1/ml$
$P_{0,rv}$	Gradient	1.2001	$mmHg$
B_{la}	Constant, controlling the rise and peak of the left atrial systole	84.375	$1/s^2$
C_{la}	Constant, controlling the rise and peak of the left atrial systole	0.32	s
α_1	Constant controlling the steepness of the LV elastance curve	0.4	–
α_2	Constant controlling the steepness of the LV elastance curve	0.4	–
n_1	Constant controlling the steepness of the LV elastance curve	1.3	–
n_2	Constant controlling the steepness of the LV elastance curve	200	–
	Circulations		
E_{rv}	Elastance of the right ventricle	0.6526	$mmHg/ml$
E_{pa}	Elastance of the pulmonary artery	0.3375	$mmHg/ml$
E_{pv}	Elastance of the pulmonary vein	0.0062	$mmHg/ml$
E_{ao}	Elastance of the aorta	3.2906	$mmHg/ml$
E_{sa}	Elastance of the systemic arteries	0.8851	$mmHg/ml$
E_{sv}	Elastance of the systemic veins	0.010	$mmHg/ml$
E_{vc}	Elastance of the vena cava	0.0154	$mmHg/ml$
$V_{d,lv}$	Unstressed volume of the left ventricle	10	ml
$V_{d,rv}$	Unstressed volume of the right ventricle	10	ml
$V_{d,la}$	Unstressed volume of the left atrium	3	ml
$V_{d,ra}$	Unstressed volume of the right atrium	3	ml
$V_{d,pa}$	Unstressed volume of the pulmonary artery	160	ml
$V_{d,pv}$	Unstressed volume of the pulmonary vein	200	ml
$V_{d,ao}$	Unstressed volume of the aorta	197	ml

$V_{d,sa}$	Unstressed volume of the systemic arteries	521	ml
$V_{d,sv}$	Unstressed volume of the systemic veins	1908	ml
$V_{d,vc}$	Unstressed volume of the vena cava	1648	ml
R_{pul}	Pulmonary resistance	0.1425	$mmHg/ml$
R_{sys}	Systemic resistance	0.62	$mmHg/ml$
R_{vc}	Vena cava resistance	0.1935	$mmHg/ml$
R_{ao}	Aorta resistance	0.2915	$mmHg/ml$
R_{la}	Left atrium resistance	0.01	$mmHg/ml$
R_{ra}	Right atrium resistance	0.01	$mmHg/ml$
P_{th}	Intrathoracic pressure	-4	$mmHg$
	Cardiac valves		
ρ	Blood density	1.6	g/cm^3
$K_{vc,ao}$	Rate coefficient for aortic valve closure	0.15	$1/Pa{\cdot}s$
$K_{vo,ao}$	Rate coefficient for aortic valve opening	0.12	$1/Pa{\cdot}s$
$l_{eff,ao}$	Effective length for aortic valve	2.2	cm
$K_{vc,tc}$	Rate coefficient for tricuspid valve closure	0.4	$1/Pa{\cdot}s$
$K_{vo,tc}$	Rate coefficient for tricuspid valve opening	0.3	$1/Pa{\cdot}s$
$l_{eff,tc}$	Effective length for tricuspid valve	2	cm
$K_{vc,mt}$	Rate coefficient for mitral valve closure	0.4	$1/Pa{\cdot}s$
$K_{vo,mt}$	Rate coefficient for mitral valve opening	0.3	$1/Pa{\cdot}s$
$l_{eff,mt}$	Effective length for mitral valve	2	cm
$K_{vc,pu}$	Rate coefficient for pulmonary valve closure	0.4	$1/Pa{\cdot}s$
$K_{vo,pu}$	Rate coefficient for pulmonary valve opening	0.3	$1/Pa{\cdot}s$
$l_{eff,pu}$	Effective length for pulmonary valve	2	cm
$Aann_{ao}$	Cross-sectional area of aortic valve	to define$*$	cm
$Aann_{tc}$	Cross-sectional area of tricuspid valve	6	cm
$Aann_{mt}$	Cross-sectional area of mitral valve	5	cm
$Aann_{pu}$	Cross-sectional area of pulmonary valve	2.8	cm

Table C.1: Parameters, descriptions and values of the AS model.

$*$ to define with patient cross-sectional area of aortic valve.

Appendix

D Complete and ordered ridge features selection

name	value
Apical aneurysm	0.603682
Unexplained syncope	0.479694
Peak work (predicted LVEF ($< 50\%$)	0.367399
DTW^{MI}	0.295140
E/A ratio	0.276473
Mean E/e' ratio	0.244052
DTW^{MS}	0.203555
$S^{AL}_{peak} - S^{AL}_{avc} diffSavcminAL$	0.198312
LAV	0.189649
$S^{AA}_{peak} - S^{AA}_{avc}$	0.175610
HR (predicted %)	0.165722
E^{AA}	0.159778
NSVT	0.156570
$S^{MI}_{peak} - S^{MI}_{avc}$	0.154209
DTW^{ML}	0.150154
Female gender	0.139217
Apical LVH	0.138657
$S^{BS}_{peak} - S^{BS}_{avc}$	0.137950
$std(MI)$	0.137619
E^{D2}	0.135929
LVH septal localization	0.132580
DTW^{BL}	0.130960
Lateral localization on MRI	0.128673
Bêta-blocker treatment	0.128320
$S^{apex}_{peak} - S^{base}_{peak}$	0.127792
DTW^{AI}	0.127722
S^{BA}_{peak}	0.121578
DTW^{MA}	0.117785
t^{AAs}_{min}	0.115933
S^{AA}_{peak}	0.114654

VTSVG (ml)	0.110123
DTW^{MAs}	0.106426
HCM mutation gene	0.105879
DTW^{AP}	0.103770
I_{peak}^{D2}	0.102701
Mitral reduction (mild)	0.099613
S_{avc}^{BS}	0.098541
DTDVG (mm)	0.097201
Myomectomy/PTSMA	0.096148
t_{min}^{AS}	0.094672
DTW^{BA}	0.094383
VTDVG (ml)	0.089700
t_{min}^{ML}	0.089415
Mitral reduction (severe)	0.087793
I_{peak}^{BA}	0.086750
S_{peak}^{AI}	0.086415
$std(std)$	0.084990
E^{D4}	0.083752
normal	0.083225
DTW^{AL}	0.082425
$S_{peak}^{4CH} - S_{avc}^{4CH}$	0.077401
MRI localization inferior	0.076842
Ea moyen	0.076837
Localisation HVG septal	0.076509
$S_{peak}^{BL} - S_{avc}^{BL}$	0.076248
S_{avc}^{BA}	0.075697
E^{BI}	0.074696
LVOT gradient	0.074422
DTW^{AA}	0.073100
A	0.072012
E	0.071209
$S_{peak}^{MAs} - S_{avc}^{MAs}$	0.069638
I_{peak}^{D4}	0.068872
Mass ind ASE (g/m^2)	0.068067
t_{min}^{BAs}	0.067182
E^{BP}	0.065961
IEC/ ARA2 treatment	0.064976

$std(t_{min})$ =mechanical dispersion	0.063988
$std(ML)$	0.063471
t_{min}^{AI}	0.063109
I_{peak}^{AL}	0.062382
E^{AL}	0.061930
$I_{peak}^{I} - I_{peak}^{A}$	0.061474
MRI localization septal	0.061121
S_{peak}AL	0.060257
E^{BA}	0.059086
t_{min}^{BS}	0.058990
$S_{peak}^{AS} - S_{avc}^{AS}$	0.058630
$std(S_{peak})$	0.057917
$S_{peak}^{BI} - S_{avc}^{BI}$	0.057134
S_{peak}^{MI}	0.056457
Q wave or PRWP	0.056277
t_{min}^{BL}	0.055997
E^{MS}	0.055849
ST changes	0.055789
I_{peak}^{AA}	0.055492
LGE	0.054570
HR (bpm)	0.053876
S_{avc}^{MS}	0.052771
t_{min}^{BI}	0.052441
S_{peak}^{BI}	0.052098
S_{avc}^{ML}	0.051876
$S_{peak}^{2CH} - S_{avc}^{2CH}$	0.051635
I_{peak}^{BI}	0.051552
Coronary artery disease	0.050942
I_{peak}^{BS}	0.050798
t_{min}^{MI}	0.049785
LV GLS	0.049510
S_{avc}^{MA}	0.048407
S_{avc}^{AA}	0.048259
I_{peak}^{MI}	0.048243
t_{min}^{AL}	0.048114
DTW^{MP}	0.047469
DTW^{BP}	0.047166

DTSVG (mm)	0.046999
t_{min}^{BP}	0.046851
Calcium-blocker treatment	0.046707
t_{min}^{MAs}	0.046430
$std(BP)$	0.046372
OAC	0.045833
SBP (mmHg)	0.045505
HCM family history	0.045355
E^{MA}	0.043647
S_{peak}^{MAs}	0.042232
E^{AAs}	0.041196
max thickness $\geq$ 30 mm	0.039502
S_{avc}^{AS}	0.039252
t_{min}^{3CH}	0.038412
t_{min}^{AA}	0.038167
E^{BAs}	0.037539
AP OG (mm)	0.037263
E^{MI}	0.036871
I_{peak}^{AAs}	0.036610
S_{avc}^{AL}	0.036592
$std(MS)$	0.036229
$S_{peak}^{AP} - S_{avc}^{AP}$	0.035408
I_{peak}^{I}	0.034907
S_{avc}^{MI}	0.034649
$std(BI)$	0.034487
S_{avc}^{BL}	0.034275
I_{peak}^{AS}	0.034272
$std(AI)$	0.034193
$std(AAs)$	0.033822
$std(BAs)$	0.033656
S_{avc}^{AP}	0.033648
BMI	0.033489
Gradient LV at rest	0.032578
E^{MP}	0.031225
S_{avc}^{BP}	0.031213
I_{peak}^{BL}	0.030865
E^{AI}	0.030828

E^{P}	0.030650
E^{I}	0.030647
$S^{AI}_{peak} - S^{AI}_{avc}$	0.030281
$std(BL)$	0.029430
E^{BS}	0.029291
I^{MAs}_{peak}	0.028223
E^{3CH}	0.028208
S^{MP}_{avc}	0.028160
$S^{BAs}_{peak} - S^{BAs}_{avc}$	0.027512
E^{AP}	0.027297
MS family history	0.027162
Localization HVG septal	0.026859
S^{A}_{avc}	0.026454
t^{4CH}_{min}	0.026359
I^{ML}_{peak}	0.025952
t^{AP}_{min}	0.025710
t^{MA}_{min}	0.025193
S^{2CH}_{avc}	0.024907
moderate MR	0.024881
age	0.024653
$std(MP)$	0.024635
E^{A}	0.024600
I^{L}_{peak}	0.024517
E^{As}	0.024462
t^{BA}_{min}	0.023928
S^{L}_{avc}	0.023275
$S^{BP}_{peak} - S^{BP}_{avc}$	0.023096
S^{I}_{avc}	0.022846
BS (m^2)	0.022846
S^{ML}_{peak}	0.022509
S^{4CH}_{avc}	0.022461
E^{S}	0.022459
E^{MAs}	0.021971
$std(AMs)$	0.021604
Localisation HVG ant	0.021482
S^{S}_{avc}	0.021126
S^{BS}_{peak}	0.020905

$std(AA)$	0.020345
DTW^{BAs}	0.020118
S_{avc}^{AI}	0.020066
I_{peak}^{2CH}	0.020056
S_{avc}^{MAs}	0.019905
NYHA	0.019640
E	0.019634
I_{peak}^{BP}	0.018238
$std(BA)$	0.017931
I_{peak}^{BAs}	0.017112
QRS enlargement	0.016947
S_{avc}^{AAs}	0.016759
$std(BS)$	0.016265
TDE	0.016103
$S_{peak}^{MS} - S_{avc}^{MS}$	0.015803
$S_{peak}^{MP} - S_{avc}^{MP}$	0.015700
I_{peak}^{AP}	0.015645
S_{peak}^{MS}	0.015503
$S_{peak}^{BA} - S_{avc}^{BA}$	0.015305
E^{ML}	0.015296
SIVd (mm)	0.015078
E^{L}	0.014947
S_{peak}^{AS}	0.014471
I_{peak}^{4CH}	0.014191
S_{avc}^{BAs}	0.013916
$S_{peak}^{AAs} - S_{avc}^{AAs}$	0.012994
E^{BL}	0.012342
LVEF (%)	0.012030
I_{peak}^{P}	0.011986
S_{peak}^{BAs}	0.011909
I_{peak}^{3CH}	0.011909
MRI localization anterior	0.011804
S_{peak}^{AAs}	0.011706
I_{peak}^{As}	0.011538
std^{mean}	0.011198
PWEDT (mm)	0.010502
S_{avc}^{D3}	0.009888

t_{min}^{MP}	0.009812
DTW^{BI}	0.009745
$std(AL)$	0.009577
$I_{peak}^{apex} - I_{peak}^{base}$	0.009040
S_{peak}^{MP}	0.009037
size (cm)	0.008363
DTW^{AS}	0.008185
DTW^{BS}	0.008014
DTW^{AAs}	0.007820
T wave inversion	0.007731
S_{peak}^{BP}	0.007678
S_{avc}^{P}	0.007465
HCM mutation	0.007264
E^{D3}	0.007192
S_{peak}^{3CH}	0.007021
S_{avc}^{BI}	0.006750
$std(AP)$	0.006545
S_{peak}^{AP}	0.006303
Diastolic blood pressure (mmHg)	0.006236
$I_{peak}^{S} - I_{peak}^{L}$	0.005938
$S_{peak}^{ML} - S_{avc}^{ML}$	0.005057
S_{avc}^{3CH}	0.004989
S_{peak}^{MA}	0.004748
$S_{peak}^{3CH} - S_{avc}^{3CH}$	0.004733
$std(MAs)$	0.004267
t_{min}^{MS}	0.004254
$t_{peak}^{AAs} - t_{avc}^{AAs}$	0.004079
I_{peak}^{A}	0.004078
E^{4CH}	0.003838
$t_{peak}^{AI} - t_{avc}^{AI}$	0.003750
E^{2CH}	0.003671
S_{peak}^{BL}	0.003475
I_{peak}^{S}	0.003327
$std(MA)$	0.003240
$t_{peak}^{ML} - t_{avc}^{ML}$	0.003122
I_{peak}^{MP}	0.003026
$t_{peak}^{BL} - t_{avc}^{BL}$	0.002910

$t_{peak}^{BAs} - t_{avc}^{BAs}$	0.002909
S_{avc}^{As}	0.002773
$t_{peak}^{BS} - t_{avc}^{BS}$	0.002683
$t_{peak}^{AA} - t_{avc}^{AA}$	0.002592
I_{peak}^{D3}	0.002474
S_{avc}^{D4}	0.002288
avc timing	0.002275
$t_{peak}^{4CH} - t_{avc}^{4CH}$	0.002215
$t_{peak}^{BP} - t_{avc}^{BP}$	0.002214
S_{peak}^{2CH}	0.002160
$t_{peak}^{MS} - t_{avc}^{MS}$	0.002149
$t_{peak}^{AL} - t_{avc}^{AL}$	0.002142
$t_{peak}^{3CH} - t_{avc}^{3CH}$	0.002039
S_{avc}^{D2}	0.001974
weight (kg)	0.001937
S_{peak}^{4CH}	0.001930
$std(I_{peak})$	0.001775
$t_{peak}^{2CH} - t_{avc}^{2CH}$	0.001757
$t_{peak}^{MA} - t_{avc}^{MA}$	0.001667
E^{AS}	0.001559
$t_{peak}^{AP} - t_{avc}^{AP}$	0.001442
$t_{peak}^{BA} - t_{avc}^{BA}$	0.001403
t_{min}^{2CH}	0.001212
I_{peak}^{AI}	0.001212
$t_{peak}^{MI} - t_{avc}^{MI}$	0.001029
$I_{peak}^{As} - I_{peak}^{P}$	0.000934
$t_{peak}^{MAs} - t_{avc}^{MAs}$	0.000834
$t_{peak}^{MP} - t_{avc}^{MP}$	0.000757
max thickness	0.000633
$t_{peak}^{AS} - t_{avc}^{AS}$	0.000284
I_{peak}^{MA}	0.000278
$t_{peak}^{BI} - t_{avc}^{BI}$	0.000101
I_{peak}^{MS}	0.000041

Table D.1: Complete table of features in HCM study. Features are classed by decreasing Ridge coefficients importance.

COLLEGE SCIENCES
DOCTORAL DE LA VIE
BRETAGNE ET DE LA SANTE

Université de Rennes

Titre : Approche hybride, combinant des modèles computationnels et d'apprentissage automatique pour l'analyse du strain myocardique et l'évaluation de la fonction cardiaque.

Mot clés : Modèle computationnel, apprentissage automatique, jumeau numérique, echocardiographie, sténose aortique, bloc de branche gauche, cardiomyopathie hypertrophique

Résumé : L'évaluation de la fonction cardiaque est un enjeu majeur en cardiologie, en particulier dans la prise en charge des patients atteints d'insuffisance cardiaque. Malgré les avancées technologiques, telles que les courbes de *strain* extraites de l'échocardiographie, cette évaluation reste difficile et incomplète en raison de sa nature multifactorielle. L'objectif est de proposer de nouvelles méthodes permettant une compréhension plus précise et personnalisée de la fonction ventriculaire gauche chez les patients insuffisance cardiaque. Des approches hybrides combinant la modélisation in silico, traitement du signal et apprentissage automatique ont été proposées.
Quatre problématiques associées à différents phénotypes d'insuffisance cardiaque sont abordées dans cette thèse : i) Les courbes de *strain* de 10 sujets sains et 20 patients atteints de bloc de branche gauche ont été analysées à l'aide d'un modèle computationnel. ii) Une caractérisation des profils de réponse à la thérapie de resynchronisation cardiaque a été proposée sur 250 patients éligibles grâce à des approches hybrides. iii) Une estimation non invasive de la pression ventriculaire gauche a été proposée et évaluée sur 67 patients atteints de sténose aortique afin d'obtenir des indices de travail myocardique. iv) Une classification du risque de mort subite chez les patients atteints de cardiomyopathie hypertrophique a été développée à partir de paramètres cliniques, d'imagerie et extrait du *strain* de 434 patients.
Ces approches originales utilisent principalement des mesures non invasives issues de l'échocardiographie et introduisent de nouveaux outils d'intelligence artificielle dans la pratique clinique. Elles visent à être spécifiques à chaque patient afin d'être intégrées dans un processus de médecine personnalisée.

Title: Hybrid approach, combining computational and machine-learning models, for the analysis of myocardial strain and cardiac function evaluation.

Keywords: Computational model, machine learning, digital twin, echocardiography, aortic stenosis, left bundle branch block, hypertrophic cardiomyopathy

Abstract: The cardiac function evaluation is a major health issue in cardiology, and particularly for the management of patients with heart failure. Despite technological progress and the arrival of myocardial deformation curves extracted from echocardiography: strain curve, the cardiac function evaluation remains difficult and incomplete due to its multifactorial nature. The objective of this thesis is to propose new methods allowing a more precise and personalized understanding of the left ventricular function of heart failure patients. Hybrid approaches, combining in-silico modeling, classical signal processing and machine learning, were proposed.
Four issues associated with different heart failure phenotypes are addressed in this thesis: i) Strain curves of 10 healthy subjects and 20 patients with left bundle branch block were analyzed by a computational model. ii) A characterization of the responder profiles for cardiac resynchronization therapy were proposed thanks to the application of hybrid approaches on 250 eligible patients. iii) Non-invasive left ventricle pressure estimation was proposed and evaluated on 67 aortic stenosis patients to obtain myocardial work indices, iv) A classification of sudden death risk in patients was developed on clinical, imaging and strain extracted parameters of 434 patients with hypertrophic cardiomyopathy.
Original approaches combining both machine learning algorithms and digital twin cohorts have been proposed and applied. The proposed methods mainly use non-invasive measurements from echocardiography and bring new artificial intelligence tools to clinical practice. They aim at being patient-specific in order to be integrated in a personalized medicine process.